Author:
Algharaibeh, Sana W A R

Title:
Fabrication and characterisation of biomimetic nacre-like ceramic/polymer composite a potential CAD/CAM dental material

Fabrication and characterisation of biomimetic nacre-like ceramic/polymer composite a potential CAD/CAM dental material

Sana Algharaibeh

A dissertation submitted to the University of Bristol in accordance with the requirements for award of Doctor of Philosophy in the Faculty of Health Science

Bristol Dental School

October 2019

Word counts: 50,148

Abstract

Objective. To fabricate and characterise a biomimetic nacre-like ceramic/polymer composite material, comprising a highly aligned lamellar ceramic scaffold infiltrated with polymer, as a potential chairside CAD/CAM dental material.

Method. Bi-directional freeze-casting was used to fabricate highly aligned Al_2O_3 ceramic scaffolds. Different lamellar microstructures were created by controlling processing parameters such as cooling rate, mould slope angle, solid loading, binder and MgO sintering aid concentrations. Once created, the green body scaffolds underwent two separate sintering steps, along with an intermediate uniaxial pressing stage, to produce densified ceramic scaffolds. These were then silanised with γ-MPS coupling agent before being infiltrated with UDMA/TEGDMA polymer to fabricate biomimetic composite materials with anisotropic microstructure and tuneable ceramic fractions. The mechanical properties (flexural strength, elastic modulus, hardness and fracture toughness) of the composite materials were characterised and compared to a commercial CAD/CAM composite material (Vita Enamic). Microstructural characterisation included optical microscopy, scanning electron microscopy (SEM) and micro-computerised tomography (micro-CT).

Results. Highly aligned lamellar ceramic scaffolds were produced by freezing under dual (bi-directional) temperature gradients. Ceramic scaffolds with a lamellar microstructure and different ceramic volume fractions were created by first-step sintering, followed by uniaxial pressing and then second-step sintering. Densified ceramic scaffolds with a brick-and-mortar structure were obtained similar to that seen in nacre. Silanisation of the final scaffold enabled good bonding between the ceramic and polymer phases, as confirmed by SEM. Biomimetic nacre-like ceramic/polymer composites (BCPCs) were fabricated with different ceramic volume fractions ranging from (70% to 76%). The flexural strength of the BCPCs ranged from 135.08 to 172.65 MPa, the elastic modulus from 57.75 to 105.4 GPa, hardness from 3.07 to 4.58 GPa and fracture toughness from 2.54 to 3.19 $MPa.m^{1/2}$. These were all superior to that seen with commercially available Vita Enamic. The BCPCs also demonstrated good machinability.

Significance. Bi-directional freeze casting is a suitable method by which to fabricate highly aligned lamellar ceramic scaffolds. These scaffolds can be further engineered to produce a unique nacre-like ceramic preform capable of infiltration with a second phase of polymer. There was a correlation between the ceramic microstructure and the mechanical properties of the composite materials. These novel composite materials show potential as chairside CAD/CAM dental materials.

Acknowledgements

First, I would like to praise **Allah** (Our Lord, to You is all praise, abundant, beautiful and blessed praise).

I would like to express my sincere gratitude to my supervisors **Prof. Bo Su** and **Prof. Antony Ireland,** for the continuous support during my PhD study, for their motivation, patience and immense knowledge. Their guidance helped me in all the time of research and writing this thesis.

I want to acknowledge my lab mates for their wonderful collaboration and for the helpful discussions. Also, special thanks to the Biomaterial lab technician **Mark Ginty**, his dedicated work in the lab made it a good working place.

From the bottom of my heart I would like to say big thank you to my husband, **Mohamed Yousef**, without your constant co-operation and understanding, I would not have done this hard work. I am incredibly appreciative of my daughters **Layan** and **Sara** for being very patient with the busy mum they have. I would like to thank my family: my parents and my sisters and my brother for supporting me spiritually throughout the whole PhD journey. Honestly, I feel speechless in front of your unconditional love and support. In some ways, it is your achievement too. I would also like to thank my friend **Dr. Mincy Naduthottathil**, for being a lovely office mate who ended up being one of my best friends. I would like to express my gratitude and appreciation to my friends **Zahra** and **Saadiyah,** for their constant support and help taking care of the girls.

Finally, I would like to gratefully acknowledge the financial support offered by Jordan University of Science and Technology.

Author’s Declaration

I declare that the work in this dissertation was carried out in accordance with the requirements of the University's Regulations and Code of Practice for Research Degree Programmes and that it has not been submitted for any other academic award. Except where indicated by specific reference in the text, the work is the candidate's own work. Work done in collaboration with, or with the assistance of, others, is indicated as such. Any views expressed in the dissertation are those of the author.

SIGNED: ……. DATE: ……

Table of contents

List of Figures

List of Tables

Abbreviations

γ-MPS	3-(trimethoxysilyl)propyl methacrylate
3D	Three-Dimension
°C	Cellulose degrees
Al_2O_3	Alumina
Bis-GMA	Bisphenol A-glycidyl methacrylate
CAD/CAM	Computer Aided Design/Computer Aided Manufacturing
cm	Centimetre
DEJ	Dentine-Enamel Junction
g	Gram
GPa	Gigapascal
h	Hours
H_2O_2	Hydrogen peroxide
H_2SO_4	Sulphuric acid
IEP	Isoelectric point
kV	Kilovolt
mbar	Millibar
MgO	Magnesia
micro-CT	Micro Computerised Tomography
mins	Minutes
ml	Millilitre
mm	Millimetre
µm	Micrometre
mol	Mole
MPa	Megapascal
mV	Millivolts
MW	Molecular Weight
N	Newton
PDMS	Polydimethylsiloxane
PICN	Polymer-infiltrated-ceramic-network
PMMA	polymethyl methacrylate
PVA	Polyvinyl alcohol
rpm	Revolutions per minute
SD	Standard Deviation
sec	Seconds
SEM	Scanning Electron Microscopy
SiC	Silicon Carbide
SR	Silicon Rubber
TEGDMA	Triethylene glycol dimethacrylate
UDMA	Urethane dimethacrylate
vol	Volume
wt	Weight

Chapter 1. Introduction

Restorative dentistry is constantly developing, providing dentists with a wide range of restorative materials to satisfy the biosafety and aesthetic demands of the market [1]. Worldwide, many dental clinics and even countries consider metal-based restorations to be old fashioned and are shifting toward aesthetic restorative materials, such as composites and ceramics, providing patients with more natural-looking restorations [2]. This has led to a new era in aesthetic dentistry [3, 4] and new materials have to meet these challenges both aesthetically and mechanically. Moreover, the emerging concept of minimally invasive dentistry, which aims to preserve as much intact tooth tissue as possible, has further increased the mechanical demands on the newly fabricated restorative dental materials [5].

Computer aided design/computer aided manufacture (CAD/CAM) ceramics, in various forms, are increasingly becoming the material of choice to restore severly damaged, broken down teeth [6]. Current chairside CAD/CAM materials are either ceramics or ceramic/polymer composites with a multiphase, or interpenetrating network structure. Ceramic CAD/CAM materials are brittle, stiff and very hard, and as a result, pose problems such as a potential for catastrophic failure, difficulties in machinability and unwanted wear of opposing tooth structure [7]. Ceramic/polymer CAD/CAM materials were introduced in an attempt to overcome some of these issues. They are less brittle, have a lower stiffness and hardness, and so are more machinable and tooth friendly [8]. Despite these advantages, they can still suffer mechanical failure during use [9]. In addition, all CAD/CAM materials are isotropic with none of them possessing the anisotropic microstructure of natural tooth tissue.

In restorative dentistry, there are two important criteria for restorative materials to fulfill. Firstly, they should possess good mechanical properties to enable the material to withstand the harsh oral environment. Secondly, they need to be aesthetically pleasing to meet the high aesthetic demands of patients. The recent development in CAD/CAM systems makes the aesthetic criterion easy to fulfill, but possessing superior mechanical properties is still a problem[10]. The definition of superior mechanical properties differs according to different applications. To be able to define these properties for dental applications, we need to consider natural tooth tissue and how the microstructure contributes to the mechanical properties necessary for a lifetime of use. Human teeth comprise two principal tissues, enamel and dentine, with totally different microstructures and hence characteristics. While enamel is hard and brittle, dentine is soft and tough. This huge difference in their mechanical properties is due to their underlying microstructure. Enamel consists mainly of hydroxyapatite mineral (96 wt.%) and water (3%), with a very low (1wt.%) organic material content. This high mineral content gives enamel high compressive strength and hardness. Dentine, on the other hand, contains a higher percentage of organic material (20 wt.%), which makes it a softer and tougher tissue than enamel [11]. Due to its hierarchical structure, dentine also possesses high compressive and flexural strengths. It is one of the natural materials that combines both strength and toughness. However, these two properties alone are not sufficient to withstand the high masticatory forces inside the mouth, hence the covering of the much harder enamel. These two dissimilar materials, therefore, work together to give human teeth the ability to function perfectly inside the oral environment. The large difference in composition and mechanical properties is bridged at the dentine-enamel junction (DEJ), which joins the enamel and dentine to produce a

biomechanically compatible structure [12]. Ideally, any new restorative material should combine the same degree of strength, toughness and hardness all in one material.

To fabricate new materials with superior properties in fields as diverse as the construction industry, space exploration and biomedical industry, scientists have looked at other natural materials with good mechanical properties [13]. One such material is nacre. Nacre is a biological composite comprising aragonite platelets (0.5μm thick) arranged in a highly aligned continuous way, joined by a very thin sheet of protein material (20-30 nm). This arrangement makes it both strong and tough [14, 15]. It is well documented in the literature that synthetic composites materials with a "brick and mortar" nacre-like microstructure can combine both high mechanical strength and toughness [16]. Launey *et al.* (2009) fabricated an aligned alumina scaffold by freeze casting and infiltrate it with polymethyl methacrylate (PMMA) to produce a nacre-like composite material. The material flexural strength of 200 MPa and the fracture toughness (K_{IC}) of 5 $MPam^{1/2}$ were the highest ever reported for ceramic/polymer nacre-like materials [17]. However, the fabrication cost is high, requiring both isostatic pressing and three sintering cycles. Another nacre-like hydroxyapatite/PMMA composite material was fabricated using the same principle, and the reported strength was the highest among other isotropic non-nacre like hydroxyapatite/PMMA composites and monolithic hydroxyapatite materials [18]. Bouville *et al.* (2007) succeeded in fabricating a nacre-like composite by freeze casting a ceramic suspension of alumina platelets, alumina nanoparticles, silica and calcia followed by field-assisted sintering. The composite material showed high stiffness with ultrahigh flexural strength (470 MPa) and a high fracture toughness (K_{IC}) (6.1 $MPam^{1/2}$). The strength of the material was the same as pure dense alumina, but with a much higher fracture toughness

[19]. Once again, a limitation is the high cost of the alumina platelets used as the main constituent of the composite material.

For a long time, porosity within any ceramic was considered to be a problem due to the detrimental effect on mechanical performance. More recently, however, pores in ceramics have been used as spaces to fill with a second phase polymer, in order to design a functionally biomimetic ceramic with enhanced structural and mechanical properties [20, 21]. Typical processing methods for dental ceramic blocks include extrusion moulding [22], pressure casting [23], dry pressing [24] or hot isostatic pressing [25]. A new method to fabricate such dental ceramics is freeze casting [26], which is a novel technique capable of producing structurally ordered porous ceramics [27-31]. The hierarchical structure [32] is formed by freezing a ceramic suspension, then removing the solvent within it [33]. The potential advantages of this technique include: the ability to tailor the microstructure by monitoring the processing parameters, applicability to different materials (e.g., ceramic, metal and polymer), simple equipment and being environmentally friendly [34]. As a result, it has potential applications in biomedical and industrial fields, including orthopaedics [35, 36], dentistry [20, 21], wound dressings [37] electrical and thermal applications [38-40] and filtration [41]. Although the freeze casting process is customisable, controlling the development of the network microstructure during processing can be challenging. Being able to reproducibly fabricate materials with a highly aligned microstructure on a large-scale using freeze casting would be a great asset in materials design. Highly aligned porous materials can be of benefit for both biological [42] and non-biological applications [43]. Several attempts have been made to control lamellar growth orientation during the solidifying step of freeze casting, e.g. by modifying the surface of the cooling substrates [44], or by “freezing under flow” [45], These methods are limited by being complex and the

microstructure can be difficult to replicate. Another promising method, namely “bi-directional freeze casting” has recently been reported. It is possible to fabricate large size (up to the cm scale) highly aligned ceramic scaffolds by this technique [46]. Although macroscopically aligned, on a smaller microscopic scale, this alignment was not always observed over the entire ceramic scaffold, and the effects of different processing parameters were also not systematically investigated. It is very important to understand how the lamellar alignment develops within the ceramic suspension, and how different processing parameters affect this alignment, particularly, if the bi-directional freezing technique is to be used to fabricate reproducible, highly aligned materials for practical applications.

This PhD research work aimed to fabricate a composite material that is strong, tough and hard, using a very simple and cheap methodology. The fabrication strategy depends on having a highly aligned ceramic scaffold infiltrated with a second phase polymer. Bi-directional freeze casting was used to fabricate large porous ceramic scaffolds with aligned lamellar microstructures using a modified mould configuration [46]. The effect of different processing parameters (cooling rate, mould slope angle, initial solid loading and binder concentration) on the final microstructure was investigated in order to determine how freezing under a dual temperature gradient can control ice crystals nucleation and growth. The highly aligned partially sintered scaffold was pressed uniaxially to break the ceramic walls inside into short and densified ceramic bricks that resemble the aragonite platelets of nacre. These densified scaffolds were sintered again, silanised and infiltrated with UDMA/TEGDMA polymer material to fabricate a biomimetic nacre-like ceramic/polymer composite material. The effect of different first-step sintering temperatures and different uniaxial pressures on the microstructure, physical and mechanical properties were studied.

In this project, the disadvantages of existing materials used as CAD/CAM materials could potentially be overcome by fabricating a biomimetic ceramic/polymer composite (BCPC), which combines the advantages of the design and the constituent materials best properties. The fabricated composite materials were tested for flexural strength, fracture toughness and hardness.

This research can be divided into three main studies. The first was to investigate the parameters that can affect the ceramic scaffold alignment during bi-directional freeze casting. Following on from the results of the initial bi-directional freeze casting study, and using the best of the fabrication parameters, in the second study biomimetic ceramic/polymer composite materials (BCPCs) were fabricated. The effect of different first-step sintering temperatures on the microstructure and hence, on the mechanical properties of the composite material were investigated. Finally, in the third study, four different BCPCs were fabricated and mechanically tested and compared to the mechanical properties of dense ceramic, pure polymer and a commercially available CAD/CAM dental material (Vita Enamic).

The thesis consists of seven chapters, with the first being this introduction. In the second chapter, a detailed literature review covering all the related aspects of the study is presented along with the research aims and objectives.

The third chapter covers the materials and methods with the experimental methods divided into three main sections. The first covers the study of bi-directional freeze casting of alumina ceramic suspension. The second section covers the fabrication process of the biomimetic ceramic/polymer composite materials, while the third section describes how dense ceramic and pure polymer were fabricated. Material characterisation and mechanical

testing procedures were also presented in this chapter. The fourth chapter covers the results and discussion of the bi-directional freeze casting study. The fifth chapter reports the results and discussion of the fabrication and characterisation of biomimetic nacre-like ceramic/polymer composites. The sixth chapter presents the results and discussion of the fabrication of four experimental CAD/CAM composite materials and the mechanical properties comparison between them and dense ceramic, pure polymer and Vita Enamic. The seventh chapter includes conclusions and possible future works.

Chapter 2 Literature review

2.1 Morphology of the tooth structure

Human teeth consist of three specialised calcified tissues, namely enamel, dentine, and cementum. Their structure is depicted in Figure 2-1.

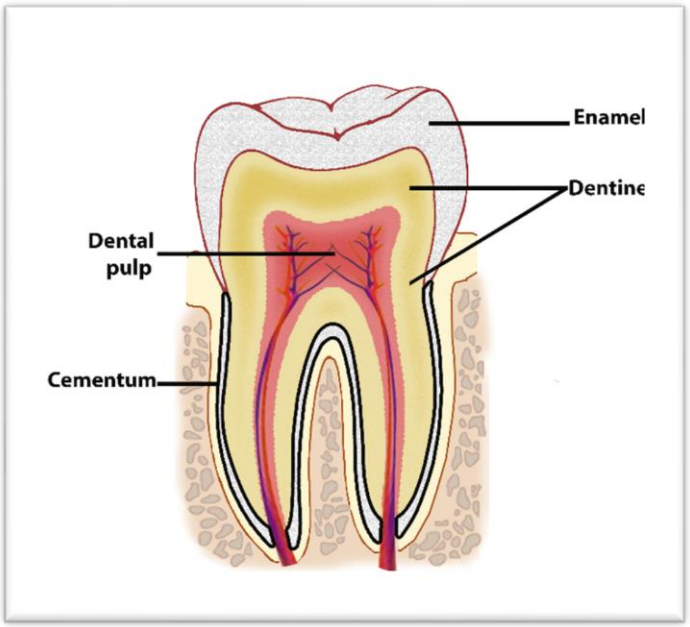

Figure 2-1: Schematic diagram of a longitudinally cut human tooth showing the enamel, dentine, cementum and the pulp chamber.

Enamel is the hardest tissue in the human body and as the outermost layer of the tooth, it provides resistance to wear due to mastication, hopefully over a lifetime. Dentine forms the bulk of the tooth, and it is covered by cementum, which is a thin layer covering the dentine of the roots attaching the teeth to the alveolar bone via the periodontal ligament. Both tissues, dentine and cementum, are hydrated, vital, composite structures composed mainly of collagen type I, mineralised with apatite (Calcium phosphate mineral). The dentine-enamel junction (DEJ) forms the boundary between dentine and enamel, and it is from this

site during tooth development that ameloblasts proceed outwards to form enamel, and odontoblasts proceed inward to form the dentine.

An understanding of the properties of these calcified dental tissues, in particular, their relationship to each other in providing the optimum performance for function, is crucial to the design of the next generation dental materials that will be used to replace such tissue lost through trauma or disease [47]. Not only should the function be restored but also natural tooth appearance. The three tissues will now be described in more detail.

2.1.1 Enamel

Enamel, in its mature state, is a highly calcified crystalline material. It is an avascular, nonvital tissue and, therefore, not renewable and once lost is lost forever. The cells responsible for enamel formation are the ameloblasts, which proceed outwards from the DEJ towards the tooth surface. As they do so, they deposit amelogenins and enamelins, which are the main organic content of enamel. These are eventually resorbed during tooth maturation, leaving a highly calcified tissue composed mainly of mineral and sparse organic matrix [48]. The overall composition of mature enamel by weight is 96% mineral or inorganic matter, principally calcium hydroxyapatite ($Ca_{10}(PO_4)_6(OH)_2$), 1% organic matter (lipid and protein) and 3% water [49]. The basic structural unit of enamel is the enamel prism or rod, which has a keyhole-shaped structure approximately 5 µm in cross-section (Figure 2-2). Within this rod, the calcium hydroxyapatite enamel crystals can be seen. These enamel crystals or crystallites lie perpendicular to the DEJ and longitudinally oriented from the DEJ to the enamel surface within the rod. In the cuspal areas, the rods are more curved, known as decussation, which is thought to enhance the fracture resistance of enamel [50, 51].

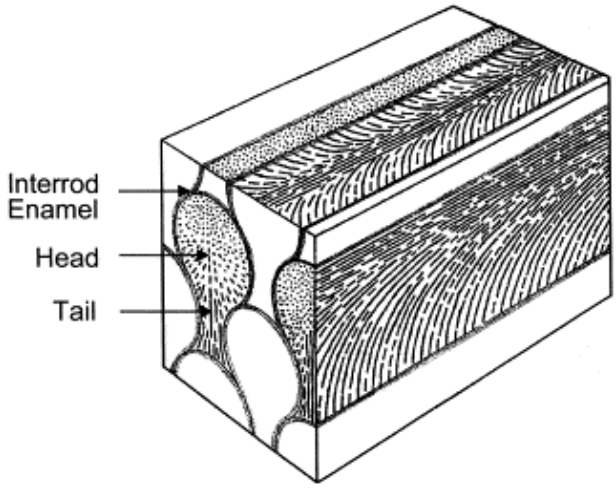

Figure 2-2: Schematic illustration of the enamel rod, the basic unit of enamel [52].

As the enamel thickness varies between different locations within the anatomical crown of the tooth, the length of the enamel rods length will vary [12]. This unique structure of enamel of the rods with their enamel crystals is what is utilised during bonding in clinical dentistry using the acid etch technique [53]. Figure 2-3 shows how the rods are revealed easily by acid etching and how the tail portion of the rod is continuous with the interrod area (arrows).

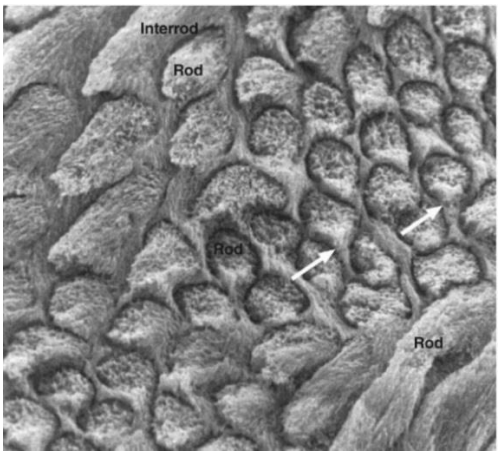

Figure 2-3: SEM image of etched enamel rods and interrod enamel of the tooth. The arrows point to the tail of the enamel rods [54].

2.1.2 Dentine

The bulk of tooth structure is composed of dentine, a vital hydrated tissue comprising hydroxyapatite (70%), organic matter (20%), and water (10%), by weight. The dentinal tubules represent a distinct feature of dentine. They are tunnels penetrating the whole thickness of the dentine (Figure 2-4) [11], and their density, orientation and diameter vary with their location within the tooth. Tubule density is highest at the junction with the pulp chamber and lowest at the DEJ, and their diameter increases from the DEJ (<0.5 μm) toward the pulpal surface (>2.0 μm) [55].

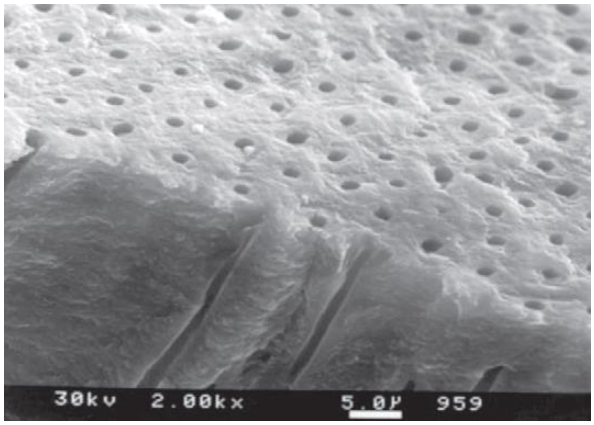

Figure 2-4: SEM image of dentine showing the dentinal tubules in two planes [47].

The internal side of the dentinal tubules is aligned with peritubular dentine, which is characterised by its high apatite crystal and low organic content. The intertubular dentine, which surrounds the tubules, consists mainly of a type I collagen matrix reinforced by apatite crystals, Figure 2-5 [56].

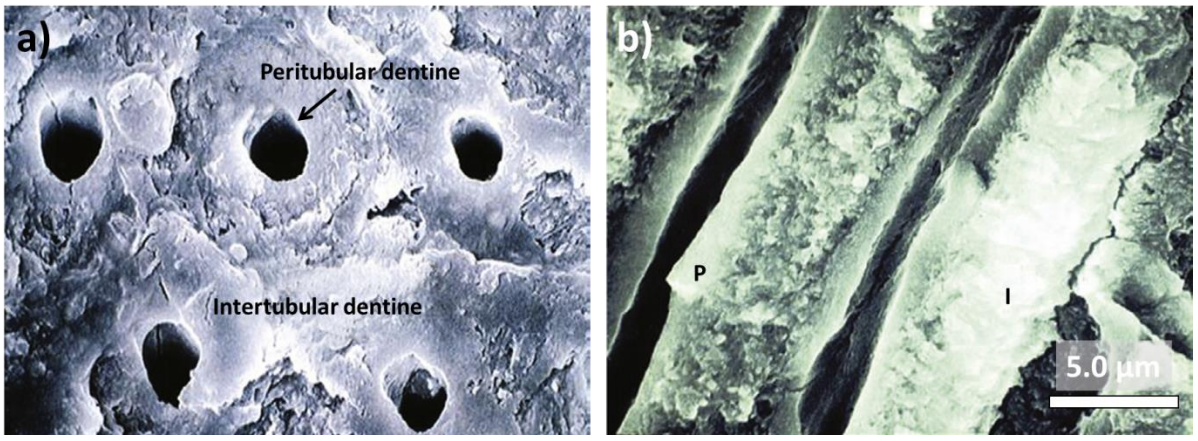

Figure 2-5: SEM images for a) the occlusal surface and b) longitudinal views of the dentine surface of dentine. These images show the peritubular dentine (P) lining the dentinal tubules, separated by intertubular dentine (I) [47].

2.1.3 Cementum

Cementum is the thin "bone-like" tissue layer covering the dentine of the tooth root and is produced by the Cementoblasts. It is softer than both the enamel and the dentine. The periodontal ligament fibres are embedded in both the alveolar bone and the cementum, and it is these that hold the teeth within the alveolar bone. Inorganic matter forms 45-50% by weight of the cementum (apatite) with the remainder comprising organic matter (glycoproteins and collagen) and water [57].

2.1.4 Mechanical properties of tooth tissues

The pronounced differences in the microstructure of both enamel and dentine, when studied at different locations within the tooth, lead to inhomogeneous anisotropic characteristics [58, 59]. The availability of newer methods of micromechanical testing of materials has facilitated the study of the dental tissues in some detail. Such that it is now possible to understand how the mechanical properties of these tissues are linked to their unique anisotropic characteristics [56, 60].

Enamel is the hard outer shell of the tooth that can withstand the high masticatory forces, which might reach up to 1000 N [61], while dentine is the elastic substrate that can absorb the stress applied to the brittle enamel. Table 2-1 summaries the mechanical properties of both enamel and dentine.

	Flexural strength (MPa)	Elastic modulus (GPa)	Fracture toughness ($MPa.m^{1/2}$)	Hardness (GPa)
Enamel	60-90 [62]	48-105 [63, 64]	0.67-0.95 [65]	3.4-5.4 [66, 67]
Dentine	245-280 [47]	17-20 [68]	2.2-3.1 [69, 70]	0.6-0.95 [70, 71]

Table 2-1: The range of reported mechanical properties of enamel and dentine, with references in brackets.

The biomimetic approach in dentistry has evolved to design new and improved restorative materials that mimic the compositional and mechanical properties of the dental tissues. Restoring the aesthetic, biomechanical, and structural integrity of damaged teeth by using these promising new materials constitutes the driving force of this approach [20, 72]. Mimicking tooth tissue structure has so far been challenging, as it is the anchorage of two dissimilar tissues at a strong, unique junction (the DEJ) that enables these two tissues to perform in the best possible way mechanically. Another biomimetic approach is to mimic the mechanical properties of these tissues. Fabricating a dental material that can combine the right strength, toughness and hardness to replace missing tooth structure was the driving force for this research.

2.2 Materials for Tooth Restoration

2.2.1 Resin Composites

In materials science, the word “composite” implies that there are two or more dissimilar materials, which when combined, produce a new material with different and hopefully superior properties when compared to the individual constituents [73].

In clinical dentistry, the word composite resin commonly refers to a filled polymer system, which is used as an aesthetic restorative material used to replace missing tooth structure [47]. Dental composite resin materials are composed of four basic components: an organic polymer matrix, surface-modified fillers, a coupling agent and a polymerisation initiation system [74]. These materials were developed to replace earlier unsatisfactory acrylic-based filling materials. The advantages of the composite resin materials compared to the pure acrylics are improved mechanical properties, less polymerisation shrinkage and higher wear resistance [75].

2.2.1.1 Resin Matrix

The most commonly used monomers for the resin matrix of dental composites are Bis-GMA, 2,2-bis [p-(2-hydroxy-3-methacryloxypropoxy)-phenyl] propane and urethane dimethacrylate (UDMA). UDMA was introduce to the dental market in 1974 as a replacement for Bis-GMA [76]. Compared to Bis-GMA, UDMA is less viscous, which allows for a greater filler loading, and it is more resilient due to its flexible linkages [77]. Other materials are also used in dental composites, either as the principal or co-monomer in order to alter the properties of the matrix. Of these, triethyleneglycol dimethacrylate (TEGDMA) is commonly used as a diluent comonomer for UDMA in a 1:1 ratio, in order to reduce resin

matrix viscosity and create a more workable material [78]. Other materials include Glycol dimethacrylate urethane dimethacrylateethoxylated bisphenol-A-dimethacrylate (Bis-EMA) and decanediol dimethacrylate (D3MA) [79]. Figure 2-6 shows the chemical structure of the most commonly used monomers in dental composites.

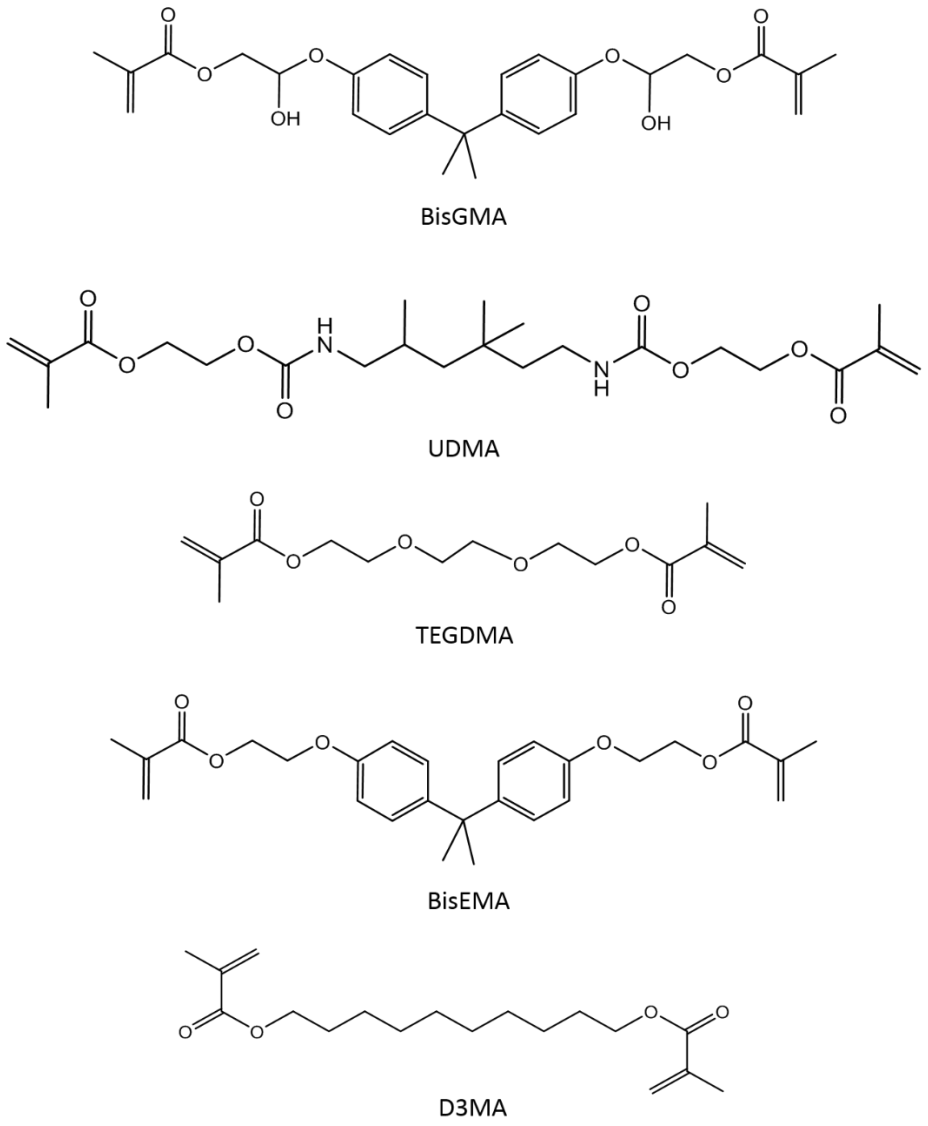

Figure 2-6: The chemical structures of the most commonly used monomers in dental resin composite.

Due to increased public awareness of the negative effects of Bisphenol-A on the development or reproductivity of humans, new (Bisphenol-A-free) monomer/combinations

have been developed and marketed [80]. However, more recently, Chen and Suh reviewed the literature on Bisphenol-A in dental materials. They concluded that the amount of Bisphenol-A from BisGMA or BisEMA released is negligible, and far below the daily intake from the surrounding environment [81].

In order to reduce polymerisation shrinkage, a limitation of some resin based dental composites, bicyclic compounds have been used as the monomer. Such monomers depend on ring-opening polymerisation [82]. Silorane is one of these monomers, and it was developed by combining siloxanes and oxirane chemical blocks. Figure 2-7 shows the chemical structure of the silorane monomer. This material has a low polymerisation shrinkage due to oxirane ring-opening cross-linking, and high hydrophobicity as a consequence of the presence of the siloxane [83]. In an in vitro study, silorane-based resin composite proved to have better marginal integrity and less microleakage compared to methacrylate-based resin composite [83].

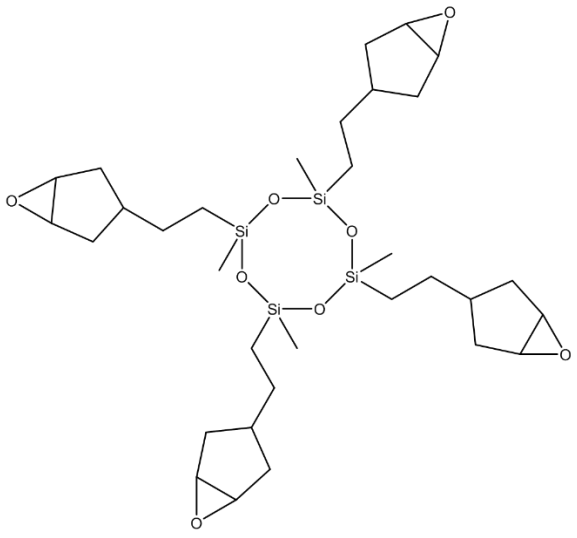

Figure 2-7: The chemical structure of silorane.

2.2.1.2 Fillers

The principal aims of adding dispersed filler particles to dental resin are, to reinforce the resin matrix and to reduce volume shrinkage during polymerisation. Other desirable effects include ease of handling and improved aesthetics [84]. Generally, the fillers comprise the major portion of the resin composite by weight (70-80 %) or volume (40-70%) [85]. They consist of different types of inorganic materials, and in the first generation of resin composites, crystalline quartz and aluminosilicate glasses were used [74]. More recently, they comprise different types of amorphous silica and ceramics [86].

There are many different classifications of dental composites, and one of these is based on the characteristics of the filler particles, mainly their size. Traditional dental composites are macrofills, where the average particle sizes are 10 to 50 μm and where they are either spherical or irregular in shape. These composites are strong, but at the same time, have low wear resistance. To solve this problem, which affects both longevity and aesthetics, new highly aesthetic microfill composites were formulated. However, these materials were relatively weak due to their lower filler content [87]. To address this issue, hybrid materials, that contain two types of fillers with different sizes mixed together, were developed. The average size of the fine particles is 2 to 4 μm and of the microfine particles 0.04 to 0.2 μm. This difference in particle sizes allows for a higher filler loading, which provides efficient packing and good handling properties[47].

The current trend in dental composites is to minimise the filler size to the nanoscale, aiming to increase the filler content still further, to improve the mechanical properties and clinical performance [88]. There are two main types of dental composites containing nanoparticles: nanofills that contain only nanoparticles (size range: 1-100 nm) in the resin matrix, and

nanohybrids that contain nanoparticles plus larger particles of 0.4 to 5 µm in size [47]. Other fillers that have been tried include glass fibres [89], glass whiskers [90] and metallic filler particles [91].

2.2.1.3 Silane coupling agents

Having a chemical bond between the organic resin matrix and the inorganic fillers within a resin composite restorative material is useful in an attempt to improve clinical performance. Most commonly, a coupling agent such as 3-methacryloxypropyltrimethoxysilane (MPS) is used. The chemical structure of the MPS (Figure 2-8) contains typical bifunctional groups. Through an acid/base reaction, the methoxy groups (CH_3) in the silane coupling agent convert to hydroxyl groups that then attach by covalent bonds to the hydroxyl groups on the surface of the filler particles. In addition, the free double bonds then copolymerise with the polymer methacrylate matrix via carbon-carbon double bonds during the curing step of the monomer [79]. There are several advantages of the formed silane link between the resin matrix and the filler particles. As mentioned earlier, it improves the mechanical properties of the material, helps in stress distribution between the weak organic matrix and the strong inorganic fillers and reduces water absorption [92].

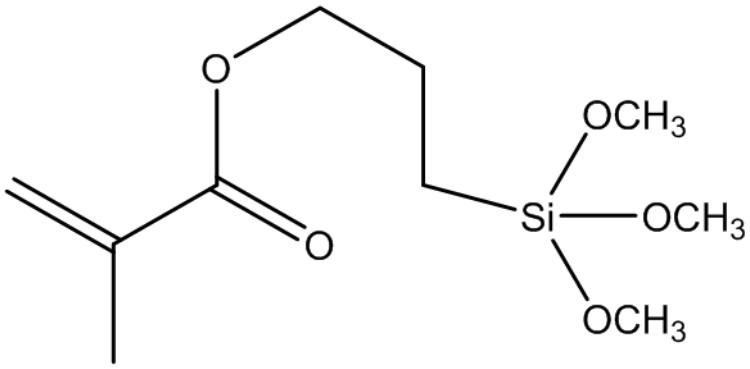

Figure 2-8: Chemical structure of 3-methacryloxypropyltrimethoxysilane (MPS).

2.2.1.4 Polymerisation initiation systems

The polymerisation of composite resin materials can be initiated either chemically (self-curing), by the use of visible light (light-curing) or by a combination of both (dual-cure). In chemically cured systems, this depends on the activation of the initiator material, usually benzoyl peroxide, by a tertiary amine accelerator to produce free radicals that begin the polymerisation process. In light-cured systems, a camphoroquinone initiator activated by light is typically used as the source of free radicals [93].

The polymerisation process starts with free radical initiation of the initiator material, creating a free-radical, which then joins a monomer molecule to create an active monomer radical. Following this, additional monomer attaches to the active centre by covalent bonding in an addition reaction to form a highly cross-linked polymer. This conversion of a relatively long chain monomer into a short chain polymer is the reason polymerisation shrinkage occurs, and which is a problem when using such materials in the clinical environment [94, 95].

2.2.1.5 Limitation of resin composites

Despite the long and widespread use of resin based dental composites, they still suffer from certain limitations in clinical applications. One of the main limitations is polymerisation shrinkage, resulting in the development of marginal gaps, which in turn may lead to aesthetic concerns and recurrent caries [96]. The degree of conversion of the monomer to polymer has a direct bearing on the amount of polymerisation shrinkage. Factors controlling the degree of conversion including filler type, curing temperature, curing time, film thickness and the initial amount of monomer within the composite material. As it is impossible for the degree of conversion to reach 100 %, the mechanical properties of the resin composite are also related to how much monomer has been converted to polymer during the curing phase, the rang of degree of conversion is between 55 % to 75% in dimethacrylate monomers [97, 98].

Within the oral cavity, resin based composites should be able to withstand both normal functional (100-500 N) and abnormal parafunctional forces (900-1000 N) [99]. Another limitation of these materials is surface loss due to wearing with clinical use. Even though the degree of wear seen with the more recently introduced hybrid composite materials is less than seen with the older macro filled materials, the fact that composites comprise discontinuous filler particles dispersed in a continuous polymer matrix plays an important role in determining wear resistance, along with other mechanical properties. Great care needs to be exercised when restoring large cavities and functional cusps using these materials [87].

2.2.2 Dental ceramics

A ceramic is defined as a non-metallic, inorganic material fabricated by sintering together the raw minerals at very high temperatures. Dental ceramics are considered as one of the three major classes of dental restorative materials. The other two classes are metals and polymers (and their composites) [47]. As a result of their aesthetic properties, dental ceramics can easily mimic the natural look of enamel, if handled properly [100]. In general, they are brittle materials with high compressive strength and low tensile strength. This means they may fracture under low tensile strain. In addition, they possess a low fracture toughness compared to metals, which means they lack the ability to resist crack initiation and propagation, which limits their clinical usefulness [101, 102].

There are different ways to classify dental ceramics, and one such is based on the fabrication technique [103].

2.2.2.1 Dental ceramic fabrication techniques

2.2.2.1.1 Powder compaction and sintering

Powder compaction and sintering is the traditional method used to fabricate ceramic crowns. It entails preparing a ceramic slurry and applying it over a refractory die using a brush. The ceramic crown should be dried in ordered to create a compact dense material before then being sintered. During sintering the ceramic grains start to consolidate and grow larger in size and the grain-gas interface replaced by grains boundaries to form dense ceramic [104]. IPS Empress (Ivoclar-Vivadent, Schaan, Liechtenstein) layering ceramic (Leucite $KAlSi_2O_6$) and Procera Allceram (Alumina Al_2O_3) (Nobel Biocare, Go¨ teborg, Sweden) are examples of products using the powder compaction method [47].

2.2.2.1.2 Hot pressing

This fabrication technique utilises the lost wax principle in a similar way to that used with metals alloys. The modelled wax restoration is invested in a phosphate bonded refractory material that forms the mould for the final restoration. A pre-sintered ceramic block is heated to a high temperature near the ceramic soften point, and external (0.3 to 0.4 MPa) pressure is applied through a plunger to press the soften ceramic into the mould. The temperature dwell time is 10 to 20 mins. A special automated furnace is required for this fabrication technique [105]. The first-generation product was Leucite ($KAlSi_2O_6$) IPS Empress (Ivoclar-Vivadent, Schaan, Liechtenstein). The amount of leucite is varying between 35 vol.% to 55 vol.%. After heat pressing the leucite forms crystals (1 to 5 μm) impeded in a glassy matrix. Due to its low flexural strength (120 MPa), a second-generation material IPS e.max Press (lithium disilicate $Li_2Si_2O_5$) (Ivoclar-Vivadent, Schaan, Liechtenstein) was later introduced to the dental market. The final microstructure of the ceramic has 65 vol.% of interlocking prismatic (5 μm) lithium disilicate crystals. This interlocking crystals improves the flexural strength to 300 MPa [47].

2.2.2.1.3 Slip casting

As the name implies, this technique starts by preparing a ceramic slip. A slip is an aqueous slurry of fine alumina, magnesia or zirconia particles. The slip is applied over a gypsum die that extracts the water by capillary action. This step results in the production of a highly compacted ceramic body. The produced ceramic core is then sintered at high temperature over the refractory die to produce a porous interconnected ceramic structure that enables later glass infiltration. The most commonly used glass is lanthanum aluminosilicate ($LaAl_2O_3SiC_2$). The melted glass is infiltrated into the porous structure by capillary action at a high temperature. This technique produces a ceramic microstructure of two

interpenetrating phases, the crystalline infrastructure and the glassy phase. In Ceram Alumina, In Ceram Spinell and In Ceram Zirconia (Vident, Brea, USA) are examples of materials use the slip casting technique [47, 100, 105].

2.2.2.1.4 Machining

Machinable ceramics are milled either from fully or partially sintered ceramic blocks using a CAD/CAM (Computer aided design/computer aided manufacturing) machine. This method allows the fabrication of dental restorations in one clinical visit. It will be fully discussed in a later section.

2.2.2.2 Mechanical properties

The two important mechanical properties that are often reported for dental ceramics intended for clinical applications are flexural strength and fracture toughness. Flexural strength is a material property that measures the material's ability to withstand applied load in the middle of a specimen that is supported at each end. A flexural strength test, like three-point bending, uses both compression and tension forces applied to the specimen at the same time. This is more closely mimicking the clinical forces inside the oral cavity [106]. Fracture toughness measures the material's ability to absorb energy before crack initiation and propagation. Since ceramics fail by catastrophic crack growth, fracture toughness is an essential material's property for dental ceramic that is constantly under cyclic loading [107].

Ceramics are generally regarded as strong, but brittle materials and ceramic dental restorations sometimes fail under mechanical loading by brittle and catastrophic fracture [108]. Of the available ceramic materials, leucite reinforced ceramics show the lowest flexural strength of 104 MPa. Lithium disilicate reinforced ceramics exhibit higher flexural strength of 306 MPa, followed by slip-cast ceramics (378-630 MPa). In recent years the

focus has shifted to the material loading capacity, rather than the flexural strength. Flexural strength tests are performed on highly polished rectangular specimens, and this is far from the conditions seen inside the oral cavity, where the material will be used in the shape of the tooth or part of it [109].

Fracture toughness is a very important mechanical property of dental ceramics as it controls the crack propagation under cyclic loading. This means a material with high fracture toughness is more clinically useful in the fabrication of dental restorations, as it requires more energy for crack propagation [102].

Transformation toughening of zirconia and crystalline reinforcement are examples of toughening mechanisms. Transformation toughening works by crack tip shielding, where the applied load transforms the zirconia crystals from the tetragonal form into the larger monoclinic form. This change in volume induces compressive force at the head of the crack tip and stops it from propagating [110]. In the crystalline reinforcement method, the crystals work as crack deflectors, interacting with the crack tip and preventing it from propagating in a straight direction [111].

2.3 CAD/CAM technology

Computer aided design/computer aided manufacturing (CAD/CAM) was introduced in dentistry in the 1970s [112], and the first CAD/CAM restoration was fabricated in 1985 [113]. CAD/CAM technology has evolved as an alternative fabrication technology to the traditional indirect lab-based methods of ceramic fabrication. And recent improvements in technology have resulted in reduced fabrication time, reduced material waste, improved quality and accuracy of fit [114, 115].

CAD/CAM technology depends on taking an optical impression of either the prepared dental tissue or a model of it using a scanning device, then visualising and processing this optical impression on the computer in order to design the restoration (CAD). The software allows the clinician to view the prepared dental tissue from different angles and design the occlusal and proximal contacts and final wax-up of the restoration. All the processed data are then sent to the machining unit to manufacture the final restoration (CAM) [116].

CAD/CAM technology has been applied to different stages of the process of restoration fabrication. Of these different treatment possibilities using CAD/CAM system, chairside CAD/CAM with one visit dental restoration is considered the most appealing [115]. For the patient, this means that all of the treatment can be carried out at a single visit, rather than the two to three visits for more traditional laboratory fabrication techniques. Any new materials introduced should, therefore, also ideally be compatible with this single visit concept.

2.3.1 Dental CAD/CAM materials

Even though most of the developments in CAD/CAM systems were related to software and machining options, the last decade has witnessed a huge development in material options. Feldspathic porcelain was the first material used to fabricate inlays. Currently, dental restorations are fabricated from many different materials, including different types of ceramics, resin composites, ceramic/polymer composites, semi-crystalline polymers and metals.

Dental CAD/CAM materials can be classified into four groups: glass ceramics, polycrystalline ceramics, polymers and ceramic/polymer composite materials.

2.3.1.1 CAD/CAM glass ceramics

The first generation of CAD/CAM restorations was limited to feldspathic porcelain (Vita Mark I, Vita Zahnfabrik, Bad Sackingen, Germany) [113]. In 1990 a new processing method, "extrusion moulding" was adapted to produce Vita Mark II (Vita Zahnfabrik, Bad Sackingen, Germany) specifically for the CEREC machine (CEREC 1-Siemens GmbH, Bensheim, Germany). This material displayed improved mechanical characteristics compared to Vita Mark I [114]. Due to its excellent optical properties, it was recommended for use in highly aesthetic restorations in the anterior and premolar regions. However, it is not recommended for high load-bearing areas such as molar teeth [117-119].

The most commonly used ceramic materials, particularly for chairside milling, are leucite-reinforced ceramics and lithium disilicate reinforced ceramics [118]. Ivoclar Vivadent was the first company to produce leucite-reinforced ceramics, ProCAD (Ivoclar-Vivadent, Schaan, Liechtenstein). Its structure is similar to the conventional hot pressed leucite-reinforced ceramics Empress (Ivoclar-Vivadent, Schaan, Liechtenstein), and hence restorations fabricated from it showed favourable properties compared to the Empress restorations [120]. The second generation of ProCAD was Empress CAD. Optimising the manufacturing procedure allows the use of about 45% leucite with a finer particle size (1–5 µm) that improves the material machinability [121]. Paradigm C (3MESPE, Seefeld, Germany) is another CAD/CAM material processed from leucite-reinforced ceramics.

The only currently marketed lithium disilicate CAD/CAM reinforced ceramic block is IPS e.max CAD (Ivoclar-Vivadent, Schaan, Liechtenstein). The use of SiO_2-Li_2O as filler particles in the process of glass formation leads to the production of lithium disilicate ($Li_2Si_2O_5$). The microstructure of the produced material consists of small interlocking, randomly oriented

needle-like crystals. The homogeneity of lithium disilicate glass vastly improves its mechanical properties in comparison to other glassy (feldspathic) and reinforced (leucite) glassy ceramics [122].

The pressure casting technique is used to produce IPS e.max CAD blocks that are defect free. The blocks are provided in the blue state (pre-crystallised state), and the microstructure in this state consists of 40 % lithium metasilicate crystals. In the fully crystallised state, it comprises 70 % fine grain lithium disilicate crystals [123].

In 2013 a new lithium silicate/phosphate material was introduced to the market [1]. It contains 10 wt.% zirconia particles. Of this group, Celtra Duo (Sirona Dentsply, Milford, USA) is a fully sintered form that has two crystal phases. One phase is elongated (1μm) lithium metasilicate crystals (Li_2SO_3), and the other is rounded (nanometric size) lithium orthophosphates (Li_3PO_4) [123]. An optional heat treatment protocol described by the manufacturer for Celtra Duo is said to result in a material with a higher flexural strength [124, 125].

The last CAD/CAM material in the glass group is InCeram (InCeram Alumina, Spinell and Zirconia, Vita Zahnfabrik, Bad Sackingen, Germany). In this material, a strong slip cast ceramic core is infiltrated by a glass phase, such that it comprises two interpenetrating phases interweaved with each other. After milling of the substructure, a veneer layer is required for surface characterisation. InCeram Spinell has the lowest flexural strength, and it is mainly indicated for anterior restoration due to its high translucency. InCeram Alumina is indicated for both anterior and posterior restoration. InCeram Zirconia is the strongest of the InCerams, and its use is limited to the posterior region as a crown or bridge substructure due to its high opacity [23, 24].

2.3.1.2 CAD/CAM polycrystalline ceramics

Polycrystalline ceramics, such as alumina and zirconia, consist of densely packed crystals with no intervening glassy matrix around them [10, 38]. The good mechanical properties of these ceramics are due to a dense crystal lattice that prevents crack propagation. Their high strength makes it impossible to fabricate well-fitting restorations without the use of CAD/CAM systems. The opacity of polycrystalline ceramics, combined with high strength, makes them excellent materials for the construction of restoration copings upon which a veneering layer of glass ceramic is placed for aesthetic purposes [126]. Hot isostatic pressing is the method used in the processing of the fully sintered blocks [25]. Procera AllCeram (Nobel Biocare, Go¨ teborg, Sweden) and Vita InCeram AL cubes (Vita Zahnfabrik, Bad Sackingen, Germany) are examples of Alumina based polycrystalline ceramics [126].

In the case of zirconia, most CAD/CAM systems use yttria partially stabilised tetragonal zirconia polycrystals (3Y-TZP). Some of these materials are processed as a partially sintered block, e.g., LAVA (3MESPE, Seefeld, Germany), e.Max ZirCAD (Ivoclar-Vivadent, Schaan, Liechtenstein), Cercon (Dentsply, York, USA), Vita YZ (Vita Zahnfabrik, Bad Sackingen, Germany) and Procera Zirconia (Nobel Biocare, Go¨ teborg, Sweden), while DCS-President, DC Zirkon (Smartfit Austenal, Chicago, USA) blocks are supplied in a fully sintered state [23].

2.3.1.3 CAD/CAM polymers

A new addition to the dental CAD/CAM family is a group known as the Polyaryletherketones (PAEKs). PAEKs are thermoplastic polymers well known for their good mechanical properties. As the name implies, they comprise an aromatic backbone connected by ketones and ether functional groups [127]. Their biocompatibility means they have found medical

[128] and, more recently, dental applications [129]. They are considered an exciting new material option for dental applications, such as implant superstructure, veneered superstructure for crowns and bridges, monolithic crowns, removable partial dentures and orthodontics wires [130, 131]. Two types of PAEKs were introduced commercially for dental applications: polyetherketoneketone or PEKK (Pekkton®, Cendres-Meteaux, Biel/Bienne, Switzerland) and polyetheretherketone or PEEK (Bredent GmbH & Co. KG, Senden, Germany; Evonik Industries, Essen, Germany; Juvora Ltd. Thornton Cleveleys, Lancashire, UK). Pekkton® has been suggested as a suitable material for monolithic crowns, as its strength is almost four times higher than resin composite restorative materials. The main shortcoming of the Pekkton® is its low hardness, which is comparable to that of dentine [132]. This means it can wear faster compared to other CAD/CAM materials, which might raise concerns about its suitability for use in long term restorations.

2.3.1.4 CAD/CAM ceramic-polymer composites

This new group of CAD/CAM materials consists of two interpenetrating phases; an inorganic ceramic phase provides the structural strength and is intertwined with an organic resilient polymer phase. It is hoped that this new composite material would be less brittle, with excellent mechanical properties and high edge stability, combined with good aesthetics [133]. Based on the abundance of each phase, these materials can be divided into two groups: predominant organic polymer phase with dispersed ceramic nanofillers like Lava Ultimate, and predominant inorganic ceramic framework infiltrated by polymer like Vita Enamic.

2.3.1.4.1 Lava Ultimate

Lava Ultimate (3MESPE, Seefeld, Germany) is the first material introduced as a composite of a highly cross-linked resin matrix and a blend of nano-ceramic particles and nano-particles clusters all embedded within the resin. The resin phase is a dimethacrylate, and the nano-ceramic particles are mixtures of silica (20 nm) and zirconia (4-11 nm) nanoparticles and an aggregated cluster of both. The total solid loading is approximately 65 % by volume [134]. Figure 2-9 shows a Lava Ultimate CAD/CAM block and SEM image showing the ceramic nanocluster.

Figure 2-9: Lava Ultimate CAD/CAM block and SEM showing the ceramic nanocluster [134].

2.3.1.4.2 Vita Enamic

In 2013, Vita Enamic (Vita Zahnfabrik, Bad Sackingen, Germany) was introduced to the dental market as the ceramic material of the future. Different terms have been used to describe this new ceramic material, including hybrid ceramic and polymer-infiltrated-ceramic network (PICN). It is composed of two interconnected phases, namely a porous ceramic phase infiltrated with a polymer phase. The ceramic network is a silanised feldspathic ceramic strengthen by capillary action, with a continuous phase of methacrylate polymer matrix [135]. This fabrication process combines the advantages of a ceramic

backbone with the advantages of a polymer, with fewer of the disadvantages of the individual materials [136]. The ceramic phase accounts for 75 % by volume of the whole material, and it is composed of 58-63% silicon oxide (SiO_2), 20-23% aluminum oxide (Al_2O_3) and other oxides including zirconia. The polymer phase (25 vol.%) is a mixture of UDMA and TEGDMA [136]. This mimetic material is reported to have mechanical properties similar to that of enamel and dentine [137]. Figure 2-10 shows a Vita Enamic CAD/CAM block and an SEM image of the internal structure.

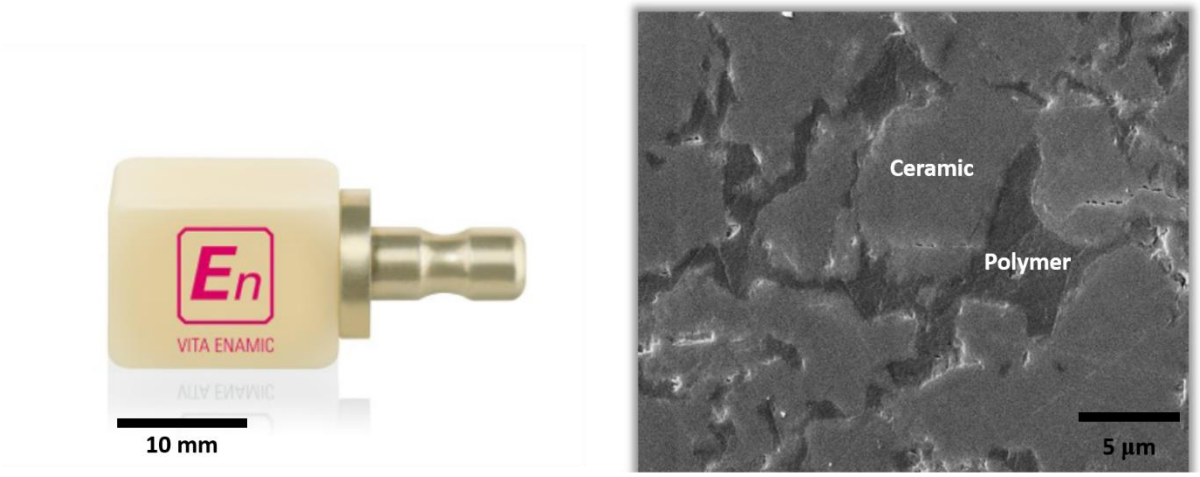

Figure 2-10: Vita Enamic CAD/CAM block [136] and SEM image of the polymer-infiltrated-ceramic-network [10].

Coldea et al. (2013) tested four different PICNs with different ceramic densities for their suitability as dental restorative materials. The reported flexural strength and hardness values were similar to tooth tissues. Moreover, cracks induced by indentation during hardness testing were arrested by the polymer phase, suggesting a better damage tolerance and less marginal chipping [10].

2.3.1.5 Mechanical properties of CAD/CAM materials

Different CAD/CAM materials have different flexural strengths due to their composition and the manufacturing technique. Figure 2-11 represents some commercial CAD/CAM dental restorative materials from different material groups along with their flexural strength values.

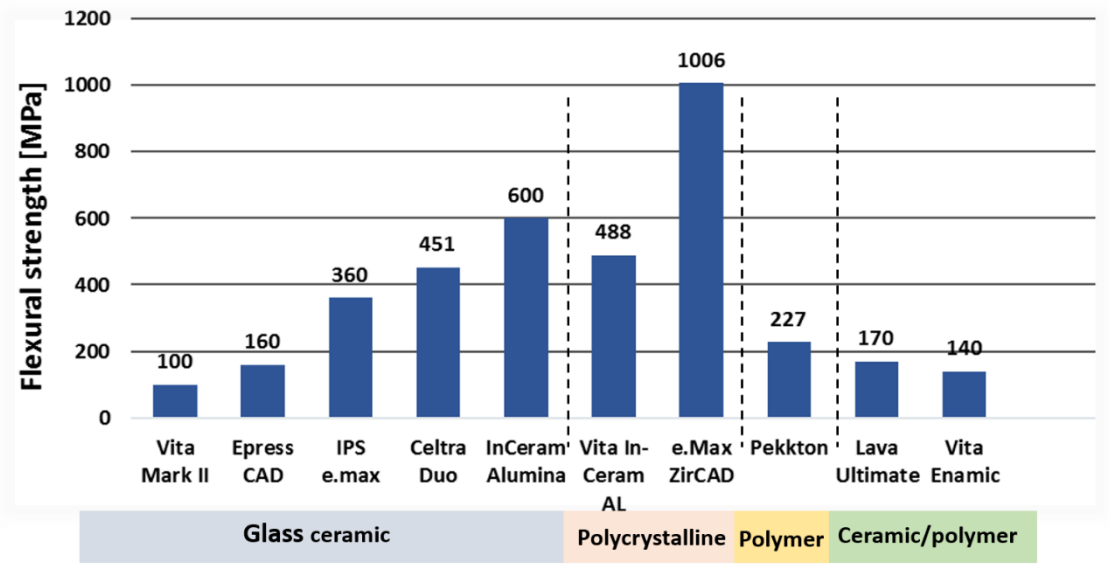

Figure 2-11: Some commercial CAD/CAM dental restorative materials represent different materials group and their flexural strength values.

Vita Mark II has the lowest flexural strength of around 100 MPa [138] due to its high volume of SiO_2 glassy matrix (60-64%) compared to the volume of aluminium silicate oxide (20-23%) [139]. Empress CAD is a 45% leucite based glass ceramic, and the smaller particle size improves the machinability of the material and improves the flexural strength to 160 MPa [23]. IPS e.Max is a fully sintered material with high strength of 360 MPa due to the high content of interlocking crystals (70 vol%) [140]. The flexural strength of heat treated Celtra Duo is 451 MPa, and it is higher than the as-milled material (300 MPa). This can be due to

the heat used repairs any surface machining defects [125]. The last material in the glass ceramic group is the InCeram Alumina, with high flexural strength of 600 MPa [141].

For the polycrystalline materials, Vita InCeram AL and e.Max ZirCAD have a flexural strength of 488 MPa and 1006 MPa, respectively. The flexural strength of polycrystalline zirconia is about twice that of alumina. That does not mean it won't fail as it would still fracture under a sufficiently high load [23, 142]. The flexural strength of Pekkton is 227 MPa. In the ceramic/polymer composite group, there are two commercial materials; Lava Ultimate and Vita Enamic. Although Lava ultimate has the ceramic nano-particles suspended inside the polymer matrix, its reported flexural strength (170 MPa) is higher than Vita Enamic (140 MPa), which has a connected ceramic network [143].

The fracture toughness of a material describes the ability of a material to resist crack propagation under loading. Ceramic materials commonly have surface defects, which can act as a stress raiser and become a site from which a crack can initiate and ultimately propagate. This can result in catastrophic material failure. The most frequently used variable to describe fracture toughness in dentistry is "*crack initiation fracture toughness* K_{IC}", which can be defined as the energy absorbed by the material before the initiation of crack propagation. That means a material with high K_{IC} can better resist crack initiation [144].

Figure 2-12 shows the fracture toughness K_{IC} values of some commercially available CAD/CAM dental restorative materials [144-149]. The only material that is not represented in Figure 2-12 is the Pekkton from the polymer group, as no values of fracture toughness (K_{IC}) could be found in the literature.

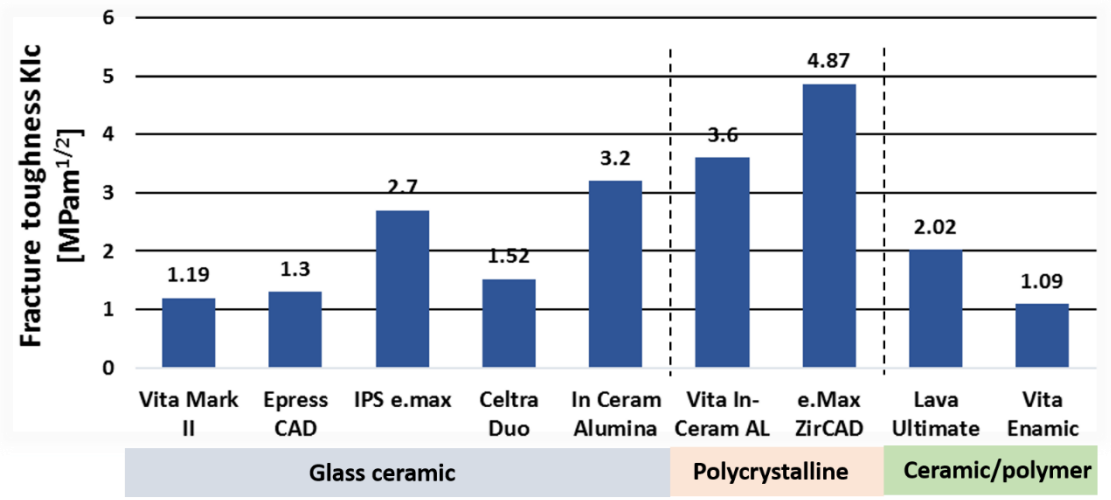

Figure 2-12: Some commercially available CAD/CAM dental restorative materials representing the different materials group and their fracture toughness K_{IC} values.

2.4 Fabrication of biomimetic ceramic/polymer composites

Bio-inspiration, biomimetics or biomimicry are all terms used to describe the same process of fabricating artificial materials that mimic natural ones. Either the base components, structure, function or process, can be mimic to solve practical problems. From the previous definition, any technological invention can be described as bio-inspired, as long as there is a natural biological model that has been followed in the design [150].

The process of biomimeticing starts with a deep understanding of the microstructure of the natural system and analysing the effect of the structure on the preferable mechanical properties of that system, followed by synthesis of a reproducible artificial material that is less complex compared to its natural counterpart [151]. Recreating an exact copy of a natural material like bone or tooth is still not possible, even with the advent of new

technologies. Nevertheless, reaching the end goal of biomimicking functionality is more achievable [152].

Some of the natural materials that attract scientists are biological composite materials. They are often composed of individually weak materials, but in combination their complex hierarchical structure may lead to exceptional mechanical performance, e.g. teeth and nacre of seashells [153]. The structure and mechanical properties of human teeth have already been covered earlier in this review. Even though the individual components of teeth and tooth tissues comprise weak organic matrices and brittle minerals, their arrangements and connections enable them to tolerate high masticatory loads [154]. Mimicking tooth structure in bulk is extremely difficult. One attempt to fabricate abiotic tooth enamel was made by growing ZnO nanowires from nanoparticle seeds, followed by polymer deposition to fill the spaces between the nanowires. This technique produced nanocomposites with lower inorganic content compared to tooth enamel and hence, lower elastic modulus and hardness [155]. Other attempts have tried to mimic the graded functionality of the tooth structure [156]. Niu et al. [157] fabricated a graded functional material to try to mimic the transition in functionality from the hard enamel to the tough dentine by bonding a top layer of zirconia ceramic, to a bottom layer of ceramic rich polymer [157]. This simple two layered approach would not lend itself easily for use as a bulk CAD/CAM block material.

Nacre is another example of natural composite material that combines strength and toughness. Despite its very high mineral content, it is a very tough material that far exceeds the values seen for its individual component parts. The main reason for this is the unique brick and mortar structure [158]. Nacre is seen on the inner surface of seashells and is composed of aragonite calcium carbonate platelets (95 vol.%) and protein sheets (5 vol.%).

These calcium carbonate platelets, which are 0.5 µm thick, resemble the bricks, while the organic sheets (20-30 nm in thickness) act as the mortar. Analysing the smart structure of nacre reveals how calcium carbonate platelets, arranged in a continuous lamellar way to provide a strong backbone, when glued together by a viscoelastic organic layer creates a tough material [159]. Figure 2-13 show the calcium carbonite platelets inside a blue mussel.

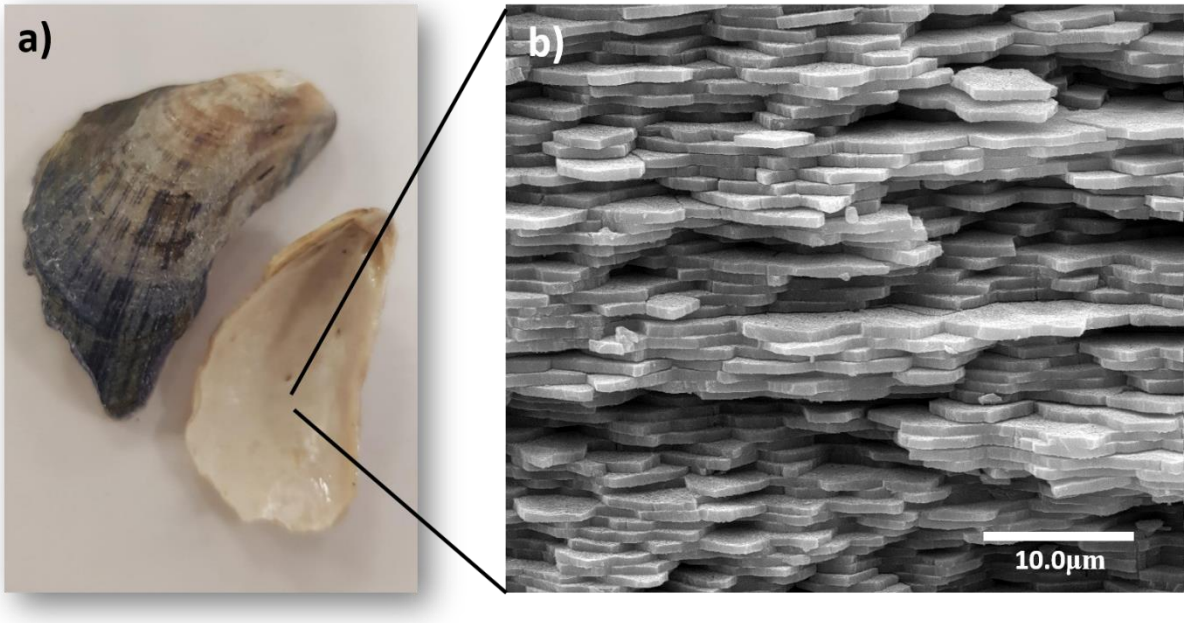

Figure 2-13: a) Blue mussel shells. The external colour of the shell is often dark blue, while the interior is nacreous, b) SEM image of the nacreous side of the mussel showing the calcium carbonate platelets.

2.4.1 Biomimetic nacre-like composite materials

It is well documented that synthetic nacre-like materials, with a brick and mortar microstructure, can possess both high mechanical strength and toughness. Combining these two mechanical properties, strength and toughness, have always been the goal in designing and developing structural materials for different applications [16]. Many different fabrication techniques and different material combinations have been recruited to build

nacre-like composite materials. Of these materials combination ceramic/polymer composite has been well reported in the literature. The ceramic scaffold provides a strong backbone (the bricks) while the soft polymer phase (the mortar) provides elasticity and flexibility of the material improving the toughness [160]. The main point that joins all these attempts is the incorporation of the brick and mortar microstructure in the fabricated composite material. This layered microstructure resists crack propagation by different mechanisms like: crack deflection, crack blunting and ceramic bricks pull-out [43].

Launey *et al*. [17] described the fabrication of a composite material made of 80 vol.% alumina bricks infiltrated with polymethyl methacrylate (PMMA) polymer with good mechanical properties, namely: a tensile strength of 200 MPa, crack initiation fracture toughness (K_{IC}) of 5 $MPam^{1/2}$ and a crack growth fracture toughness (K_{JC}) of 30 $MPam^{1/2}$. To date, this is the highest toughness of a ceramic based composite material ever reported. The use of in-situ fracture toughness measurement revealed the presence of different toughening mechanisms at work within the material. These included wide damage distribution due to inelastic deformation ahead of the crack tip, polymer tearing, ceramic bricks sliding over each other and processing void elongation [17]. Incorporating these toughening mechanisms into dental materials might be of a great benefit.

One tempting material combination is hydroxyapatite and PMMA, which is currently extensively used as a bone substitute. Using a bi-directional freeze casting technique to fabricate a nacre-like hydroxyapatite/PMMA composite has resulted in the fabrication of a material with a bending strength of 100 MPa, which is the highest seen with any hydroxyapatite/PMMA composite. Also, this composite has different toughening mechanisms that are not possible with monolithic hydroxyapatite [18].

A nacre-like composite based on alumina platelets and silica-calcia glasses, again using a brick and mortar approach, was fabricated by Bouville *et al*. [19]. This material demonstrated an ultrahigh flexural strength (470 MPa), crack initiation fracture toughness (K_{IC}) (6.1 $MPam^{1/2}$) and a high crack growth fracture toughness (K_{JC}) (17.3 $MPam^{1/2}$). The ultrahigh flexural strength is due to the materials combination and the brick and mortar microstructure. This nacre-like composite material was as strong as pure alumina (flexural strength), but with a much higher fracture toughness [19].

Similarly, Naglieri et al. [161] managed to fabricate a strong, tough bioinspired silicon carbide/PMMA composite material. It had high flexural strength and high resistance to crack propagation [161].

In summary, mimicking nacre's brick and mortar structure has been shown to be a promising approach to the fabrication of strong and tough composite materials. Utilising this mimicking approach has recently been introduced for the fabrication of dental materials [162] and forms the basis of this research.

2.5 Fabrication techniques of ceramic scaffolds

Previously, pores within dental ceramics were considered as flaws that should be eliminated in order to achieve a high strength for structural applications. More recently, porous ceramics have found applications in biological and industrial systems, where open pores within the ceramic are infiltrated with a second phase to produce composite materials with different and useful properties. Ceramic/polymer composite materials have also been used extensively as biomedical materials. Of these materials, hydroxyapatite/PMMA composite for bone replacement in orthopaedic applications [18] and sodium aluminum

silicate/BisGMA composite for dental applications [163]. Aiming to combine the advantages of the individual materials, while minimising their disadvantages.

This section will describe the techniques of creating suitable ceramic scaffolds that can be infiltrated with a second polymer phase to create the final composite material for clinical use.

2.5.1 Processing of ceramic scaffolds

Porous ceramic scaffolds can be produced using different techniques, including replica templating, direct foaming, partial sintering, rapid prototyping and sacrificial fugitives. Regardless of the processing technique, the ideal properties of a porous ceramic scaffold include high mechanical strength, an interconnected pore network and chemical stability [164].

In the replica templating method, a porous template, usually a polyurethane sponge, is impregnated with a ceramic slurry, then drained of its excess by centrifugation before being heat treated to remove the template. The ceramic scaffold created is then sintered at a very high temperature to densify it. An example of a porous ceramic scaffold fabricated using this method is shown in Figure 2-14. This method of fabrication is simple and flexible, and the maximum achieved porosity is around 90%. However, the mechanical properties of the final scaffold are usually poor, mainly as a result of the voids created within the ceramic scaffold walls during the burnout stage (Figure 2-14b) [165, 166].

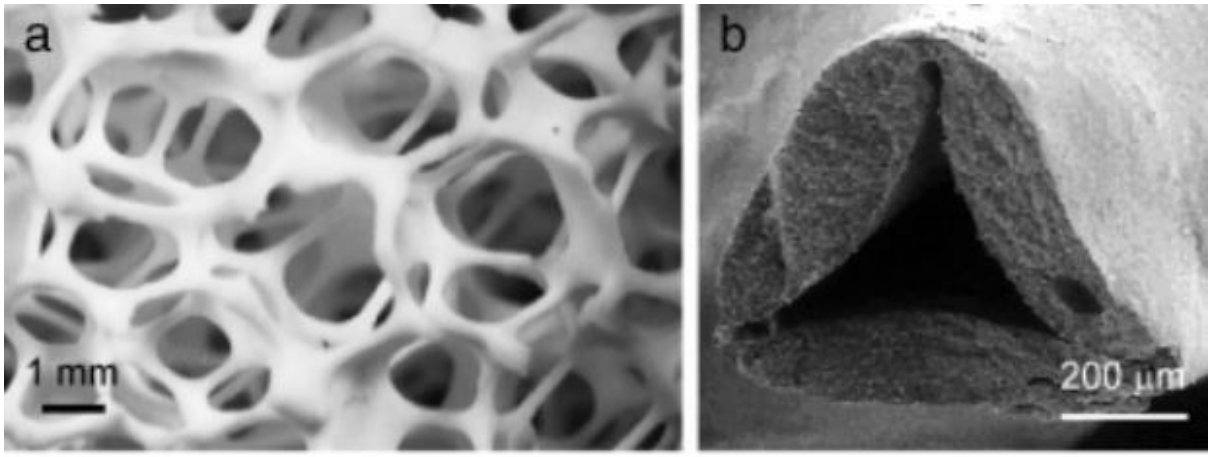

Figure 2-14: SEM images of a) porous ceramic scaffold fabricated via the replica templating method [167], b) voids in the ceramic wall [168].

In the direct foaming technique, air or gas is incorporated into the ceramic suspension to create a foam. The ceramic is then stabilised, drained and sintered to produce a highly (up to 95%) porous ceramic scaffold [164]. Although a relatively easy low-cost technique, it is hard to produce a uniform, graded, porous network structure. In particular, control over the interconnectivity of the pores is poor because the air bubbles within the foam tend to coalesce [165]. Figure 2-15 shows an SEM image of a ceramic scaffold fabricated via direct foaming. The inhomogeneous gradient structure is obvious.

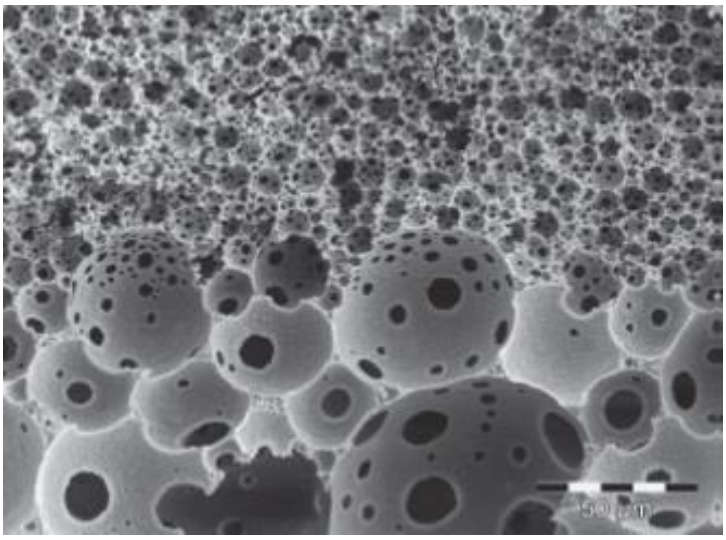

Figure 2-15: SEM image of inhomogeneous graded ceramic fabricated by direct foaming method [169].

The partial sintering technique is one of the most commonly used techniques to fabricate porous ceramics. It produces homogeneous porous structures with potentially good mechanical properties. It relies on compacting the ceramic powder into a mould, then partially sintering the green body at a relatively low temperature. The ceramic powders diffuse into each other under the heat treatment, but because the sintering process is stopped before full consolidation, this leaves pores between the ceramic particles. The main disadvantage of this technique is that there is no control over the pore structure [165, 170]. Figure 2-16 shows an SEM image of a partially sintered ceramic scaffold.

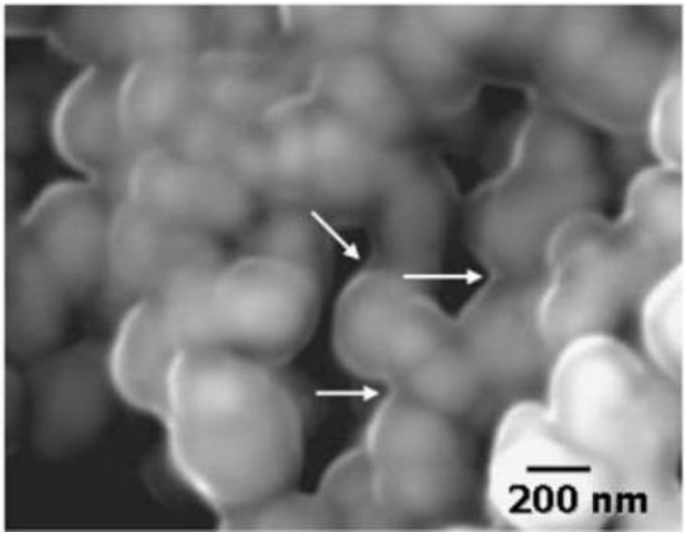

Figure 2-16: SEM image of a partially sintered ceramic scaffold; arrows indicate neck formation between ceramic particles without complete consolidation, which leaves pores between them [171].

Rapid prototyping techniques have become more popular in recent years as they allow the fabrication of ceramic scaffolds with controlled pore geometries. The principle depends on modelling the geometry using a computer design program, and then print it as a 3D object,

layer by layer from the bottom-up. Rapid prototyping allows the printing of an object of any geometry, shape, size and gradient porosity [164]. The most common technique of rapid prototyping is 3D printing. 3D printing has been used in dentistry in many different forms including medical modelling before surgery and creating models for the fabrication of crowns, copings, partial denture frameworks and orthodontic appliances [172]. However, the fabrication of a permanent restoration to replace missing tooth structure is still not possible using this technique due to the lack of suitable materials for printing. This is an area under development [152]. The main limitations of rapid prototyping are the high cost of the machine and its maintenance, as well as the need for specific training. However, it is suitable to fabricate ceramic scaffolds. Figure 2-17 shows an optical image of a 3D printed porous ceramic scaffold.

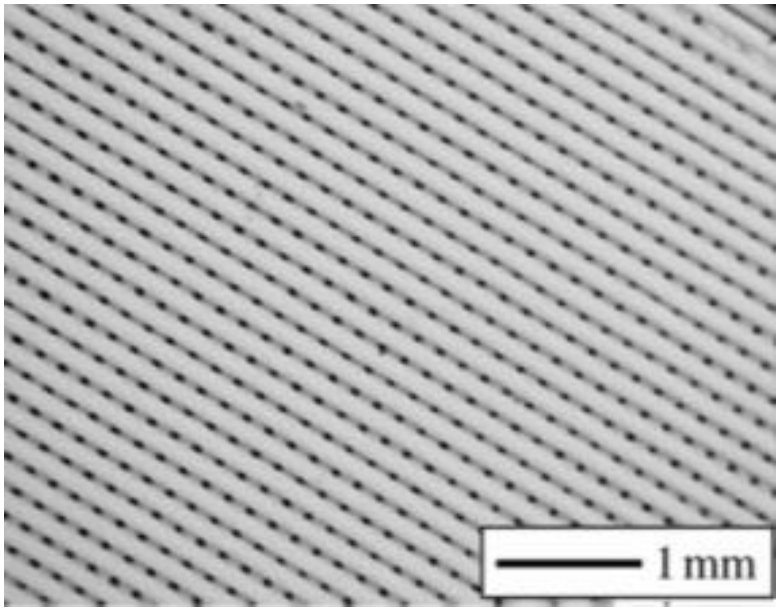

Figure 2-17: Optical microscopy image showing complex geometry of porous ceramic scaffolds fabricated via 3D printing [166].

The sacrificial template technique involves mixing a ceramic powder with a sacrificial template that works as a pore forming agent, which is then evaporated or burnt out during

sintering to forms the pores. Freeze casting is an example of this approach [170]. In freeze casting, an aqueous ceramic suspension gets frozen, and the growing ice crystals eject and concentrate the ceramic particles between them. Once this is lyophilised (transformed from the solid state to the gas state without passing in the liquid state), a porous green ceramic scaffold is created. This is then sintered to densify the ceramic powder into a densified ceramic scaffold suitable for infiltration with a second organic phase [173]. Figure 2-18 shows a freeze cast ceramic scaffold.

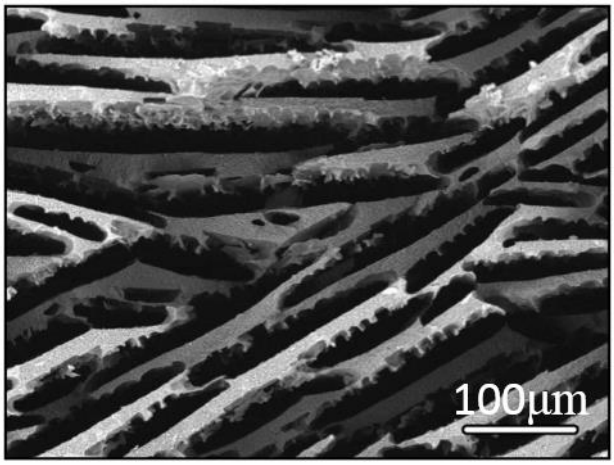

Figure 2-18: SEM image for freeze cast alumina ceramic scaffold [174].

The freeze casting technique has gained much attention in recent years and has become the most popular technique in producing porous ceramic scaffolds. It is the method used in this current research, where the possibility of creating a freeze cast alumina ceramic scaffold to fabricate a CAD/CAM dental composite material was investigated. Freeze casting will be further reviewed in the following section.

2.5.2 Freeze casting

The freeze casting technique comprises four steps (Figure 2-19): initially preparing a stable aqueous ceramic suspension, freezing the liquid (water in this case) within the suspension, followed by lyophilisation of the frozen media under low pressure and finally sintering the green body to create a dense ceramic scaffold [175]. The densified porous ceramic scaffold produced has a pore structure that is a replica of the frozen template. This pore structure can either be lamellar, dendritic or honeycomb, depending on the solvent used within the slurry [160].

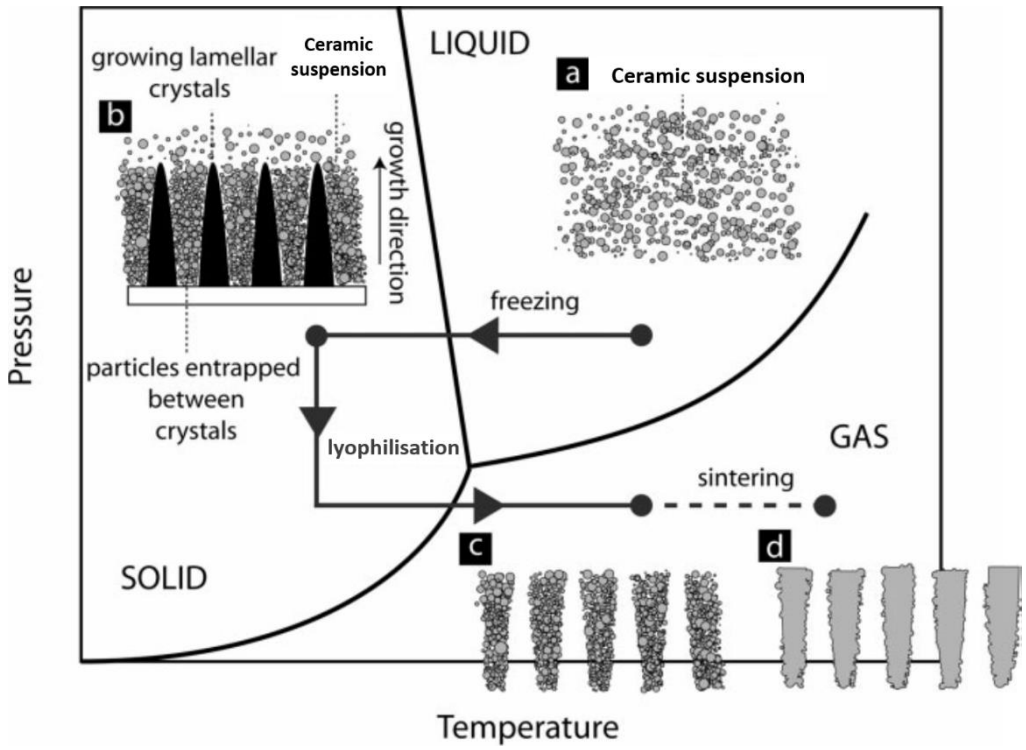

Figure 2-19: The four steps of freeze casting techniques [173].

The advantages of this method include: a normal ceramic sintering process without a burn out by-product. A wide range of porosity (30% to 99%) can be produced, dependant on the initial solid loading of the slurry and the freezing conditions. A variety of materials can be

used, and it is relatively cheap and cost-effective as a result of the simple equipment requirement. Also, no purifying step is necessary when sublimating the solvent, and therefore, the resulting scaffold will be free of impurities. It is also possible to produce materials with different structural features by changing the freezing conditions [31, 34].

Although there are many advantages of freeze casting, it is not without its limitations. For example, it is necessary to understand the complexity of the physical principles that govern the freezing process. There is a volume increase when freezing water, and it can be difficult to freeze ceramic suspensions with high initial solid loading [160, 176]. Once the solidification process has started, the solvent crystals (forming the solidification front) will start to grow and eject the ceramic particles within the suspension, causing them to pile up [177]. The main principle of freeze casting technique, therefore, relies more on the physical characteristics of the materials being used rather than on any chemical interactions, and this can be clearly seen by the variety of materials processed using this technique [173]. The steps of freeze casting technique are illustrated in Figure 2-19.

The history of freeze casting dates to the 1980s, where silica fibres were produced by freeze casting a polysilicic acid aqueous solution [178]. However, it was not until 2001 that the concept of using freeze casting to produce a porous ceramic scaffold was introduced to the ceramic community by Fukasawa [27].

The four stages in the freeze casting process (Figure 2-19) will now be described.

2.5.2.1 Ceramic suspensions preparation

In this step, ceramic powder is added to a liquid medium (solvent) to create a ceramic suspension, and to aid this process; a dispersant agent is often added. When preparing the

suspension, the solvent should stay in the liquid state and in the case of water as the solvent, this can be done at room temperature. If other solvents are used, e.g. tert-butyl alcohol or a camphene-based solvent, then different temperatures, i.e. 8 °C and 60 °C respectively, are required, which can make preparation more difficult. The desired total porosity and mechanical properties of the final scaffold are controlled to a large extent by the initial ceramic slurry solid loading, which is normally in the range of 10–40 vol. %. Finally, a binder is considered a very important additive, as its presence gives the green body ceramic its strength and prevents it from collapsing following the sublimation stage [173].

A suspension is a dispersed system where one solid phase is dispersed in a second continuous liquid phase. If the size of the particles within the solid phase is in the range of 1nm to 1μm, the resulting suspension is called a colloidal system [179, 180]. In ceramic processing, the stability of the suspended particles in the colloidal system is crucial to obtain the high packing density of the green body ceramic. This will ultimately result in a more homogenous structure [181].

The stability of the colloidal system depends on the total interparticle potential energy, which determines the interaction between particles, and hence its stability. The DLVO theory, named after Boris **D**erjaguin, Lev **L**andau, Evert **V**erwey and Theodoor **O**verbeek, defines two kinds of forces that rule the stability of a colloid in a suspension, namely an attractive van der Walls force and repulsive electrostatic force. If there is a strong long-range attractive van der Walls force, the particles will be attracted to each other, resulting in suspension flocculation accompanied with increased viscosity. On the other hand, if the repulsive electrostatic forces predominate, the particles will not aggregate [182, 183]. One way to control the electrostatic force is by changing the pH of the suspension. By increasing

or decreasing the pH, the adsorption or desorption of ionic species in the solution will change accordingly. Ions of opposite charge will be attracted by the surface charge of the particle and form a strongly bound Stern layer. Another layer, known as the diffuse layer, is formed around the Stern layer. It is composed of more ions being attracted by the charge of the particles, but as they have the same charge of the Stern layer, they are still repelled by it [184]. A model for a negatively charged particle surrounded by a double layer is illustrated in Figure 2-20.

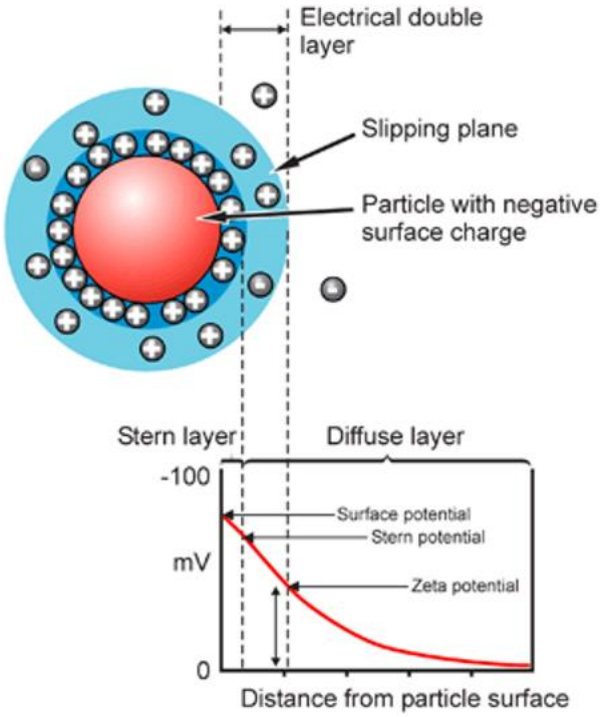

Figure 2-20: Schematic diagram of the zeta potential of a negatively charged particle [185].

In ceramic processing, a dispersant is used as a stabilising additive to maintain the colloidal suspension stability. The dispersant is adsorbed onto the powder particles in solution, and it can charge them and thereby alter their behaviour [186]. They either modify the electrostatic or steric properties of the particles in such a way as to improve the dispersion

process. Some dispersants, known as electrosteric dispersants, can modify the two properties at the same time [187]. Electrostatic forces can be generated by charging the surface of the suspended particles with the same strong charges, which maintains the suspension stability as a result of repulsive forces. Steric stabilisation comprises the absorption of organic molecules into the particle surface to generate steric repulsions. Polyelectrolyte dispersants can be cationic (positively charged) or anionic (negatively charged) [188]. These dispersants have long chain molecules and work as a steric hindrance. They usually have hydrophobic heads, which attach to the surface of the particles, while the hydrophilic tails point to the direction of the water molecules [189, 190]. When the optimal concentration of dispersant is present, it ensures that each powder particle is surrounded entirely with the highest surface charge and subsequently increases the separation distance between these particles to maintain a homogenous and well-stabilised ceramic suspension [191].

2.5.2.2 Solidification of the ceramic suspension

During this step, solvent crystals (namely ice in the case of water as a solvent) are nucleated under specific cooling conditions and grow into the suspension. The moving solidification front starts to reject the ceramic particles within the suspension, resulting in packing and entrapment of the particles between the solvent crystals [26]. To make sure that this segregation phenomenon is taking place, the suspension is poured in a mould which is cooled using either single or dual temperature gradient conditions [46]. Many different types of apparatus have been designed and built to control the freezing conditions [26, 27, 192, 193].

The choice of the solvent determines the solidification conditions, the shape of the growing crystals and subsequent macrostructure and surface texture of the ceramic walls of the pores. These, in turn, will affect the mechanical properties of the final ceramic scaffold [44]. Using water as a solvent requires low temperatures (< 0 °C) for freezing in order to produce a porous lamellar microstructure [28, 194-196]. In the case of camphene, room temperature is sufficient as the freezing point is 48 °C and it will produce dendritic structured pores [197-200]. A prismatic structure will result when using tert-butyl alcohol as a solvent, and the freezing point is 25.3 °C [201].

Ice crystals have a lamellar shape and can grow in two directions: horizontally along c-axis and vertically along a-axis as shown in Figure 2-21. As ice crystal growth in a-axis is more preferable than in c-axis, this leads to the production of vertical lamellar ice crystal. This explains the lamellar microstructure produced in the ceramic scaffold when water used as the solvent [173].

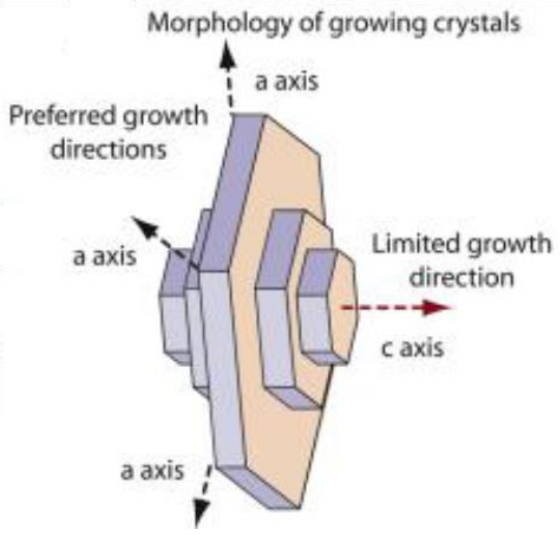

Figure 2-21: Schematic illustration of the morphology of growing ice crystals [173].

The conditions under which solidification takes place play a crucial role in determining the microstructural homogeneity of the final ceramic scaffold. Pore size and morphology can be altered by changing the freezing behaviour of the solvent and the resistance of the solid particles to the solidification front of the solvent. The parameters that have been investigated are freezing temperature, freezing time and freezing rate. Hue *et al.* (2010) [202] studied the effects of different freezing temperatures on the pore channel size in yttria stabilised zirconia (YSZ) ceramics. The results showed that as the freezing temperature decreased so did the pore channel size. This is because the freezing conditions control ice nucleation and crystal growth. Using a higher freezing temperature (low supercooling) leads to a higher crystal growth rate and lower nucleation rate, so that ice crystal growth is more favourable than ice nucleation. Therefore, a small number of large ice crystals form resulting in larger pores within the ceramic scaffold. Contrary to this, if the freezing temperature is low (high supercooling), a large number of smaller ice crystals form during solidification, which will result in smaller pores within the ceramic scaffold after freeze drying [202-206].

With increasing freezing time, the pore size in ceramics can increase significantly, as the large crystals will continue to grow and finally merge with small ones and result in a continuous interface [206].

The freezing rate also has a significant effect on ice crystal growth. As the freezing rate increases, so does the ice front velocity, which will hinder the lateral growth of the crystals along the c-axis resulting in a finer microstructure[207].

Another important parameter to consider when using freeze casting is the temperature gradient. Most freeze casting is done under a single vertical temperature gradient or so-called “uni-directional freeze casting”, and this allows ice crystals to nucleate and grow

randomly, producing a random microstructure [207]. The other type of freeze casting is freezing under dual temperature gradients (a horizontal gradient and a vertical gradient); this is called bi-directional freeze casting. Bi-directional freeze casting forces ice crystals to grow in an aligned way to produce a highly aligned microstructure [46].

2.5.2.3 Lyophilisation of the solvent

Once the sample is completely frozen, it should be kept at low temperature and reduced pressure. The initial choice of the solvent determines the lyophilisation conditions. This stage aims to convert the solidified solvent into a gas without passing through the liquid state. A green body sample is obtained where the pores are a direct replica of the solvent crystals. This green body has sufficient strength to maintain its shape and structure due to the presence of the binder network surrounding the ceramic particles, holding them together. In the case of water, a conventional freeze-dryer can be used. When using camphene, lyophilisation can be done at room temperature without the use of a specific machine [34, 173, 208].

2.5.2.4 Sintering of the green body

Once the lyophilisation process is complete, the green body is sintered using a conventional sintering furnace to obtain a strong ceramic scaffold [34, 209]. As the amount of organic binder is low, it does not require any special equipment for the binder burnout process. Ceramic sintering is a process of consolidation and grain densification by the action of necking. In the sintering stage, the ceramic walls lose any microporosity as a result of grain boundary solidification, while retaining the desired macroporosity created by the solidified solvent crystals [173].

During ceramic sintering, there are two competing processes: densification and grain growth. Densification can be defined as the process of minimising porosity to make ceramics denser; this happens by reducing the volume of the grain-gas interfaces through grain boundary formation, Figure 2-22 [210]. Grain growth is the act of increasing the grain size by grain boundary movement. For a grain to grow larger in size, it should have a low grain boundary energy. Indeed, larger grains have a smaller surface area per volume and hence low grain boundary energy, encouraging their growth at the expense of the smaller size grains [211].

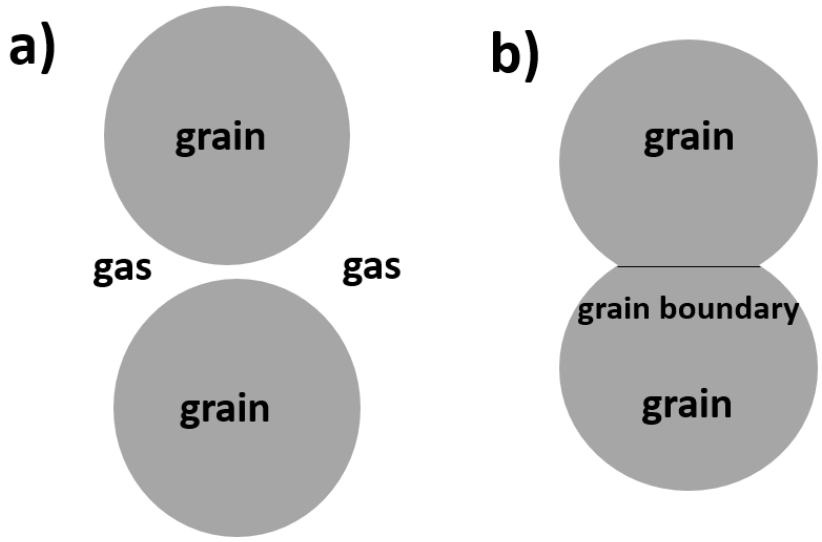

Figure 2-22: Schematic diagram showing a) grain-gas interfaces and b) replacing the grain-gas interface by a grain boundary.

Improving the mechanical properties of ceramic materials can be achieved by having a high relative density with small grain size. Which means the densification process should be enhanced over grain growth. One way to achieve this is by using a sintering aid to help in the process of sintering [212]. MgO is one of the most commonly used sintering aids for alumina. A very small addition of this material has a noticeable effect on alumina densification by preventing abnormal grain growth [213]. However, although various studies

have been conducted to try to understand the precise mechanism by which MgO improves alumina sintering, no clear conclusions have so far been reached [214]. The most commonly used explanation is due to the different charges between the magnesium (+2) and aluminium ions (+3). As a result, charge point defects (like vacancies) are generated to compensate for the extra charge, and these point defects improve the boundary diffusion coefficient and hence improve the density and limit abnormal grain growth [215].

Once sintered, the porous ceramic scaffold is ready to be infiltrated with a second phase material such as a polymer, glass or metal, depending on the desired properties and final application.

2.5.2.5 Microstructure formation mechanism

In order to achieve a lamellar structure in the ceramic samples, it is important to satisfy two essential conditions. First, the advancing ice front must reject the ceramic particles. Second, the solid-liquid interface must remain nonplanar. As the ice front breaks into sections, the ceramic particles can accumulate and pile up between the columns of lamellar ice crystals resulting in ceramic lamellar walls.

The rejection phenomenon can be explained by the thermodynamic principle stated by Korber *et al*. [216]. For a particle to be rejected by the advancing ice front the interfacial free energy between the particle and the solid phase (σ_{sp}) should be larger than the sum of the surface free energies of the solid-liquid phase (σ_{sl}) and liquid-particle phase (σ_{lp}) [216].

$$\Delta\sigma = \sigma_{sp} - \left(\sigma_{lp} + \sigma_{sl}\right) > 0$$

This principle can be used to predict whether the particle will be rejected or engulfed, assuming the ice front critical velocity (v_c) is not exceeded. Keeping the ice front velocity

below this critical limit maintains sufficient thickness of liquid film between the particles and the ice front. The liquid film is essential to allow the transport of particles away from the growing ice front. When the ice front critical velocity (v_c) is exceeded, particles are no longer rejected but become engulfed in the solid phase, and an isotropic ice structure is obtained[207].

The transition of a planar to a columnar interface can be triggered by the constitutional supercooling or by the presence of particles. When ice crystals start to form, they will eject the solutes that are initially present in the water. This separation of solutes will increase its concentration ahead of the ice front, which eventually generates a constitutional supercooling zone in an unstable condition [207]. This instability in the system is called Mullins-Serkerka instability, and it is responsible for the breakdown of the interface from planar to columnar [217].

Over the last 15 years, freeze casting in different forms has become the focus of a great deal of research and for many different materials, including ceramics. The versatility of this technique makes it easy to fine-tune the ceramic microstructure by altering the processing parameters, e.g. freezing conditions, solid loadings, solvent and additives [194, 196-198, 200, 201, 218-221]. Much of the research has been analysed in a meta-analysis by Deville *et al*. [222] and a recent literature review by Kristen *et al*. [160]. However, most of the published research and literature reviews have concentrated on conventional uni-directional freeze casting as a technique to fabricate ceramic scaffolds, where there is no control of lamellar orientation. In terms of controlling the microstructure, only a few studies have reported on the efforts to control lamellar orientation. One study reported the use of a patterned freezing surface to control the orientation of ice crystals arising from the planar

ice front to the lamellar, and hence the production of well-oriented microstructures [44]. Bouville et al. (2014) used “freezing under flow” as a novel method to control ice crystal growth to produce a textured macroporous material. The resulting samples showed aligned lamellar ceramic walls with a small domain mismatch compared to samples produced by conventional freezing methods [45]. It was Bai et al. (2015) who reported on the bi-directional freezing technique in which the introduction of a PDMS (Polydimethylsiloxane) wedge between the slurry and the cold finger created dual temperature gradients. These dual temperature gradients controlled ice crystal nucleation and growth and resulted in a large-scaled lamellar hydroxyapatite ceramic scaffold [46].

Bi-directional freeze casting was chosen to use in this research for the fabrication of the ceramic scaffolds, as it produces interconnected open pore structure, which can be fine-tuned by altering the processing parameters to obtain a large domain highly aligned lamellar structure.

2.6 Creation of nacre-like ceramic/polymer CAD/CAM dental material

Enamel and dentine are strong biological materials; at the same time, they do not break catastrophically under loading. Both tissues pose high fracture resistance to crack propagation and work together to provide human teeth with the best combination of strength, toughness and hardness. This is due to their anisotropic microstructure. Current chairside CAD/CAM dental materials are either ceramics or ceramic/polymer composites with a multiphase, or interpenetrating network structure. In addition, all CAD/CAM materials are isotropic with none of them possessing the anisotropic microstructure of natural tooth tissue. Based on that, there is a need of a new material that can mimic the natural tooth tissue mechanical properties. This was the motivation of the current research,

where the fabrication of material with a unique anisotropic microstructure was possible by mimicking nacre. Freeze casting was used to fabricate the ceramic scaffold that was pressed uniaxially to break the long ceramic walls into small ceramic bricks, followed by polymer infiltration that resemble the mortar in between the ceramic bricks. This fabrication technique produced a brick and mortar ceramic/polymer composite material. The hypothesis is that a ceramic/polymer composite dental material with brick and mortar anisotropic microstructure would better mimic the tooth tissue mechanical properties especially the fracture behaviour.

2.7 Aims and Objectives

This project aimed to fabricate and evaluate biomimetic nacre-like ceramic-polymer composite materials, with a brick and mortar structure and acceptable mechanical properties that might ultimately be used as a potential CAD/CAM dental restorative material.

The objectives of the project were:

- To investigate the effect of different processing parameters such as cooling rate, dual temperature gradients, initial solid loading and binder concentration on ceramic scaffold alignment and microstructure, when using bi-directional freeze casting.
- To characterise highly aligned ceramic scaffolds using light microscopy, SEM and micro-CT to fully understand the mechanism of ice nucleation and growth under dual temperature gradients.
- To investigate the use of MgO as a sintering aid in Al_2O_3 ceramic suspensions, to use it in the fabrication of highly aligned ceramic scaffolds to produce biomimetic nacre-like ceramic/polymer composite materials.
- To characterise the mechanical properties of biomimetic ceramic/polymer composite materials, including flexural strength, modulus of elasticity, fracture toughness and hardness. Commercially available Vita Enamic CAD/CAM dental material was used as a benchmark material for comparison.
- To assess the machinability of the biomimetic ceramic/polymer composites for their possible application as chairside CAD/CAM restorative materials.

Chapter 3. Materials and methods

The ultimate goal of this research is to fabricate nacre-like ceramic/polymer composite materials for CAD/CAM dental applications. The first step of the fabrication process is to fabricate the bricks like ceramic scaffold then infiltrate it with a second phase polymer material. For the scaffold to be fabricated a stable ceramic suspension was prepared then freeze casted by bi-directional freeze casting to produce a highly aligned ceramic scaffold that was lyophilized to remove the frozen solvent medium and get a green body. The green body had to go through a first-step sintering to burn out the binder and strengthen the scaffold to withstand the following uniaxial pressing step. In this step the long ceramic walls broken down into short bricks and the ceramic volume fraction inside the scaffold increased. After that the scaffold went to the furnace for second-step sintering to fully consolidate the ceramic grains and to create connections between the ceramic bricks. The fully sintered scaffold is now ready to be infiltrated by the monomers mixture but before that a silanisation step in mandatory to create a bond between the inorganic ceramic scaffold and the organic polymer. After monomers infiltration, polymerisation started under controlled temperatures as the last step in the fabrication process of a ceramic/polymer composite material.

3.1 Raw materials

3.1.1 Ceramic powders

Alumina (Al_2O_3) powder [density, 3.96 g/cm^3; size, 0.5µm] (CT3000SG, Almatis GmbH, Germany) was used in this study to prepare the ceramic suspensions. Alumina was chosen

due to its good thermal and mechanical properties and ready availability. It also shows high wear resistance and is biocompatible [223].

Magnesium oxide (MgO) nanopowder [density, 3.58 g/cm^3] (MG-OX-04-P, American Element, USA) was added as a sintering aid to produce ceramic scaffolds for composite material fabrication. MgO is well known for being a highly effective sintering aid for alumina [213].

3.1.2 Processing additives

Two different dispersants were used in the study, namely:

- Dolapix CE64 (D-CE64) (Zschimmer& Schwarz, Germany) was used as an electrosteric dispersant for the Al_2O_3 ceramic suspensions and is an anionic surfactant with a negatively charged head group and an average molecular weight of 320 g/mol. It is a commonly used dispersant for Al_2O_3 [224].
- Tiron 4,5-dihydroxy-1,3-benzenedisulfonic acid (Aldrich-Chemie, Germany) was used as an electrostatic dispersant for the Al_2O_3/MgO ceramic suspensions. Compared to Dolapix, Tiron can disperse both Al_2O_3 and MgO particles by stronger electrostatic charging (higher negative zeta potential) [224].

To increase the strength of the ceramic green bodies, Poly (vinyl alcohol) (PVA) (Sigma Aldrich, USA MW: 9,000- 10,000) was used as a binder. It shapes ice crystals into a lamellar microstructure, which is desirable in the fabricated ceramic scaffold [225].

To prevent the formation of air bubbles within the ceramic suspension, 1-octanol (Fisher Scientific, UK) was added as a debubbliser.

3.1.3 Polymer materials

Two polymer systems were used to infiltrate the ceramic scaffolds, namely:

- Epoxy resin (Specifix, Struers, UK) was used for the microstructural characterisation of the scaffold materials.
- Urethane dimethacrylate (UDMA) (MW:470.56g/mol, Density: 1.09g/mol, Sigma-Aldrich, UK) and triethylene glycol dimethacrylate (TEGDMA) (MW: 286.32 g/mol, Density: 1.09 g/mol, Sigma-Aldrich, UK) monomer mixture was also used for the fabrication of biomimetic ceramic/polymer composites. This is because UDMA/TEGDMA is commonly used in currently available dental resin composites.

Benzoyl peroxide (Luperox, MW: 242.23 g/mol, Sigma-Aldrich, UK) was used as a heat activator in the case of the monomer mixture.

3.1.4 Vita Enamic CAD/CAM material

Vita Enamic CAD/CAM blocks (0 M1-T, EM-14) (Vita Zahnfabrik, Germany) were chosen for direct comparison with the biomimetic ceramic/polymer composites made in this study. This is because it is a commercially available ceramic/polymer composite used in chairside CAD/CAM dental restoration fabrication. The samples were cut and polished for mechanical testing using the same testing parameters used to test all of the fabricated composite materials in this research.

3.2 Experimental methods

3.2.1 Bi-directional freeze casting of highly aligned alumina ceramic scaffolds

3.2.1.1 Preparation of the ceramic suspensions

In this part of the study, different alumina ceramic suspensions were prepared in order to investigate their effect on ceramic scaffold fabrication using a bi-directional freeze casting technique. These were colloidal suspensions, meaning the alumina particles were dispersed in water with the aid of an additive, namely a dispersant. The concentrations of all additives were calculated with respect to the dry weight of the ceramic powder.

Alumina (Al_2O_3) powder was used to prepare ceramic suspensions with different solid loadings (15 to 40 vol.%). In each case, the alumina was mixed with distilled water and a dispersant (Dolapix CE64, 0.6 wt.% of the powder by weight) inside a 500ml polyethylene bottle. 250g of yttria-stabilised zirconia balls (5 and 10mm diameter) were also added to the bottle to help in ball milling the suspension. A roller mixing machine (1600-VS-A, Pascall Engineering, UK) at a speed of 3 on the machine (range of 1 – 10), was used for this step. The suspensions were ball milled for 1 h to ensure the dispersant fully covered the alumina particles before adding the binder.

3.2.1.2 Preparation of the PVA/ceramic suspensions

In order to use polyvinyl alcohol (PVA) powder as a binder, a 10 vol.% PVA solution was prepared. 450ml of distilled water was placed into a 500 ml glass beaker on a hot plate with a magnetic stirrer (Fisher Scientific, UK) and heated to a temperature of 90°C. 63.45g of PVA powder was then added to the water in four increments, and once the solution appeared clear, the heat source was removed, and the solution was stirred overnight.

The PVA binder solution, at 2wt.% of the powder weight, was added to the alumina suspensions in order to improve the strength of the green ceramic scaffolds after water lyophilisation. Once added, the whole mixture was ball milled for a further 24 h to create a colloidal system of highly dispersed alumina. One hour before freeze casting, the suspensions were again ball milled at a low speed following the addition of 1-octanol (Fisher Scientific, UK) (0.1 vol.% of the dry powder weight). Octanol was added to prevent the formation of air bubbles, which might create closed pores inside the scaffold and adversely affect the mechanical properties of the final composite material.

The amount of water used to create the initial ceramic suspension was dependent on the initial ceramic solid loading, taking into consideration the amount of water in the PVA solution. Table 3-1 shows the recipes used to prepare each of the different initial solid loadings.

Initial ceramic solid loading (vol.%)	Ceramic powder weight (g)	Volume of water (ml)	Dolapix dispersant (ml)	PVA binder solution (ml)
15	59.4	75.34	0.29	9.36
20	79.2	67.12	0.39	12.48
25	99.0	58.9	0.49	15.6
30	118.8	50.7	0.59	18.7
35	138.6	42.5	0.69	21.8
40	158.4	34.3	0.79	24.9

Table 3-1: Recipes of the different ceramic solid loadings.

The flow chart Figure 3-1 illustrates the preparation process of the alumina ceramic suspensions.

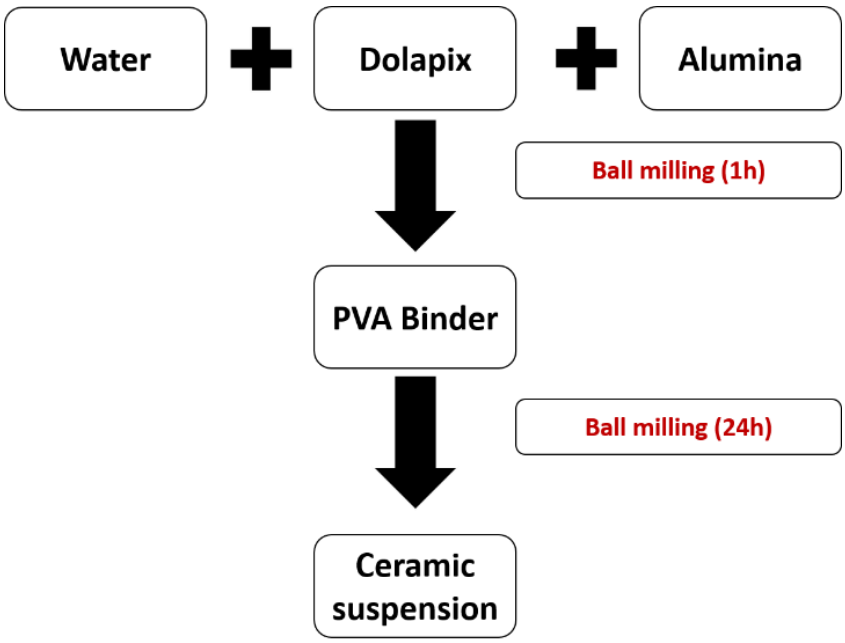

Figure 3-1: Flow chart of Al_2O_3 ceramic suspensions preparation used for scaffold alignment study.

To study the effect of PVA binder concentration on the ceramic scaffold microstructure, four different PVA concentrations (1, 2, 4 or 8 wt.% of the dry ceramic powder weight) were added to 20 vol.% ceramic solid loading according to the recipes in table 3-2.

PVA binder weight %	Ceramic powder weight (g)	Volume of water (ml)	Dolapix dispersant (ml)	PVA binder solution (ml)
1	79.2	73.36	0.39	6.24
2	79.2	67.12	0.39	12.48
4	79.2	54.7	0.39	24.9
8	79.2	29.8	0.39	49.8

Table 3-2: Recipes of the 20 vol.% ceramic solid loaded suspensions prepared with different PVA binder concentrations.

3.2.1.3 Freeze casting apparatus and moulds

3.2.1.3.1 Freeze casting apparatus

A conventional freeze casting apparatus, with upper and lower cooling rods, was used [209], as shown in Figure 3-2. The temperature of the top rod was held at a constant 20 °C throughout all of the experiments using an immersion cooler (FT200, Julabo, Germany). Meanwhile, the temperature of the bottom rod was reduced at three different cooling rates (1, 5, 10°C /min) to reach -30 °C. For the 1°C/min cooling rate, only an immersion cooler (PolyScience, USA) was used, but to get 5 and 10°C cooling rates, a liquid nitrogen tank was used along with the immersion cooler. Band heaters (MI, 400W, Watlow, USA) and thermocouples (type J, Watlow, USA) connected to a PID control console (TCP-200, Tempco, USA) were used to control both the freezing temperature and cooling rate. The bottom thermocouple was placed inside the mould copper base, while the top thermocouple was placed close to the band heater. Before each experiment, the top surface of the bottom rod was covered with a thin layer of silicone thermal grease (RS Pro silicone thermal grease, RS, UK). This was done to ensure good contact between it and the copper mould base to improve thermal conductivity.

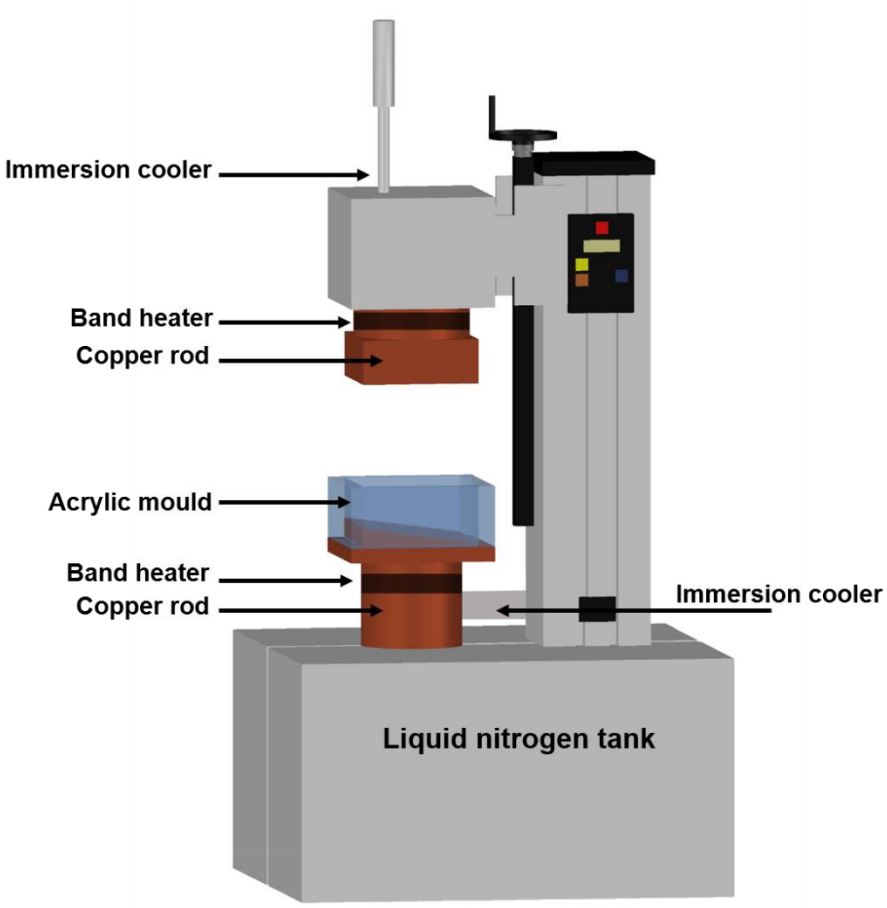

Figure 3-2: Schematic illustration of freeze casting apparatus.

3.2.1.3.2 Moulds

In conventional uni-directional freeze casting, a single flat copper base is used as one end of the temperature gradient apparatus, and vertical unidirectional crystal growth takes place from this surface. For bi-directional freeze casting, specially designed, custom-made copper and polydimethylsiloxane (PDMS, Sylgard 184, Dow Corning, USA) wedges (60 x 60 mm) were fabricated with three different slope angles (5°, 10° and 20°). The copper wedge in each case was covered by an equivalent PDMS wedge but upside down in order to generate a horizontal temperature gradient that is essential for bi-directional freezing (Figure. 3-3). The purpose of the two wedges, one copper and one PDMS isolating material, was to provide a flat base from which to generate the ceramic sample using the freeze casting

apparatus. In order to contain the ceramic suspension during freeze casting, an acrylic box was constructed to a height of 20mm surrounding the copper wedge. The PDMS wedge was prepared by hand mixing the silicone elastomer base with the curing agent in a 10:1 ratio for 5 mins and pouring it on top of the copper wedge. The mould was then left at room temperature for 1 h to allow air bubbles escape, before placing it in an oven (Thermo Scientific, Heratherm OMS60, Germany) at 60 °C for 1 h to cure.

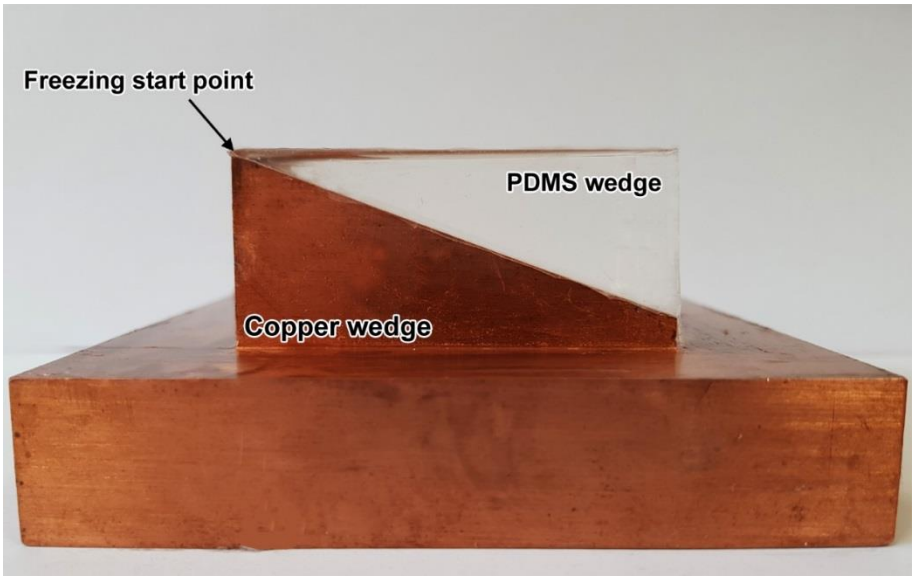

Figure 3-3: Copper/PDMS wedge mould (α= 20°).

3.2.1.4 Freeze casting

For each experiment, 80 ml of ceramic suspension was poured into the mould. The mould was then placed on top of the cold, bottom rod of the freeze casting machine, and the top rod was lowered slowly to be just above the ceramic suspension. The freeze casting process starts inside the ceramic suspension as a result of the temperature gradient, which leads to ice crystal formation. As ice crystals grow, from the coldest area toward the least cold area, they begin to repel the suspended ceramic particles, which then accumulate between the ice to form a continuous ceramic scaffold, as illustrated in Figure 3-4.

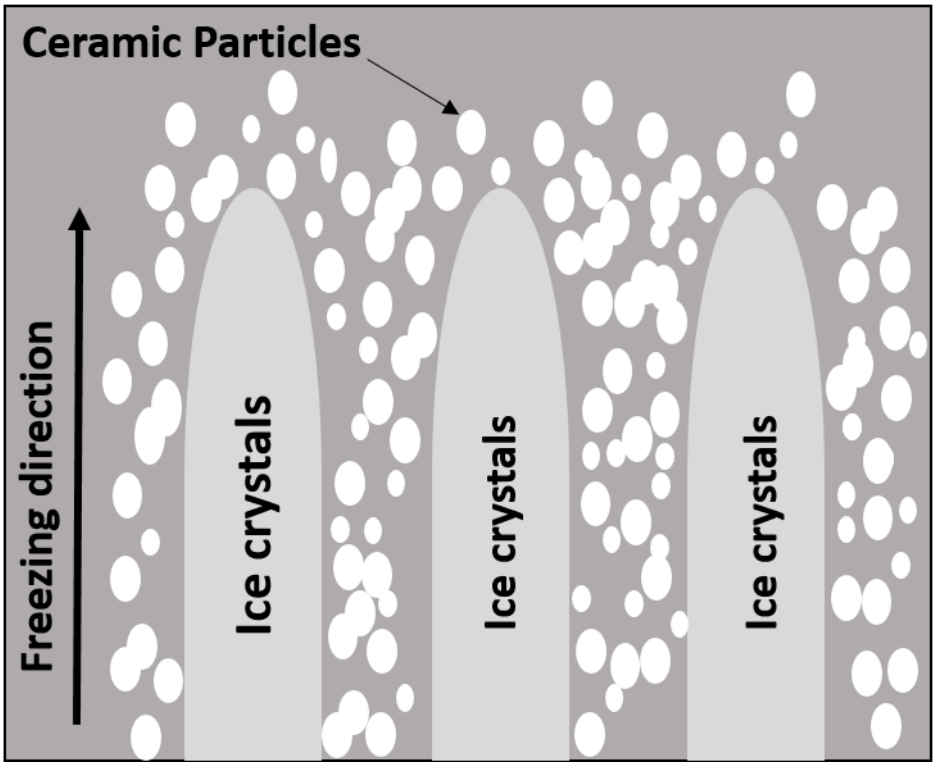

Figure 3-4: Schematic illustration showing ice crystal growth inside the ceramic suspension, repelling the ceramic particles to form a ceramic scaffold.

3.2.1.5 Freeze drying or lyophilisation

Following freeze casting, the mould with the frozen sample inside was removed from the freeze casting machine and transferred to a freeze dryer (Modulyo, Edwards, UK). Here the ice within the ceramic scaffold was lyophilized (turned from a solid into a gas without passing through the liquid state) at -55 °C, under vacuum at 0.01 mbar, for 24 h. The green body ceramic scaffold created was then carefully removed from the casting mould using a custom-made wooden device with a copper top.

3.2.1.6 Sintering

Once created, the green body ceramic scaffold was sintered (Elite Thermal Ltd., UK) using two heating cycles: the first used a heating rate of 2°C/min up to 450°C, which was then held for 2h. The second cycle had a heating rate of 10°C/min, up to 1600°C, which was held for another 2h. The purpose of sintering was to burn out the binder in the first cycle and increase the density and strength of the green ceramic scaffold in the second cycle. The sintered specimens were left inside the furnace to cool down to room temperature before removal. The ceramic microstructural changes following freeze casting, freeze drying and final sintering are illustrated in Figure 3-5.

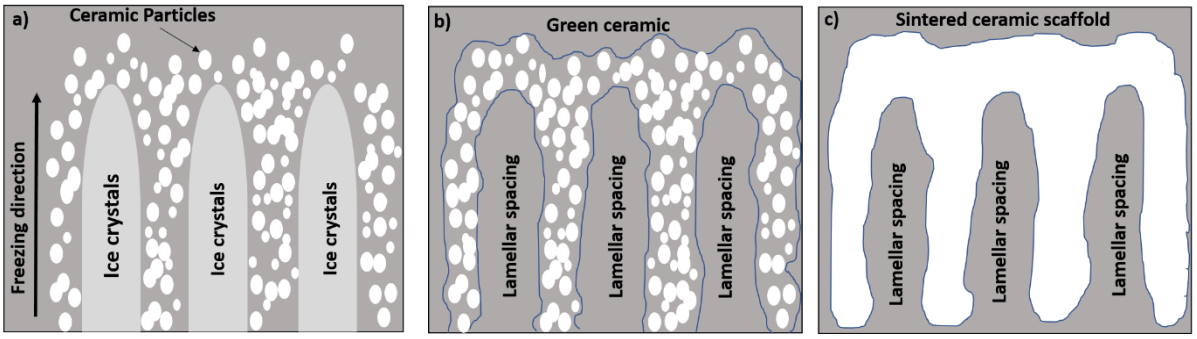

Figure 3-5: Schematic illustration of the ceramic microstructural changes during a) freeze casting, b) freeze drying and c) sintering.

The spaces that were originally occupied by ice crystals in the frozen specimen, after sintering are known as lamellar spaces. The scaffold produced by bi-directional freeze casting consists of two areas, a small area where the lamellar spaces are randomly oriented and a much larger area where the lamellar spaces are highly aligned, as shown in Figure 3-6.

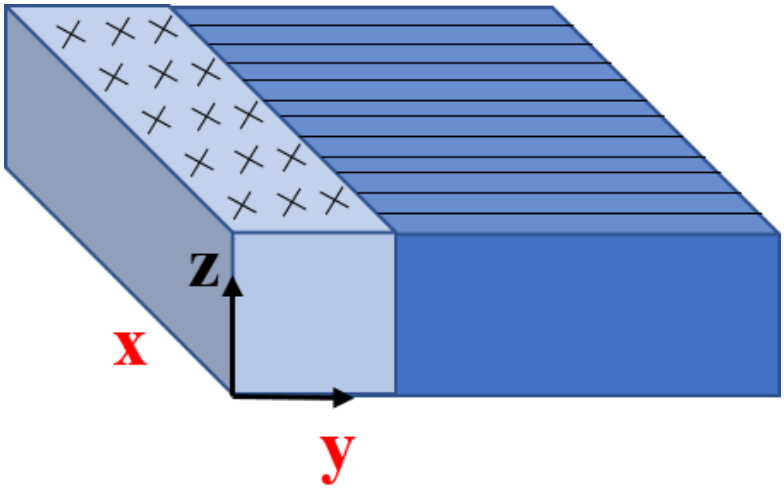

Figure 3-6: Schematic illustration showing how the final ceramic scaffold consists of two areas; a small random lamellar area and a larger aligned lamellar area following bi-directional freeze casting.

3.2.1.7 Epoxy resin infiltration

Epoxy resin was used to infiltrate the porous ceramic scaffolds to facilitate the sample preparation for microstructural characterisation. The epoxy resin was mixed using a wooden spatula in a 7:1 ratio of the base monomer (Bisphenol-A-epichlorohydrin, MW≤700, Struers, UK) to the curing agent (2-Methyl-1,5-pentamethylen-diamine, Struers, UK). To improve imaging contrast under light microscopy, methylene blue dye was added to the epoxy polymer. A casting impregnation system (Cast N' Vac 1000, Buehler, USA) was used for the infiltration step. Once infiltrated the scaffolds were removed from the machine and left at room temperature overnight to allow the polymer to fully cure.

3.2.2 Fabrication of biomimetic ceramic/polymer composite materials

Magnesium oxide (MgO) is a sintering aid used to improve the densification of alumina based ceramics and help prevent abnormal grain growth. For the fabrication of the composite materials used in this study, MgO was added to the alumina ceramic suspension in order to improve the overall mechanical properties of the final composite materials. The basic nature of MgO powder makes it difficult to disperse using the conventional dispersant Dolapix, and for this reason, Tiron, a strong electrostatic dispersant, was used instead.

The flow chart Figure 3-7 shows the biomimetic composite material fabrication steps.

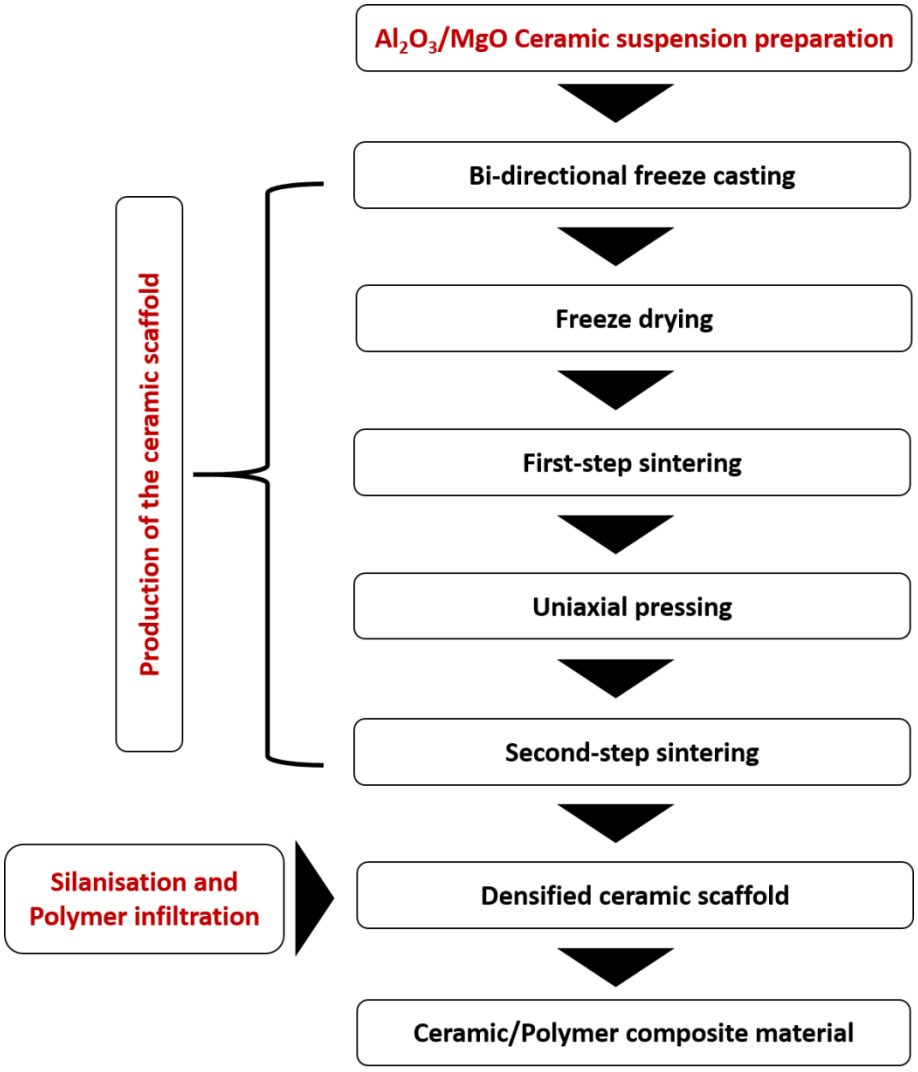

Figure 3-7: Flow chart of the biomimetic composite material fabrication steps.

3.2.2.1 Ceramic suspension preparation and optimisation

Ceramic scaffolds used for composite material fabrication were produce using 20 vol.% Al_2O_3/MgO ceramic suspensions, as shown in Figure 3-8. In a 200 ml glass beaker, distilled water and the dispersant 4,5-dihydroxy-1,3-benzenedisulfonic acid (Tiron, Aldrich-Chemie, Germany, 0.1 wt.% of the powder weight) were mixed using a magnetic stirrer (Fisher Scientific, UK) for 2 mins. MgO powder was then added to the solution, which was stirred for a further 30 mins so that the dispersant fully covered the MgO particles. This MgO Tiron

solution was then added to the alumina powder in a 500 ml polyethylene bottle, and ball milled for 1 h in a roller mixing machine (1600-VS-A, Pascall Engineering, UK) at a speed of 3 on the machine (range of 1 – 10), along with 250 g of yttria-stabilised zirconia balls (5 and 10 mm diameter). Following this, PVA solution (Sigma Aldrich, USA MW: 9,000-10,000, 2 wt.% of the powder weight) was added to ensure the green body strength after freeze drying. This mixture was ball milled for a further 24 h before the zirconia balls were removed. Mixing within the bottle was continued for another 24 h to stabilise the suspension. One hour before freeze casting, 0.1 vol.% of 1-octanol (Fisher Scientific, UK) was added as a debubbliser, and the suspension was ball milled at a slow speed of 1 for 30 mins.

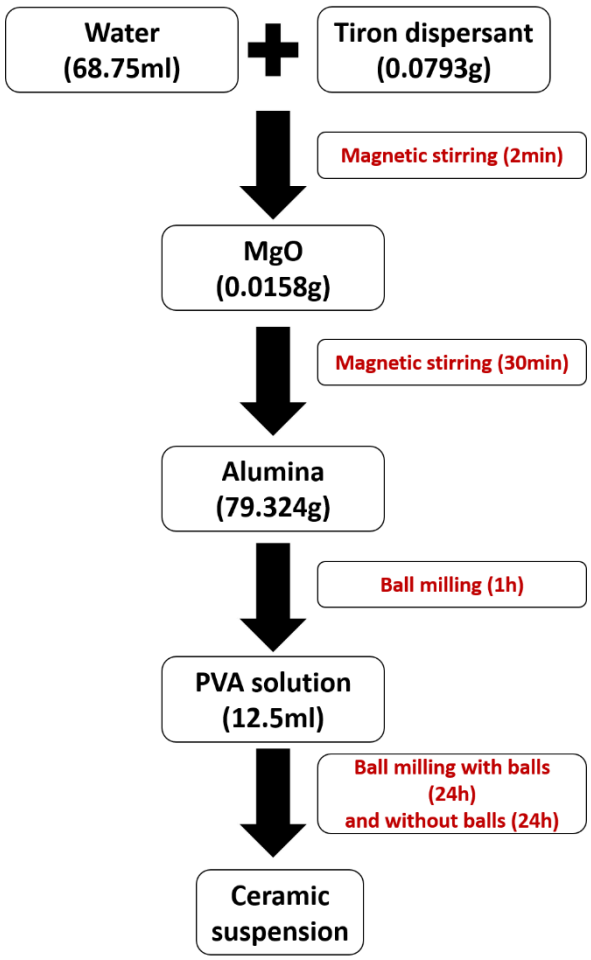

Figure 3-8: Flow chart of Al_2O_3/MgO ceramic suspension preparation used for scaffold fabrication for the composite material.

3.2.2.1.1 Zeta potential of the ceramic suspension

In order to determine the effect of the dispersant Tiron on the surface charge of the ceramic particles, the zeta potentials of both Al_2O_3 and MgO ceramic suspensions were measured using a Zetasizer (Nano series, Malvern, UK). Solutions of 0.2 vol.% of Al_2O_3 and 0.2 vol.% MgO were prepared with Tiron and without Tiron, as shown in Table 3-3. One millilitre of each suspension was extra diluted using 100 ml of water, HCl and NaOH, to adjust the pH, which was measured using a pH meter (3510 Jenway pH meter, Barloworld Scientific Ltd., UK). Buffered solutions with a pH 7 and 10 (BS07 and BS10, Thermo Fisher Scientific, UK) were used to calibrate the pH meter. The zeta potential for each suspension was measured at different pH values.

	Ceramic powder weight (g)	Volume of water (ml)	Tiron dispersant (g)
Al_2O_3	0.79	100	0.197
Al_2O_3	0.79	100	0
MgO	0.79	100	0.197
MgO	0.79	100	0

Table 3-3: Recipes used to prepare Al_2O_3 ceramic suspensions and MgO ceramic suspensions with and without Tiron.

3.2.2.1.2 Rheology of the ceramic suspension

To determine the effect of different Tiron dispersant concentrations (0.05, 0.1, 0.25, 0.5, 1.0 wt.% of the ceramic powder) on ceramic suspension viscosity, a high initial solid loading of 40 vol.% of Al_2O_3/MgO ceramic was used. A high initial solid loading creates a more viscous suspension, which makes it easier to observe the effect of the different dispersant concentrations on the rheology. Since we just wanted to determine the effect of the

dispersant, no binder was added to the solution. The recipes for the ceramic suspensions under test are shown in Table 3-4. In each case, the viscosity was measured using a rheometer with a cone-plate geometry and at a controlled shear rate of 0.1 to 500 s^{-1} at 20°C (Kinexus Pro Rheometer, Malvern Panalytical, UK).

Tiron dispersant amount wt.%	Al_2O_3 weight (g)	MgO weight (g)	Water volume (ml)	Tiron dispersant (g)
0.05	158.36	0.031	60	0.0792
0.1	158.36	0.031	60	0.1584
0.25	158.36	0.031	60	0.396
0.5	158.36	0.031	60	0.792
1.0	158.36	0.031	60	1.584

Table 3-4: Recipes for different ceramic suspensions prepared using different concentrations of Tiron.

3.2.2.2 Production of the ceramic scaffolds

The parameters used to fabricate the Al_2O_3/MgO ceramic scaffolds for biomimetic composite materials were chosen based on the results obtained from the bi-directional freeze casting experiment. Firstly, the PDMS wedge was replaced with a silicon rubber (SR) material wedge (Elite double 32, Zhermack, Italy). The SR wedges were prepared by mixing equal quantities of the silicon rubber base and catalyst using a wooden spatula for 2 min. This was then poured over the copper wedge and left on the bench to self-cure at room temperature for 30 min. The reason SR was used instead of PDMS in the remaining experiments was its low cost and ease of fabrication. Not only does SR cure at room temperature, but it does so in a relatively short time.

Secondly, a copper/SR mould slope angle of α= 10° was used to produce the ceramic scaffolds for the composite materials as it produced the best coherency in lamellar alignment compared to slope angles of α= 5° and 20°. Thirdly, a higher cooling rate was used. The aim was to increase the number of nucleation crystals and hence decrease the ceramic wall thickness and improve the mechanical properties. To achieve a high cooling rate (>10°C/min) a polystyrene tank containing liquid nitrogen was used. Polystyrene is a very good insulator, and as a result, less liquid nitrogen was required to reduce the copper rod temperature when compared to the metal tank used for freeze casting described earlier in section (3.2.1.3.1). The set-up is shown in Figure 3-9.

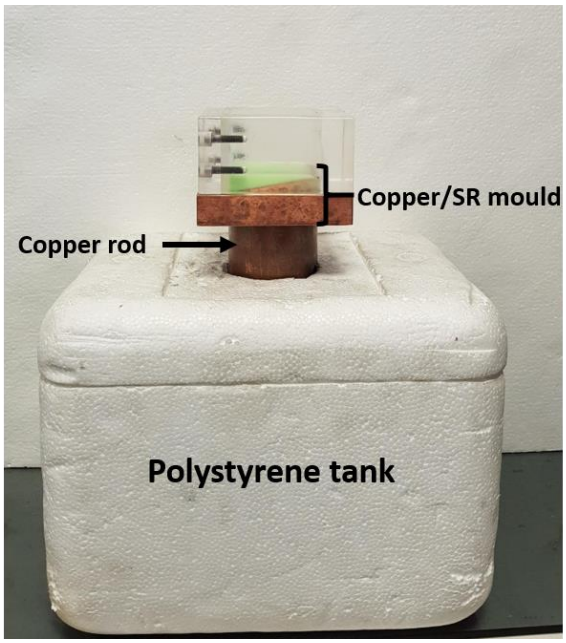

Figure 3-9: Polystyrene tank used to freeze cast Al_2O_3/MgO ceramic suspensions.

3.2.2.3 First-step sintering

The freeze-dried ceramic green bodies were sintered (Elite Thermal Ltd., UK) using two steps. First-step sintering was used to strengthen the ceramic green bodies in preparation for the subsequent pressing process, and it comprises two cycles: the first cycle used a

heating rate of 2°C/min up to 600°C, which was then held for 2 h; the second cycle had a heating rate of 10°C/min, up to different temperatures (from 1200°C to 1600°C) and again held for another 2 h. Following this, the scaffolds were partially sintered.

3.2.2.4 Uniaxial pressing

To break the long lamellar ceramic walls into small bricks and to increase the ceramic fraction in the final composites, uniaxial pressing was performed on the partially sintered scaffolds. As mentioned previously, ceramic scaffolds produced by bi-directional freeze casting consists of two areas: random and aligned lamellae. The random areas were cut out from the partially sintered scaffolds by hand using a mini saw (Eclipse 675, UK), and the remaining aligned areas were then infiltrated with blue inlay casting wax (Kerr, Czech Republic), the casting wax was used as it does not leave residue inside the ceramic scaffolds after burning it out. Wax infiltration was done to preserve the lamellar structure during subsequent uniaxial pressing and was performed by immersing the aligned scaffolds in melted wax over a hot plate (Fisher Scientific, UK) at 100°C. Figure 3-10 is an aligned ceramic scaffold fully infiltrated with blue inlay wax.

Figure 3-10: Aligned ceramic scaffold infiltrated with blue wax.

Once the scaffold was fully infiltrated with wax, the hot plate was turned off, and the sample left at room temperature to cool down. The wax infiltrated aligned scaffold was then ground using SiC sandpaper (P 80, Struers, Denmark) until it was able to fit into a 28 x 18 mm square stainless steel mould. The mould was then placed in a hydraulic press (PerkinElmer, Germany) and heated to 80 °C using a temperature controller device (WK-1, MTI Co, USA) (Figure 3-11). The temperature was kept at 80°C for 5 min before pressing to ensure that the wax was in the liquid state and could flow out under pressure. Upon cooling, the wax maintained the integrity of the pressed scaffold. The pressure was applied manually, perpendicular to the lamellar direction. Figure 3-12 shows two scaffolds before and after uniaxial pressing. Four different pressures (100, 150, 200, 250 MPs) were used to produce ceramic scaffolds with different ceramic volume fractions in the final composites.

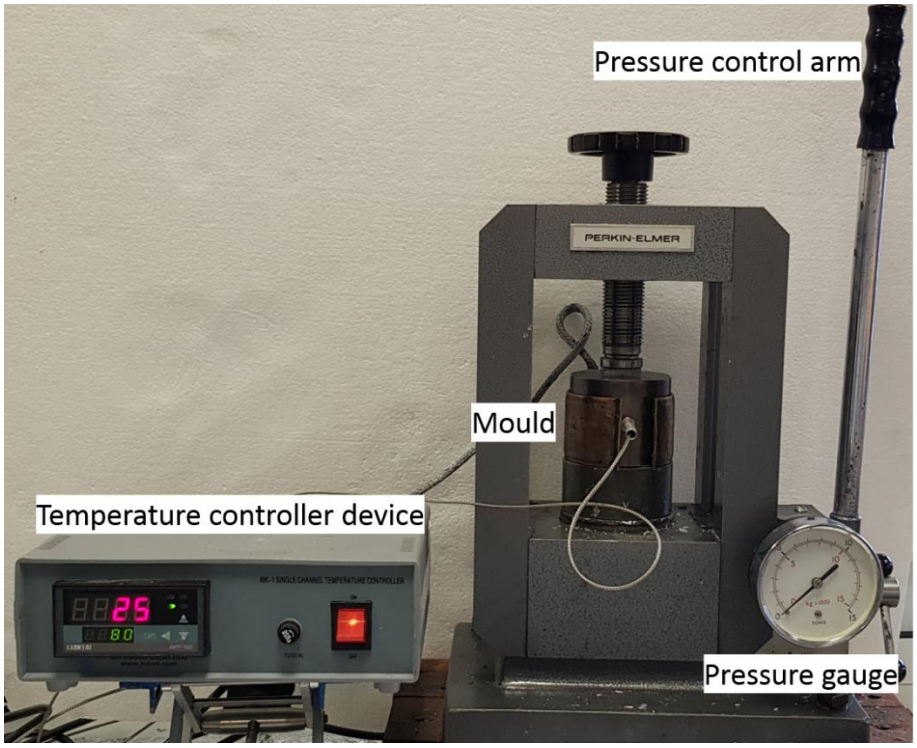

Figure 3-11: Table-top hydraulic press with the mould and the temperature controller device used to uniaxially press the ceramic scaffolds.

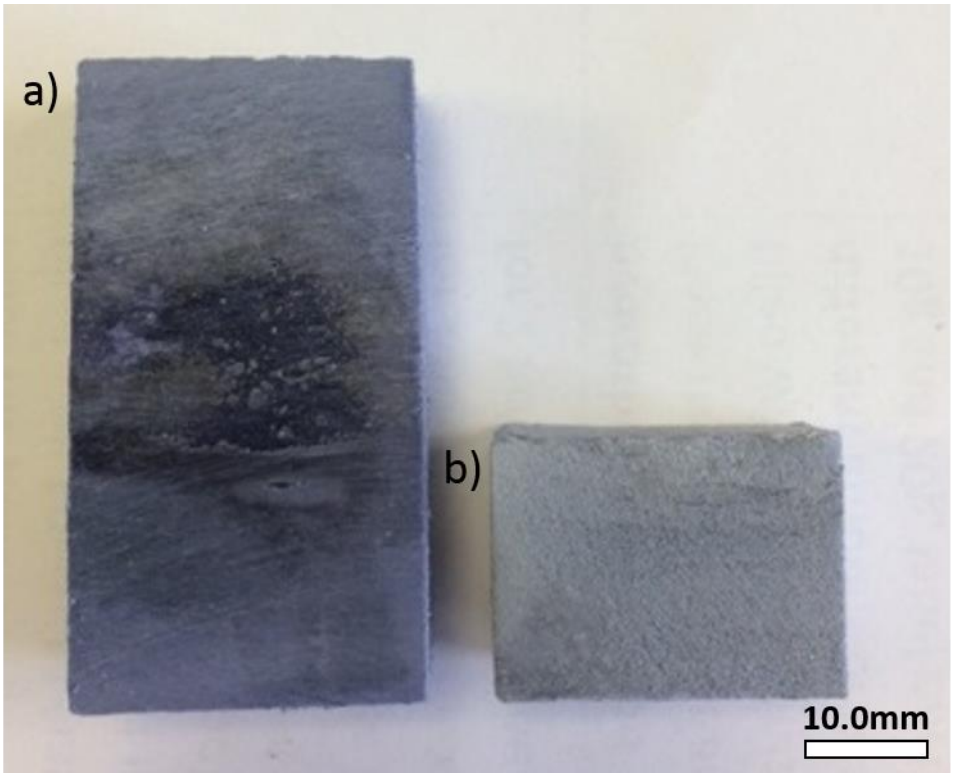

Figure 3-12: Partially sintered scaffolds filled with wax a) before and b) after uniaxial pressing.

3.2.2.5 Second-step sintering

A second-step sintering was mandatory after the uniaxial pressing to burn out the wax in the pressed scaffolds and to fully sinter them. After the uniaxial pressing step, the scaffold was removed from the mould and sintered once again. The sintering regime again comprised two cycles: the first used a heating rate of 1°C/min up to 600°C, held for 2 h, in this cycle the wax was fully burn out without leaving any residue. The second cycle had a heating rate of 10°C/min, up to 1550°C, held for another 2 h, during which the ceramic grains consolidate together to give fully sintered ceramic scaffolds.

3.2.2.6 Silanisation

After the second-step sintering a fully sintered porous ceramic scaffold was produced. To ensure good adhesion between the inorganic ceramic scaffold and the organic UDMA/TEGDMA polymer, a silane coupling agent, 3-(trimethoxysilyl)propyl methacrylate(γ-MPS) (Sigma Aldrich, UK), was used to graft on the ceramic walls (Figure 3-13). The structure of the UDMA, TEGDMA and the γ-MPS are shown in Figure 3-13, a. Grafting was achieved by firstly treating the ceramic scaffold with a Piranha solution [226] in order to remove any further organic debris and to produce hydroxyl groups on the scaffold surfaces. The Piranha solution was created by adding hydrogen peroxide (H_2O_2) (Hydrogen peroxide, for analysis, 35 wt.% solution in water, stabilized, ACROS ORGANICS, Netherland) to 30 vol.% sulphuric acid (H_2SO_4) (97.5+%, Sigma Aldrich, UK) in a 1:1 ratio. The fully sintered scaffold was treated in the solution for 1h to form hydroxyl groups on the alumina ceramic walls (Figure 3-13, b). After adequate rinsing and careful sonication in an ultrasonic bath (Grant Scientific, UK) using distilled water, the scaffold was then immersed in the silane coupling agent solution, prepared by mixing 50 vol.% γ-MPS and 50 vol.% acetone (Analytical reagent grade, Fisher Chemical, UK), for 6 h. This step aimed to form a chemical bond between the hydroxyl group on the alumina ceramic surface and the OH group of the γ-MPS (Figure 3-13, b). The carbon-carbon double bond of the γ-MPS is then able to bond chemically to the carbon-carbon double bond in UDMA/TGDMA monomers (Figure 3-13, c). In this way, the γ-MPS acted as an interfacial bridge between the ceramic walls (inorganic phase) and the UDMA/TEGDMA polymer (organic phase) to ensure a strong adhesion between the two phases.

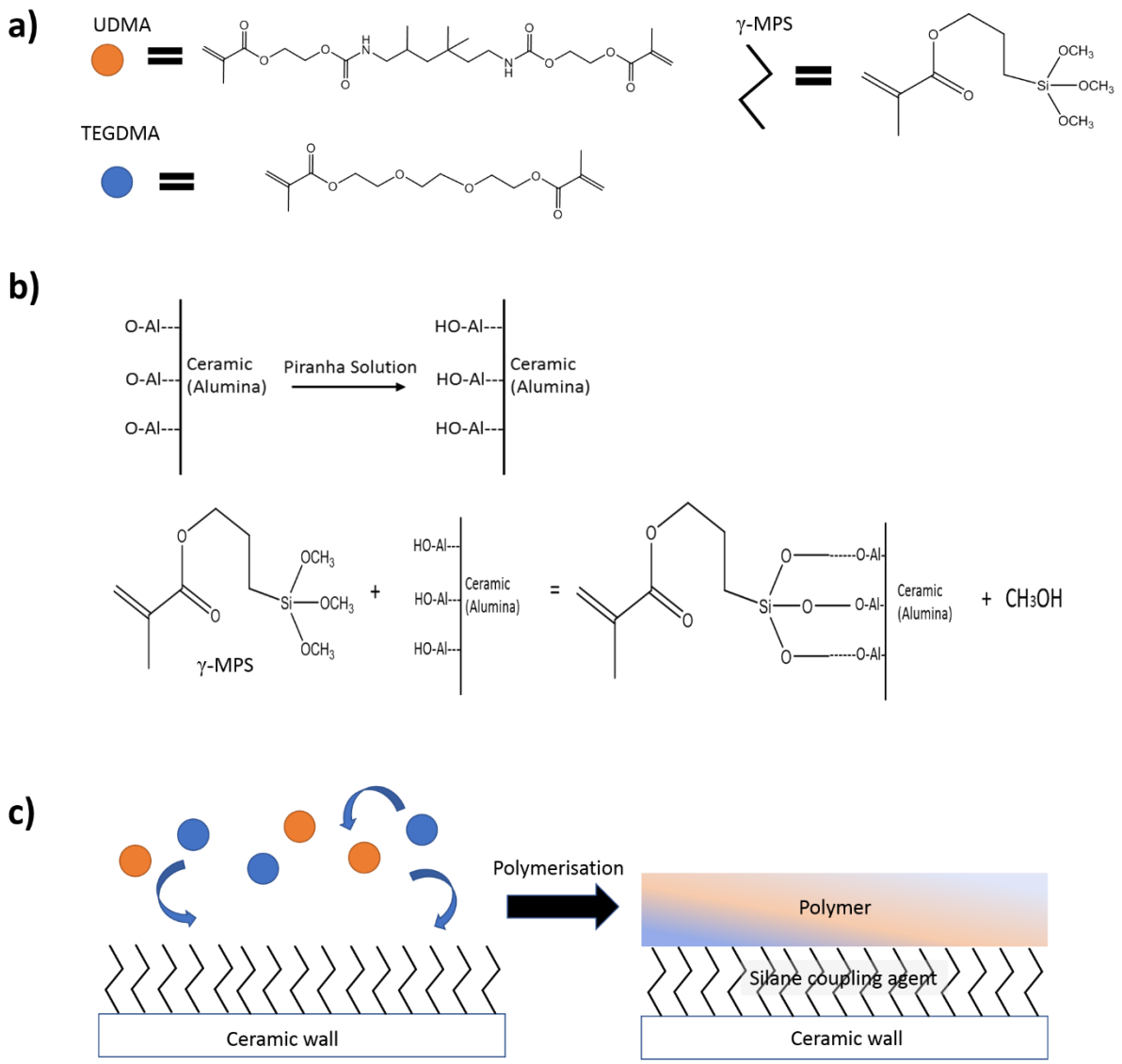

Figure 3-13: Schematic drawing showing a) the structure of UDMA, TEGDMA and γ-MPS, b) ceramic wall treatment by Piranha solution to form the OH group and the bonding between the ceramic wall and the γ-MPS, c) the bond between the polymer and the γ-MPS following polymerisation.

3.2.2.7 UDMA/TEGDMA infiltration and polymerisation

The grafted scaffolds were finally infiltrated with UDMA/TEGDMA monomers in a 1:1 weight ratio to fabricate the final composite materials. Initially, 49.5 wt.% of TEGDMA was mixed with 1g benzoyl peroxide (Luperox, Sigma-Aldrich, UK), which was used as a heat activator, in a glass beaker on a magnetic stirrer (Fisher Scientific, UK) for 1 h. When the benzoyl

peroxide powder had totally dissolved, 49.5 wt.% of UDMA was added and all of the constituents were mixed using the magnetic stirrer to create a homogenous resin mixture. The same casting impregnation system (Cast N' Vac 1000, Buehler, USA) used for epoxy polymer infiltration in section 3.2.1.6 was used for UDMA/TEGDMA infiltration. Once infiltrated, the scaffolds were removed from the machine and left at room temperature for 3 days to allow any air bubbles to escape. They were then heat treated in an oven (Thermo Scientific, Heratherm OMS60, Germany) and a thermal treatment protocol was applied to polymerise the monomers. The starting temperature was 40°C held for 2 h, followed by 50°C, 60°C, 70°C, 80°C, 90°C each held for 2 h. The heating rate was 1°C/ 10 min. Following heat treatment, the temperature was increased immediately to 120°C and held for a further 2 h. Figure 3-14 is the schematic of the fabrication steps used in the production of the biomimetic composite materials.

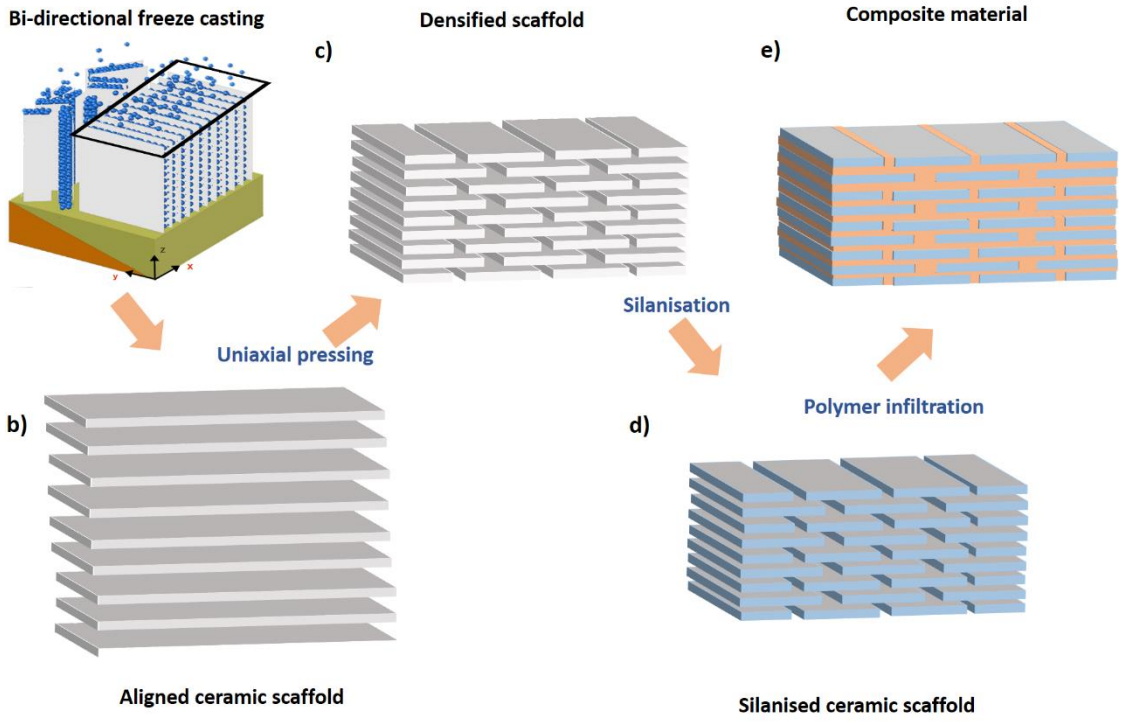

Figure 3-14: Schematic drawings of the fabrication process of biomimetic composite materials.

3.2.3 Fabrication of pure ceramic and polymer materials

Pure Al_2O_3/MgO dense ceramic blocks and pure UDMA/TEGDMA polymer blocks were also fabricated and tested mechanically for comparison with the biomimetic ceramic/polymer composite materials.

Alumina ceramic powder (79.324 g) was mixed with 0.02 wt.% MgO powder (0.0158g) and Ethanol (40 ml) (Sigma Aldrich. UK) and ball milled in 500ml polyethylene bottles using 250g yttria-stabilised zirconia balls (5 and 10mm diameter), in a roller mixing machine (1600-VS-A, Pascall Engineering, UK) at a speed of 3 for 24 h. This was done to ensure the two ceramic powders were a homogenous mixture within the ethanol. Following ball milling, the powder/ ethanol mixture was placed on an aluminum foil over a heating plate (Fisher Scientific, UK) at 40°C to remove the ethanol. The retrieved powder was used to fabricate the alumina ceramic block by adding 0.1 wt.% of the 10 % PVA solution and mixing in a glass beaker by hand using a wooden spatula until a homogenous ceramic mixture was produced. The mixture was then pressed inside a 38 mm cylindrical die using a hydraulic press (Perkin Elmer, Germany) with a load of 5 tons for 1 h. The pressed powder was then sintered (Elite Thermal Ltd., UK) using two cycles: the first used a heating rate of 2°C/min up to 600 °C, held for 2 h. The second cycle had a heating rate of 10°C/min, up to 1550 °C, held for a further 2 h.

For the fabrication of pure polymer, the same UDMA/TEGDMA mixture for the composite material was poured into a square rubber mould (15x17x27 mm) and polymerised using the same initiator and heat regime used for the composite material, as described in section 3.2.2.7.

3.3 Cutting and polishing

All cutting procedures were carried out using a high speed precise cutting machine (Accutum-50, Struers, UK) with a diamond saw (15 LC IsoMet diamond wafering blade, Buehler, USA), except for the pure polymer where the specimens were cut using a toothed saw (SAW13 Saw blade, Struers, UK).

Once cut, all of the samples were polished using a resin bonded diamond grinding disc (MD-Piano 1200, Struers, Denmark) in order to remove any damage introduced during cutting and to produce a flat surface. Further polishing was done with the aid of a 3µm diamond suspension (DiaPro Largo3, Struers, Denmark) using a maintenance free disc (MD-Largo, Struers, Denmark) followed by final polishing using a cloth (MD-Nap, Struers, Denmark) with a 1 µm diamond suspension (DiaPro Nap B, Struers, Denmark). All of the polishing steps were carried out on a grinding machine (Tegra Pol 15, Struers, UK) with water cooling.

3.4 Characterisation of the scaffold and composite material

All characterisation process where done on at least three samples, prepared from the same ceramic suspension.

3.4.1 Optical microscope

The epoxy infiltrated scaffolds were cut parallel to the x-y plane (see Figure 3-6) to examine the lamellar alignment using light microscopy (Leica DMI6000, Germany). The samples were put on a motorised stage, which enabled multi position image capture. The stage was controlled using Leica Las X software (Leica Application Suite X software, Germany). Multiple consecutive images of each scaffold were taken at 5x magnification using a photometrics

camera (Prime 95B sCMOS camera, Teledyne Photometrics, USA) attached to the microscope. The images were then stitched together using Leica Las X software (Leica Application Suite X software, Germany) to produce one image for the whole horizontal length of the scaffold.

In addition, the epoxy infiltrated scaffolds were directly observed under light microscopy (Nikon SMZ-U Zoom 1:10, Japan) and using Motic Software (Motic images plus 2.0, Motic China Group Co. Ltd., China) to measure the interlamellar spacing and ceramic wall thicknesses.

3.4.2 Optical image processing

To determine the axis orientation of the lamellae and the coherence in alignment, the stitched optical images, obtained from Leica Las X software, were processed using ImageJ – Fiji software (N.I. Health, USA) [227]. The images were treated using the orientation J plugin in the Fiji software, in which each lamellar ceramic wall was given a specific colour code according to the angle it forms within the horizontal plane. Coherence measurements were taken every 2mm throughout the section of the scaffold along the x-y plane.

3.4.3 Scanning electron microscope

Scanning electron microscopy (Quanta 400 - FEI Scanning Electron Microscope, USA) was used to observe the morphology of different samples from all directions. Before imaging, the samples were coated with a thin layer of a gold-palladium mixture using a sputter coater device (Emitech K575X, Quorum Technology Ltd, UK).

3.4.4 Micro computerised tomography

One sample (3x7x25mm) of epoxy infiltrated alumina scaffold was also examined using a micro-CT scanner (Nikon XTH 225 ST, UK) at 120 kV and a resolution of 3µm. From this, a 3D model was constructed using Avizo software (Avizo 8.1, Thermo Fisher Scientific, UK).

3.5 Physical characterisation

3.5.1 Density and porosity of the ceramic scaffolds

Apparent density and porosity of the sintered ceramic scaffolds were measured using the Archimedes principle of buoyancy in water (ASTM C373-16) [228]. Three specimens of each experimental group (different first-step sintering temperatures and different pressing pressures) were used to measure the density and porosity. For the dry and wet weight measurements, an analytical balance (Sartorius, MC1 AC 210 S, Germany) was used. The same balance was converted by the density determination kit (YDK01, YDK01-0D, Sartorius, Germany) to measure the suspended weight. Before measurement, the sintered scaffolds were first boiled in distilled water for 5 h to make sure that the pores are fully filled with water, then the samples were left to cool down in the same water to room temperature for 1 day. They were then immersed in water and weighed using a wire loop suspended inside the balance (*Suspended weight*), and the temperature of the water was measured in order to determine the water density. Following this, the surface water was removed using a damp chamois cloth before the samples were weighed again (*Wet weight*). Finally, the scaffolds were heated in an oven at 150°C for 1 day to make sure that the samples are totally dry. To prevent moisture absorption, the samples were left to cool down in a

desiccator before the dry weight was measured. The porosity was calculated in volume percent using the following equation:

$$\text{Porosity} = \frac{\text{Wet weight-Dry weight}}{\text{Wet weight-Suspended weight}} \text{x}100\%$$

The apparent density g/cm^3 was calculated using the following equation:

$$\text{Apparent density} = \frac{\text{Dry weight } (\boldsymbol{\rho}_{water} - \boldsymbol{\rho}_{air})}{\text{Dry weight-Suspended weight}}$$

Where $\boldsymbol{\rho}_{water}$ is the density of the deionised water, and $\boldsymbol{\rho}_{air}$ is the density of the air. The water density was determined from its temperature, and the air density was considered to be 0.0012 g/cm^3 as the room temperature was approximately 20°C.

The ceramic volume fraction inside the scaffold was calculated according to the following equation:

$$\text{Ceramic volume fraction} = 100 - \text{Porosity}$$

3.5.2 Dense area extension measurements

The bottom side of the bi-directional freeze cast scaffolds consists of two areas: a small dense area and a large aligned area. The bottom side of the scaffolds was directly observed under light microscopy (Nikon SMZ-U Zoom 1:10, Japan) to identify the extension of the dense area, which was measured by a ruler.

3.5.3 Linear shrinkage

To investigate the effect of different first-step sintering temperatures on the linear shrinkage of the ceramic scaffolds, the horizontal length of the green ceramics (from the random area to the aligned area) was measured using a digital calliper (Absolute Digimatic,

Mitutoyo, UK). It was measured again after the first-step sintering to calculate the linear shrinkage. Also, the width of the densified pressed scaffold was measured before and after the second-step sintering.

Linear shrinkage was calculated using the following equation:

$$\text{Shrinkage} = \frac{\text{Length before sintering-length after sintering}}{\text{Length before sintering}} \times 100\%$$

3.5.4 Grain area measurements

Alumina ceramic scaffolds were fabricated with and without the addition of MgO, and images of each type were captured using SEM to determine the grain area distribution. Three images of each sample were taken and processed using ImageJ – Fiji (N.I. Health, USA) software, using the plugin Modular Image Analysis (M.I.A) created by the Wolfson Bioimaging Facility of the University of Bristol. The plugin identifies the grain boundaries, isolates individual grains, measures their areas and ports out the measurements into a spreadsheet. This data was processed to identify the distribution of the grain sizes with and without the addition of MgO.

3.6 Mechanical testing

The Academy of Dental Material (ADM) has published guidance for dental materials mechanical properties, and they ranked these properties according to the priority of being tested. Of these mechanical properties, flexural strength, fracture toughness and hardness ranked first [229]. In line with the ADM guidance three-point bending, single-edge-notched beams and Vickers hardness tests were used to measure the flexural strength, fracture toughness and hardness, respectively.

A Zwick Roell universal testing machine (Z020, Zwick Roell, Germany) was used to carry out the compressive strength, flexural strength and fracture toughness tests. All samples were tested with a cross head speed of 60 µm/min. Due to the anisotropic characteristic of the fabricated ceramic scaffolds, the composite blocks were tested from two different directions (x and z) for the compressive and flexural strength, while for the fracture toughness the material was just tested from x direction, as we were interested in understanding the crack propagation mechanism inside the brick and mortar structure, (Figure 3-15).

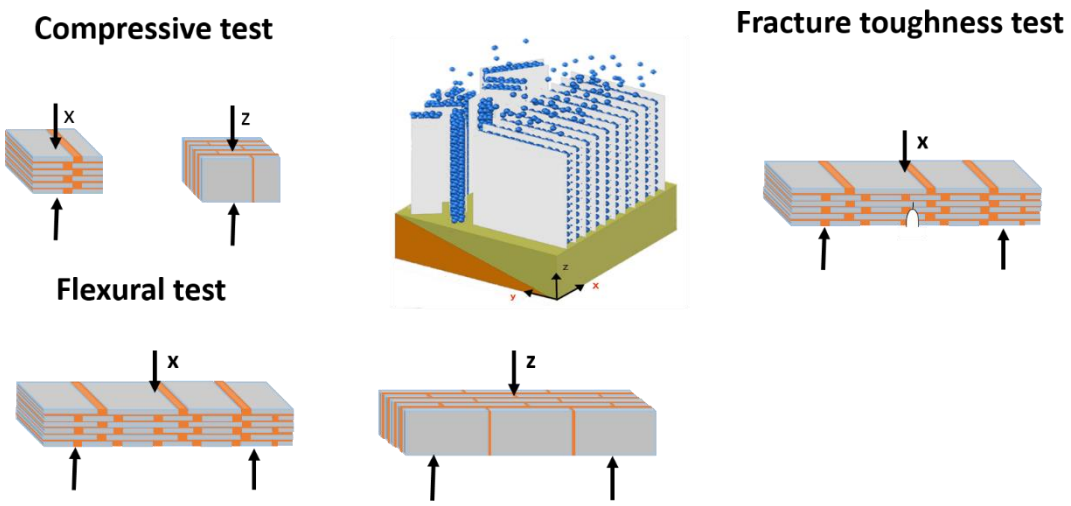

Figure 3-15: Schematic showing the two directions (x and z) from which the samples were tested mechanically.

3.6.1 Compressive strength

For compressive strength, composite blocks were cut into 2.5x2.5x5 mm cross-section samples (n=5). The compressive strength (σ_c) was calculated according to the following formula:

$$\sigma_c = \frac{F}{A}$$

Where:

F = the maximum load at fracture.

A = the cross-sectional area.

3.6.2 Flexural strength and elastic modulus

Three-point bending test was used for flexural strength measurements, as it is in line with the current guidance from the academy of dental material. Vita Enamic, pure alumina ceramic, pure polymer and composite specimens were cut into rectangular bars measuring approximately (17 to 25) × (3.0 to 3.2) × (1.3 to 1.5) mm in size (n≥3). Each bar was polished, chamfered and tested using three-point bending. In the test all bars were loaded to failure, and the maximum load was registered and used to calculate the flexural strength (σ_f) according to the following formula according to the ASTM standard D790-15 [230]:

$$\sigma_f = \frac{3FL}{2WH^2}$$

Where:

F = the maximum load at fracture.

L = the support span length, 12.5mm.

W = the bar width.

H = the bar height.

The flexural elastic modulus (E_f) was calculated by the following formula:

$$E_f = \frac{L^3F}{4DWH^3}$$

Where:

D = the deflection corresponding to load.

3.6.3 Fracture toughness (K_{IC})

For fracture toughness measurement, single-edge-notched beams with dimensions of ~(17-25) × (3.0-3.2) × (1.3-1.5) mm (n≥3) were prepared according to the ASTM standard E1820-18, USA [231]. The specimens were notched with a slow speed cutting machine (IsoMet, Buehler, USA), then a razor blade was used with a diamond paste (1µm paste, Struers, UK) to introduce a micro crack (~ 200 µm). The notch length was measured using an optical microscope (Leica DMLB, USA) at x40 magnification. A digital camera (Olympus, Japan) was used to capture the images, and the notch size measurements were done using cellSens software (cellSens 1.5, Olympus, UK).

All beams were tested to failure under three-point bending test, and the fracture toughness (K_{IC}) was calculated according to the following formula:

$$K_{IC} = \left[\frac{FL}{B^{1/2}W^{2/3}}\right] f\left(\frac{\alpha}{w}\right)$$

Where:

F = the load at fracture.

L = the support span length, 12.5mm.

B = the breadth of the beam.

W = the width of the beam.

α = the length of the notch.

f(α/w) = the geometrical factor and was calculated using the following formula:

$$f\left(\frac{\alpha}{w}\right)=\frac{3\left(\frac{\alpha}{w}\right)^{1/2}\times\left[1.99-\left(\frac{\alpha}{w}\right)\left(1-\frac{\alpha}{w}\right)\left(2.15-3.93\left(\frac{\alpha}{w}\right)+2.7\left(\frac{\alpha}{w}\right)^{2}\right)\right]}{2\left(1+2\frac{\alpha}{w}\right)\left(1-\frac{\alpha}{w}\right)^{3/2}}$$

3.6.4 Hardness test

In Vickers hardness test a pyramidal shape diamond indenter is forced into a highly polished sample under specific load for a defined time before removal. The diagonal length of the left indentation is measured to calculate the hardness. Vickers hardness was determined using a micro indentation system (Duramin Ver 0.08, Struers, UK) according to the Standard of Advanced Technical Ceramics, EN843-4:2005[232]. For the composite materials, Vita Enamic and dense ceramic, a load of 19.807 N (HV 2) was used, while for the polymer, a smaller load of 1.961 N (HV 0.2) was used. In each case, the load was held for 20 sec. Five (3x6x7 mm) samples were tested with five indents made in each case. All indentation diagonal lengths were measured using the light microscope within the indentation machine and hardness values calculated on the HV scale which were then converted to GPs using the following equation:

Hardness [GPa]= Hardness [HV]* 0.009807

3.7 Machinability of the composite material

As the fabricated composite materials are intended for chairside CAD/CAM application, the machinability of the biomimetic composite was assessed and compared with commercial Vita Enamic. A Computer Numerical Control (CNC) milling machine (ModelaPro, MDX-650,

UK) was used to machine the specimens. A 2.4 mm diameter end-cutting diamond coated bur (Duratool, UK) was used to dry mill a 6x6 mm^2 square box within the material. On one side of the square box, a 1.5 mm deep groove was then milled to make an edge. The tool spindle speed was set at 12000 rpm, which is the maximum of the machine, and a 3D model of the desired cut pathway was fabricated using c-MODELA software (c-MODELA Player 4, UK). One specimen of the composite material and one from Vita Enamic (4x12x17mm in size) were clamped tightly on the working platform of the CNC machine before the machining process started. A new diamond coated bur was used for each specimen. The machined surfaces and the edges of the cut were visualised using SEM (Quanta 400 - FEI Scanning Electron Microscope, USA).

Chapter 4. Fabrication and characterisation of highly aligned alumina ceramic scaffolds using bi-directional freeze casting

4.1 Introduction

A highly aligned ceramic scaffold, with an open pore network that can be infiltrated with a second polymer phase to mimic the brick and mortar structure of nacre, would find multiple applications as a biomedical material, e.g. CAD/CAM dental restorative material or an orthodontic aesthetic bracket. This is because the resultant composite would combine the advantages of both the ceramic and the polymer phases while reducing the disadvantages of the two separate materials.

The principal aim of this part of the research was to investigate the feasibility of producing a highly aligned ceramic scaffold using a new technique, namely bi-directional freeze casting. Here freeze casting was undertaken using dual temperature gradients: one being a vertical temperature gradient between the top and bottom cooling rods, and the second a horizontal temperature gradient from one side of the mould to the other. The results are presented both qualitatively and quantitatively using different imaging techniques and imaging processing in order to demonstrate the usefulness of the scaffold fabrication method.

The results of this study would help in determining the optimal fabrication parameters to produce highly aligned ceramic scaffolds, as the first step in the development of biomimetic nacre-like ceramic/polymer composites for potential use as CAD/CAM dental materials.

4.2 Results

4.2.1 Microstructural features of uni-directional freeze cast ceramics

In more conventional uni-directional freeze casting, the ceramic particles within the suspension are repelled by the growing ice crystals and as a result, accumulate between them (Chapter 3, Figure 3-4). Following lyophilisation, where the ice crystals are removed from the material, a unique porous ceramic microstructure is produced where the pores are a direct replica of the original frozen ice crystals. Figure 4-1 shows the typical macroscopic appearance of a green body ceramic produced using the uni-directional freeze casting

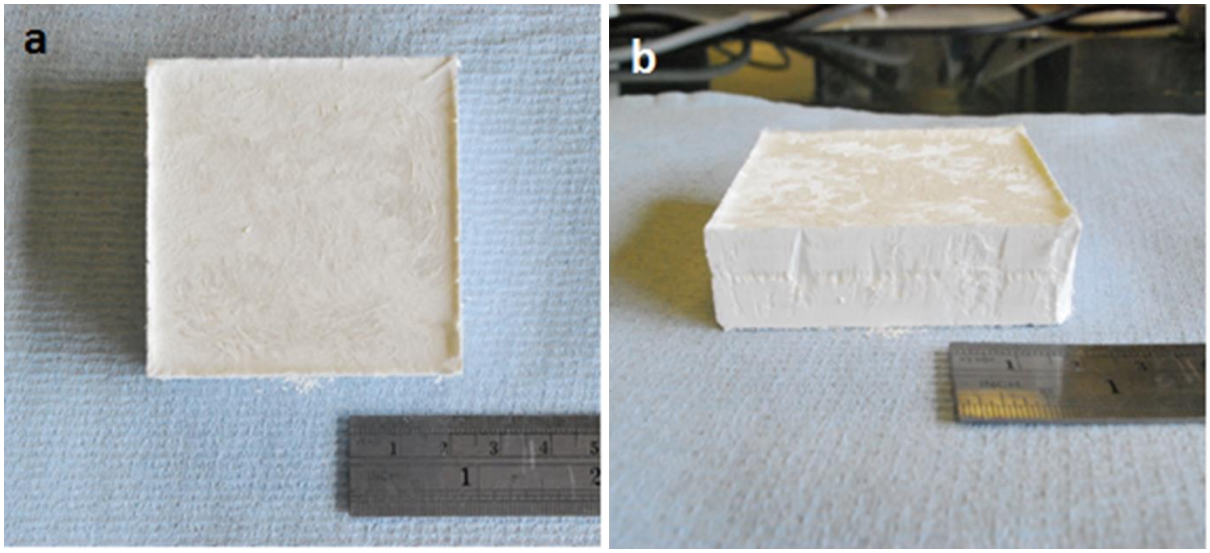

Figure 4-1*:* Typical green ceramics samples after lyophilisation, a) showing the sample from the top and b) showing a side view.

In producing a uni-directional freeze cast ceramic scaffold, the ceramic suspension was poured into a flat copper mould that was placed directly in contact with the lower copper rod in the freeze casting apparatus. As the copper rod temperature decreased, a single vertical temperature gradient was generated, and the transition of the planar ice front to the lamella resulted in random ice crystal nucleation and growth over the cross section, perpendicular to the freezing direction[44]. This was reflected in the microstructure of the ceramic scaffold, as shown in Figure 4-2, a. This random orientation resulted in a final structure with multiple, randomly oriented domains of lamellar structure. The SEM image in Figure 4-2 b shows clearly the morphology of the pores at higher magnification. The pore structure is defined by the shape of the growing ice crystals within the suspension. As water was used as the solvent, the pores take on the lamellar shape of ice crystals.

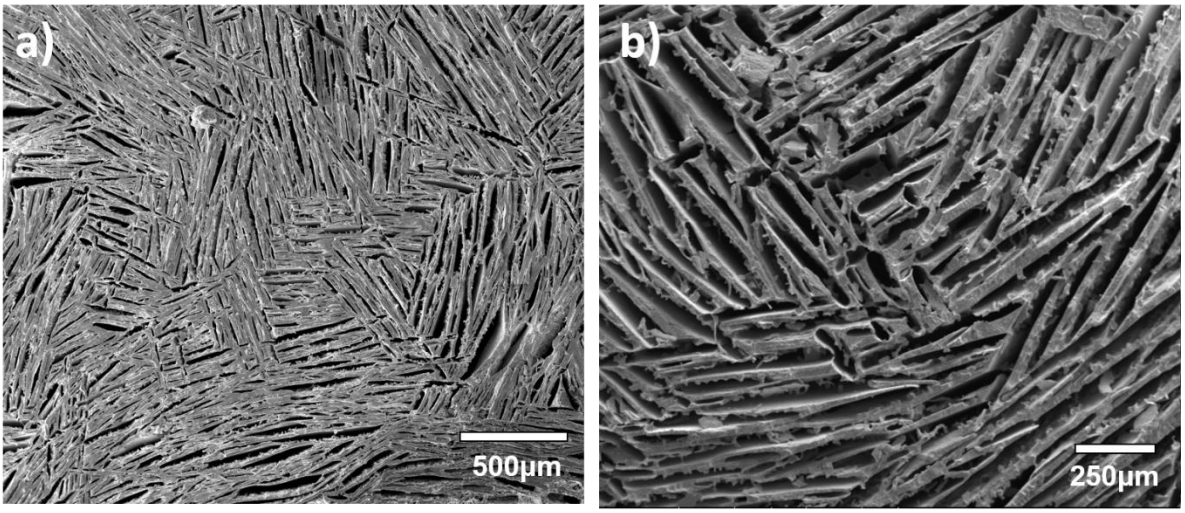

Figure 4-2: SEM images of a horizontal cross section perpendicular to freezing direction of 20 vol% sintered ceramic scaffold showing a) random orientation of the lamellar microstructure, b) higher magnification image showing the morphology of the pores. Freezing conditions: top temperature: +20 °C, bottom temperature: -30 °C, cooling rate: 5 °C/min.

SEM images of the longitudinal cross section within the ceramic scaffold (parallel to the freezing direction) reveal the morphology of the surfaces of the ceramic walls, Figure 4-3.

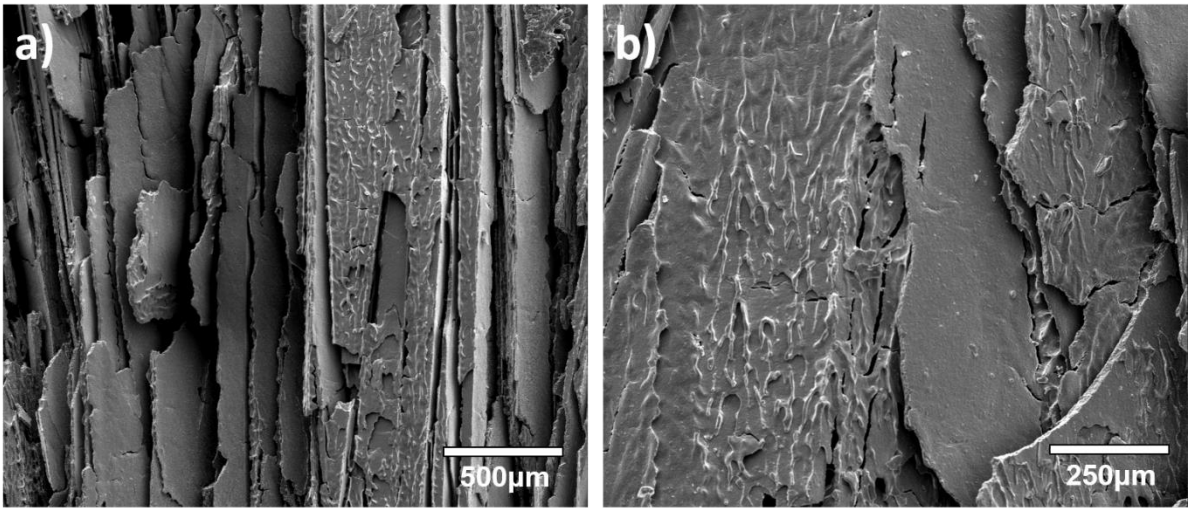

Figure 4-3: SEM images of a longitudinal cross section parallel to the freezing direction of 20 vol% sintered ceramic scaffold showing the surfaces of the ceramic walls at two different magnifications, a) x110, b) x220. Freezing conditions: top temperature: +20 °C, bottom temperature: -30 °C, cooling rate: 5 °C/min.

It can be seen that the microstructure of the ceramic walls has a topography determined by the way in which the ice crystals grow. They are either smooth or rough, with the rough surfaces demonstrating dendritic-like features, Figure 4-4.

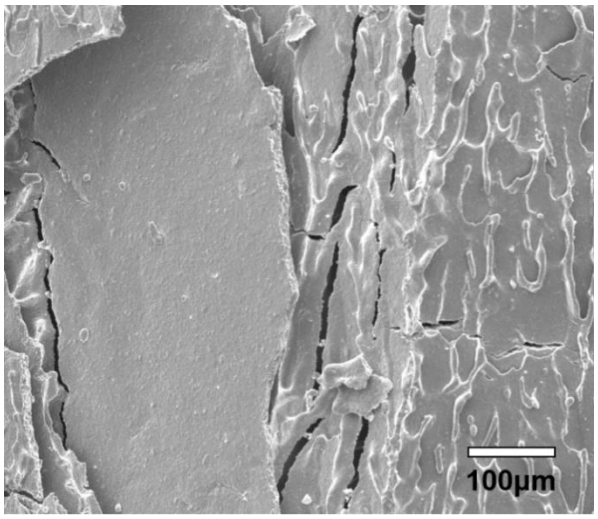

Figure 4-4: SEM image of a longitudinal cross section, parallel to the freezing direction of 20 vol% sintered ceramic samples, showing the smooth surface of the ceramic wall and the surface with the dendritic-like features. Freezing conditions: top temperature: +20 °C, bottom temperature: -30 °C, cooling rate: 5 °C/min.

When considered as a whole, the microstructure of the freeze cast ceramic scaffolds demonstrated three distinctive zones along the freezing direction. The first zone (Figure 4-5 Zone 1) was at the bottom of the scaffold closest to the copper mould. It can be seen to be less porous compared to the other zones. The second zone (Figure 4-5 Zone 2) had a more cellular microstructure, while the third zone (Figure 4-5 Zone 3) can be seen to comprise lamellar pores running parallel to the direction of freezing direction.

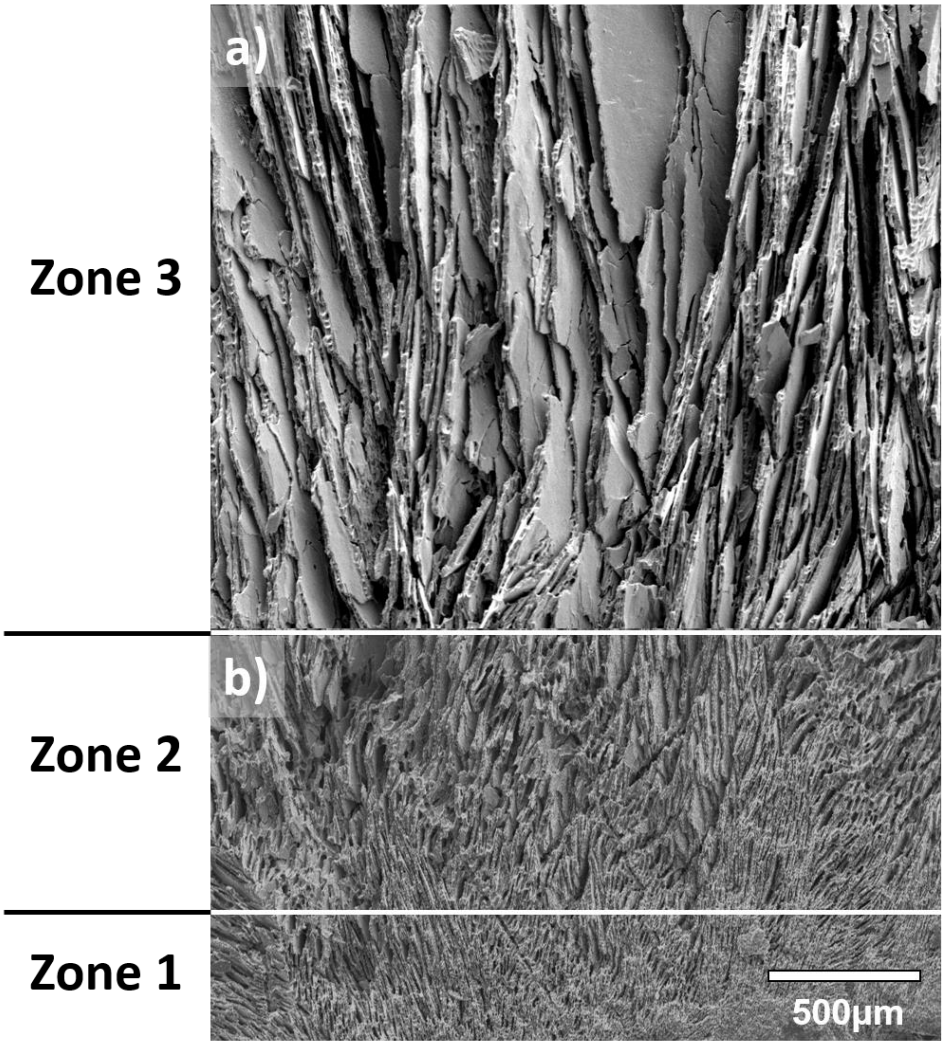

Figure 4-5: SEM images of a longitudinal cross section parallel to the freezing direction of 20 vol% sintered ceramic scaffold showing the three zones. At the bottom of the specimen is Zone 1 (dense), followed by Zone 2 (cellular) and finally Zone 3 (lamella), Magnification x110.

Another microstructural feature that can be seen within a freeze cast ceramic scaffold is the ceramic bridge, as shown by the arrows in Figure 4-6. Such bridges connect adjacent ceramic walls when the space between them is sufficiently small.

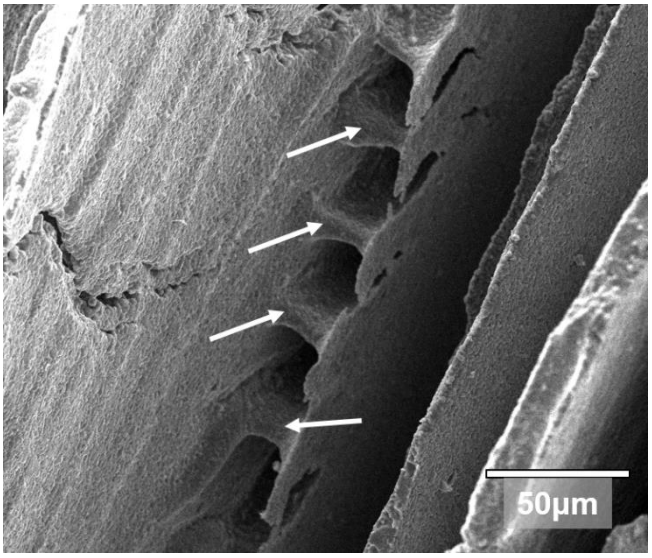

Figure 4-6: SEM image of a longitudinal cross section parallel to the freezing direction of 20 vol% sintered ceramic scaffold showing the ceramic bridges (arrows). Freezing conditions: top temperature: +20 °C, bottom temperature: -30 °C, cooling rate: 5 °C/min.

4.2.2 Uni-directional versus bi-directional freeze casting: Lamella alignment

To compare the effect of uni-directional versus bi-directional freeze casting on the lamella alignment, a 20 vol% ceramic suspension with 2 wt.% PVA concentration was used. A previous study had described the fabrication of highly aligned ceramic scaffolds using the same suspension [46]. Figures 4-7 a and 4-7 d are schematics of the two freeze casting techniques alongside coloured stitched light microscopy images (Figures 4-7 b and e), and SEM images of the respective ceramic scaffolds (Figures 4-7 c and f). The coloured light microscopy stitched images were taken from the top surface of the scaffolds in the x-y plane, and the colours represent different angles of the ceramic lamellae relative to the y-axis. By comparing the two freeze casting techniques, it can be seen that uni-directional freeze casting produced a more random lamella alignment. This was also seen on the SEM images. In the case of the scaffolds fabricated using bi-directional freeze casting, the coloured light microscopy stitched images demonstrate two distinct areas: a smaller

multicoloured area, where the lamellae have a more random orientation, and a larger area (shown as blue colour) indicating the lamellae are in the same orientation.

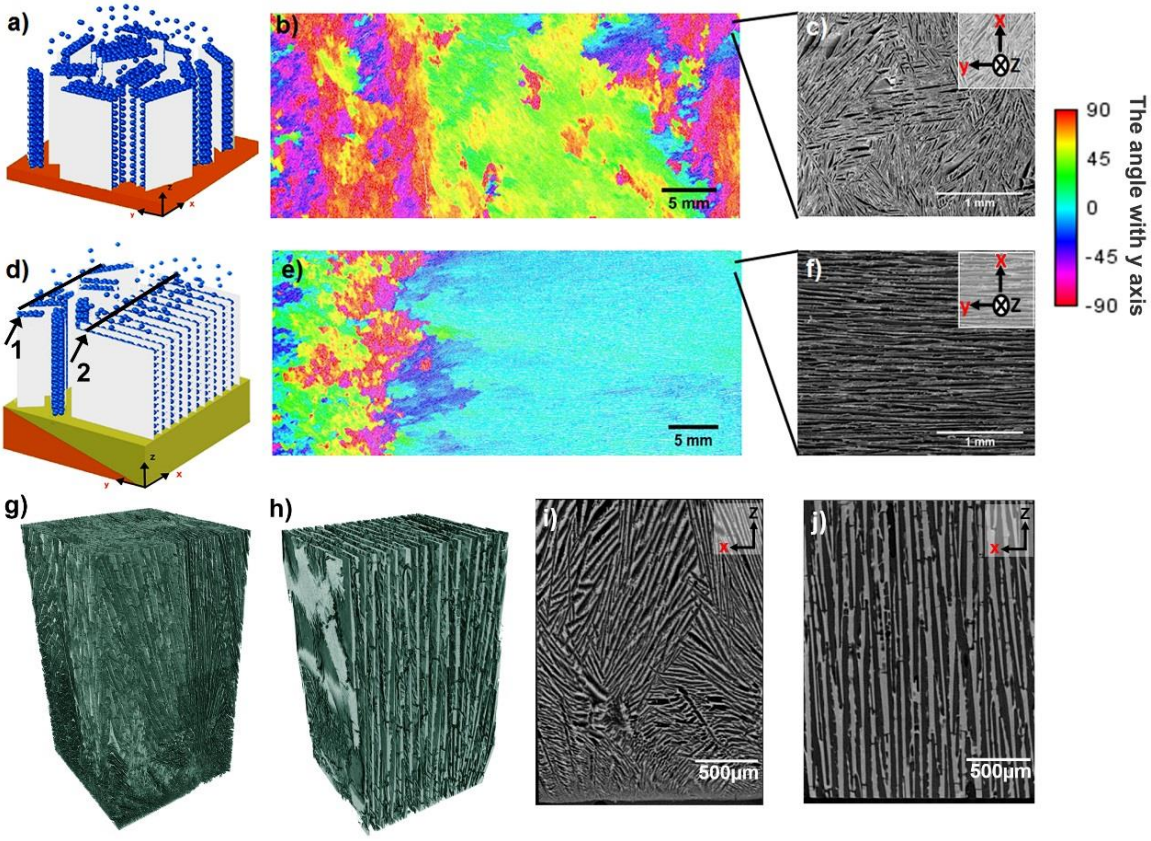

Figure 4-7: Comparison of uni-directional and bi-directional freeze casting. (a) Schematic of uni-directional freeze casting, (b) coloured stitched light microscope images of random ceramic scaffold, (c) SEM image of random ceramic scaffold; (d) schematic of bi-directional freeze casting, (e) coloured stitched light microscope images of bi-directional freeze casted ceramic scaffold, (f) SEM image of the highly aligned area in the ceramic scaffold, (g) reconstructed 3D micro-CT model for the random area in bi-directional freeze cast ceramic, (h) reconstructed 3D micro-CT model for the aligned area in bi-directional freeze cast ceramic, (i) Micro-CT scan image of section 1 in (d), (j) Micro-CT scan image of section 2 in (d). The colour represents different angles of lamellar alignment. Scaffolds were prepared from 20 vol.% alumina suspensions and 2 wt.% PVA. (Freezing conditions: top temperature +20°C, bottom temperature -30°C, cooling rate 10°C/min).

Micro-CT scan images of a scaffold prepared using bi-directional freezing were reconstructed to create 3D images, and these are illustrated in Figure 4-7 g and h. Figure 4-7 g is a 3D micro-CT model for the random area in the bi-directional freeze cast ceramic, the

same as area 1 in the schematic in Figure 4-7 d. It is clear that the lamellar structure is randomly aligned. By contrast, the 3D micro-CT model for the aligned area of the bi-directional freeze cast ceramic is shown in Figure 4-7 h, which is the area 2 in the schematic in Figure 4-7 d.

The micro-CT image in Figure 4-7 i shows the typical three-layered structure of freeze cast ceramics, namely the dense, cellular and lamellar zones. In this image, the lamellar layer is still randomly aligned. However, in the image further away from the thinner part of the PDMS wedge, the lamellar structure becomes more aligned (Figure 4-7 j).

4.2.3 Effects of cooling rate and mould slope angle on lamellar alignment

Temperature parameters, especially cooling rate, have a large influence on the freeze casting process [233]. Therefore, three different cooling rates and three different copper/PDMS mould slope angles were used to study their effect on lamella alignment. The same ceramic solid loading of 20 vol.% and a 2 wt.% PVA concentration was used in all experiments. Three samples were prepared for each experiment.

The optical images in Figure 4-8 show that using different cooling rates and different copper/PDMS mould slope angles changes the lamellar alignment significantly. An increase in cooling rate from 1 to 10°C/min, at a fixed slope angle of α = 5°, 10° or 20° increases the size of the aligned lamellar area and the uniformity of the lamellar alignment. A similar trend was observed with a fixed cooling rate of 1 or 5°C/min and by increasing the slope angle from α = 5° to 20°. While a cooling rate of 10°C/min and a slope angle of α =20° (Figure 4-8, l) produced a scaffold with a larger aligned area, but with less uniformity in alignment compared to that with a slope angle of α =10°, (Figure 4-8, k). For a mould slope angle of α =0° (i.e. the flat copper base), the produced scaffolds showed no lamellar

alignment, regardless of the cooling rate. From the previous results it is obvious that a higher cooling rate and larger copper/PDMS mould slope angle produces a ceramic scaffold with a larger lamellar aligned area and at the same time increasing the uniformity of the alignment.

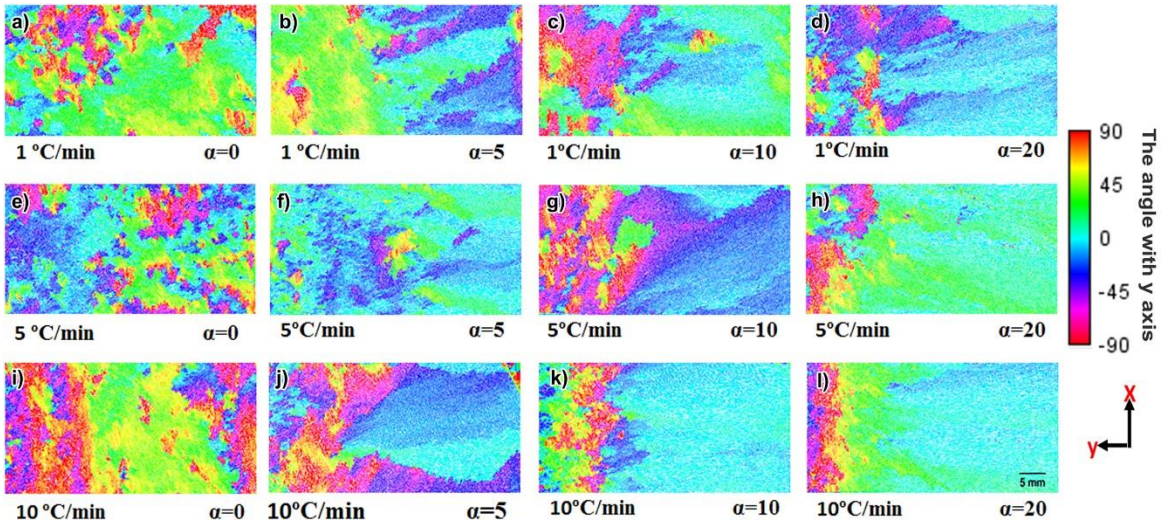

Figure 4-8: Light microscope images (a-l) show the alignment of lamellar structure of ceramic samples produced at different cooling rates (1, 5 and 10 °C/min) and using copper/PDMS moulds with different slope angles (α =0°, 5°, 10° and 20°). The colour gradient represents different angles of lamellar alignment. Scaffolds were prepared from 20 vol.% alumina slurries and 2 wt.% PVA concentration. (Freezing conditions: top temperature +20°C, bottom temperature -30°C).

To demonstrate the uniformity in lamellar alignment, the coherency in alignment of the ceramic lamellae was measured as described in Chapter 3, Page 81. Figure 4-9 shows the coherency in alignment for scaffolds prepared using different cooling rates, but the same copper/PDMS mould slope angle of α =10°. For all the scaffolds, the coherency measurements were low at the initial frozen part of the scaffold (random lamellar area), but beyond a distance of 14 to 16 mm from the initial frozen plane, the coherency began to increase, indicating a highly aligned lamellar structure in the final frozen part of the scaffold (aligned lamellar area). It is obvious that increasing the cooling rate increased both the size

of the aligned lamellar area and the coherency in alignment. A cooling rate of 10°C/min gave the highest coherency of almost 90%.

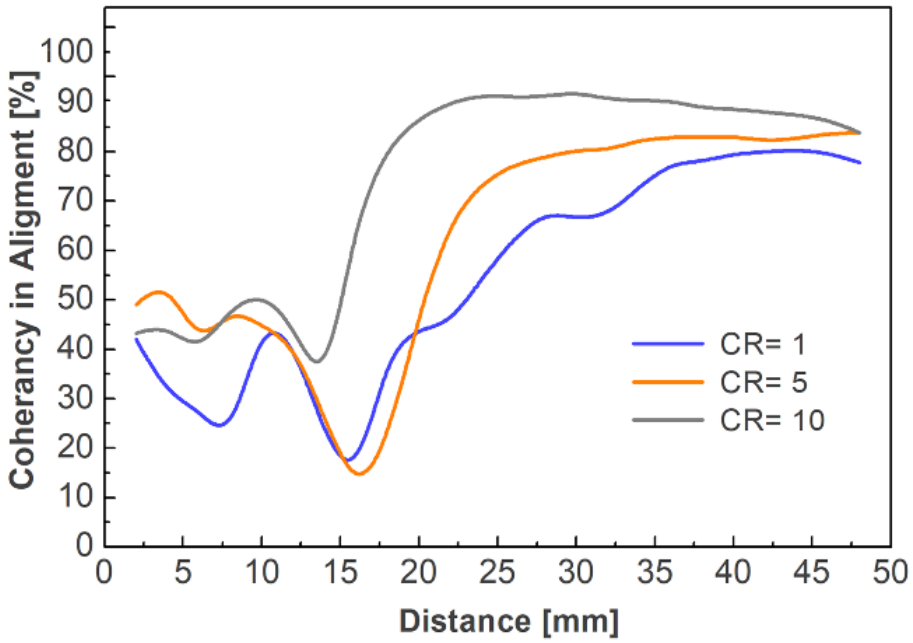

Figure 4-9: Coherency in alignment [%] of the ceramic lamellae of ceramic scaffolds as a function of cooling rate (CR). (Freezing conditions: top temperature +20°C, bottom temperature -30°C, copper/PDMS mould slope angle α =10°, cooling rates: 1, 5 and 10°C/min).

The same coherency measurements were also performed for scaffolds prepared using different copper/PDMS mould slope angles, but the same cooling rate of 10°C/min, Figure 4-10. A mould slope angle of α =20° produced the largest area of aligned lamellar scaffold, but with slightly lower coherency in alignment compared to a slope angle of α =10°. Both slope angles, α =10° and 20°, produced higher coherency and a larger size of the aligned lamellar area compared to a slope angle of α =5°.

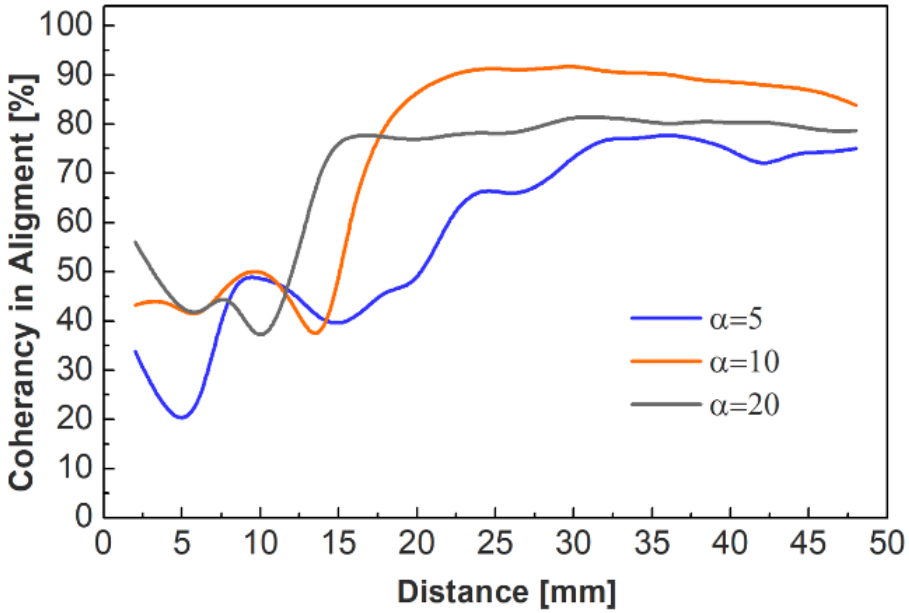

Figure 4-10. Coherency in alignment [%] of the ceramic lamellae of ceramic scaffolds as a function of slope angle. (Freezing conditions: top temperature +20°C, bottom temperature -30°C, cooling rates 10°C/min, copper/PDMS mould slope angles α =5°, 10° and 20°).

4.2.4 Effect of cooling rate and copper/PDMS mould slope angle on interlamellar spacing

To study the effect of cooling rate and copper/PDMS mould slope angle on the interlamellar spacing, ceramic scaffolds were prepared using the same cooling rate (CR = 10°C/min), but different copper/PDMS mould slope angles (α = 5°, 10° and 20°). The interlamellar spacing of these scaffolds was measured on both the top and bottom surfaces (Figure 4-11). The measurements were taken from the last 5 mm of the aligned lamellar area of each of the scaffolds.

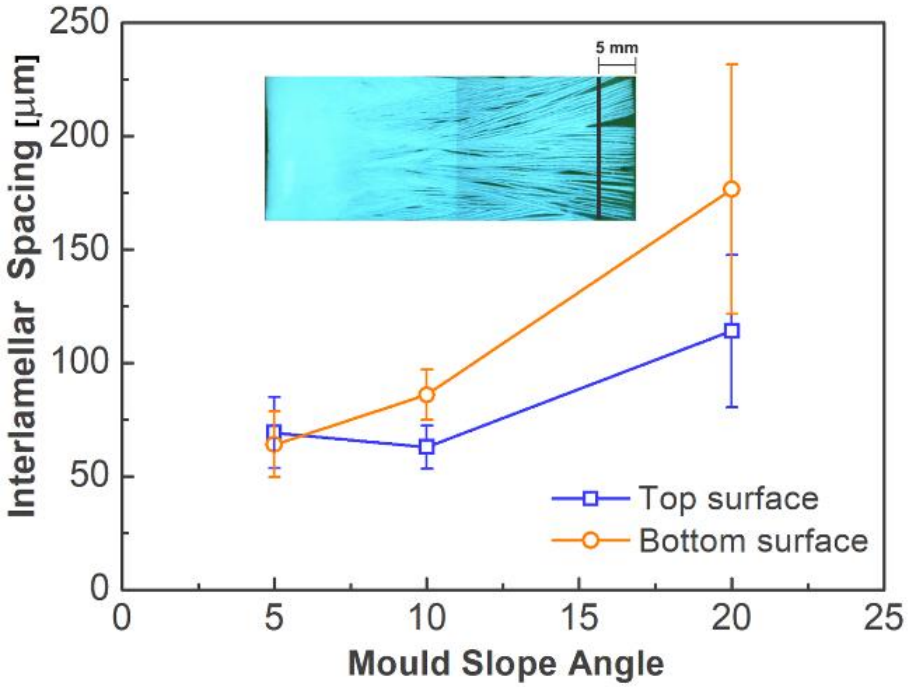

Figure 4-11: Mean and SD of interlamellar spacing measurements [µm] for the top and bottom surfaces of ceramic scaffolds prepared using a cooling rate of 10°C/min and different copper/PDMS mould slope angles (α = 5°, 10° and 20°). Inner image is a stitched light microscope image of the bottom side of a ceramic scaffold prepared using a cooling rate of 10°C/min and mould slope angle of 20°.

As seen in Figure 4-11, there is a difference in interlamellar spacing between the top and bottom surfaces for scaffolds prepared using copper/PDMS mould slope angles of α = 10° and 20°. Which means that these scaffolds have a more graded porous network compared to the scaffold prepared using a copper/PDMS mould slope angle of α = 5°, where a more homogenous porous network was present, but with a shorter aligned lamellar area.

Scaffolds fabricated by bi-directional freeze casting have a unique bottom side that is different from the typical whole dense bottom side seen in scaffolds fabricated using uni-directional freeze casting. Freezing a ceramic suspension using bi-directional freeze casting produced a distinct bottom side made of two areas: a short dense area and a large aligned lamellar area. The extent of the dense area at the bottom of scaffolds prepared using

different cooling rates: 1, 5 and 10°C/min, and different copper/PDMS mould slope angles (α = 5°, 10° and 20°), were measured and are illustrated in Figure 4-12. It can be seen that increasing both the cooling rate and copper/PDMS mould slope angle decreases the extent of the dense area. Using a cooling rate of 10°C/min with a copper/PDMS mould slope angle of α = 20° produced the smallest extension of the dense area.

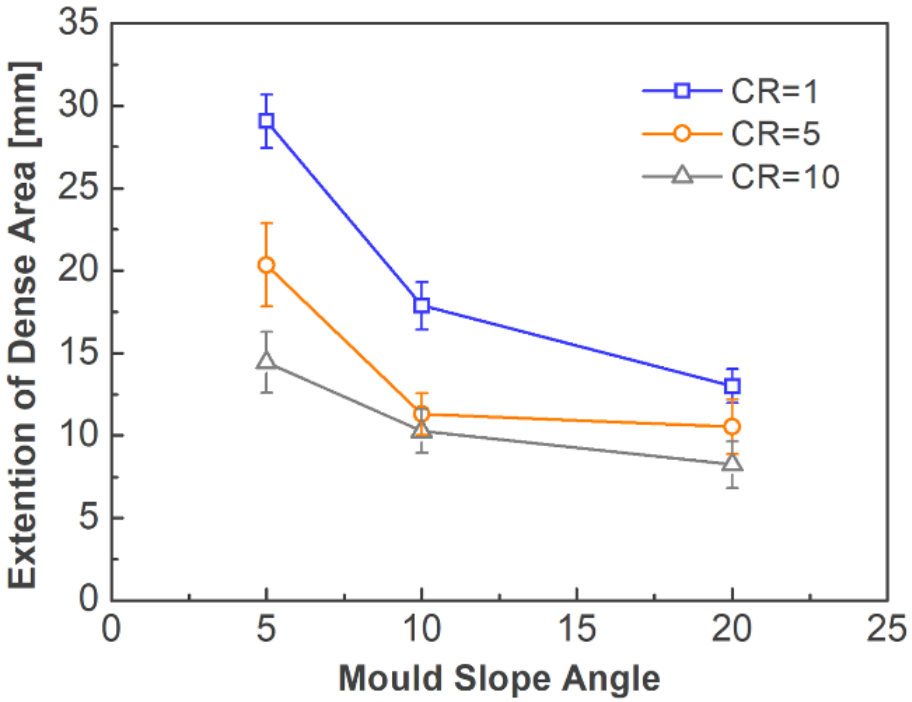

Figure 4-12: Mean and SD of dense area measurements [mm] for ceramic scaffolds prepared using different cooling rates: 1, 5 and 10°C/min and different copper/PDMS mould slope angles (α = 5°, 10° and 20°).

4.2.5 Effects of solid loading on lamellar alignment and interlamellar spacing

Freezing a ceramic suspension converts the water within the suspension into ice. After freeze drying, the space that was originally occupied by ice becomes the porous network within the scaffold. Different solid loadings contain different volumes of water available for freezing, which might have an effect on the subsequent scaffold microstructure, particularly

the lamellar alignment. In order to investigate this, different solid loadings (10 to 40 vol.%) were used to fabricate ceramic scaffolds using bi-directional freeze casting. A cooling rate of 10°C/min was used to freeze the samples as the previous results had shown it produces a larger area of lamellar alignment within the scaffold. In the case of 10 vol.% solid loading, the green body scaffold produced was very weak and collapsed on removal from the mould. For all other solid loadings, it was possible to produce highly aligned ceramic scaffolds (Figure 4-13).

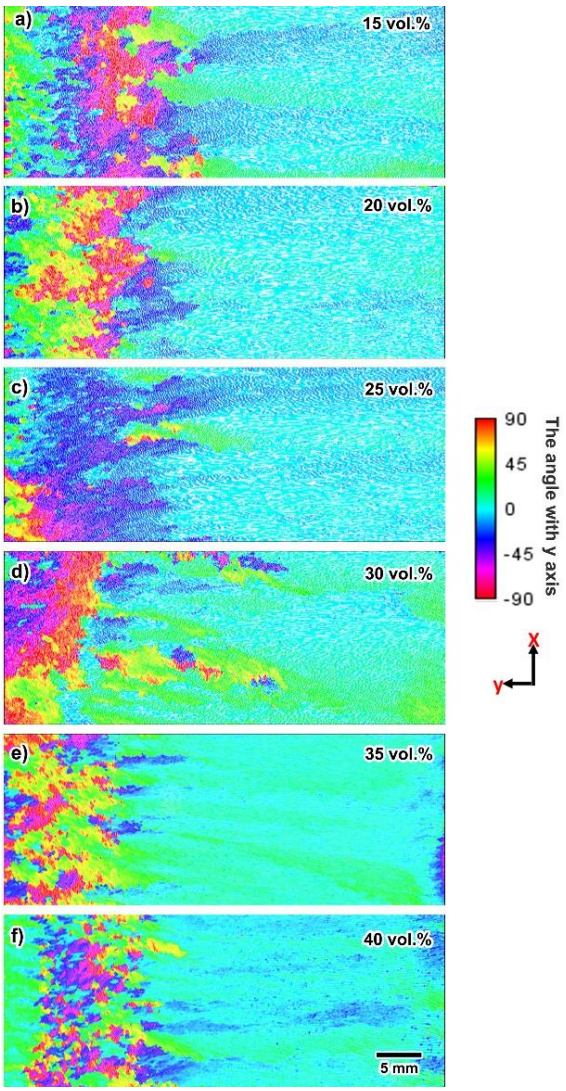

Figure 4-13: Coloured stitched light microscope images of ceramic scaffolds prepared with different solid loadings, (a) 15 vol.%, (b) 20 vol.%, (c) 25 vol.%, (d) 30 vol.%, (e) 35 vol.% and (f) 40 vol.%. (Freezing conditions: top temperature +20°C, bottom temperature -30°C,

cooling rate 10°C/min, copper/PDMS mould slope angle (α =10°), PVA concentration: 2 wt.%).

Both the interlamellar spacing and the ceramic wall thickness were measured using light microscopy on the last 5 mm of the aligned lamellar area, at the top surface of the scaffold, prepared using the different solid loadings (Figure 4-14).

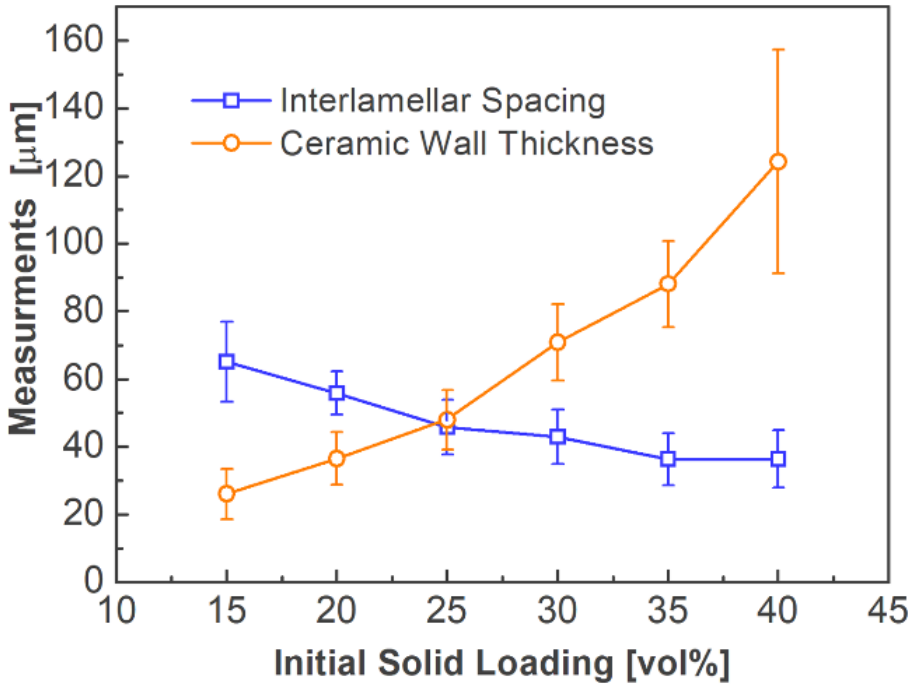

Figure 4-14: Mean and SD of interlamellar spacing and ceramic wall thickness [µm] as a function of solid loading. (Freezing conditions: top temperature +20°C, bottom temperature: -30°C, cooling rate: 10°C/min, copper/PDMS mould slope angle α =10°, PVA concentration: 2 wt.%).

It can be seen that increasing the solid loading from 15 vol% to 40 vol% increases the mean ceramic wall thickness dramatically, from 26.0µm to 124.1µm. At the same time, the mean interlamellar spacing decreased from 65.1µm to 36.4µm. Therefore, it is obvious that using lower initial solid loadings produces ceramic scaffolds with larger interlamellar spacing and thinner ceramic walls. For nacre-like material a thinner ceramic wall is more desirable. A 20 vol.% initial sold loading was used for farther parameters investigation because it has the

thinnest ceramic wall and at the same time the ceramic scaffold was strong enough to withstand the following processing steps compared to the 15 vol.%.

4.2.6 Effects of binder concentration on lamellar alignment and interlamellar spacing

The effect of using different polyvinyl alcohol (PVA) binder concentrations (1, 2, 4 and 8%) on the ceramic scaffold microstructure was tested. Initial solid loading of 20 vol.% was used for all samples. Figure 4-15 and Figure 4-16 are SEM images for ceramic scaffolds prepared with different PVA concentrations at two different magnification. The images indicate that increasing the PVA concentration decreases the interlamellar spacing and produces more ceramic bridges between the walls. Also, in all scaffolds, the ceramic walls maintained some degree of alignment, regardless of the PVA concentration. Figure 4-15 shows the ceramic scaffolds at lower magnification.

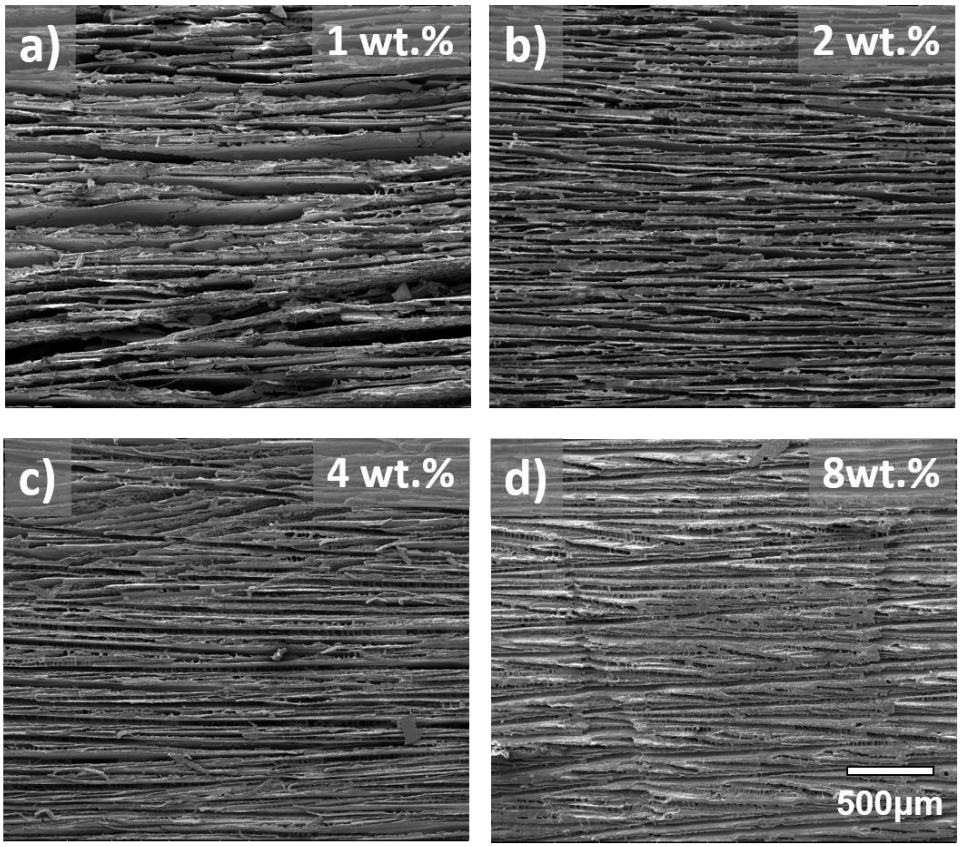

Figure 4-15: SEM images for four ceramic scaffolds prepared with different PVA concentrations, (a) 1 wt.%, (b) 2 wt.%, (c) 4 wt.% and (d) 8 wt.%. Magnification: x100. (Freezing conditions: top temperature +20°C, bottom temperature -30°C, cooling rate 10°C/min, copper/PDMS mould slope angle α= 10°, solid loading: 20 vol.%).

Figure 4-16 shows SEM images of the ceramic scaffolds at higher magnification. Once again, it can be seen that interlamellar spacing decreases, with the ceramic walls becoming closer together, as the PVA binder concentration increases from 1 wt.% to 8 wt.%. The bridging effect appears more pronounced at 4 wt.% (Figure4-16, c) and 8 wt.% (Figure 4-16, d) PVA binder concentrations. Less ceramic bridges is more desirable as the ceramic scaffold will go farther densification step under uniaxial pressing, the presence of bridges in between the ceramic walls can prevent the ceramic walls from getting closer to each other.

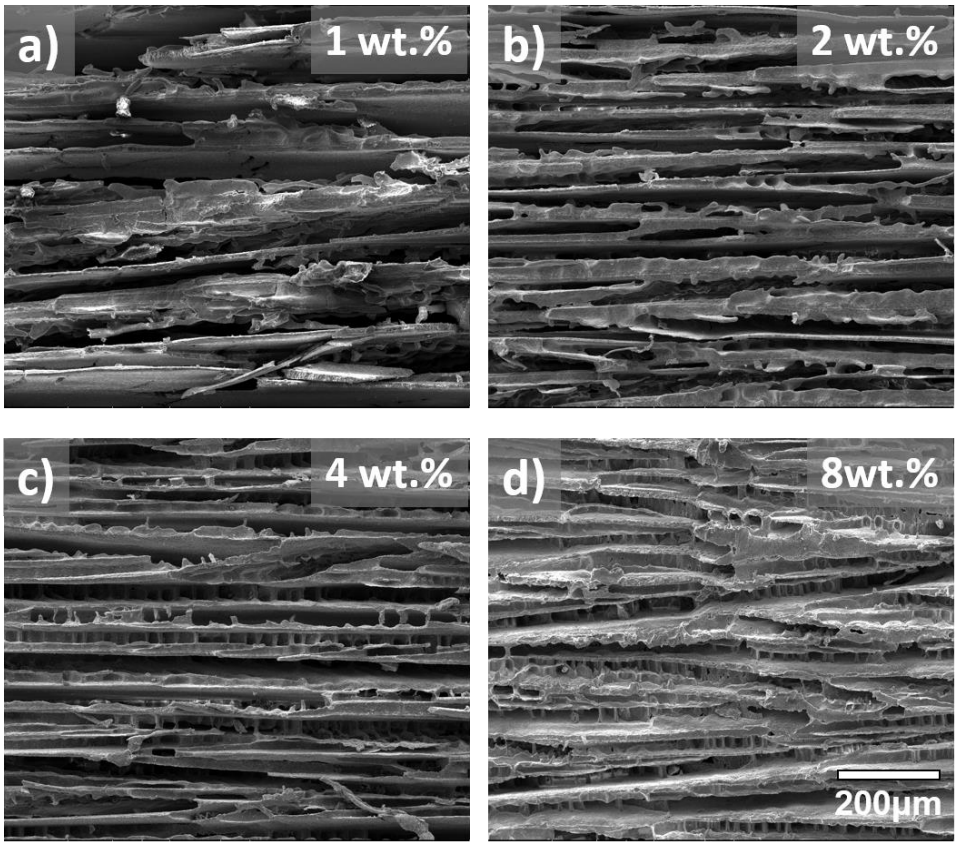

Figure 4-16: SEM images for four ceramic scaffolds prepared with different PVA concentrations, (a) 1 wt.%, (b) 2 wt.%, (c) 4 wt.% and (d) 8 wt.%. Magnification: x300 (Freezing conditions: top temperature +20°C, bottom temperature -30°C, cooling rate 10°C/min, copper/PDMS mould slope angle α= 10°, solid loading: 20 vol.%).

Figure 4-17 shows the mean interlamellar spacing and the mean ceramic wall thickness of the scaffolds prepared using different PVA concentration. All measurements were taken under light microscopy from the last 5 mm of the aligned lamellar area on the top surface of the scaffolds. The results show that increasing the PVA concentration from 1 wt.% to 8 wt.% decreases the mean interlamellar spacing from 82.1µm to 48.9µm, and increases the mean ceramic wall thickness from 35.1µm to 49.0µm.

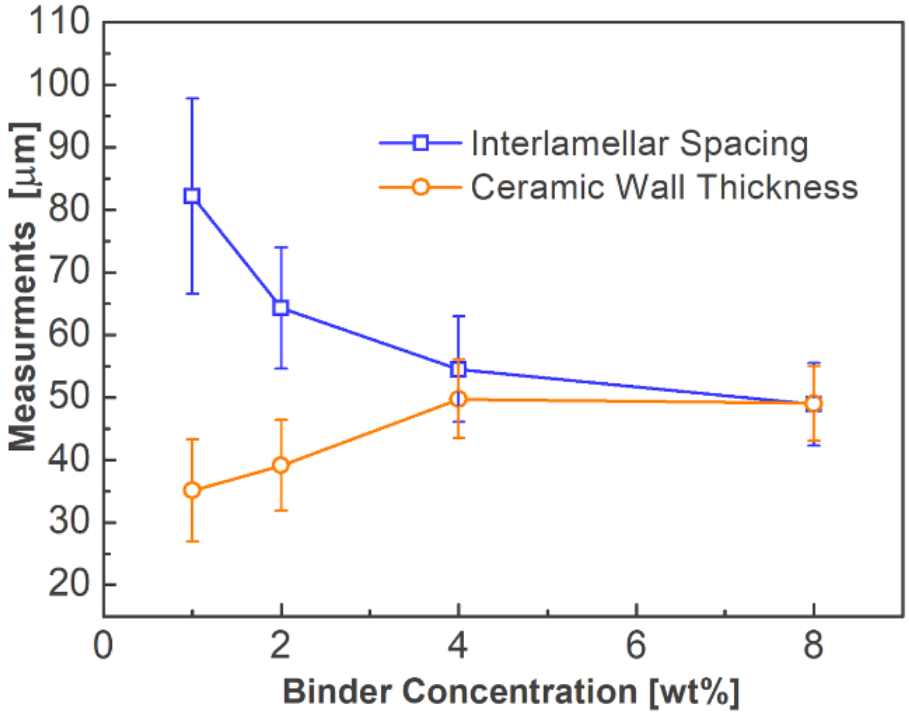

Figure 4-17: Mean and SD of interlamellar spacing and ceramic wall thickness [µm] as a function of PVA binder concentration. (Freezing conditions: top temperature +20°C, bottom temperature -30°C, cooling rate 10°C/min, copper/PDMS mould slope angle α= 10°, solid loading: 20 vol.%).

In addition, the coloured light microscopy images of the scaffolds (Figure 4-18) show that increasing the PVA concentration seems to affect the lamellar alignment by reducing its uniformity. A PVA concentration of 1% or 2wt.% does not appear to affect the lamellar alignment, whereas in the case of using higher PVA concentrations of 4% and 8 wt.% the lamellar alignment became less uniform.

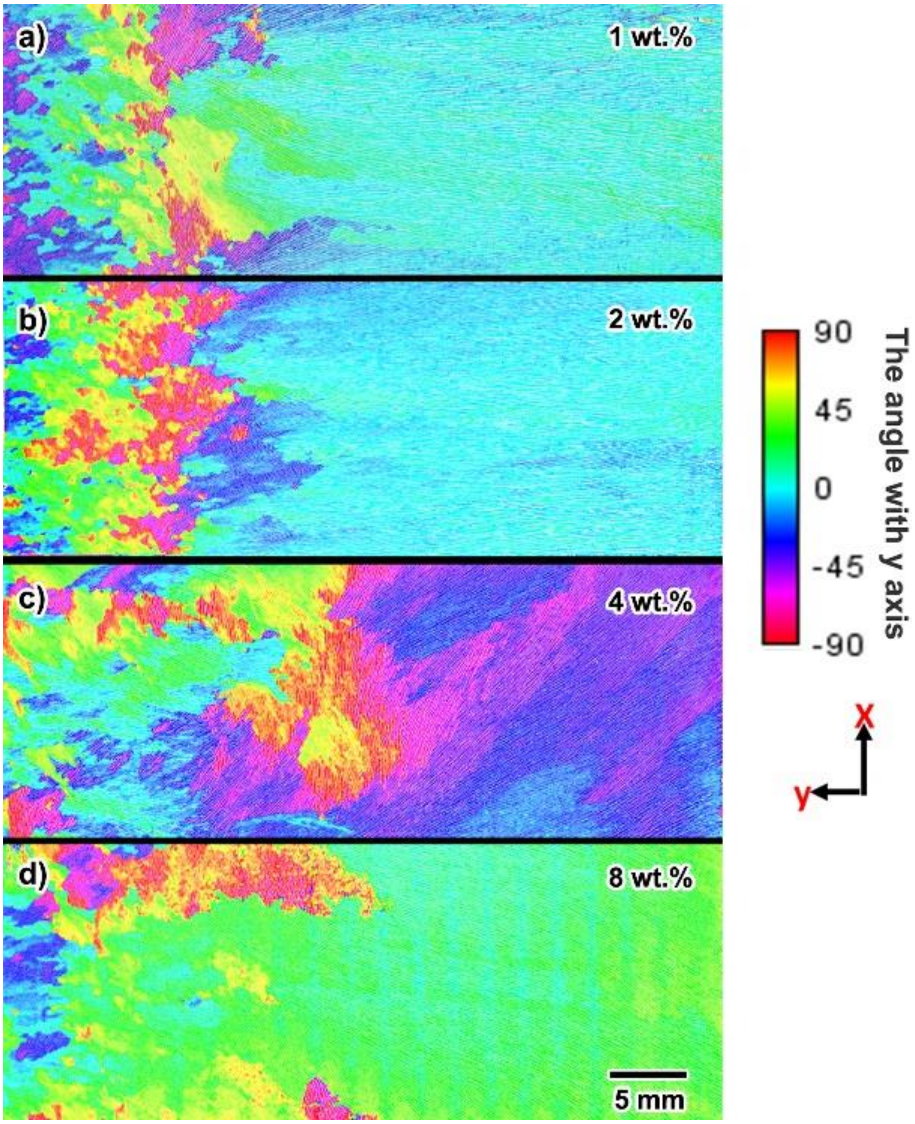

Figure 4-18: Coloured stitched light microscope images of ceramic scaffolds prepared with different PVA concentration, (a) 1 wt.%, (b) 2 wt.%, (c) 4 wt.% and (d) 8 wt.%. (Freezing conditions: top temperature +20°C, bottom temperature -30°C, cooling rate 10°C/min, copper/PDMS mould slope angle α= 10°, solid loading: 20 vol.%).

4.3 Discussion

Producing biomimetic ceramic/polymer composite materials necessitates the fabrication of a porous ceramic scaffold as the first step, followed by infiltration of a second polymer phase. In this study, conventional uni-directional freeze casting was first used to produce alumina ceramic scaffolds with an open pore network and lamellar pore structure (Figure 4-

2). This is the usual structure of a freeze cast ceramic when water is used as the solvent [234]. The lamellar structure can be understood by returning to the basic shape of ice crystals and their growth pattern. Ice crystals possess a lamellar shape and can grow in two directions: horizontally along the c-axis and vertically along the a-axis, as illustrated in Figure 2-21. As ice crystal growth on the a-axis occurs preferentially to that on the c-axis, this leads to the production of vertically oriented lamellar ice crystals [173].

Previous literature has described how the presence of dendritic-like features on one side of the ceramic scaffold wall can occur as a result of ice crystals preferring to grow in a tilted direction with respect the temperature gradient, as illustrated in Figure 4-19 [207]. This tilted growth leads to the ice crystals having one featured side and one smooth side, and this is reflected on the ceramic walls, as described in section 4.2.1 and illustrated in Figure 4-4. This finding is in agreement with that of Deville *et al*. [207], who also reported the same feature on one side of the scaffold ceramic walls, and explained it as being due to the ceramic particles becoming trapped between the secondary branches of the tilted ice crystal.

Other distinct features of freeze cast ceramic scaffolds include trans-lamellar ceramic bridges as described in section 4.2.1 and illustrated in Figure 4-6. These bridges form during ice crystal growth, due to crystals splitting and healing. This process leads to ceramic particle engulfment between some of the crystals, which then become the bridges connecting the ceramic walls [235]. It is worth mentioning that these bridges are totally different from the dendritic-like features covering the ceramic walls.

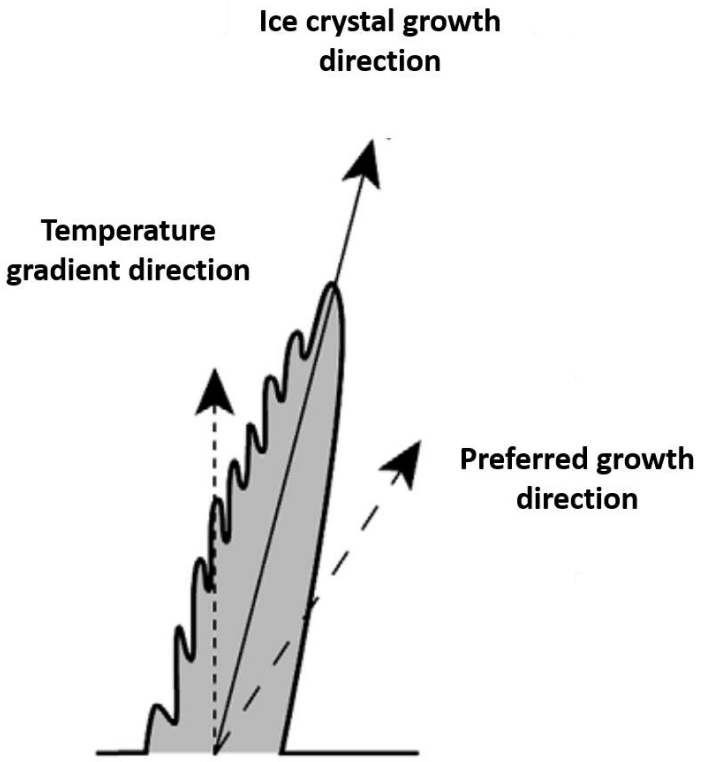

Figure 4-19: Schematic illustration showing ice crystal growth direction with respect to the temperature gradient direction and the preferred direction of growth [207].

The requirement for a highly aligned lamellar ceramic scaffold that resembles the microstructure of nacre, necessitates the use of bi-directional freeze casting. To achieve this, we designed a novel sloped copper mould that was covered by an isolating polymer (PDMS) to introduce a second horizontal temperature gradient during the freeze casting process. This mould design allowed the production of regular square shaped highly aligned ceramic scaffolds.

Uni-directional and bi-directional freeze casting techniques have different freezing conditions that develop inside the mould once the cooling process starts. In the case of uni-directional freeze casting, freezing occurs under single vertical temperature gradient, while in bi-directional freeze casting freezing occurs under dual temperature gradients (one

horizontal and one vertical). This difference in the freezing conditions is the main reason behind the difference in lamellar alignment of the produced scaffolds, i.e. random alignment in uni-directional freeze casting and the uniform alignment in bi-directional freeze casting.

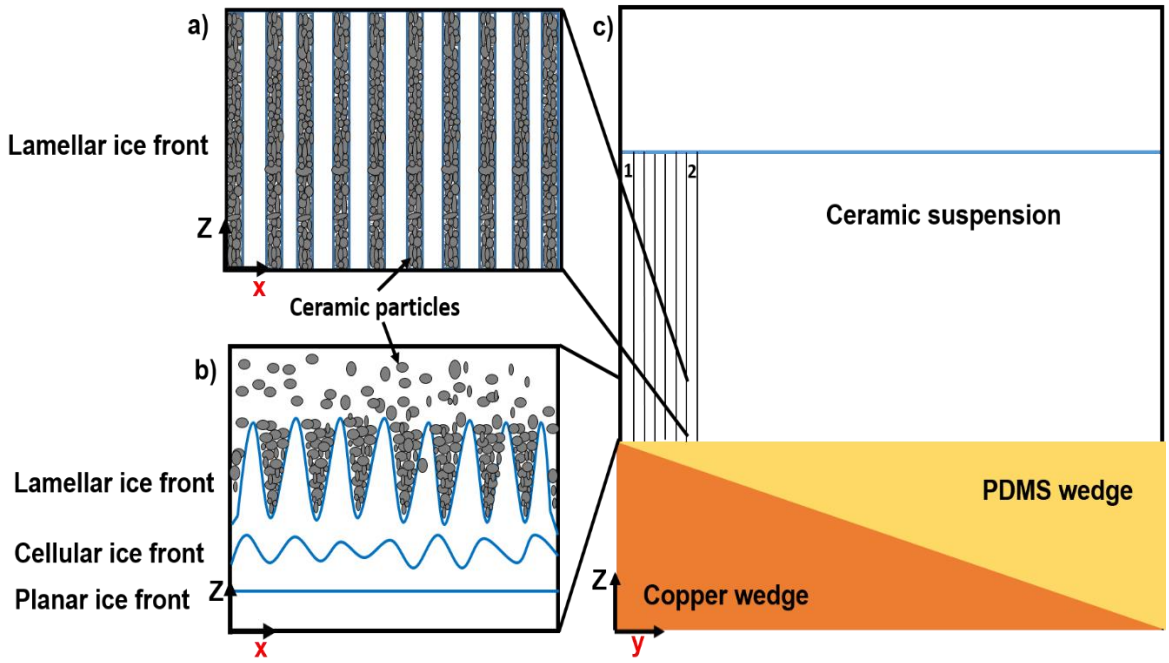

Figure 4-20: Schematic diagram of a) growing lamellar ice front, b) transition of the ice front, c) the copper mould covered by PDMS wedge and the ceramic suspension inside.

To understand the microstructure formation in bi-directional freeze casting, it is necessary to analyse the freezing process at different sections inside the mould. At the beginning of the freezing process, the first part of the suspension where freezing takes place is at the thinnest part of the PDMS wedge which separates the solution from the thickest part of the copper base (Figure 4-20 Section 1). The freezing of the ceramic suspension then progresses in different steps. Firstly, a planar ice front forms and traps the ceramic particles to produce the typical dense layer at the bottom side of the scaffold. After that, the planar ice front

transforms to cellular and then to lamellar crystals, and once these ice crystals start to grow, they repel the ceramic particles that have accumulated between them (Figure 4-20, b) [173]. Ice front transformation from planar to lamellar leads to random ice crystal nucleation, which is reflected by the random lamellar area seen in the ceramic scaffold. Once the ceramic suspension has nucleated ice crystals, they start to grow both vertically and horizontally. The time required for this transition depends on the cooling rate, and the higher the cooling rate, the faster the transition. With time the temperature in the subsequent sections of the suspension goes down, and the same freezing process begins. When the system reaches a steady state, ice crystals grow in a continuous ordered way under the influence of dual temperature gradient throughout the suspension (Figure 4-20, a) and no further random ice crystal nucleation occurs [207]. This process results in a small random lamellar area and a large ordered and highly aligned lamellar area in the ceramic scaffold. The micro-CT scan (Figure 4-7) confirms the previous analysis. The micro-CT image at section 1 (Figure 4-7, i) shows the three typical zones of a conventional freeze cast ceramic: dense, cellular and lamellar, and the random alignment of the lamellar zone reflects the random ice crystal nucleation and growth. The micro-CT image in section 2 (Figure 4-7, j) shows a highly aligned lamellar structure, resulting from aligned ice crystal growth under the influence of the dual temperature gradient.

From the previous analysis of the freezing process, we can conclude that in order to increase the size of the aligned lamellar area, two conditions should be fulfilled:

1. A rapid ice front transition from planar to lamellar in order to produce nucleated ice crystals that are ready to grow.

2. Delaying the freezing process in the following sections as much as possible in order to give more time for water in the first sections to nucleate and produce ice crystals.

To fulfil the first condition, a high cooling rate can be used, while the second can be fulfilled by increasing the copper/PDMS mould slope angle. This was observed in this study (Figure 4-8) and it is in agreement with the results of Bai *et al*. (2016) [46], who reported that increasing both the cooling rate and the wedge slope angle increases the size of the domain of highly aligned lamellar orientation [46]. Another effect of cooling rate and copper/PDMS mould slope angle was observed on the extent of the dense area at the bottom of the scaffold. Increasing both the cooling rate and the copper/PDMS mould slope angle decreases the extent of the dense area, which means a larger lamellar area (Figure 4-12). This means that the usual process of freeze casting (having a planar ice front that produces the dense layer) is restricted to this area and once the suspension contains nucleated ice crystals that are ready to grow under the dual temperature gradient in a highly aligned way, no further planar ice front formation takes place, it is just a process of ice crystal growth. The direction of lamellar crystal growth is parallel to the temperature gradient, as the growth of ice crystals with a crystallographic c-axis perpendicular to the temperature gradient is more favourable [207].

Using a copper/PDMS mould slope angle of α=20° produced scaffolds with lower coherency in alignment (Figure 4-10) and a more graded porous network (Figure 4-11) compared to a mould slope angle of α=10°. This can be explained by the fact that the α=20° mould produces a higher temperature gradient and ceramic suspension needs more time to totally solidify inside this mould. Under these two conditions (i.e. a higher temperature gradient and longer freezing time), ice crystals will grow larger in size and in a graded fashion to

produce an inhomogeneous pore structure (Figure 4-11, inner image)[236]. The different sizes that ice crystals can grow to results in a larger variation of the measurements obtained from the scaffold prepared using a copper/PDMS mould slope angle of α=20° (Figure 4-11).

Ceramic solid loading is an important processing parameter that has a pronounced effect on the microstructure of the freeze cast ceramic scaffolds [173]. Freezing ceramic suspensions, where water is the solvent, produces ice crystals that grow vertically and horizontally under the effect of dual temperature gradients. While growing, these crystals repel the ceramic particles away from their aligned growing direction. Ceramic suspensions with high initial solid loadings have less water, but this appears to have little effect on the ability of the ice crystals to grow in a highly aligned fashion, repelling the well suspended and freely moving ceramic particles. However, scaffolds prepared from higher solid loadings have lower interlamellar spacing and greater ceramic wall thicknesses (Figure 4-14). This is to be expected and is in agreement with the literature [34]. After ice crystal lyophilisation, the space previously occupied becomes the interlamellar spacing. Therefore, using a ceramic suspension with high solid loading reduces the amount of water and increase the viscosity. As a result, ice crystal growth in the c-axis is hindered, leading to a lower interlamellar spacing and higher ceramic wall thickness [173].

Pore morphology inside freeze cast ceramic scaffolds can be controlled by using additives such as PVA [225], and on freezing a ceramic suspension containing PVA binder, two stages are seen. In the first stage (above 0°C), although the water is still in the liquid state, the PVA starts to gel and cover the ceramic particles, producing a particle-PVA gel network. In the second stage (below 0°C), the water starts to solidify producing nucleated ice crystals that are ready to grow, but their growth is restricted by the previously formed particle-PVA gel

network [31]. From the previous analysis, it can be concluded that a lower PVA concentration produces a weak gel network that not only allows ice crystals to grow in a more aligned direction but also larger in size, thereby creating scaffolds with higher interlamellar spacing and lower ceramic wall thickness (Figure 4-17). On the other hand, a PVA concentration of 4 and 8 wt.% produces a stronger initial interconnected gel network with increased viscosity, that leads to an obvious change in pore morphology. There are more trans-lamellar ceramic bridges (Figure 4-16 c and d) which restricts ice crystal growth in c-axis, leading to smaller interlamellar spacing and greater ceramic wall thickness (Figure 4-17). Also, it deflects the ice crystals from their preferable aligned growth direction (Figure 4-18).

4.4 Summary

In this section of the research, highly aligned ceramic scaffolds were fabricated for further densification and polymer infiltration, to create a composite material that might be used as a CAD/CAM dental restorative material. Highly aligned alumina ceramic scaffolds, with different coherencies in alignment and anisotropic graded porous network structures, were successfully produced, using the bi-directional freeze casting technique. Bi-directional freeze casting with the use of PVA as a binder created highly aligned porous scaffolds with a lamellar microstructure that could be modified by changing different processing parameters. Different imaging techniques showed that it is possible to fabricate highly aligned ceramic scaffolds with a lamellar structure using freeze casting. The coherency alignment measurements with the micro-CT imaging allowed a better understanding of ice nucleation and growth mechanism under dual temperature gradients.

Chapter 5. Fabrication and characterisation of biomimetic nacre-like ceramic/polymer composite materials

5.1 Introduction

A good CAD/CAM material should be strong enough to withstand the harsh oral environment and tough enough to resist crack initiation and propagation. In the previous chapter, the fabrication and characterisation of highly aligned lamellar Al_2O_3 ceramic scaffolds were described. As a result of the previous study, specific parameters were chosen to fabricate Al_2O_3/MgO ceramic scaffolds to be used for the production of the biomimetic nacre-like ceramic/polymer composite material. The fabricated ceramic scaffolds were also put through a second densification step to increase further the ceramic volume fraction, followed by polymer infiltration to produce the composite materials. UDMA/TEGDMA polymer was used to infiltrate the ceramic scaffolds as they are widely used in dental materials, are biocompatible, aesthetically pleasing and have low viscosity and good mechanical properties after polymerisation.

MgO was added to the Al_2O_3 ceramic suspension as a sintering aid. It was important to optimise the ceramic suspension before freeze casting. First, the zeta potential of the ceramic powders was determined. Then the viscosity of the colloidal suspension was assessed. Achieving a homogeneous and stable colloidal ceramic suspension is crucial to obtain a ceramic scaffold with optimum microstructure and properties. The effect of MgO addition on the microstructure was evaluated both qualitatively using SEM images and quantitatively by grain area measurement.

The as-freeze-cast ceramic scaffolds have low ceramic volume fractions; therefore, it was necessary to increase further the ceramic content in the final scaffolds by using a uniaxial

pressing method. As the green ceramics were very weak and could not withstand the pressing force, it was important to strengthen them before the pressing step. This was achieved by sintering the green ceramics at different high temperatures; this step is called first-step sintering. The effects of different first-step sintering temperatures on the final microstructure, linear shrinkage and density of the ceramic scaffolds were investigated. Uniaxial pressing was used to densify the ceramic scaffolds as it is an easy and cheap process compared to other densification methods such as hot pressing or isostatic hot pressing. The densified scaffolds were eventually put through second-step sintering to produce fully sintered scaffolds with a nacre-like brick microstructure. These scaffolds were finally silanised and infiltrated with polymer to produce nacre-like ceramic/polymer composite materials.

The mechanical properties of the fabricated composite materials were tested and correlated to the ceramic volume fraction and ceramic scaffold microstructure.

5.2 Results

5.2.1 Characterisation of Al_2O_3/MgO ceramic suspension

5.2.1.1 Zeta potential

The zeta potentials for both Al_2O_3 and MgO suspensions, with and without Tiron dispersant, were measured at a low solid loading of 0.2 vol.%. This step was important to find out the surface charges of the particles, as both of these ceramic particles must have the same charge within the suspension in order to repel each other to prevent agglomeration. For the Al_2O_3 suspension (Figure 5-1) it can be clearly seen that Tiron caused a significant change in the powder surface charge, shifting the whole curve to the negative region even under

acidic conditions. The isoelectric point (IEP) of alumina is at pH 8.1. Adding Tiron to the alumina ceramic suspension shifted the IEP to approximately pH 2.6. Alumina particles are negatively charged under basic conditions, with or without the addition of Tiron. Adding Tiron increased the zeta potential more towards the negatively charged region.

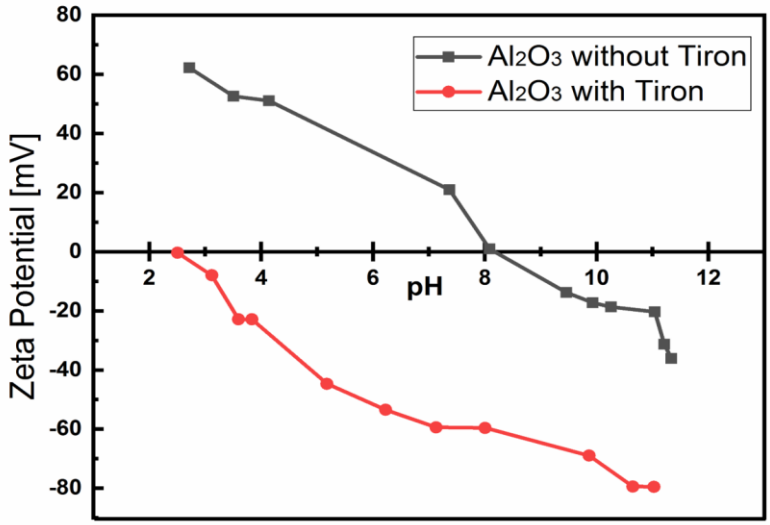

Figure 5-1: Effect of Tiron on the zeta potential values for alumina ceramic particles as a function of pH.

For the MgO suspension alone (Figure 5-2), the zeta potential curve was in the positive region with an IEP around pH 10.9. Adding Tiron to the MgO suspension shifted the zeta potential curve to the negative range and enabled further zeta potential measurements at lower pH values. It was impossible to measure the zeta potential at a pH value of less than 7.9 due to the high solubility of MgO in the acidic medium.

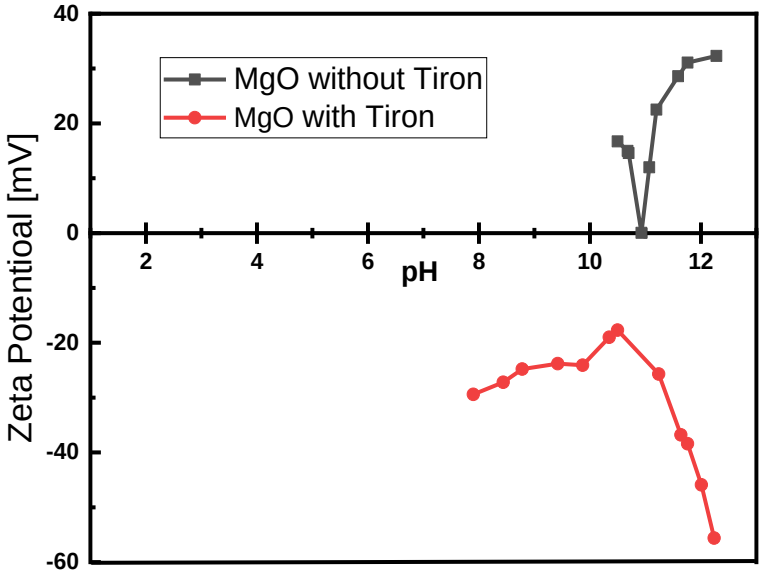

Figure 5-2: Effect of Tiron on the zeta potential values of MgO powder particles as a function of pH.

Using Tiron to disperse Al_2O_3/MgO ceramic powders is effective, as both particles have negative charges at high pH values. Adding MgO to disperse the solution increases the pH and ensures the ceramic suspension is prepared under basic conditions with both particles negatively charged.

5.2.1.2 Rheological behaviour

The rheological behaviour of the ceramic suspensions was studied to determine the effect of altering the concentration of Tiron dispersant. Five different concentrations of Tiron (0.05, 0.1, 0.25, 0.5, 1.0 wt.% of the ceramic dry powder weight) were used to study its effect on the Al_2O_3/MgO suspension viscosity. The results can be seen in Figure 5-3. Using 0.05 wt.% of Tiron was insufficient to disperse the ceramic powder, and the resulting suspension was viscous. When considering the other viscosity curves, it can be seen that

increasing the concentration of Tiron decreased the suspension viscosity up to 0.1 wt.%, but it then began to increase again with the use of 0.25, 0.5 and 1wt.% Tiron. 0.1 wt.% was therefore chosen as the optimum concentration to disperse the Al_2O_3/MgO suspension for the subsequent experiments.

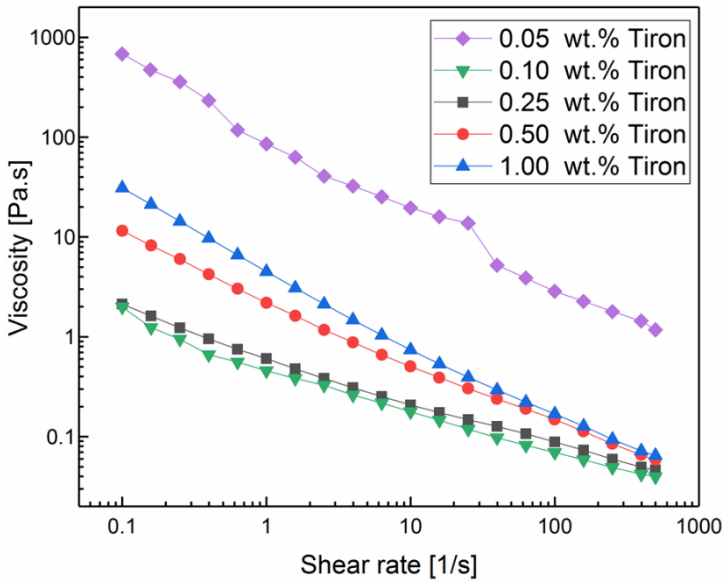

Figure 5-3: Viscosity of ceramic suspensions (40 vol.%) as a function of Tiron concentration.

5.2.2 Comparison between scaffolds prepared with and without MgO

Two 20 vol.% alumina ceramic suspensions were prepared, one without MgO and one with 0.02 wt.% MgO. Tiron (0.1 wt.%) was used as the dispersant, and PVA (2 wt.%) was used as the binder. These suspensions were freeze cast using bi-directional freeze casting in a copper/SR mould (slope angle α= 10°) with 30 °C/min as initial cooling rate. The scaffolds produced were then examined under SEM for qualitative assessment, as well as for grain area measurement. The apparent and relative densities of the scaffolds were measured using Archimedes' method.

5.2.2.1 SEM images and grain area measurement

SEM images of scaffolds prepared with and without MgO addition were obtained. Figure 5-4 are the SEM images of the smooth surface of the ceramic walls at x6000 magnification, while Figure 5-5 is the SEM images of the featured surface of the ceramic walls at x1200 magnification. The images show differences in the grain sizes and the degree of densification between scaffolds. Abnormal grain growth can be observed in the scaffolds prepared without MgO, Figure 5-4 a and Figure 5-5 a. Conversely, adding MgO encourages more homogenous rounded grain growth, as shown in Figure 5-4 b and Figure 5-5 b.

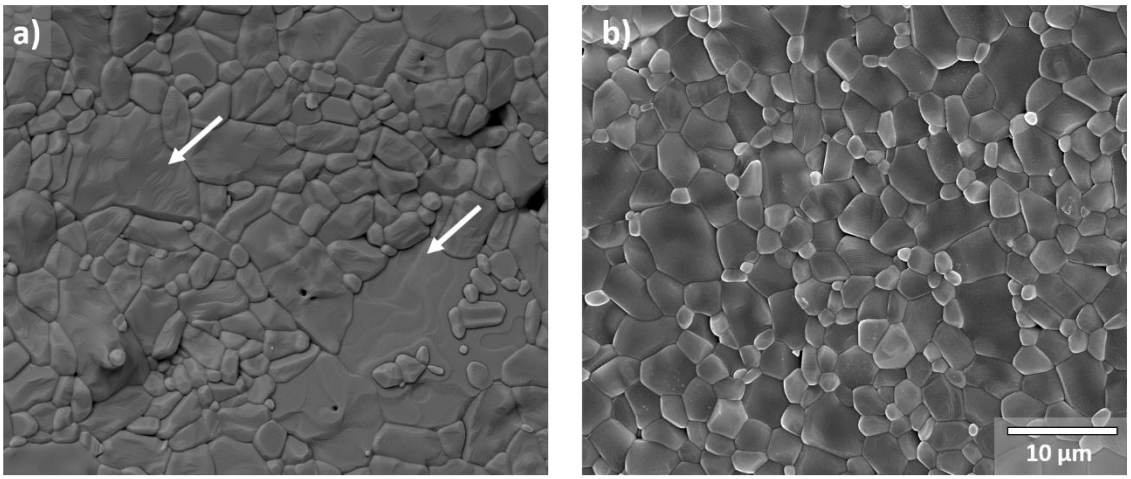

Figure 5-4: SEM images for smooth surface inside a) ceramic scaffold prepared without MgO, arrows indicate abnormal grain growth b) ceramic scaffold prepared with MgO. Magnification x6000.

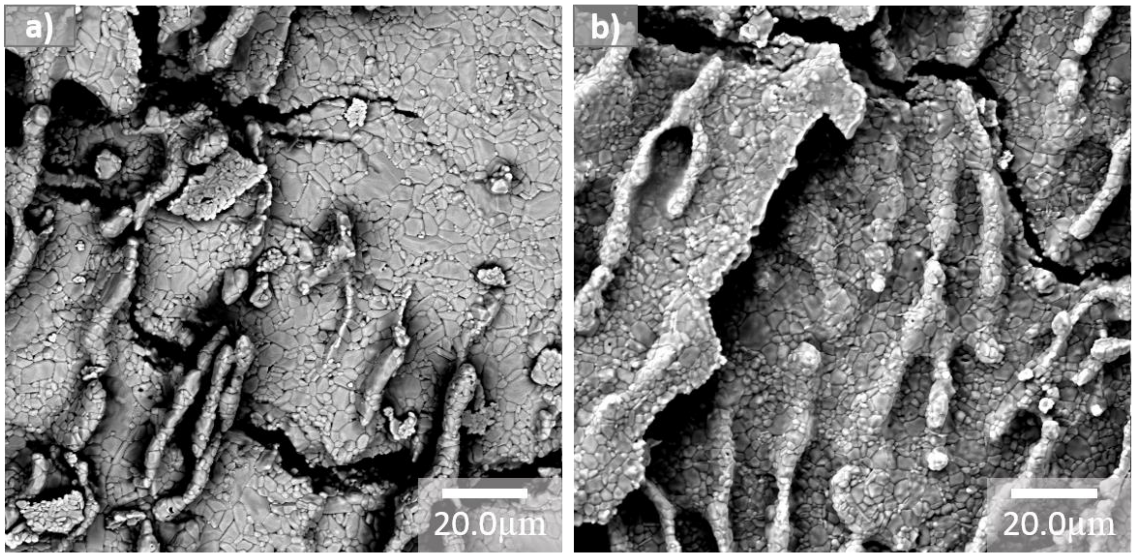

Figure 5-5: SEM images for featured surface inside a) ceramic scaffold prepared without MgO, b) ceramic scaffold prepared with MgO. Magnification x1200.

Grain area measurements were performed using ImageJ-Fiji software. SEM images for ceramic scaffolds prepared with and without MgO were taken and processed using the software. Figure 5-6 shows the probability density plot of grain area with and without MgO. It can be seen that the mode grain area in both cases was approximately 4.5 μm^2 but the measurements were more consistent in the case of the scaffolds with MgO than without MgO.

Table 5-1 shows the summary data for grain area where it can be seen the data distribution was not normal. Although the use of both the mean and standard deviation, or median and interquartile range would suggest the grain areas are similar with or without the use of MgO, consideration of the range (i.e. maxima and minima) would suggest a more consistent grain area when MgO is used, confirming the findings of the probability density plot (Figure 5-6).

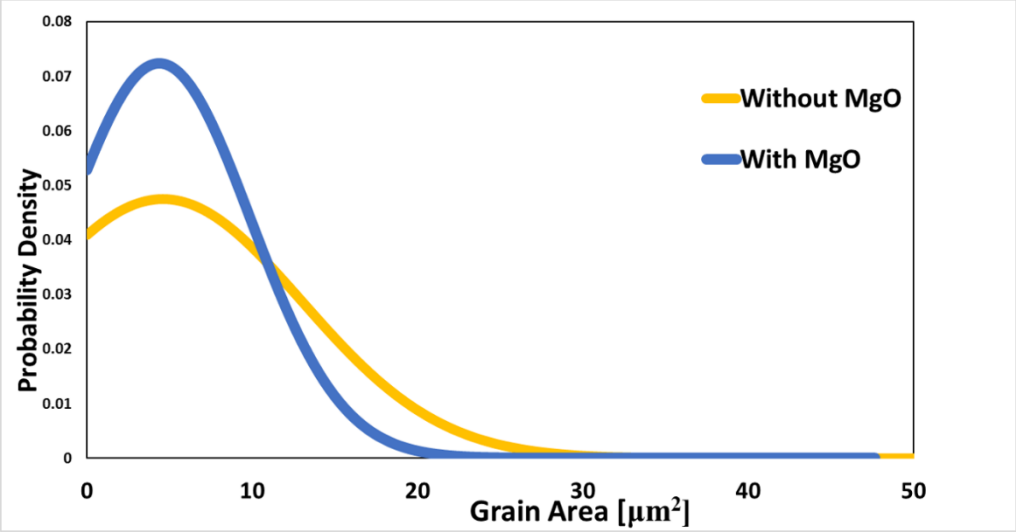

Figure 5-6: Probability density plot of mode grain area measurement [µm^2] for scaffolds prepared with and without MgO.

	Mean	SD	Median	IQR	Maximum	Minimum
Without MgO	4.58	8.40	2.25	0.67 to 5.40	196.77	0.002
With MgO	4.37	5.51	2.62	0.48 to 5.97	47.65	0.0001

Table 5-1: Summary data of grain area measurements [µm^2] for scaffolds prepared with and without MgO.

5.2.2.2 Apparent and relative densities

Table 5-2 shows the apparent and relative density values for 20 vol.% alumina scaffolds prepared with and without MgO. The theoretical density of Alumina was assumed to be 3.96 g/cm^3 . The apparent density demonstrates how closely packed the ceramic grains are within the struts of the scaffold, regardless of the porous network. Adding a small amount of MgO (0.02 wt.%) to alumina leads to a small increase in the density of the ceramic scaffold. The apparent density increased from 3.89 g/cm^3 to 3.94 g/cm^3 when MgO was added to the suspension. The relative density reached a high value of 99.50 %.

	Without MgO	With MgO
Apparent density	3.89	3.94
SD	(0.00)	(0.01)
Relative density	98.23	99.50
SD	(0.13)	(0.37)

Table 5-2: Mean and SD of apparent [g/cm^3] and relative densities [%] of the Al_2O_3 ceramic scaffolds with and without the addition of MgO.

5.2.3 Ceramic scaffold fabrication and characterisation

Since the as-fabricated ceramic scaffolds have a low ceramic volume fraction, a further densification step was needed. Uniaxial pressing of the highly aligned ceramic scaffolds was essential to increase the ceramic volume content while maintaining the aligned microstructure. For this step to be effective, the as-fabricated ceramic scaffold had to be strong enough to withstand the pressing force. A first-step sintering process was, therefore, mandatory. Sintering ceramic green bodies at lower temperatures leads to partially sintered scaffolds. These partially sintered scaffolds will then have sufficient strength to withstand the pressing force. Varying the sintering temperature can have different effects on the ceramic green bodies. It was, therefore, important to study the effect of different first-step sintering temperatures on the microstructure of the ceramic scaffolds.

5.2.3.1 Microstructure of ceramic scaffolds sintered at different first-step sintering temperatures

Ceramic green bodies were sintered at 9 different temperatures ranging from 1200°C to 1600°C. Green bodies sintered at 1200°C were very weak, and it was hard even to get them

out of the furnace in one piece. Sintering at 1200°C was, therefore, insufficient to produce densification within the green body. All that happened was the burn-out of the PVA binder during the first heat cycle (at 600°C), which explains the weakness of the samples. All other specimens sintered at 1250°C or higher were at least partially sintered and strong enough to be handled and removed intact from the furnace.

Figures 5-7 and 5-8 are the SEM images showing the grain size and shape of the ceramic scaffolds sintered at different first-step sintering temperatures, along with the unsintered green body, at two different magnifications of x6000 and x24000, respectively. It can be clearly seen that with increasing first-step sintering temperature, the grain size increases, and the pore size between the grains decreases. Sintering at 1550°C and 1600°C leads to fully sintered ceramic scaffolds (Figures 5-7 and 5-8). At 1400°C, the grains begin to consolidate with each other and grow larger in size (Figure 5-8).

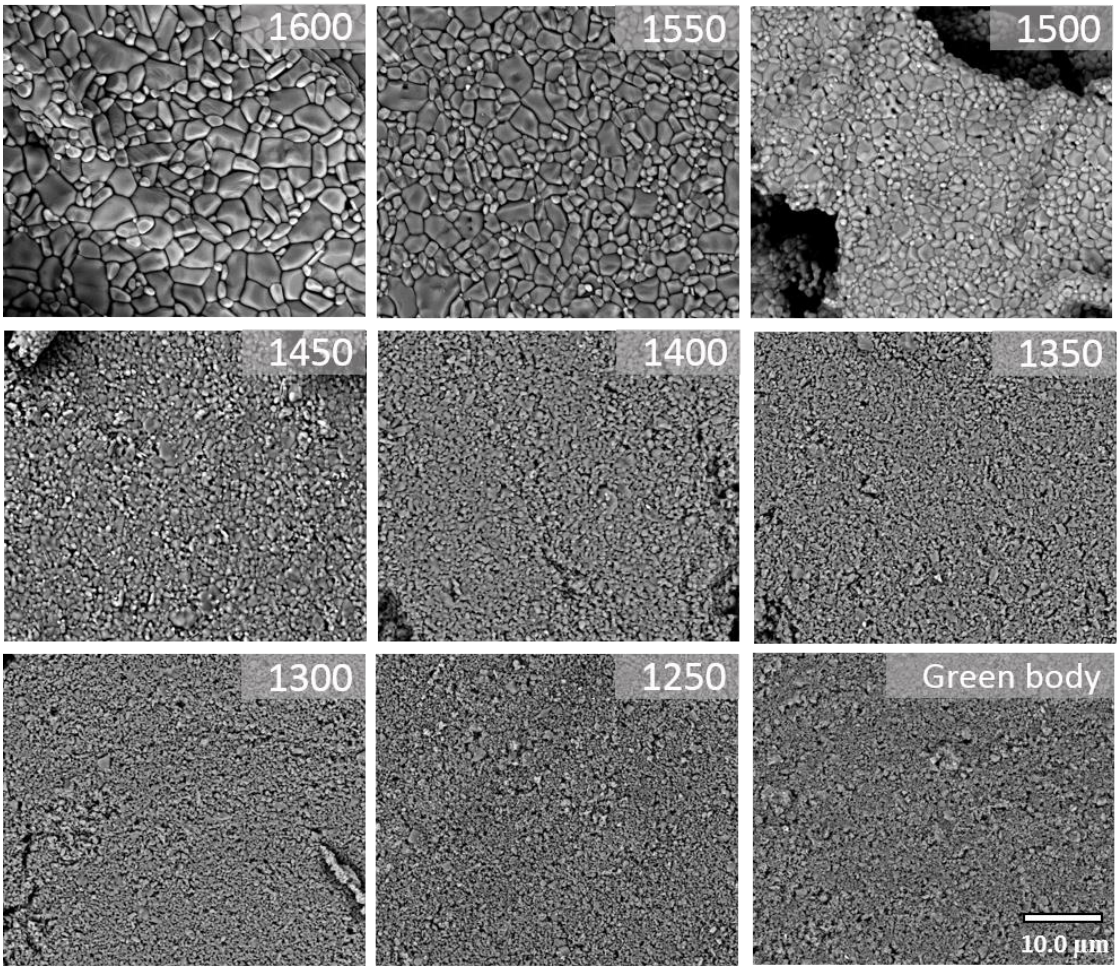

Figure 5-7: SEM images of green body and ceramic scaffolds sintered at different first-step sintering temperatures, Magnification x6000.

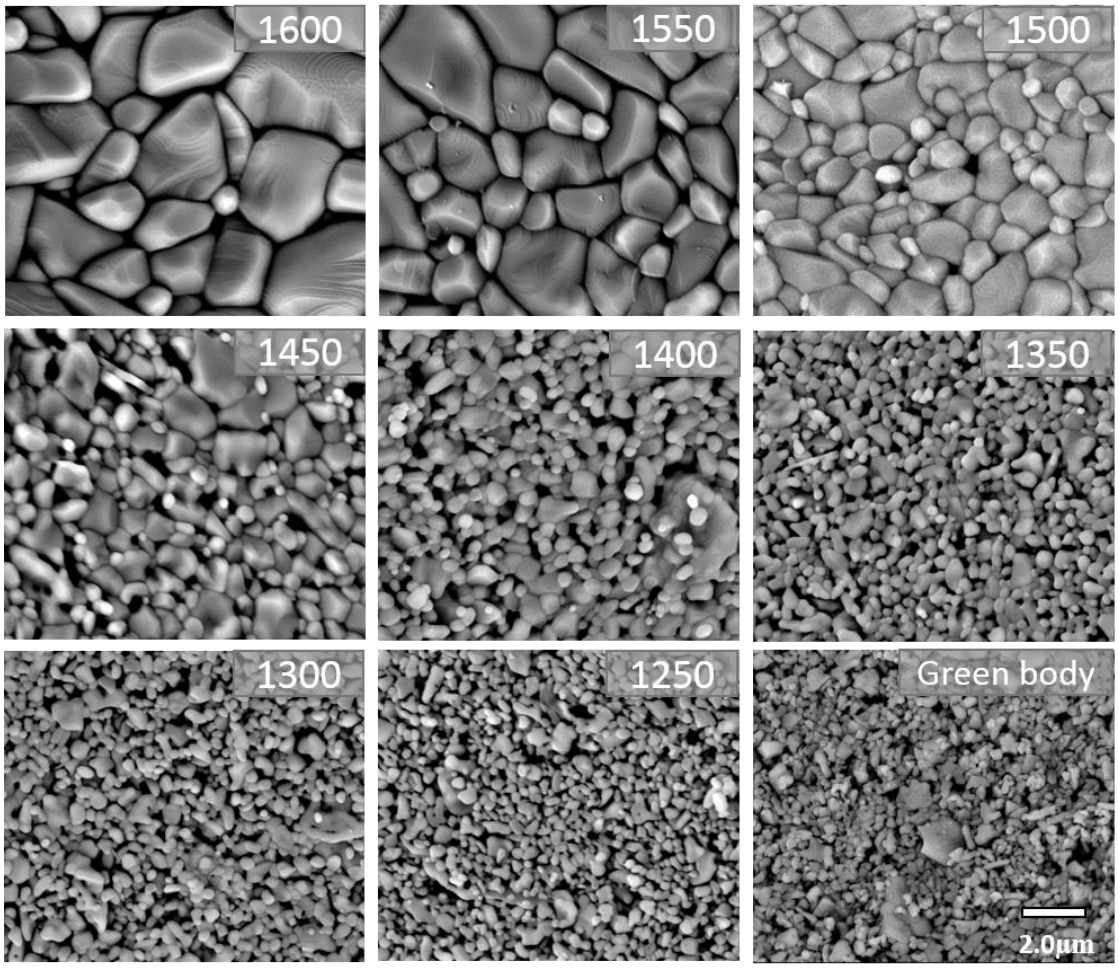

Figure 5-8: SEM images of green body and ceramic scaffolds sintered at different first-step sintering temperatures, Magnification x24000.

5.2.3.2 Microstructure of ceramic scaffolds after uniaxial pressing and second-step sintering

The way in which uniaxial pressing changes the microstructure inside the struts of the ceramic scaffold is demonstrated in Figure 5-9. The as-fabricated scaffold was sintered at 1550 °C before the pressing step at 100 MPa. Figure 5-9 a shows an as-fabricated ceramic scaffold (long) before pressing and the densified scaffold (short) after pressing. The wax inside the scaffold acts as a sacrificial phase during heating and as a binder after the uniaxial pressing step. The melted wax then helps maintain the interlamellar spaces separating the

ceramic walls during uniaxial pressing, as well as the integrity of the scaffold after pressing. Figures 5-9 b and c show the microstructure of the ceramic scaffolds before and after pressing, respectively. The as-fabricated ceramic scaffold has long connected ceramic walls with large interlamellar spacing (Figure 5-9 b), while the pressed scaffold has short, broken ceramic walls with much smaller interlamellar spacing (Figure 5-9 c). The microstructure of the pressed scaffold resembles the aragonite bricks inside nacre. When this scaffold is infiltrated with polymer, a biomimetic nacre-like ceramic/polymer composite can be fabricated.

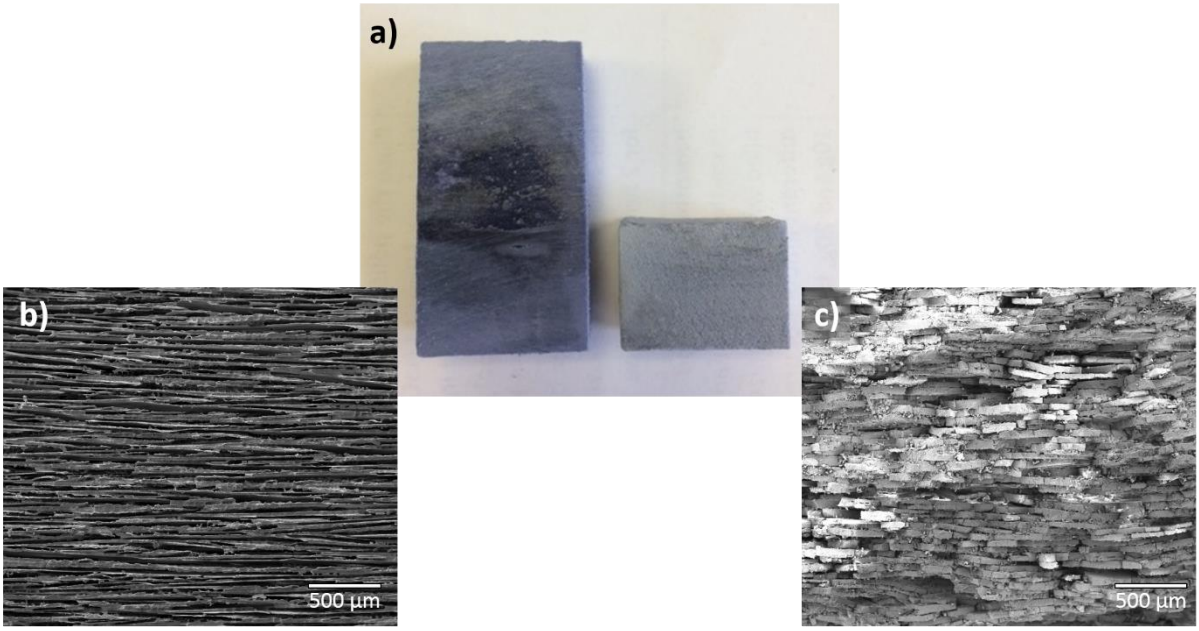

Figure 5-9: a) As-fabricated ceramic scaffold (long) before uniaxial pressing and densified scaffold (short) after uniaxial pressing. b) SEM image of the as-fabricated ceramic scaffold (sintered once at 1550°C). c) SEM image of the pressed ceramic scaffold (sintered twice at 1550°C before and after uniaxial pressing).

Uniaxial pressing of the ceramic scaffolds at 100 MPa reduces the mean interlamellar spacing from 28.62µm to 6.95µm. At the same time, the ceramic volume fraction increased from 34.12% to 64.81% (Table 5-3).

	As-fabricated ceramic scaffolds	Pressed ceramic scaffolds
Interlamellar spacing (μm)	28.62	6.95
SD	(5.9)	(2.2)
Ceramic volume fraction (%)	34.12	64.81
SD	(1.49)	(4.83)

Table 5-3: Mean and SD for interlamellar spacing [μm] and ceramic volume [%] fraction of as-fabricated ceramic scaffolds and pressed ceramic scaffolds.

In order to investigate the infiltration of the polymer phase, scaffolds sintered at 8 different first-step sintering temperatures, along with a green body, were infiltrated with blue wax and pressed uniaxially to increase the ceramic volume fraction inside the scaffolds as previously described. A pressure of 100 MPa was used, after which second-step sintering was carried out at 1550°C.

The densified sintered scaffolds were then infiltrated with epoxy resin and the microstructure investigated under the SEM. It is worth mentioning that all of the images are for scaffolds that had been sintered twice, i.e., they had undergone both first-step and second-step sintering. However, they are labelled according to the first-step sintering temperatures in Figures 5-10 with the same second-step sintering temperature of 1550°C. The green body sample was uniaxially pressed without first-step sintering. Figure 5-10 a-h show the brick and mortar structure of all the scaffolds sintered at different first-step sintering temperatures. However, the brick and mortar structure was completely diminished for green ceramic without first-step sintering (Figure 5-10 i). The higher magnification SEM

images (Figure 5-11) show the interlamellar spaces between the ceramic walls, with scaffolds sintered at 1400°C or above (Figure 5-11 a, b, c, d and e) being better able to maintain the interlamellar spacing, compared to those sintered at 1350°C or below (Figure 5-11 f, g and h).

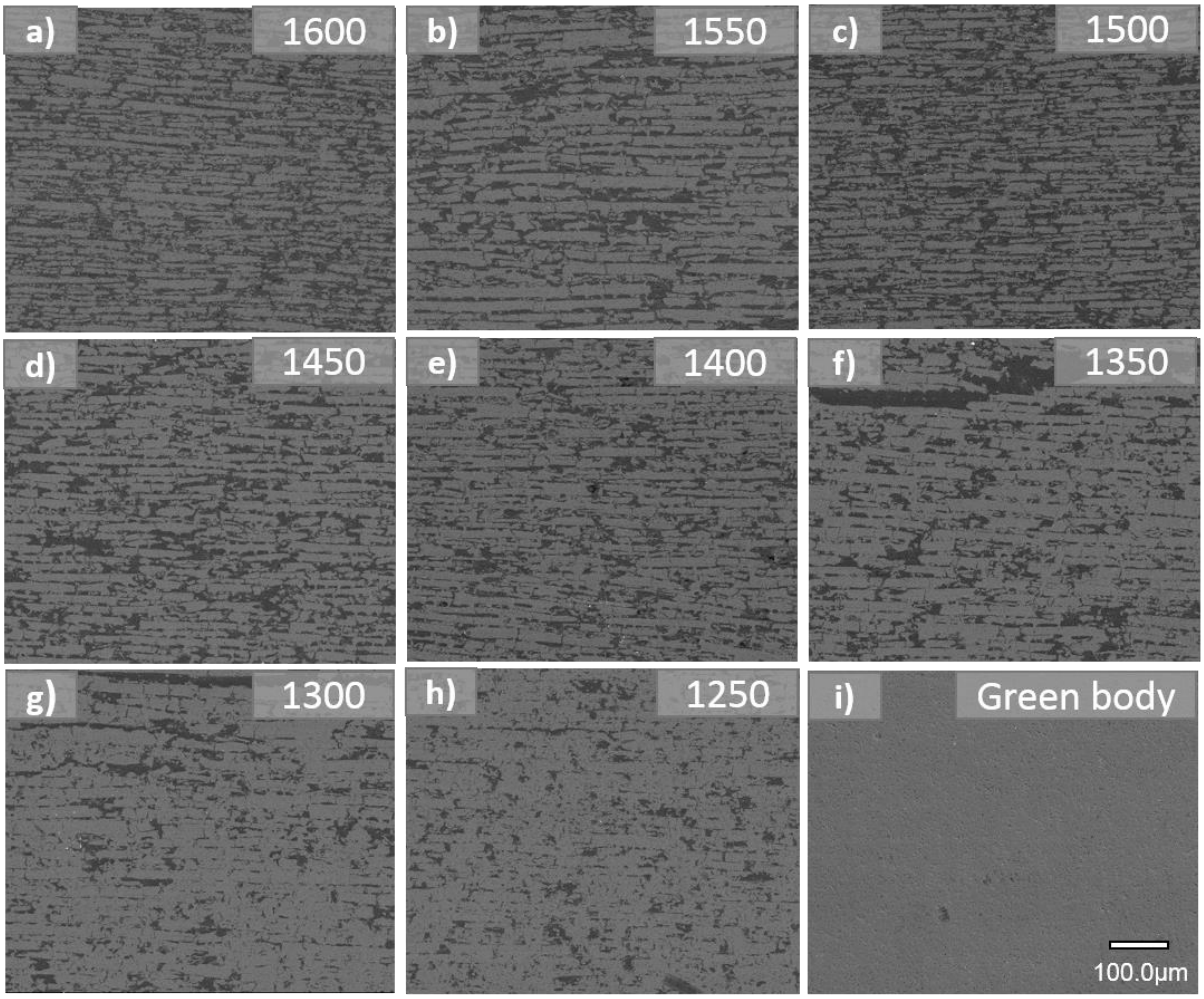

Figure 5-10: SEM images of sintered scaffolds with different first-step sintering temperatures shown in the top right corner of each image. Magnification x400.

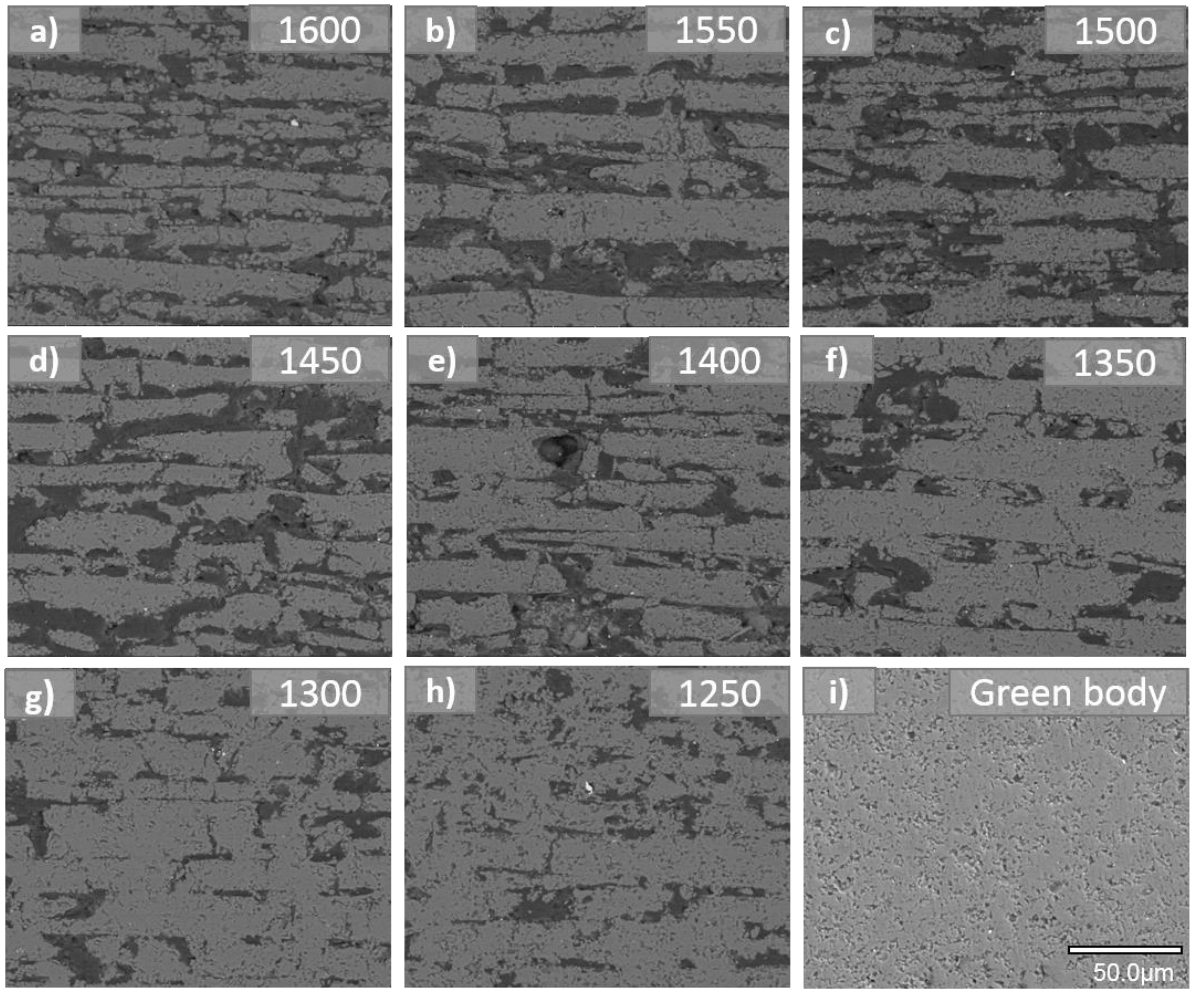

Figure 5-11: Higher magnification (x1600) SEM images of sintered scaffolds with different first-step sintering temperatures shown in the top right corner of each image.

Samples (5x5x7mm) were cut from the epoxy infiltrated scaffolds where the epoxy resin was burnt out to enable examination under SEM. In the case of samples with 1550°C and 1600°C first-step sintering temperatures, these disintegrated into powder, most probably due to insufficient connections between ceramic walls, and so were not examined further. Samples sintered at 1500°C or below have maintained the scaffold integrity due to strong interconnections between the ceramic walls and examining them under SEM confirmed the findings in Figure 5-11.

5.2.3.3 Linear shrinkage

Scaffolds sintered at different sintering temperatures shrink differently. The linear shrinkage values of the ceramic scaffolds after the first-step sintering at different temperatures, followed by pressing and then second-step sintering at the same 1550°C temperature, are illustrated in Figure 5-12.

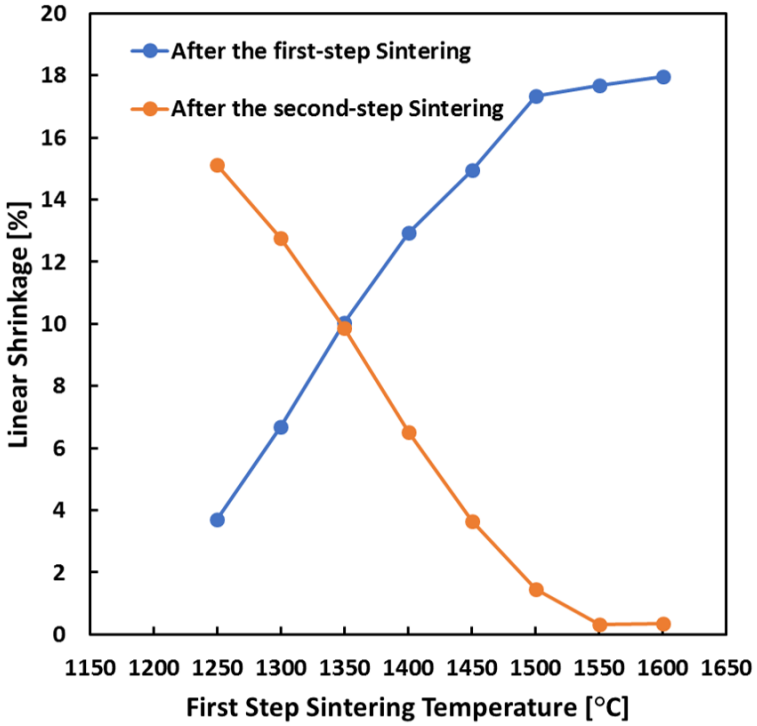

Figure 5-12: Mean percent linear shrinkage for ceramic scaffolds after first-step sintering at various temperatures and after second-step sintering at 1550 °C.

From Figure 5-12, it can be seen that the linear shrinkage increases as the first-step sintering temperature increases. After the second-step sintering, samples that were sintered at lower first-step sintering temperatures showed greater linear shrinkage.

5.2.3.4 Ceramic volume fraction

Archimedes method was used to measure the ceramic volume fraction of the densified scaffolds (sintered at different first-step sintering temperatures) following second-step sintering, Figure 5-13.

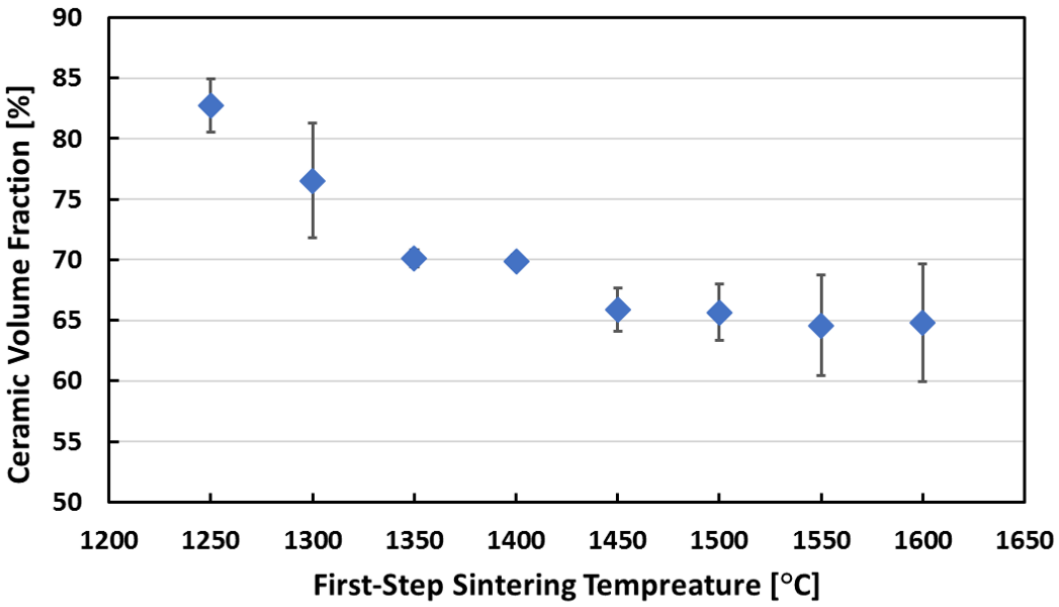

Figure 5-13: Mean and SD of ceramic volume fraction [%] of densified fully sintered ceramic scaffolds as a function of different first-step sintering temperatures.

Figure 5-13 shows the ceramic volume fraction of fully sintered ceramic scaffolds as a function of different first-step sintering temperature. Ceramic volume fraction decreased as the first-step sintering temperature increased, reducing from 82.7% at 1250°C to 64.81% at 1600°C.

5.2.4 Biomimetic nacre-like ceramic/polymer composites

In this study, UDMA/TEGDMA monomers were used to infiltrate the densified ceramic scaffolds fabricated by using different first-step sintering temperatures. Heat treatment followed the infiltration step to initiate monomer polymerisation. The whole process has previously been described in Chapter 3, Page 77.

5.2.4.1 Effect of silanisation

Ceramic scaffolds were first silanised with γ-MPS before the monomer infiltration step to ensure there was adequate chemical bonding between the inorganic ceramic scaffold and the organic polymer. To demonstrate the effect of silanisation on the bond between the ceramic and polymer, two as-fabricated ceramic scaffolds (sintered once at 1550°C) were infiltrated with UDMA/TEGDMA monomers, one of them was silanised before monomer infiltration, and the other was not. The reason for using as-fabricated ceramic scaffolds rather than densified scaffolds is that the interlamellar spacing in the as-fabricated scaffold is larger, meaning any potential effect of silanisation can be more easily seen. Figure 5-14 shows the microstructure within the two specimens. In the silanised specimen, the ceramic and the polymer are in close contact, with no gap between the two phases (Figure 5-14 a and c). By contrast, in the case of the unsilanised ceramic scaffold, there were gaps visible between the ceramic and the polymer (Figure 5-14 b and d). This shows the importance of silanisation of the ceramic scaffold prior to monomer infiltration.

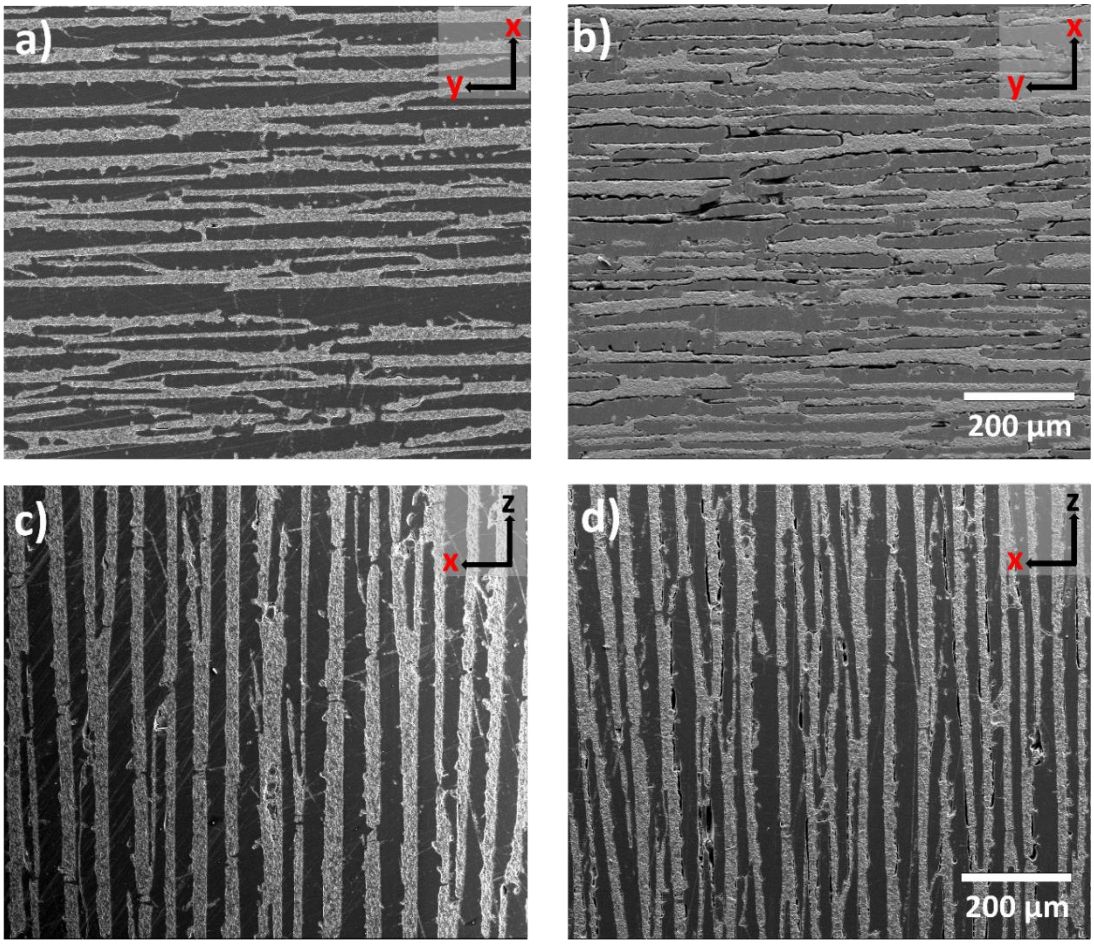

Figure 5-14: SEM images of a silanised composite material (a and c) and unsilanised composite material (b and d).

5.2.4.2 Microstructure of the composite materials

Figure 5-15 shows the microstructure of the biomimetic nacre-like ceramic/polymer composite when the first-step sintering temperature was 1550°C, it was uniaxially pressed at 100 MPa, sintered for the second time at 1550°C and silanised prior to UDMA/TEGDMA monomer mixture infiltration. These SEM images show that the polymer had completely filled the pores within the scaffold and the thickness was uniform. However, there were some areas in which the ceramic bricks had become separated by a polymer layer. Also, it is clear that the fabricated composite material has an anisotropic structure.

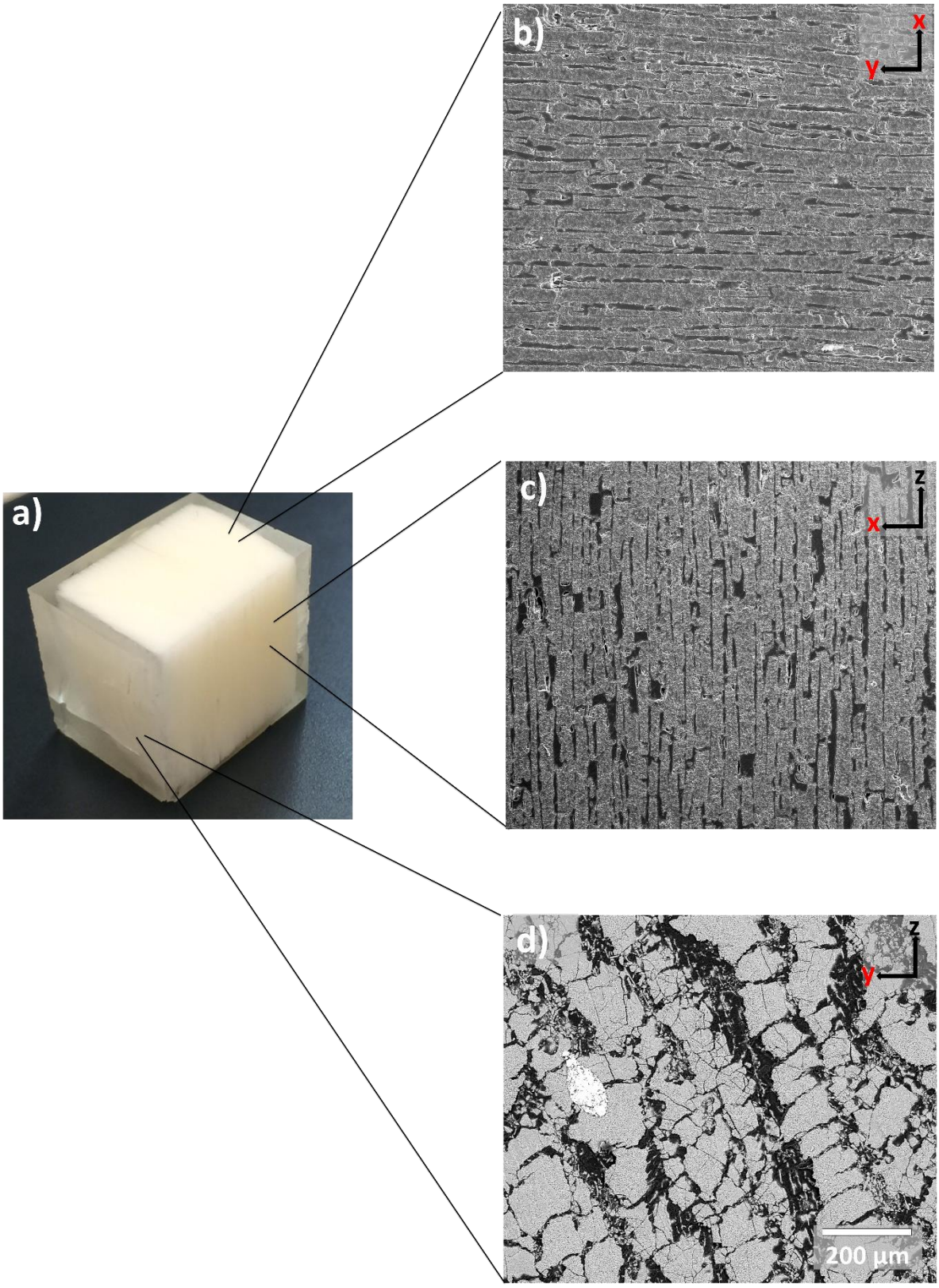

Figure 5-15: Ceramic/polymer composite block (a) and SEM images of the composite microstructure taken from different parts of the specimen (b, c and d)

5.2.4.3 Compressive strength

To study the effect of different first-step sintering temperatures on the mechanical properties of the composites, the compressive strength was measured. Silanisation of the scaffolds was not carried out before polymer infiltration in this part of the study.

The compressive strength of the composites was measured from the z and x directions. Figure 5-16 shows the results of the compressive strength as a function of different first-step sintering temperatures. Increasing the temperature decreased the compressive strength in the z direction. The compressive strength decreased from 364.4 MPa to 104.51 MPa as the first-step sintering temperature increased from 1250°C to 1600°C, respectively. First-step sintering temperature had a significant effect on the compressive strength when measured from the z direction. By contrast, compressive strength in the x direction did not demonstrate the same pronounced effect, although there was still a trend for the compressive strength to reduce as the first-step sintering temperature increased.

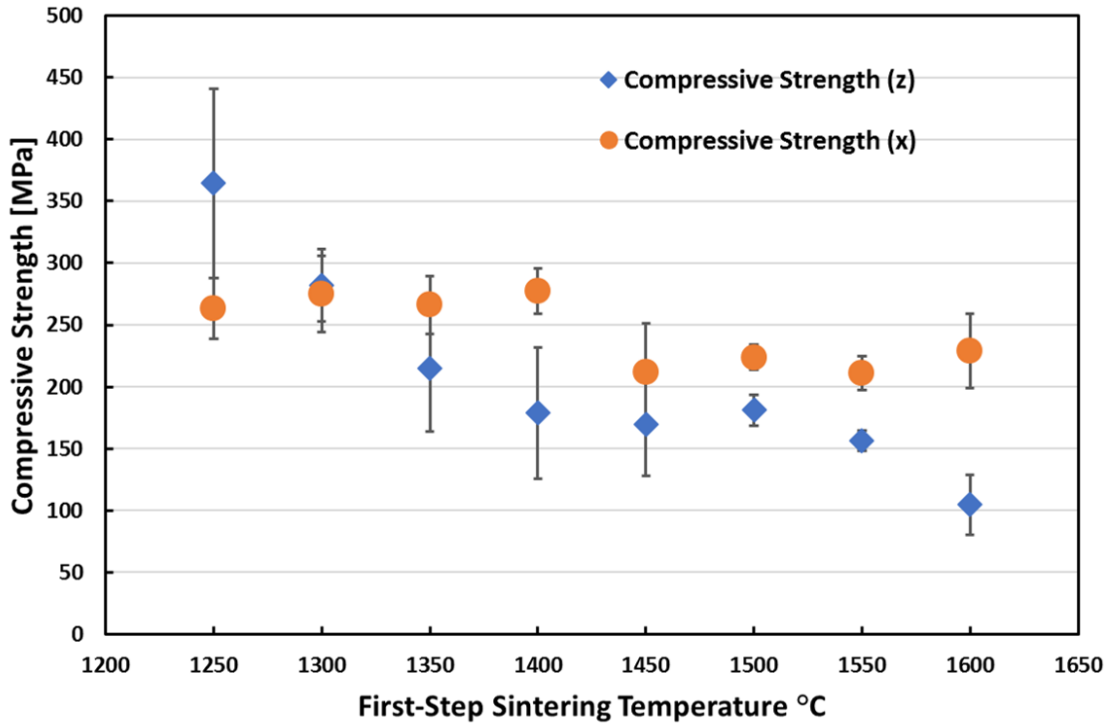

Figure 5-16: Mean and SD of compressive strength [MPa] of the composite material (in z and x directions) as a function of first-step sintering temperature. Note: the ceramic scaffolds were not silanised for this test.

5.2.4.4 Flexural strength

The flexural strength of each biomimetic nacre-like composite material was measured in the z direction and plotted against the first-step sintering temperature (Figure 5-17). The specimens were tested using the three-point bend test.

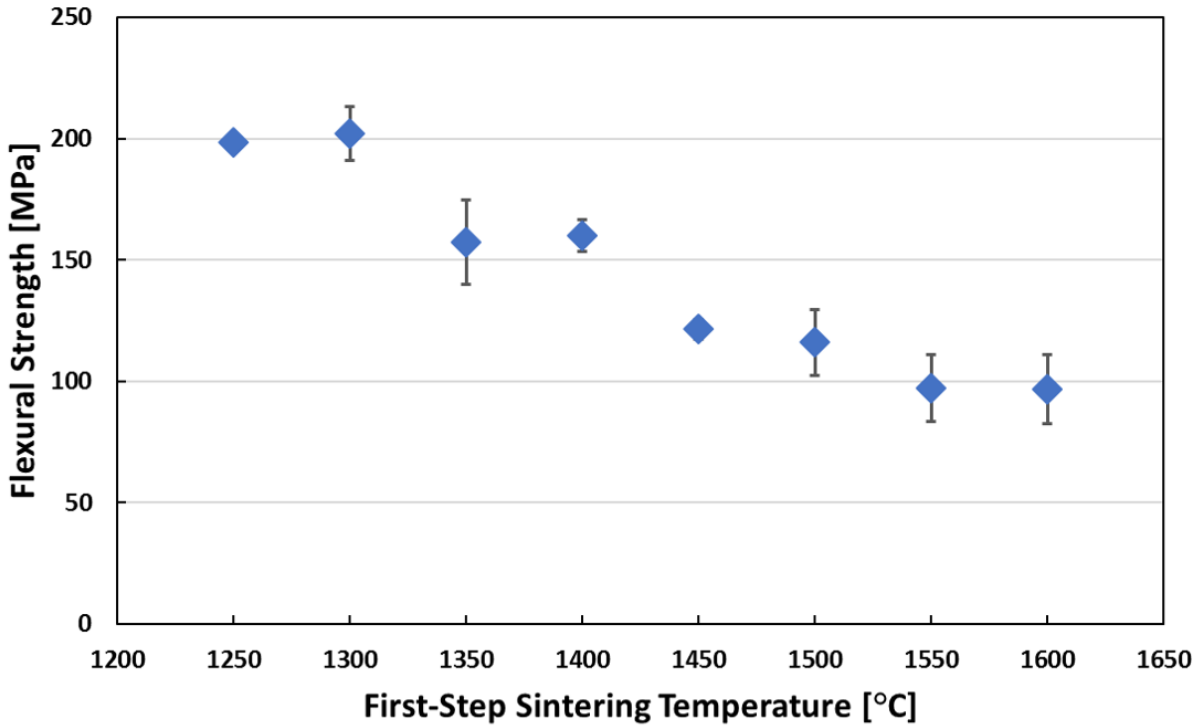

Figure 5-17: Means and SD of flexural strength [MPa] of the composite material as a function of first-step sintering temperature. The force was applied from the z direction.

It can be seen from Figure 5-17 that there was a trend for flexural strength to decrease with increasing first-step sintering temperature.

5.2.4.5 Fracture toughness (K_{IC})

The fracture toughness (K_{IC}) for the biomimetic nacre-like composite materials was measured in the x direction. Again, the values were plotted against the first-step sintering temperature (Figure 5-18).

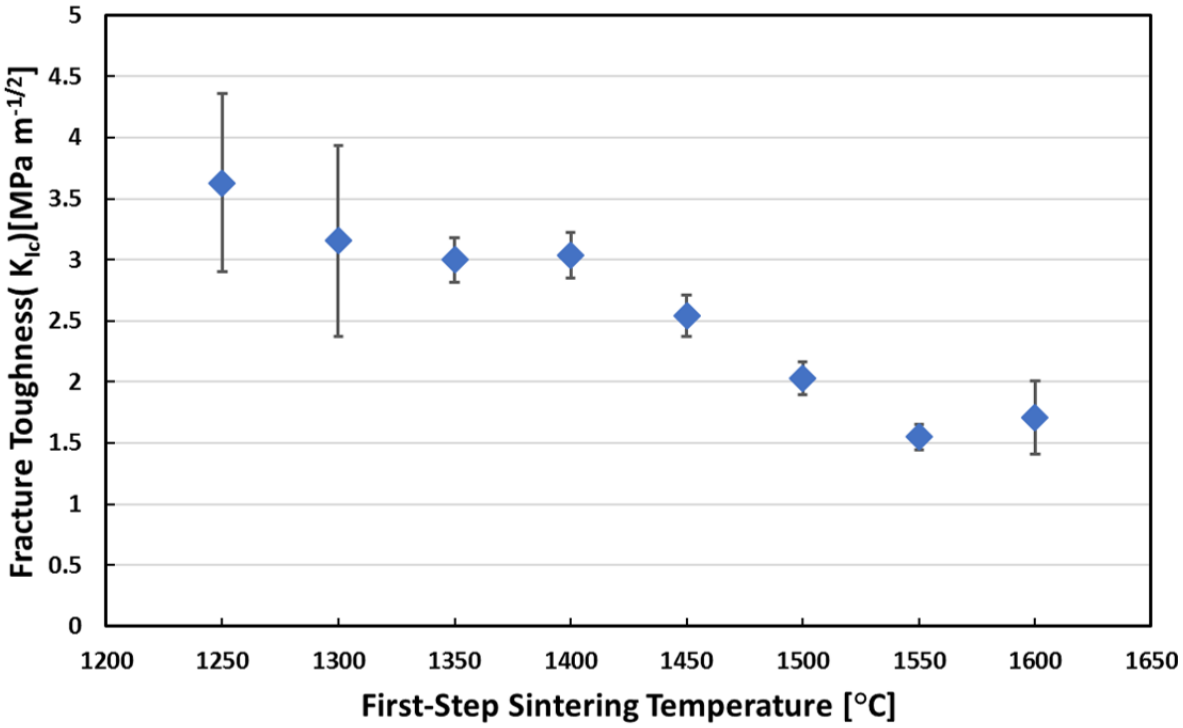

Figure 5-18: Mean and SD of fracture toughness (K_{IC}) [MPa.$m^{1/2}$] of the composite material as a function of first-step sintering temperature. The force was applied from the x direction.

When looking at the fracture toughness (K_{IC}), we can see that there was a trend for fracture toughness to increase with decreasing the first-step sintering temperature. The highest fracture toughness value was 3.63 MPa.$m^{1/2}$ for samples fabricated from scaffolds sintered at 1250°C.

Figure 5-19 shows the load versus displacement curve for the fracture toughness test of the composite materials. It can be seen that the curves vary with the first-step sintering temperature. Samples that were sintered at high sintering temperatures show greater displacement compared to samples sintered at lower temperatures, meaning they are more ductile. After the peak load was reached, the sample sintered at 1250 °C shows a sudden failure, followed by a small increased loading before final brittle fracture. This means that crack propagation was unstable. For all other samples, the tails of each of the curves exhibit

a smoother fall in loading with displacement, indicative of more stable crack propagation [237].

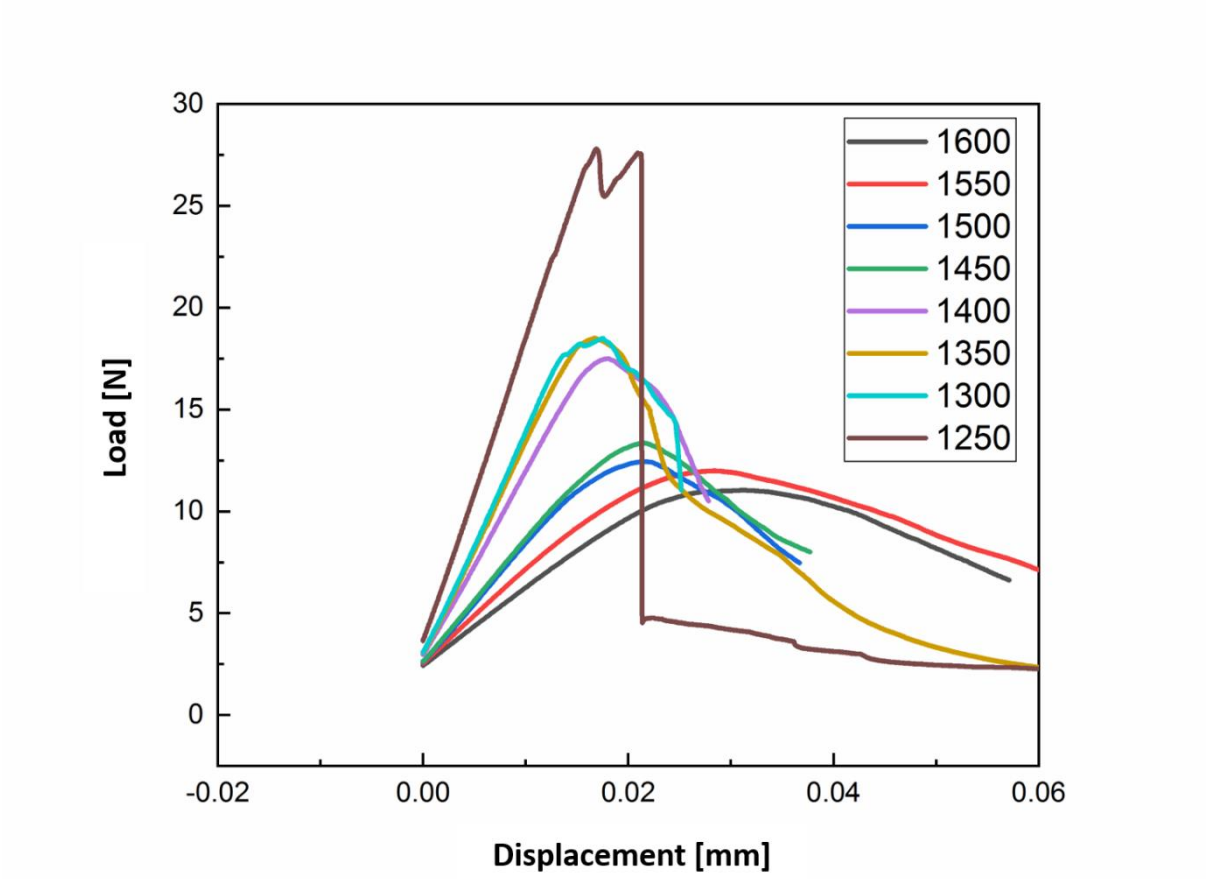

Figure 5-19: Load vs displacement curves for the fracture toughness tests of the composite material as a function of first-step sintering temperature.

SEM images were taken of the nacre-like ceramic/polymer composite (first-step sintering temperature 1400°C) after fracture toughness testing in order to assess the fracture path (Figure 5-20).

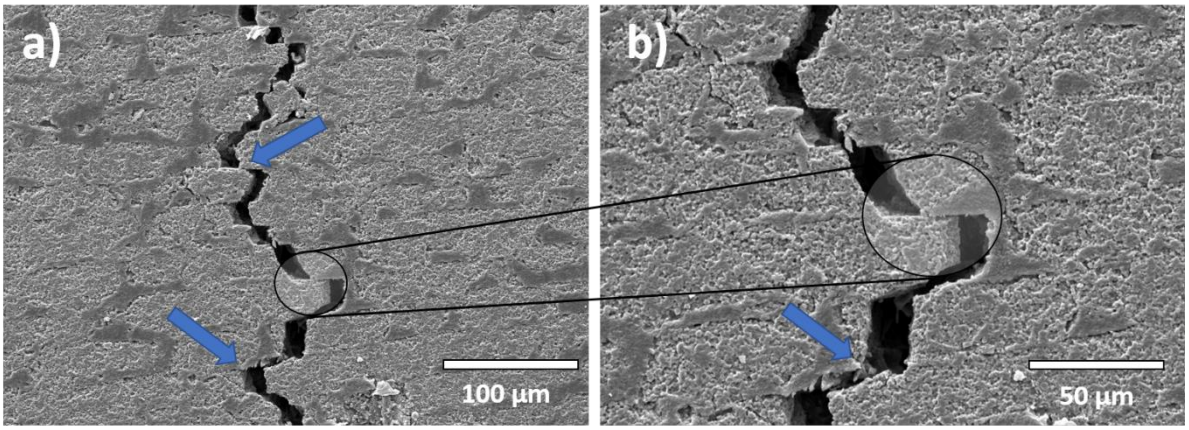

Figure 5-20: SEM images at two different magnifications for the crack propagation line within the composite (first-step sintering temperature 1400°C) following fracture toughness testing. The blue arrows point to some of the crack deflection areas.

By looking at the SEM images, we can see the crack propagated in a tortuous way through the ceramic portion in some areas, and through the ceramic/polymer interface in others. The area inside the circle illustrates where two ceramics bricks have separated and slid over each other (Figure 5-20 b.)

5.3 Discussion

5.3.1 Al_2O_3/MgO ceramic suspension

Alumina is one of the most widely used ceramic powders in the World. It has found widespread use in the industrial, electrical and biological fields due to its good thermal and mechanical properties and ready availability. It also shows high wear resistance and is biocompatible [223].

During the production and processing of ceramic powders, impurities may be introduced, and at high sintering temperatures, these impurities can concentrate forming a thin liquid phase surrounding the ceramic particle. This can lead to abnormal grain growth [238]. In the

present study, MgO was added as a sintering aid to improve alumina densification, prevent abnormal grain growth and thereby improve the scaffold strength. MgO is well known for being a highly effective sintering aid for alumina [213].

The colloidal stability of the ceramic suspension is a key element for successful ceramic freeze casting. A stable suspension leads to the fabrication of a well packed and uniform green body, producing a homogenous ceramic scaffold with desirable mechanical properties and high reliability [239, 240]. In a stable suspension, the ceramic particles are well dispersed inside the solvent, and particle agglomeration does not occur[184]. The surface charge of the particles (the zeta potential of the particles) plays an important role in determining the characteristic of the suspension. The DLVO theory describes how surface charges determine the interaction between the ceramic particles and hence, the suspension stability. If the attractive van der Waals forces are predominant at the expense of the repulsive electrostatic forces, then particle agglomeration will occur, and the opposite is also true [182, 183]. Using dispersants is one way in which to stabilise suspension. Dispersants attach themselves to the ceramic particles and generate a charged double layer. When two particles with the same charge get close to each other, a repulsive force is generated which keeps them apart [186].

An important property of MgO is its strong basic nature, especially when used in an aqueous medium. This property is reflected by its high IEP (pH 10.9) (Figure 5-2). MgO also exhibits high solubility under both neutral and acidic conditions. All of these factors make it difficult to stabilise MgO using the methods conventionally used to stabilise alumina suspension [224]. A different dispersant (Tiron) was, therefore, chosen. Dolapix is a commonly used electrosteric dispersant for alumina; however, when it is used as a dispersant, the repulsive

interparticle forces range is shorter when compared to Tiron, which means that a suspension dispersed with Dolapix has a higher viscosity than one dispersed using Tiron. Even though Dolapix has both electrostatic and steric stabilisation effects, the steric contribution is minimal, and the overall repulsive force is smaller compared to Tiron. Tiron is an anionic electrostatic dispersant, which can disperse both Al_2O_3 and MgO particles by stronger electrostatic charging (higher negative zeta potential) compared to Dolapix[224].

As MgO is highly soluble under neutral conditions and has different surface chemistry compared to Al_2O_3, the order of adding each of the components was important. MgO was initially added to the dispersant solution and mixed for 30 mins before the Al_2O_3 was added. This order of addition ensured the MgO particles had a negative charge before adding the Al_2O_3, which will also be negatively charged (Figures 5-1 and 5-2). This preparation order prevented coagulation between the Al_2O_3 and the MgO when they were then mixed in water [241].

5.3.2 Effect of MgO addition on the ceramic scaffold

The effects of MgO on the grain area (Figure 5-4) and scaffold density (Table 5-2) were very apparent. Abnormal grain growth was clear in the scaffolds prepared without MgO, as can be seen in Figure 5-4 and Figure 5-5, along with a lower density. Conversely, more homogenous grain growth and a higher density were observed in scaffolds prepared with MgO. These results can be explained by the fact that MgO is a highly efficient grain growth inhibitor, and a small addition was sufficient to improve the densification of Al_2O_3 [214]. Several attempts have been made to understand the exact mechanism of how MgO improves the densification and prevents abnormal grain growth, but it is still a highly debatable issue [242].

A possible explanation is the formation of point defects due to the different charges between the aluminium ion (+3) and magnesium ion (+2). These point defects improve the boundary diffusion coefficient and hence, the improvement in the density and limitation of abnormal grain growth [215].

5.3.3 Ceramic scaffold fabrication and characterisation

The fabrication of nacre-like ceramic scaffolds was the first step in the production of the composite material. In the present study, a combination of bi-directional freeze casting and uniaxial pressing was used to fabricate the nacre-like ceramic scaffolds.

5.3.3.1 Effect of first-step sintering temperatures

First-step sintering at different temperatures has pronounced effects on the ceramic scaffold microstructure. Sintering ceramic bodies at higher first-step sintering temperatures makes them stronger, but with fewer interlamellar ceramic bridges between the walls. Under pressure, these strong ceramic bridges can stop the ceramic walls from approaching each other during uniaxial pressing, maintaining greater interlamellar spacing (Figure 5-10 a, b, c, d, e, and Figure 5-11 a, b, c, d, e). In the case of lower first-step sintering temperatures, the interlamellar bridges were weak and collapsed easily under pressure. This allowed the ceramic walls to come closer to each other and consolidate during second-step sintering, producing denser scaffolds (Figure 5-10 f, g, h and Figure 5-11 f, g, h). Moreover, the fact that the grains inside these scaffolds maintain high sintering activity allows them to densify more and play a role in increasing the ceramic volume fraction of the scaffolds. The unsintered green ceramic sample was weak and couldn’t withstand the uniaxial pressing

force at all, and its lamellar structure collapsed completely to produce a dense ceramic after sintering (Figure 5-10 i and Figure 5-11 i).

Burning out the epoxy resin from the infiltrated scaffolds allowed for a better examination of the microstructure. Samples taken from the scaffolds sintered at 1550°C and 1600°C for the first-step sintering turned to powder after the epoxy burning process. This indicates the ceramic walls inside these scaffolds were fully sintered from the first-step sintering, and during uniaxial pressing, they were crushed under pressure into small fragments. In the second-step sintering, the grains were able to consolidate again, but with weak connections that enabled the scaffolds to be removed from the furnace in one piece. However, when they were infiltrated with epoxy resin, polished and cut into small samples to burn out the epoxy resin, these weak connections were broken by the thermal expansion of the epoxy resin during burnout. Therefore, these scaffolds turned into powder. All of the other samples were intact and strong enough to be removed from the furnace, indicating stronger interconnections between the ceramic walls. These connections developed during the second-step sintering, as the grains inside these scaffolds maintained a higher sintering activity compared to grains in scaffolds sintered at 1550°C and 1600°C for the first-step sintering. It can be seen in Figure 5-12 that samples sintered at high first-step sintering temperatures demonstrated greater linear shrinkage. This was to be expected as higher sintering temperatures lead to greater grain consolidation and densification [243]. By looking at Figure 5-8 (showing the grains sizes of all samples), it can be seen that grains start to consolidate and the pores between them decrease in size as the first-step sintering temperature increases. The pores between the grains were almost eliminated when temperatures above 1550 °C were used.

Following second-step sintering, samples that were sintered at lower first-step sintering temperatures showed greater linear shrinkage (Figure 5-12). This was because the sintering activity of the grains was still high for these samples, which allowed them to consolidate more easily, compared to the larger grains in the samples where the first-step sintering temperatures were higher.

Figure 5-13 shows the ceramic volume fraction of fully sintered ceramic scaffolds as a function of different first-step sintering temperatures. It can be seen that decreasing the first-step sintering temperature increases the ceramic volume fraction. This result can be explained by the fact that when a lower first-step sintering temperature is used, the system interfacial free energy remains high, and the grains inside the partially sintered scaffold maintain a higher level of sintering activity. Therefore, after being pressed and sintered in the second-step sintering these grains can further densify, replacing the grain-gas interfaces with grain-grain boundaries, leading to larger shrinkage and higher ceramic volume fraction.

The ceramic volume fractions of the different scaffolds ranged from 64.81% to 82.71%. Launey *et al*. (2009) managed to produce 80 vol.% alumina ceramic scaffolds by using 1500°C as the first sintering temperature, then uniaxial pressing (~ 50-100 MPa) and finally sintering again at 1500°C, followed by isostatic pressing and a third sintering step at the same temperature [17]. Also, Bai *et al*. (2015) managed to fabricate hydroxyapatite scaffolds with 75-85 vol% ceramic content. Bi-directional freeze casting was used to fabricate the highly aligned scaffolds sintered at 1300°C and held for 4 h, followed by uniaxial pressing. The amount of uniaxial pressure used was not mentioned in the paper [18].

5.3.4 Biomimetic nacre-like ceramic/polymer composites

In the present study, we managed to fabricate biomimetic nacre-like ceramic/polymer composite materials. The aim of mimicking nacre is to combine strength and toughness in one material. Bi-directional freeze casting was used to fabricate highly aligned ceramic scaffolds that were uniaxially pressed to break the long lamellar walls into short fragments or “bricks” and to increase the ceramic volume fraction inside the scaffolds. It was possible to produce ceramic scaffolds with a microstructure mimicking that of the bricks of nacre, as shown in Figure 5-9 c. These scaffolds were then silanised and infiltrated with a second phase polymer to produce nacre-like bricks and mortar composite materials.

UDMA/TEGDMA was used as the second phase polymer material in this study. UDMA is the base monomer, and it was mixed with TEGDMA in a 1:1 ratio, based on the work of Okada *et al*. (2014) [244]. UDMA was chosen for a number of reasons, namely: it has a long history of use in dental materials, it is biocompatible, and its low molecular weight allows easier infiltration. Compared to Bis-GMA polymer, UDMA has the advantage of being phenol-ring free, which improves flexibility and toughness. It has higher flexural strength and modulus of elasticity and shows less water absorption [245]. However, using UDMA as a polymer is not without its drawbacks. The monomer is highly viscous and therefore has to be mixed with a diluent monomer such as TEGDMA [246], but the diluent increases the polymerisation shrinkage [247]. This was noticed at the beginning of the study, where the samples were polymerised at a high temperature of 120°C for 2 h [244]. As a result, another heating protocol was followed in which the samples were cured initially at 40 °C and held at this temperature for 2 h, followed by 50°C, 60°C, 70°C, 80°C, 90°C each held for 2 h. Following this heat treatment, the temperature was increased immediately to 120°C and

held for another 2 h. Using a low heating rate of 1 °C/10 min and a long dwell time of 2 h, complete monomer polymerisation was achieved, with reduced shrinkage and fewer visible cracks in the specimens. This heating protocol was modified from the curing cycle used by Chaiyabutr *et al*. (2009)[248].

Various imaging techniques can be used to examine the microstructure of composite materials. Of these techniques, SEM is the most commonly used, and it has been effective in examining different dental composite materials [10, 249]. In this study, SEM was used to examine the effect of ceramic silanisation on the contact between the inorganic ceramic and the organic polymer. In Figure 5-14, the SEM images demonstrate the presence of gaps at the interface between the ceramic phase and the polymer phase when no silanisation was performed on the scaffold. In the case of the silanised specimens, the SEM images show good contact between the two phases, meaning better adhesion [153]. Silane coupling agents work in two ways: firstly, they bond the inorganic ceramic to the organic polymer, and secondly, they improve the wettability of the ceramic surface, allowing better contact between the ceramic and the polymer [250, 251]. Without silanisation the inorganic ceramic is unable to bond to the organic polymer [252]. Also, the absence of a silane coupling agent means that the hydrophobic monomer is unable to wet the hydrophilic ceramic surface, this non-compatibility between the two materials leads to gaps appearing in the interlamellar spacing [250]. Also, Using Piranha solution to treat the scaffold before silanisation leads to micro-etching of the ceramic walls and this contributes to the close adaptation of the monomer to the ceramic [252].

The same result was reported by Munch *et al*. (2008), who reported good adhesion between the alumina ceramic scaffold and PMMA polymer when the scaffold was silanised. Also, the

silanisation improved both the flexural strength and fracture toughness of the final composite material [153].

It is well documented in the dental literature that silane coupling agents improve the bond strength between ceramic based restoration and polymer based material like resin composite or resin cement [253-256].

SEM images were also used to examine the microstructure of the biomimetic nacre-like composite materials. Uniaxial pressing of the lamellar scaffold, followed by sintering, resulted in a brick-like structure, with the polymer phase becoming the mortar between these ceramic bricks. Even though these composite materials have a brick and mortar structure, they are still an order of magnitude larger than nacre. However, mimicking natural materials at a macroscopic scale is a feasible way to fabricate artificial materials with superior mechanical properties [43].

Flaws in ceramic materials such as closed pores or surface cracks have deleterious effects on mechanical properties such as flexural strength and fracture toughness [257]. However, the mechanical properties of composite materials are usually superior to those of the individual pure components [258]. Most dental composite materials are isotropic and composed of discontinuous inorganic fillers dispersed in an organic phase. Therefore, they are not mimicking the anisotropic aligned structure of natural composite materials such as tooth tissue and nacre [20]. In this study, the fabricated ceramic/polymer composites more closely mimic these natural materials in terms of having an interpenetrating polymer network within a continuous porous ceramic scaffold.

The compressive strength of the composites was tested in two directions (z and x) to demonstrate potential anisotropic characteristics. Figure 5-16 shows that increasing the

first-step sintering temperature decreases the compressive strength in the z direction. Although this effect was pronounced in the z direction it was more subtle in the x direction. Nevertheless, using a lower first-step sintering temperature increases the compressive strength in both directions. This is probably explained by the alteration in the ceramic volume fraction and microstructure of the scaffold with changing first-step sintering temperature. As the first-step sintering temperature decreases, so the ceramic volume fraction increases, and the connections between the ceramic walls also increase. It is, therefore, for this reason, scaffolds sintered at a lower first-step sintering temperature demonstrated higher compressive strengths.

As ceramics perform relatively well under compressive loading, especially when applied perpendicular to the ceramic walls (i.e., in the x direction), it was to be expected that the scaffolds might show a higher compressive strength in the x direction compared to the z direction. Indeed, except for the scaffolds sintered at 1300°C and 1250°C, this was found to be the case. In the case of the 1300°C and 1250°C sintered scaffolds, this might be explained by the fusion of the ceramic walls leading to higher compressive strength in the z direction.

Flexural strength (three-point bending test) is a meaningful test used to evaluate composite materials. It measures the maximum stress a material can withstand under bending before fracture [106]. The flexural strength of the composite materials tested in the z direction was in the range of 96.86 to 201.9 MPa (Figure 5-17). This test was done to analyse the effect of first-step sintering temperature on the strength of the final composite, and therefore to determine the optimum temperature to be used in the fabrication of the experimental CAD/CAM material. Decreasing the first-step sintering temperature increases the flexural strength, which agrees with the previous results of the compressive strength testing. The

same explanation for the results can, therefore, be applied here. Scaffolds that were sintered at lower first-step sintering temperatures maintained a higher sintering activity, allowing them to consolidate and densify further during the second-step sintering. As a result, higher ceramic volume fractions and stronger ceramic wall connections were created, leading to a higher flexural strength.

The crack initiation fracture toughness (K_{IC}) test measures the amount of energy that a material can absorb to initiate crack growth [13]. The fracture toughness (K_{IC}) of the fabricated composite materials was determined by testing in the x direction in order to assess the crack propagation path through the brick and mortar microstructure. The observed K_{IC} values were in the range of 1.5 to 3.63 MPa.$m^{1/2}$ (Figure 5-18). The load-displacement curve of the fracture toughness test shows a ductile behaviour of all the fabricated composite materials (at different degrees) except the sample fabricated at 1250°C for the first-step sintering temperature (Figure 5-19). A pure ceramic material would fail with brittle fracture under maximum load, which was not the case with these nacre-like composite materials, suggesting a toughening effect from the ductile polymer phase and the microstructural design. Composites fabricated using high first-step sintering temperatures showed more ductile behaviour (higher displacement) compared to composites fabricated using low first-step sintering temperatures. The composites, fabricated using high first-step sintering temperatures, have higher polymer volume fraction and weakly connected ceramic bricks. These two features enabled the ceramic bricks to slide inside the polymer phase, allowing larger displacement. On the other hand, the composites fabricated using low first-step sintering temperatures have a lower polymer volume fraction and strongly connected ceramic bricks. Here, the stiff ceramic scaffold plays a principal role in defining the composite properties, and this is why these composites show lower flexibility.

Examining crack propagation after fracture toughness testing revealed a tortuous crack path and a crack deflection toughening mechanism. The crack was deflected at the interface between the ceramic and polymer (Figure 5-20). A crack propagating along a tortuous path consumes more energy compared to a straight crack line and means the material is less likely to fail catastrophically. Ceramic bricks sliding is another toughening mechanism, and this was also observed inside the composite material. This frictional sliding is due to the roughness of the ceramic walls, and it helps to resist crack propagation [13].

Although the ceramic volume fraction and internal microstructure of the specimens reported in the present study make it difficult to make a direct comparison with other reported nacre-like composite materials, there are some comparisons that can be made.

Bai *et al*. (2015) fabricated Hydroxyapatite/PMMA nacre-like composites following the same fabrication technique used in this study. The reported flexural strength of the composite material was in the range of 100.8-120 MPa for 75-85 % hydroxyapatite content. The composite material showed stable crack growth due to its bricks and mortar structure [18].

Another interesting nacre-like composite material was fabricated by Launey *et al.* (2009), comprising an alumina/PMMA composite with an 80 vol.% ceramic fraction. The reported flexural strength was 200 MPa and the fracture toughness (K_{IC}) was 5 MPa.$m^{1/2}$. During in situ fracture toughness measurement, different toughening mechanisms were observed within the composite material. These included wide damage distribution due to the inelastic deformation ahead of the crack tip, polymer tearing, ceramic brick sliding and processing void elongation [17].

Synthetic nacre-like hydroxyapatite/epoxy composite fabricated by freeze casting showed good mechanical response under bending force. The load-displacement curve of the

material was similar to that of nacre, indicating that active toughening mechanism within the material led to stable crack growth. A tortuous crack pathway was observed with extensive crack deflection [26].

5.4 Summary

In the present study, ceramic/polymer composite materials were fabricated to mimic the brick and mortar structure of nacre. In the previous chapter, bi-directional freeze casting was used to fabricate highly aligned lamellar ceramic scaffolds by changing the various processing parameters. Following on from the results of the previous chapter, specific parameters were chosen to fabricate highly aligned lamellar ceramic scaffolds to be used in this study. As the ceramic volume fraction of the freeze cast scaffold was low, a densification step was required to increase the ceramic volume fraction, which was achieved by uniaxial pressing. This pressing step also helped to break the long lamellar ceramic walls into small fragments or “bricks”. As it is important to bond the inorganic ceramic to the organic polymer, ceramic scaffold silanisation was necessary. Following salinisation, UDMA-TEGDMA monomer mixture infiltration and polymerisation took place.

Characterisation also involved examining the effect of adding MgO, used to help in alumina densification and prevention of abnormal grain growth. Also, the effect of the dispersant Tiron was investigated. Using Tiron as a dispersant was effective in negatively charging both Al_2O_3 and MgO particles. The optimum concentration of Tiron was 0.1 wt.% as it produced an Al_2O_3/MgO ceramic suspension with the lowest viscosity.

Increasing the first-step sintering temperature resulted in the production of ceramic scaffolds with a lower ceramic volume fraction and lower compressive strength. It also

affected the mechanical properties of the ceramic/polymer composite materials. Sintering ceramic scaffolds at a lower first-step sintering temperature increased the flexural strength of the composites. This was a result of the higher ceramic volume fraction and a greater number of connections within the ceramic microstructure.

The fabricated composite materials showed ductile behavior under fracture toughness testing, except for the sample fabricated at 1250°C for the first-step sintering temperature, which showed a brittle fracture. Different toughening mechanisms were observed inside the specimens tested including crack deflection and ceramic brick sliding. The fabricated biomimetic nacre-like ceramic/polymer composite materials showed combined strength and toughness.

In material fabrication there is a trad-off between different fabrication parameters designed to optimise specific mechanical properties and the resulting compromise in other features and properties. From the results of this chapter it is obvious that decreasing the first-step sintering temperature increases the flexural strength but at the same time reduces the material's displacement under loading. Based on the microstructure results, the ceramic volume fraction, flexural strength and the materials behaviour under loading, 1400°C was chosen as the first-step temperature for the fabrication of the biomimetic ceramic/polymer composites (BCPCs) in the next chapter. Composite fabricated from 1400°C ceramic scaffold has 70 % ceramic volume fraction with disconnected ceramic walls. This composite has good flexural strength (~150 MPa) for dental application and it shows displacement under loading with stable crack propagation.

Chapter 6. Fabrication and mechanical properties of biomimetic nacre-like ceramic/polymer composites for CAD/CAM dental restorations

6.1 Introduction

CAD/CAM technology has become very popular among dentists to fabricate highly aesthetics restorations, and as a result, there has been a flourish of the use of CAD/CAM [2]. The main disadvantage of all ceramic systems is their brittle nature, especially when used in thin sections subject to forces other than compression, e.g., as a veneer. Another potential limitation of ceramic restorations is the wear of the opposing teeth as a result of the hardness of the material [259, 260]. Tougher ceramics, such as alumina and zirconia, have been introduced in an attempt to overcome the issue of brittleness, but they often still undergo catastrophic failure in service[261]. With respect to conventional resin based composites, their use as materials for permanent restorations is still somewhat limited by their polymerisation shrinkage, poor mechanical properties and high wear rate [87, 96].

As a result of the limitations shown by pure ceramics and resin-based composites, there has been a move to try to develop new ceramic/polymer systems, with improved properties that more closely match the mechanical and aesthetic properties of natural tooth tissue.

In 2013, the Vita company launched a new ceramic/polymer interpenetrating phase composite (Vita Enamic, VITA Zahnfabrik, Germany). This material is composed of two interconnected phases, namely a porous ceramic phase infiltrated with a second polymer phase. The ceramic network is a silanised feldspathic ceramic, strengthened by capillary action, with a continuous phase of methacrylate polymer matrix. This commercially

available material has been extensively tested, and the overall results show a promising future for this new type of material [8, 9, 136, 249].

Using CAD/CAM technology, dental restorations can be fabricated within the clinic in one visit, and in a relatively short time frame using fast restoration milling. Ceramic/polymer composites have a lower hardness compared to all ceramic materials [1], and they should, therefore, be even easier to machine. The relationship between material hardness and machinability can be predicted by the Archard wear equation [262].

In the present study, four biomimetic ceramic/polymer composites (BCPCs) were fabricated using the bi-directional freeze casting technique. They were classified according to their ceramic volume fraction. Different uniaxial pressures were used to produce densified scaffolds with different ceramic volume fractions. All were silanised and infiltrated with UDMA/TEGDMA polymer to produce biomimetic nacre-like ceramic/polymer composites. The BCPCs were tested mechanically to assess their suitability as potential chairside CAD/CAM restorative materials. The results were compared to those of commercially available Vita Enamic, pure polymer and a dense ceramic. The machinability of the composite materials was also assessed.

6.2 Results

6.2.1 Fabrication of biomimetic ceramic/polymer composites (BCPCs)

Based on the results of the work described in the previous chapters, the following parameters were used to fabricate the BCPCs, namely:

1. Ceramic solid loading of 20 vol.% of Al_2O_3 and 0.02wt.% with MgO as a sintering aid.
2. PVA binder concentration of 2 wt.% of the ceramic powder weight.

3. A cooling rate of 30°C/min and a mould slope angle of 10°.
4. First-step sintering temperature of 1400°C.
5. Different uniaxial pressures were used to fabricate ceramic scaffolds with different ceramic volume fractions.
6. Second-step sintering temperature of 1550°C.
7. Silanisation of the scaffold with MPS.
8. UDMA/TEGDMA was used as the polymer phase.

As the pressure applied to the ceramic scaffolds during uniaxial pressing might affect the microstructure and hence the mechanical properties, the effects of four different pressures (100, 150, 200, and 250 MPa) were also studied.

6.2.1.1 The effect of uniaxial pressure on the microstructure and ceramic volume fraction of the densified ceramic scaffold

During uniaxial pressing, the ceramic scaffold walls are under compression, which can affect their integrity. Figure 6-1 shows the SEM images of epoxy infiltrated scaffolds fabricated under four different pressures. These images demonstrate how increasing the uniaxial pressure leads to breakages within the ceramic walls, resulting in shorter length bricks. Figure 6-1 b shows that using 100 MPa pressure, the ceramic scaffold walls are better maintained when compared to higher pressure applications (Figure 6-1e, h, and k). With increasing pressure, the interlamellar spacing was observed to reduce (Figure 6-1 c, f, i, l)

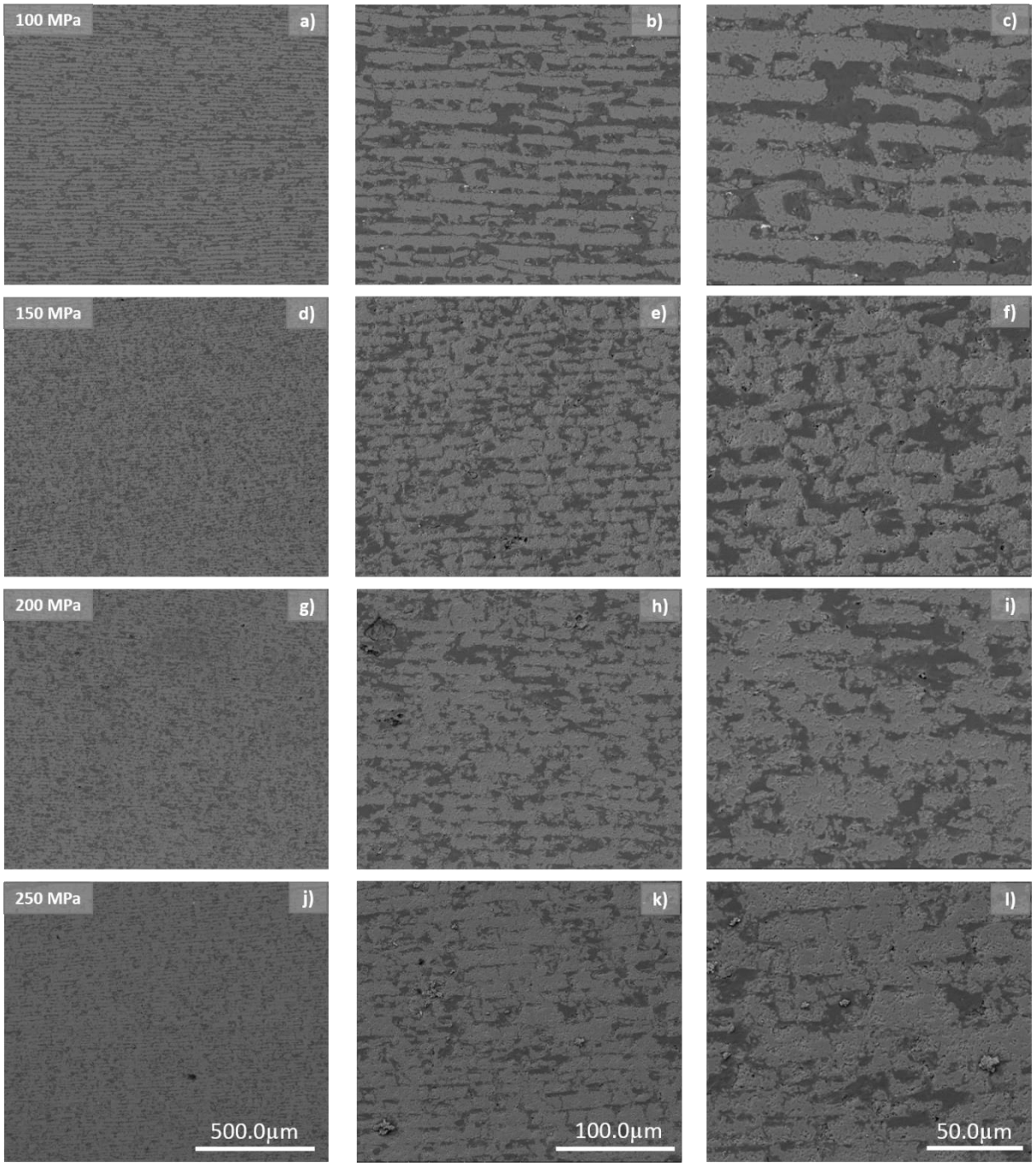

Figure 6-1: SEM images of the epoxy infiltrated densified ceramic scaffolds prepared using different uniaxial pressures (100 MPa; a, b and c, 150 MPa; d, e and f, 200 MPa; g, h and i, 250 MPa; j, k and l) at different magnifications.

Figure 6-2 shows the effect of different pressure on the ceramic volume fraction. Increasing the pressure from 100 MPa to 250 MPa increases the ceramic volume fraction from about

70% to 76%. As expected, the higher the pressure used to compress the scaffolds, the lower the interlamellar spacing, and hence the higher the ceramic fraction.

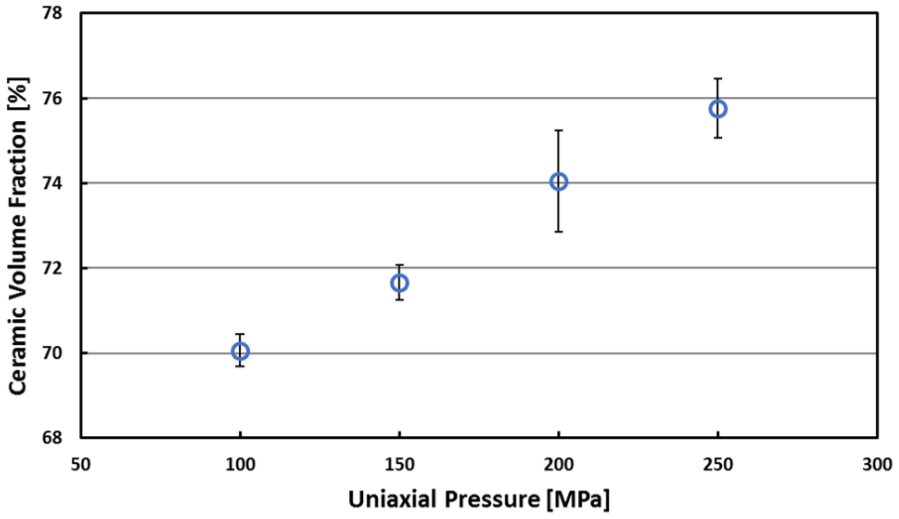

Figure 6-2: Mean and SD of ceramic volume fraction of densified ceramic scaffolds prepared using different uniaxial pressures.

Ceramic scaffolds with four different ceramic volume fractions (~70, 72, 74, 76 %) were silanised and infiltrated with UDMA/TEGDMA polymer to fabricate biomimetic ceramic/polymer composites (BCPCs).

6.2.2 Mechanical properties of BCPCs, dense ceramic, pure polymer and Vita Enamic

Dense ceramic and pure UDMA/TEGDMA polymer samples were fabricated (as described in Chapter 3, Page 79) for mechanical testing alongside samples of Vita Enamic (0 M1-T, EM-14) (Vita Zahnfabrik, Germany) and the BCPCs. Due to the anisotropic structure of the experimental BCPCs, the mechanical properties were tested from two directions (z and x), as illustrated in Figure (3-15). The results of the mechanical testing of the BCPCs, dense ceramic, pure polymer and Vita Enamic are presented in Table 6-1

	Polymer	Vita Enamic 75vol%*	Direction	BCPC 1 70vol%	BCPC 2 72vol%	BCPC 3 74vol%	BCPC 4 76vol%	Dense ceramic 100vol%
Flexural strength (SD) [MPa]	63.11 (7.11)	128.26 (7.02)	z	145.77 (13.84)	154.12 (12.58)	160.06 (6.61)	172.65 (15.25)	391.99 (57.10)
			x	135.08 (10.07)	145.12 (16.6)	148.37 (7.78)	164.71 (9.71)	
Elastic modulus (SD) [GPa]	2.20 (0.11)	25.32 (1.13)	z	61.22 (7.72)	69.07 (5.16)	89.58 (5.35)	105.4 (20.9)	171.68 (17.62)
			x	57.75 (2.37)	64.58 (0.53)	67.77 (6.23)	75.05 (3.9)	
Hardness (SD) [GPa]	0.18 (0.00)	2.31 (0.23)	z	3.07 (0.30)	3.72 (0.31)	4.01 (0.11)	4.57 (0.12)	16.55 (0.42)
			x	3.36 (0.23)	3.82 (0.39)	4.19 (0.22)	4.58 (0.22)	
Fracture toughness (SD) [MPa.m$^{1/2}$]	1.6 (0.17)	1.36 (0.23)	x	2.54 (0.19)	2.69 (0.32)	3.12 (0.38)	3.19 (0.00)	3.7 (0.01)

Table 6-1: Mean and SD of measured mechanical properties of the polymer, Vita Enamic, BCPCs and dense ceramic.(* Based on the manufacturer's information [136])

6.2.2.1 Flexural strength and elastic modulus

The flexural strengths and elastic moduli of the materials under test are presented in Table 6-1. With increasing ceramic volume fraction, the flexural strength of the BCPCs increased from 145.77 to 172.65 MPa in the z direction and from 135.08 to 164.71MPa in the x direction.

A linear regression analysis was used to investigate the mean flexural strength results tested in the z and x directions (Figures 6-3 and 6-4). The flexural strength of dense ceramic was 391.99 MPa plotted as 100% ceramic volume fraction on the x-axis. The measured flexural strength of Vita Enamic was 128.26 MPa, which is lower than that of the tested BCPCs. The flexural strength of the BCPCs increased with increasing ceramic volume fraction. This was confirmed by the positive regression coefficient of the linear regression equation (8.51). The R-Square (R^2> 0.99) shows the good fit of the measured values (mean flexural strengths) around the linear regression model, which in this case is the relationship between the ceramic volume fraction and the flexural strength. This was the case when the flexural strength measured in both directions.

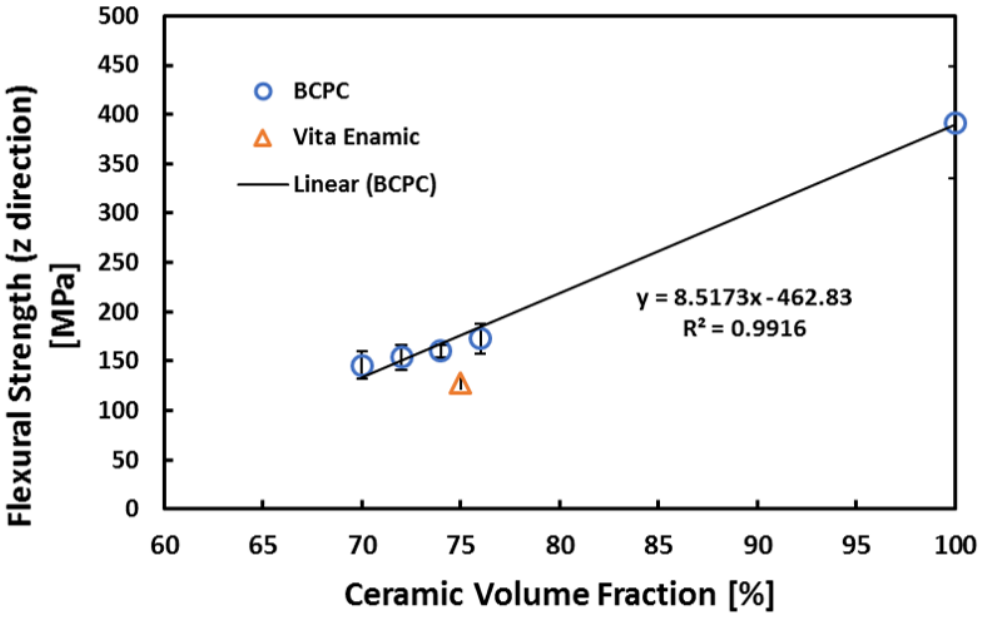

Figure 6-3: Comparison of mean and SD of flexural strength [MPa] of four BCPCs (tested in the z direction), dense ceramic (100% on x-axis) and Vita Enamic (75% on the x-axis).

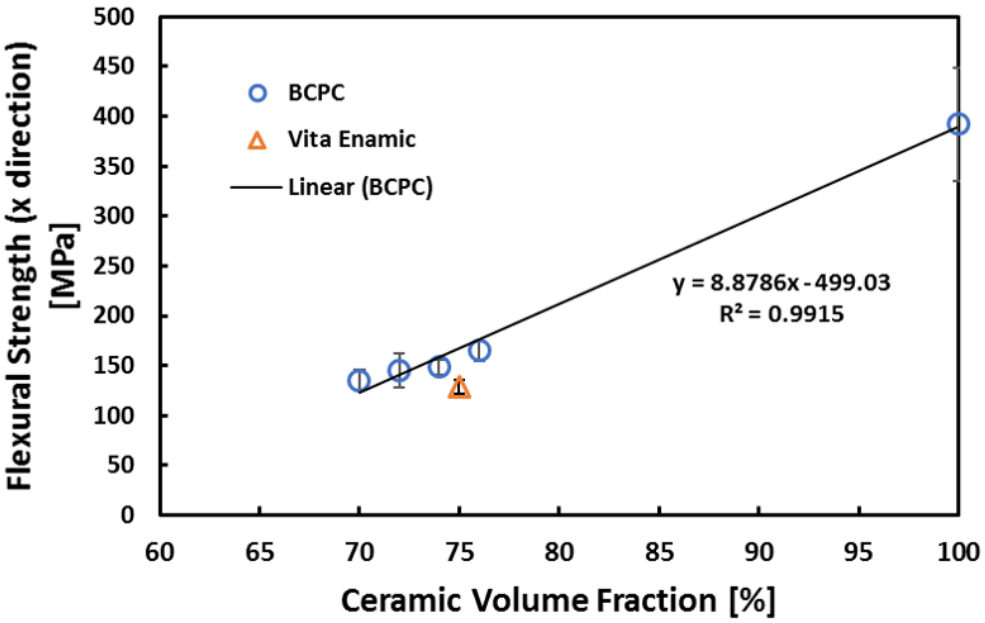

Figure 6-4: Comparison of mean and SD of flexural strength [MPa] of four BCPCs (tested in the x direction), dense ceramic (100% on x-axis) and Vita Enamic (75% on the x-axis).

An interesting observation was that all flexural strength test specimens for the BCPCs remained in one piece following testing, while all of the Vita Enamic test specimens fractured into two pieces (see Figure 6-5).

Figure 6-5: Specimens for BCPC4 and Vita Enamic after testing to failure. Note that the BCPC4 specimen is still in one piece, while the Vita Enamic specimen has fractured into two.

When considering the elastic moduli of the BCPCs, it would seem that increasing the ceramic volume fraction increases the elastic modulus when tested in both the z and x directions (Table 6-1). The values were ranging from 61.22 to 105.4 GPa in the z direction and from 57.75 to 75.05 in x direction. By contrast, the mean elastic modulus of the dense ceramic was 171.68 GPa; it was 25.32 GPa for Vita Enamic and 2.02 GPa for the pure polymer. Figures 6-6 and 6-7 illustrate the mean elastic modulus relative to the ceramic volume fraction of the BCPCs in the z and x directions. For comparison, the mean elastic modulus of the dense ceramic (100% on the x-axis), the pure polymer (0% on the x-axis) and Vita Enamic (75% on the x-axis) are also included. An exponential regression analysis equation was used to fit the wide range of data. R^2>0.98 shows the good fit of the measured values (mean elastic moduli) around the exponential regression model, which is, in this case, the relationship between the ceramic volume fraction and the elastic modulus. This was the

case when the elastic modulus was measured in both directions. It can be seen that the mean elastic modulus values of the BCPCs were much higher than the elastic modulus of Vita Enamic, which was 25.32 GPa.

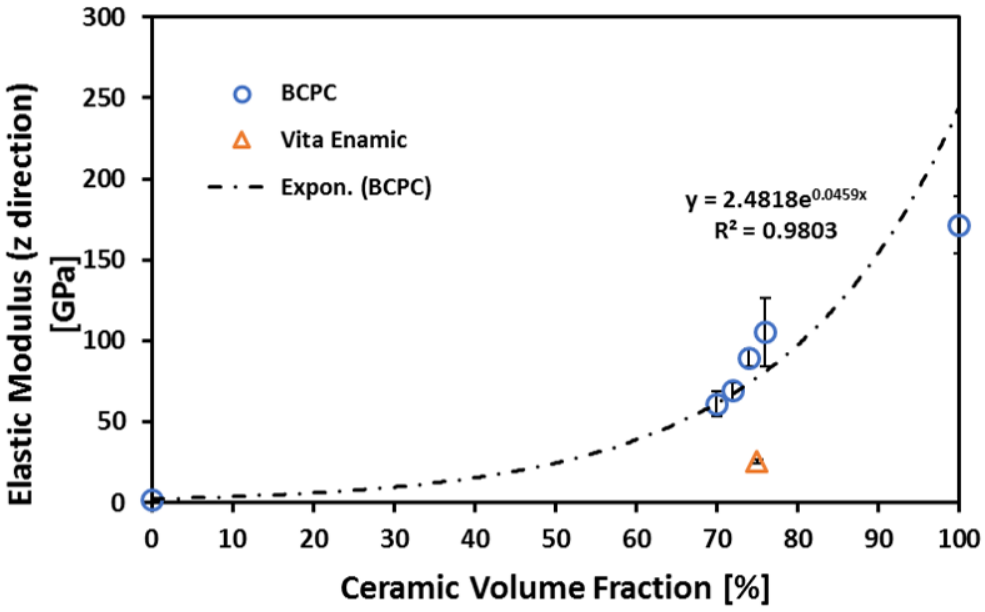

Figure 6-6: Comparison of mean and SD of elastic modulus [GPa] of four BCPCs (tested in the z direction), pure polymer (0% on x-axis), dense ceramic (100% on x-axis) and Vita Enamic (75% on the x-axis).

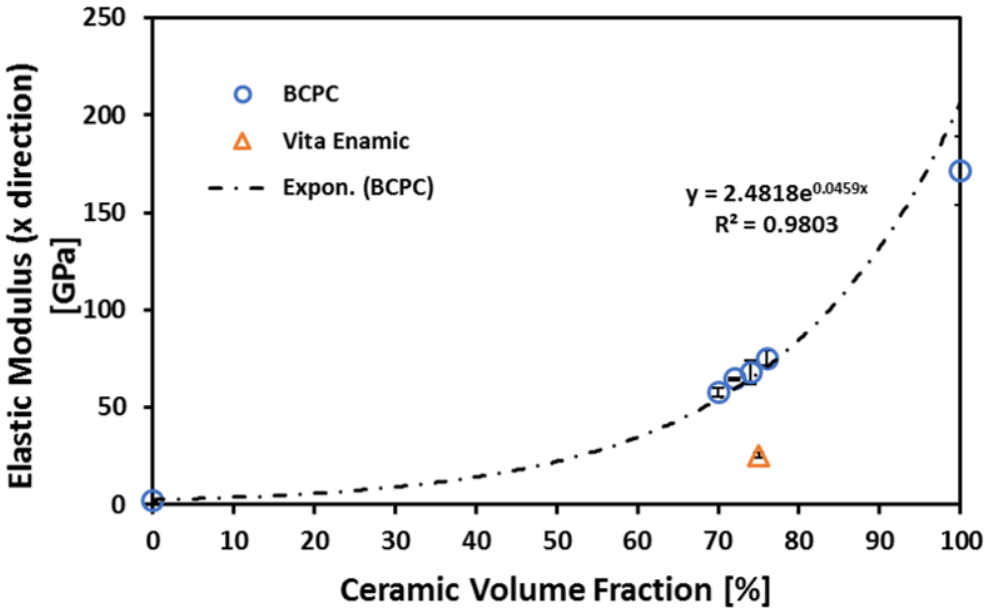

Figure 6-7: Comparison of mean and SD of elastic modulus [GPa] of four BCPCs (tested in the x direction), pure polymer (0% on x-axis), dense ceramic (100% on x-axis) and Vita Enamic (75% on the x-axis).

6.2.2.2 Vickers Hardness

The hardness values of the tested materials are presented in Table 6-1. The results show that the hardness of the BCPCs ranged between 3.07 to 4.57 GPa in the z direction and from 3.36 to 4.58 GPa in the x direction. Figures 6-8 and 6-9 illustrate the mean hardness values of the BCPCs plotted against the ceramic volume fraction in the z and x directions, respectively, along with the mean hardness of the pure polymer (0% on the x-axis), dense ceramic (100% on the x-axis) and Vita Enamic (75% on the x-axis). It can be seen that by increasing the ceramic volume fraction of the BCPCs, the hardness values increased exponentially in both directions. An exponential regression analysis equation was used to fit the wide range of data. R^2>0.99 shows the good fit of the measured values (mean hardness) around the exponential regression model, which in this case, is the relationship between the ceramic volume fraction and the hardness. This was the case when the hardness was

measured in both directions. The mean hardness value for Vita Enamic was 2.31 GPa, which is lower than the hardness values for each of the BCPCs.

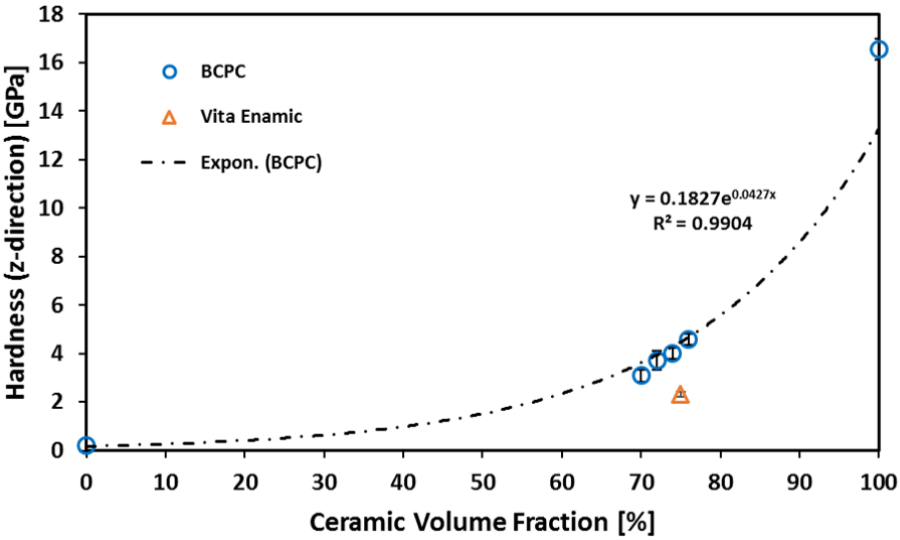

Figure 6-8: Comparison of mean and SD of Vickers hardness [GPa] of four BCPCs (tested in the z direction), pure polymer (0% on x-axis), dense ceramic (100% on x-axis) and Vita Enamic (75% on the x-axis).

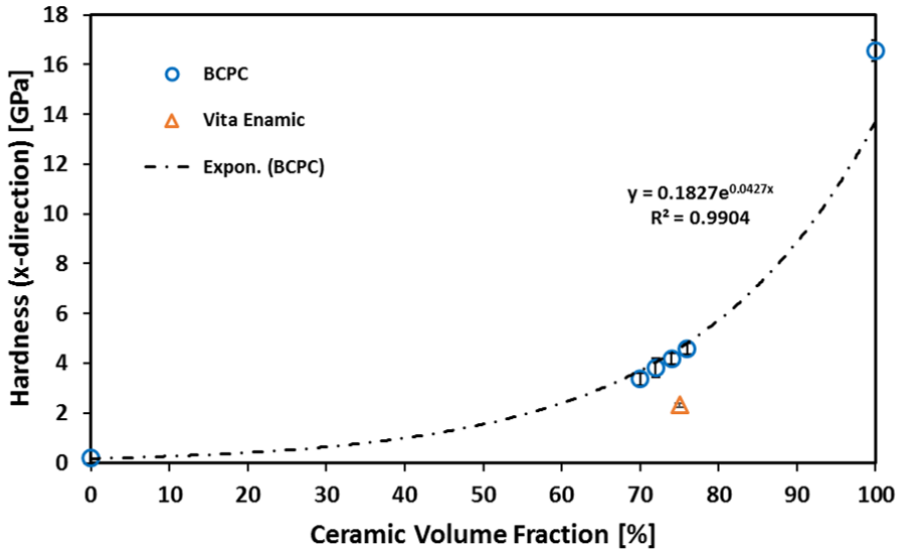

Figure 6-9: Comparison of mean and SD of Vickers hardness [GPa] of four BCPCs (tested in the x direction), pure polymer (0% on x-axis), dense ceramic (100% on x-axis) and Vita Enamic (75% on the x-axis).

6.2.2.3 Fracture toughness (K_{IC})

The mean and standard deviation values for fracture toughness K_{IC} of the tested materials are presented in Table 6-1. For the BCPCs tested in the x direction, the fracture toughness K_{IC} showed a tendency to increase with increasing ceramic volume fraction, ranging from 2.54 to 3.19 MPa.m$^{1/2}$.The mean fracture toughness of the dense ceramic was 3.7 MPa.m$^{1/2}$ and for the pure polymer, it was 1.6 MPa.m$^{1/2}$. The fracture toughness K_{IC} of Vita Enamic was 1.36 MPa.m$^{1/2}$, which was the lowest measured value of all the materials under test. Figure 6-10 shows the mean fracture toughness K_{IC} values of all the materials plotted against ceramic volume fraction.

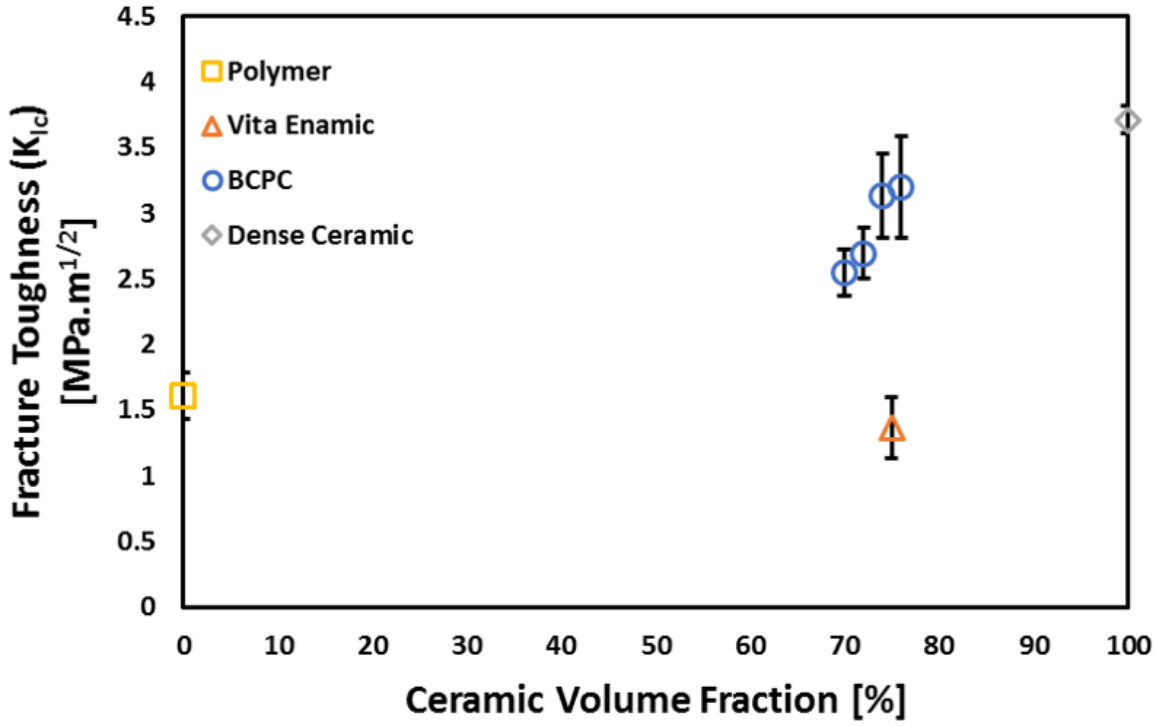

Figure 6-10: Comparison of mean and SD of fracture toughness (K_{IC}) [MPa.m$^{1/2}$] of four BCPCs (tested in the x direction), pure polymer (0% on x-axis), dense ceramic (100% on x-axis) and Vita Enamic (75% on the x-axis).

Figure 6-11 shows the load versus displacement curve for each of the materials following fracture toughness testing. It can be seen the curves varied between each of the different materials. The pure polymer specimen showed the highest displacement of up to 0.21mm (not shown completely in the graph) and was the most ductile of the materials on the test. The BCPCs showed greater displacement and, therefore, greater ductility when compared to Vita Enamic. Both the Vita Enamic and the dense ceramic specimens behaved in a much more brittle manner. With the load-displacement curve showing a sharp drop after reaching maximum load, particularly in the case of the dense ceramic, and similarly although not quite so drastic in the case of the Vita Enamic. Although there was a small toughening in the case of Vita Enamic, crack propagation was not as stable as was seen with the BCPCs. In the case of all the BCPCs, once the peak load had been reached, there was a more gradual reduction of load with respect to displacement, indicating more stable crack propagation.

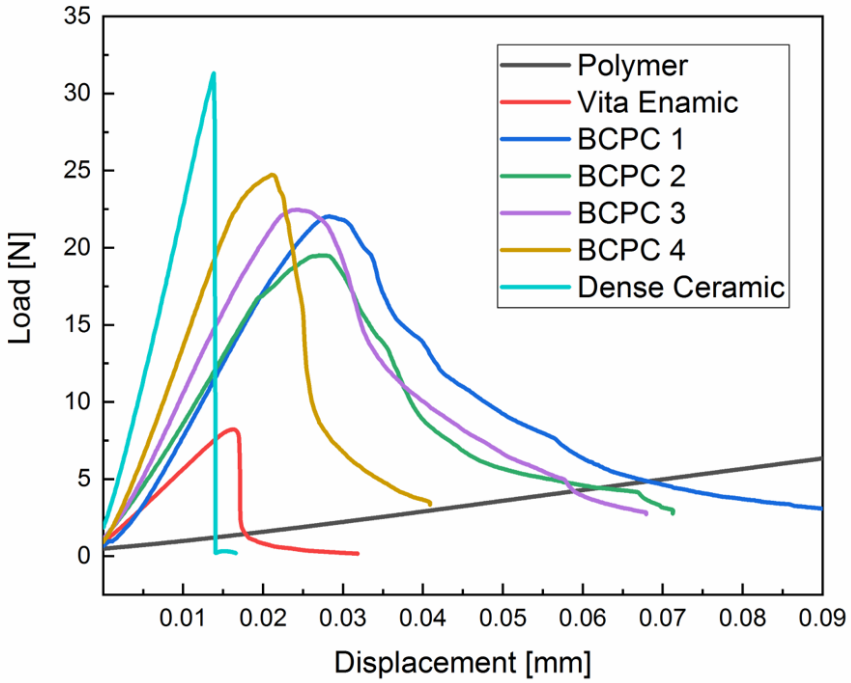

Figure 6-11: Load-displacement curves of each of the materials under test. (The polymer curve (black in colour) is not shown completely in the graph due to the high displacement of the polymer, up to 0.21 mm)

SEM images showing the crack propagation pathways induced during fracture toughness testing of the dense ceramic, BCPC1 and Vita Enamic can be seen in Figure 6-12. It is clear that for both the dense ceramic and Vita Enamic specimens, the crack propagated along a relatively straight line. By contrast, the crack pathway was much more tortuous in the case of the BCPC1 specimen, indicating the presence of a crack deflection toughening mechanism.

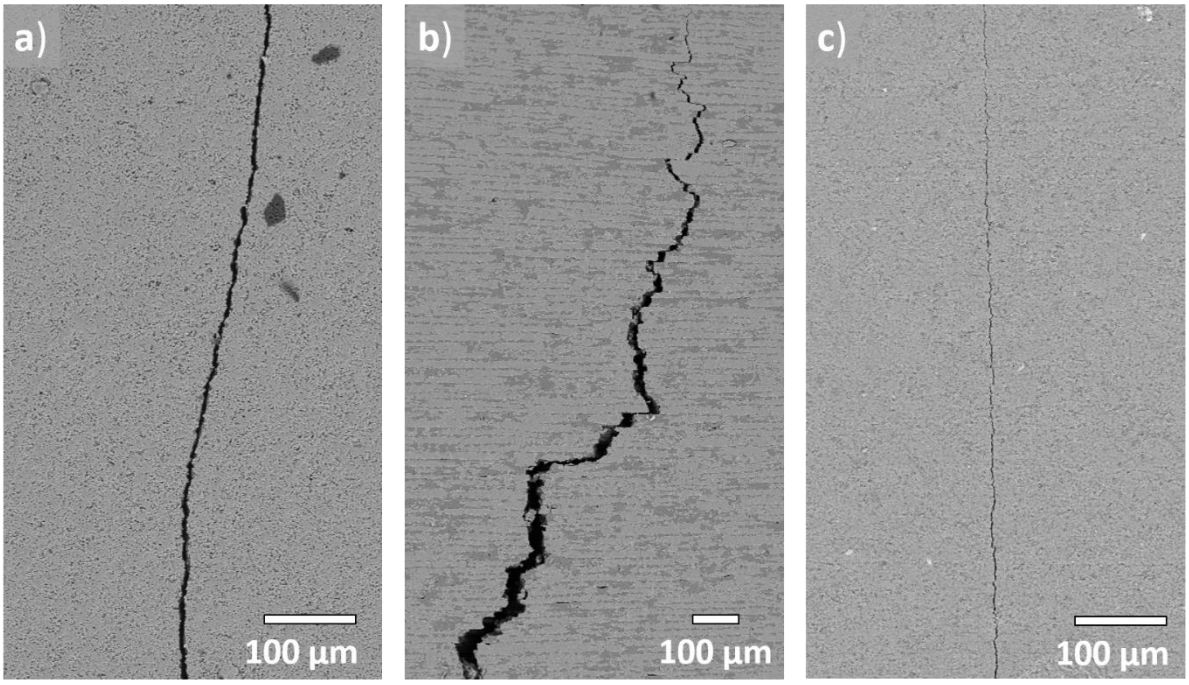

Figure 6-12: SEM images for crack propagation following fracture toughness testing of a) dense ceramic, b) BCPC1, c) Vita Enamic.

6.2.3 Machinability

A single sample of BCPC4 and one of Vita Enamic were CNC machined as part of this research. BCPC4, with its 76% ceramic volume fraction, was chosen for testing as it demonstrated the greatest hardness values of the BCPCs produced in this study. It was considered that if BCPC4 could be successfully machined, then the other BCPCs should also

be readily machinable. Figure 6-13 shows SEM images for BCPC4 and Vita Enamic surfaces after machining. It can be seen that both materials are machinable and that both have relatively rough surface finishes after milling with a diamond bur, although this roughness appeared less pronounced at the relatively smooth edges, as shown in Figure 6-14.

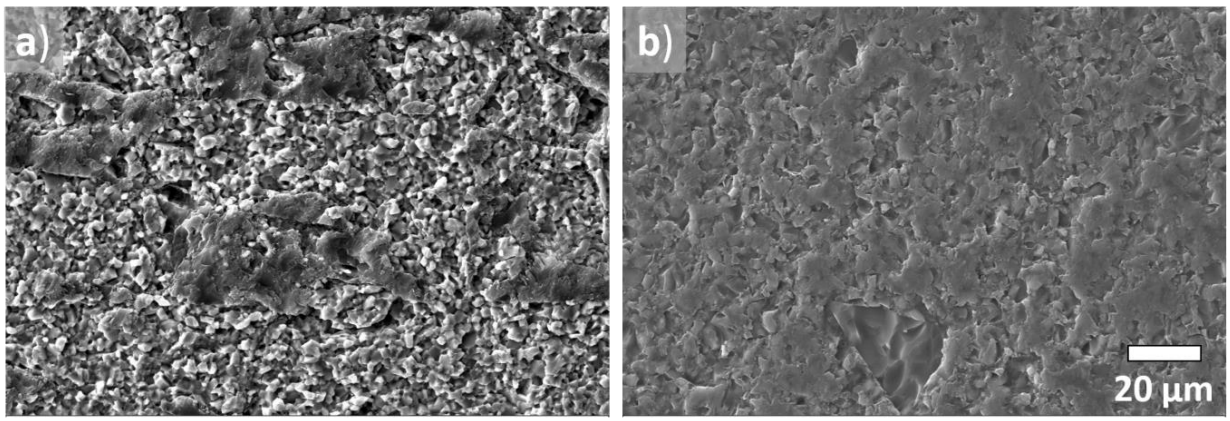

Figure 6-13: SEM images showing the machined surfaces of a) BCPC4 and b) Vita Enamic.

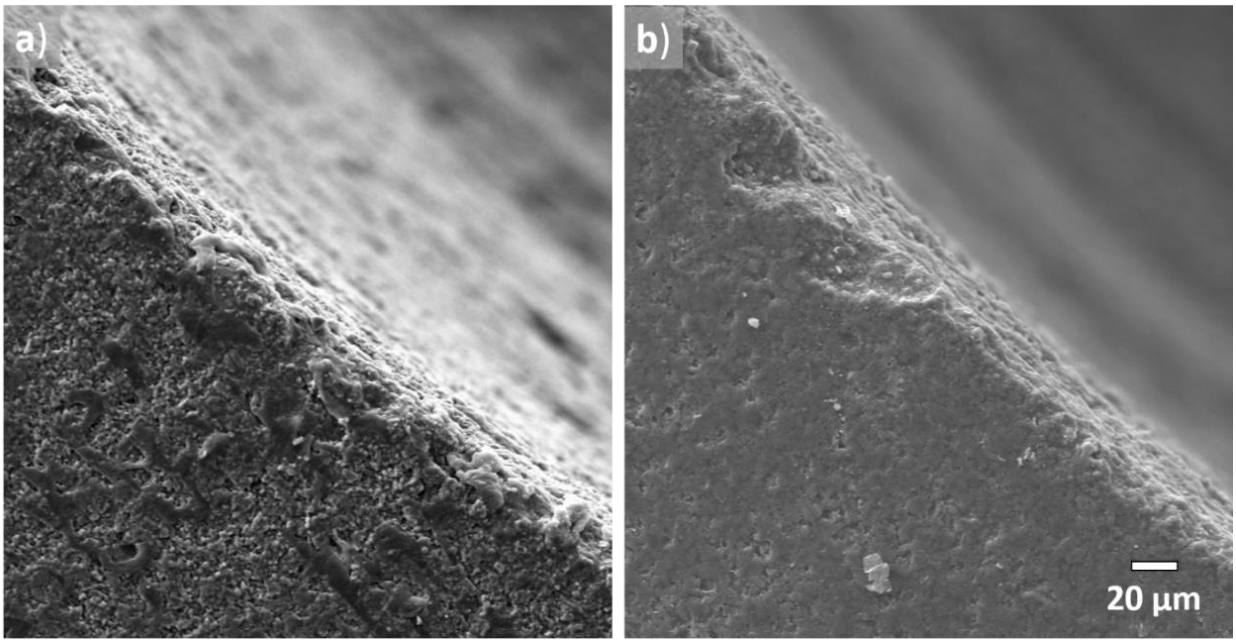

Figure 6-14: SEM images showing the machined edges of a) BCPC4 and b) Vita Enamic.

6.3 Discussion

In the present study, novel biomimetic ceramic/polymer composites (BCPCs) with different ceramic volume fractions were fabricated to investigate their mechanical properties. These properties were compared to the benchmark commercially available material Vita Enamic, along with the natural tooth structure.

The mechanical properties (flexural strength, elastic modulus and hardness) of the fabricated BCPCs were tested from two directions (z and x directions). This was done to investigate the anisotropic properties of the materials and to see whether they would be suitable as CAD/CAM restorative materials. Material testing was not carried out in the y direction as the microstructure was the same as for the z direction.

The ceramic volume fraction influenced the measured mechanical properties of the BCPCs. A high ceramic volume fraction implies a high flexural strength, fracture toughness (K_{IC}), elastic modulus and hardness.

Flexural strength (three-point bending test) is a meaningful test used to evaluate composite materials. It measures the maximum stress a material can withstand under bending before fracture [106]. The mean flexural strength of the dense ceramic was 391.99 MPa, whereas, for the pure polymer, it was 63.11 MPa. The flexural strength of the BCPCs (from both directions) was in between (Table 6-1). This suggests a reinforcement mechanism by the stronger ceramic phase when compared to the single phases tested as bulk structures [263]. This effect has been reported with more traditional dental composite materials [264].

All of the BCPCs under test showed higher flexural strengths in both directions when compared to the commercially available Vita Enamic. Even the BCPCs that had a lower

ceramic content compared to Vita Enamic showed a higher flexural strength. This might be explained by the fact that the ceramic network of Vita Enamic is mainly composed of amorphous glass silicon oxide (58-63 wt.%) with just 20-23 wt.% alumina [265], while the ceramic scaffold of the BCPCs is composed of almost 100 wt.% alumina. It is well documented in the literature that pure alumina based dental materials are much stronger than amorphous glass silicon oxide dental materials [23, 138, 141, 266, 267].

The results of the current research are comparable to the results reported by Okada *et al*. (2014) for dental CAD/CAM composite resin blocks (110 to 200 MPa) [244]. In their work, they used a different method to fabricate the composite material, namely press moulding of the silica filler followed by monomer infiltration [244]. In another study by Coldea *et al*. (2013), the reported flexural strength of their experimental CAD/CAM polymer infiltrated ceramic network ranged from 125 to 160 MPa [10], which again is comparable to the values reported in this study.

Interesting results were reported by Petrini *et al*. (2013) for freeze cast ceramic infiltrated by epoxy polymer. The reported flexural strengths of 183 to 213 MPa are higher than the BCPCs in the current study, which might be a result of using platelet alumina to improve the mechanical properties.

Al-Jawoosh *et al*. (2018) reported the flexural strength of UDMA/TEGDMA infiltrated freeze cast uni-directional alumina scaffolds of 97.73 to 145.65 MPa [21], which is lower than the values of the BCPCs. Even though the principal components of the scaffolds were the same as in this study, the difference in flexural strength can be attributed to different fabrication techniques, namely uni-directional vs. bi-directional freeze casting. Also, the uniaxial pressing of the scaffolds in this study increases the ceramic volume fraction and hence the

higher flexural strength. This will inevitably lead to different scaffold microstructures and hence different mechanical properties.

Li and Sun (2018) fabricated hybrid polymer-infiltrated ceramic-network (PICN) zirconia dental materials for CAD/CAM dental applications. The reported flexural strengths of the samples sintered at 1300 °C ranged from 106.81 MPa to 211.77 MPa. These values are close to the flexural strength range of the BCPCs fabricated in this study [268].

Tan et al. (2019) reported the first brick and mortar nacre-like zirconia/methacrylate resin composite material and introduced it as human tooth matching material. The reported flexural strength was (~190 MPa), the elastic modulus was (42 GPa), the hardness (3.1 GPa) and fracture toughness K_{IC} of (6.3 MPa $m^{1/2}$). The material showed good dissipation of applied load due to the viscoelastic nature of the composite. Also, stable crack propagation was observed due to the microstructure of the composite [162].

The BCPC flexural strength values were higher than those of enamel (60-90 MPa) [62] but much lower than those of dentine (245-280 MPa)[47]. These results would suggest that the BCPC materials, when bonded to dentine, might show a uniform strain response under loading [107].

The fact that all of the BCPC flexural strength test specimens remained intact following mechanical testing indicates that these materials are less brittle than pure ceramic. This is most probably due to the brick and mortar microstructure (Figure 6-5). This would suggest such a material would be less likely to suffer from a catastrophic failure in clinical use.

Regression analysis can be used as a statistical analysis tool to measure the relationship between a dependent variable and one or more independent variables. In this study, simple

regression analysis was used as there was one independent variable, the ceramic volume fraction. The dependent variable was either the flexural strength, elastic modulus or hardness. Linear regression analysis was used to fit the flexural strength data into a model. The regression model equation represents the relationship between the flexural strength and the ceramic volume fraction, and it was a positive linear relationship. This result disagrees with Coldea *et al*. (2013), who reported a negative linear relationship between ceramic ratio and the flexural strength of the hybrid composite material [10]. This might be due to the fact the flexural strength of the used polymer was higher than the dense feldspar ceramic. Therefore, as the ceramic ratio decreased, the polymer ratio increased as did the flexural strength. However, the results of the present study are in agreement with the result of Li and Sun (2018), where the reported flexural strength of the composite materials increased as the ceramic ratio increased [268].

Elastic modulus is a parameter used to describe the elasticity of a material under an applied load. Stiff materials, like ceramics, have a higher elastic modulus, while flexible materials, like polymers, have a lower elastic modulus [269].

The elastic moduli of the BCPCs were in the range of 57.75-105.4 GPa, lying between that of pure polymer (2.2 GPa) and dense ceramic (171.68 GPa) (Table 6-1). With increasing the ceramic volume fraction from 70% to 76%, the elastic modulus increased from 61.22 to 105.5 GPa in the z direction, and from 57.75 to 75.05 GPa in the x direction. All these values were much higher than those of other polymer composite materials, e.g., polymer infiltrated ceramic networks (16-28 GPa) [10], filler resin composite (8-10 GPa) [244] and Vita Enamic (25.32GPa). This can be due to the high modulus alumina network compared to the glassy network present in Vita Enamic. Also, in the filler resin composite, the fillers are

dispersed within the resin matrix without interconnections. The BCPC elastic modulus values were similar to the values reported for hybrid polymer-infiltrated ceramic-network (PICN) zirconia dental materials (40.2–100.5 GPa) [268]. As might be expected, the elastic moduli of the BCPCs were much lower than most CAD/CAM ceramic blocks such as In-Ceram AL (300 GPa), E.max ZirCAD (~210 GPa) and E.max CAD (~105 GPa) [123, 270], all of them comprise dense ceramic without a second polymer phase.

Materials with a very high elastic modulus, such as a dense ceramic, absorb less stress during mastication, leading to stress concentration at the interface between the restoration and the tooth due to an elasticity mismatch [268, 271]. The elastic modulus of the BCPCs was in the range of enamel (48-105 GPa) [63, 64]. The lower the elastic modulus, the better the stress distribution during mastication[272].

The Vickers hardness test results indicate that increasing the ceramic content in the BCPCs leads to a greater hardness (Table 6-1), with values of 3.07-4.58 GPa. These were in the range of the enamel hardness (3.4-5.4 GPa) reported by both He and Swain (2007) [67] and also by Min *et al*. (2016) [66]. The hardness values of the BCPCs were also between those of the pure polymer (0.18 GPa) and dense ceramic (16.55 GPa). They would appear to be closer, in terms of mechanical properties, to natural teeth than other currently commercially available CAD/CAM ceramic restorations. This is important as pure alumina-based materials risk abrading opposing tooth structure due to their increased hardness [273, 274]. In addition, these new BCPC composite materials will be easier to machine, reducing machining time and extending machine bur life [275].

For Vita Enamic, the observed hardness in this study was 2.31 GPa, which is in agreement with the work of Spitznagel *et al*. (2018) [9]. The hardness of Vita Enamic was slightly lower

than that of enamel (3.4-5.4 GPa) [66, 67], which might lead to problems of restoration wear when in masticatory contact with enamel.

An exponential regression analysis was used to fit the elastic modulus and hardness data into a model. The regression model equation represents the relationship between the elastic modulus, or the hardness, and the ceramic volume fraction. In both cases, it was a positive exponential relationship with high R-squared values. A higher ceramic volume fraction leads to an increase in both elastic modulus and hardness, which is to be expected. Ceramic itself is a stiff, hard material, so as the ceramic ratio inside the composite material increases, it plays a major role in determining the properties of the final composite, increasing both elastic modulus and hardness. These results agree with the results reported by other groups of workers [10, 21, 163, 268].

The crack initiation fracture toughness (K_{IC}) test measures the amount of energy that a material can absorb to initiate crack growth [158]. In the case of dental restorations, fracture toughness is very important as it will be related to the ability to resist unwanted failure while in function [276]. The mean values of fracture toughness (K_{IC}) of the BCPCs were in the range of 2.54-3.19 MPa.$m^{1/2}$, which was affected by the ceramic volume fraction (Table 6-1). The Vita Enamic fracture toughness (K_{IC}) of 1.36 MPa.$m^{1/2}$ was lower than all of the BCPC values and within the range of the reported values [136, 148]. Although the fracture toughness (K_{IC}) of dense ceramic was higher than that of the composite material during the crack initiation stage, the load-displacement curve in Figure 6-11 shows a typical brittle behaviour of dense ceramic accompanied with minimum displacement and complete absence of plastic deformation. This means that the crack growth inside the dense ceramic does not consume further energy to fully propagate [13]. Also, the SEM image of the nearly

straight crack pathway in the dense ceramic (Figure 6-12, a.) demonstrates the brittle behaviour of the material compared to the BCPC composite (Figure 6-12, b.). The dense ceramic material was mainly composed of alumina, which is well known for its internal, strong covalent bonds. Under load, these bonds prevent specimen deformation by dislocation such that when the maximum elastic stress has been reached, brittle fracture occurs by cohesive bond failure [277]. Moreover, the load-displacement curve (Figure 6-11) shows that the BCPCs are more ductile compared to Vita Enamic, and their curves are between those of the dense ceramic and pure polymer. These results demonstrate that the addition of polymer as a ductile second phase contributes to the toughening mechanism inside the composite.

The fracture toughness (K_{IC}) of enamel and dentine are in the range of 0.67-0.95 MPa.$m^{1/2}$ [65] and 2.2-3.1 MPa.$m^{1/2}$ [69, 70] respectively. The fracture toughness (K_{IC}) values of the BCPCs were comparable to that of dentine, meaning the composite materials should be able to absorb energy in a manner similar to natural tooth tissue before failure. The fracture toughness (K_{IC}) of polycrystalline alumina (Vita In-Ceram AL) and polycrystalline Zirconia (e.Max ZirCAD) are 3.6 MPa.$m^{1/2}$ [149] and 4.87 MPa.$m^{1/2}$ [148] respectively. Certainly the reported fracture toughness values in this study are comparable to the values reported for other ceramic/polymer composite materials by Chaiyabutr *et al*. (2009) (2.48-3.43 MPa.$m^{1/2}$) [248], slightly higher than those reported by Coldea *et al*. (2013) (1.0-1.5 MPa.$m^{1/2}$) [107]and Della Bona *et al*. (2014) (1.09 MPa.$m^{1/2}$) [249] and lower than those reported by Al-Jawoosh *et al*. (2018) (3.91-4.86 MPa.$m^{1/2}$) [21] and Launey *et al*. (2009) (3.1-5.1 MPa.$m^{1/2}$) [17].

The SEM images of the crack propagation paths (Figure 6-12) demonstrate the possible toughening mechanism inside the BCPCs, namely, crack deflection. This means that more energy has to be absorbed in order to get the crack to fully propagate through the material. The path of crack propagation in the Vita Enamic crack specimen resembled that of the dense ceramic, with the crack propagating in pretty much a straight line. The brick and mortar structure inside the BCPCs, which is not present in the commercially available ceramic/polymer composite Vita Enamic, would appear to be beneficial to the fracture toughness. The fracture toughness was increased sufficiently to make the BCPCs useful as potential CAD/CAM restorative materials.

The unique brick and mortar microstructure inside the composite materials in this study were achieved by bi-directional freeze casting and uniaxial pressing. There were; therefore, three toughening mechanisms present within the BCPCs, unlike the isotropic Vita Enamic. When the load is applied to these composites, the ductile polymer phase shows little plastic deformation constrained by the stiff ceramic network. The greater the polymer volume percentage, the greater the displacement of the composite material under load (Figure 6-11). The interpenetrating polymer within the ceramic scaffold structure facilitates crack deflection by promoting crack propagation at the ceramic polymer interface. This long, tortuous pathway of crack propagation consumes more energy and adds to the toughening effect. The final toughening mechanism is at the level of the ceramic bricks, with frictional sliding as a result of the surface roughness. All the aforementioned toughening mechanisms have previously been described in the literature for nacre-like composite materials [13, 17, 278].

One of the important features of CAD/CAM materials is their machinability. As a result of the polymer content (24-30 vol.%), the BCPCs were expected to show good machinability and edge retention. Previous work by He and Swain (2011) found that polymer infiltrated ceramics have a low brittleness index, which makes them suitable as CAD/CAM materials. In this study, in order to assess the machinability of the BCPCs, the hardest of the experimental composite materials (BCPC4) was milled using a CNC machine with a diamond bur, (as described in Chapter 3, Page 88). Also, one Vita Enamic specimen was milled for comparison. The CNC machine was able to mill both the BCPC4 and Vita Enamic samples without any problems, even though the milling tool speed (12000rpm) was much lower than the range of CAD/CAM machines (42000-60000 rpm) [275]. SEM images (Figure 6-13) showed that both materials have rough surfaces after milling, although the edges cut for both materials showed good edge definition (Figure 6-14).

Chavali *et al*. (2017) assessed the machinability of CAD/CAM materials by measuring the tool penetration rate under different applied loads. The results showed that ceramic/polymer materials had better machinability, with less chipping, compared to ceramic materials. The authors concluded that less milling time and tool wear is to be expected when a polymer containing CAD/CAM material is used to mill a dental restoration [275].

The best material to restore missing tooth structure is the one that can best match the tooth tissue for mechanical properties. Enamel and dentine joined at the DEJ, form a single unit that is capable of functioning perfectly in the oral cavity. Each dental tissue brings specific characteristics to this single unit. An ideal restorative material should combine strength, toughness and hardness to match that of natural tooth tissue [279].

Bi-directional freeze casting was used in this study to fabricate the ceramic preform for the composite material. Freeze casting as a method to fabricate porous ceramics has the advantage of tailoring the pore size, morphology and orientation to give an interconnected porous network with an anisotropic structure. This porous network can be infiltrated with a polymer material to improve the mechanical properties. Most importantly, the technique is simple and easy to apply to different materials. It uses simple freezing equipment and a simple sintering process, which makes it cost effective [34, 174].

Nevertheless, freeze casting suffers from a limitation, which is the reproducibility. The technique is highly sensitive to changes in the freezing conditions, which means any change in the freezing parameters can produce scaffolds with different characteristics. Some simple steps can be followed to improve reproducibility [280]. Preparing the ceramic suspensions in a single batch, rather than individually, is important and was done in this study for each of the studied parameters. Using a large smooth walled mould can reduce edge effects. The mould used in this study was large (60x60mm), with 20mm thick, smooth acrylic walls to isolate the ceramic suspension from the surrounding environment. Improving the reproducibility of the fabricated composite materials is a key element if it is to be introduced as a dental material.

6.4 Summary

In the present study, biomimetic ceramic/polymer composites (BCPCs) were fabricated. A good combination of strength, toughness and hardness was achieved by mimicking the "brick and mortar" architecture of nacre. Different ceramic volume fractions were made by using different uniaxial pressures. The higher the pressure, the higher the ceramic content of the final material. The ceramic volume fraction affected the mechanical properties of

BCPCs. The anisotropic structure of the BCPCs had an effect on the measured flexural strength, elastic modulus and hardness when tested from two different directions (z and x-axis). The mechanical properties of BCPC1 with 70% ceramic volume fraction showed the best combination of strength, elasticity, hardness and toughness, with final values in the range of 135.08-145.77 MPa, 57.75-61.22 GPa, 3.07-3.36 GPa and 2.54 MPa.$m^{1/2}$, respectively.

The mean flexural strength value for the vita Enamic specimens measured in this study was 128.26 MPa, which is lower than the manufacturer's reported value by 14.5%. The hardness and fracture toughness were in the reported range, but the flexural strength test revealed brittle behaviour. The hardest experimental composite material (BCPC4) produced in this current study showed good machinability and edge retention.

Chapter 7. Conclusions and future works

7.1 Conclusions

The results of this research suggest that biomimetic nacre-like ceramic/polymer composites, produced by bi-directional freeze casting, show great promise as potential chairside CAD/CAM dental restorative materials. The composites comprise an inorganic ceramic phase connected to an organic polymer phase with a unique brick-and-mortar structure, which is a relatively new approach to the production of restorative materials. The ceramic phase provides sufficient strength and hardness, while the polymer phase provides resilience and toughness to the material. The bricks and mortar structure is also important in providing adequate toughness. The intricate joining of the two phases, ceramic and polymer, to create a single material, is important in reducing the tendency to brittle fracture shown by most of the currently available ceramic restorative materials. The ultimate goal would be to mimic the natural tooth both mechanically (i.e. strength, toughness, hardness) and aesthetically.

By using bi-directional freeze casting, highly aligned porous ceramic scaffolds were fabricated by freezing a ceramic suspension under dual temperature gradients, followed by lyophilisation and sintering. The scaffolds had highly aligned interconnected pores in a lamellar structure. This structure was demonstrated using light microscopy, SEM and micro-CT scanning. The effects of cooling rate, copper/PDMS mould slope angle, initial solid loading and binder concentrations on the scaffold alignment and microstructure were determined. Both cooling rate and copper/PDMS mould slope angle have a pronounced effect on the scaffold microstructure. The higher the cooling rate and mould slope angle,

the larger the size of the aligned lamellar area and the higher uniformity in alignment. A copper/PDMS mould with a slope angle of α = 20° produced scaffolds with a more graded structure. Initial solid loading had little effect on ice crystal growth direction and subsequent ceramic alignment. Increasing the solid loading led to an increase in the ceramic wall thickness and a decrease in the interlamellar spacing. PVA binder concentration affected the porous network structure, interlamellar spacing, ceramic wall thickness and lamellar alignment. Increasing the PVA concentration decreased the interlamellar spacing, increased the ceramic wall thickness and produced more ceramic bridges. High PVA concentrations of 4 and 8 wt. % deflected ice crystals from their highly aligned direction of growth. The freeze casting technique under dual temperature gradients can be used as a viable method to fabricate highly aligned porous materials.

Adding MgO to the alumina ceramic powder as a sintering aid improved the scaffold density and reduced abnormal grain growth. Using different first-step sintering temperatures had a significant effect on the ceramic volume fraction and the microstructure of the scaffold. Higher first-step sintering temperatures (1400°C or higher) produced ceramic scaffolds with lower ceramic volume fractions, shorter and poorly connected ceramic bricks and hence lower compressive strengths. When used in composite fabrication, these scaffolds also had poorer mechanical properties but showed more ductile behaviour under load. Lower first-step sintering temperatures (1350°C or lower) produced ceramic scaffolds with higher ceramic volume fractions, longer and interconnected ceramic walls and ultimately higher compressive strengths. Such scaffolds improved the mechanical properties of the final composite materials, but they were more brittle under load.

As might be expected, the ceramic volume fraction of the densified scaffold increased linearly with the increasing uniaxial pressure. This also affected the subsequent mechanical properties of the BCPCs. Increasing the ceramic volume fraction increased the flexural strength, elastic modulus, hardness and fracture toughness. The flexural strength and elastic modulus of BCPC4, with 76 vol% ceramic content, was the highest of all the BCPCs. The hardness of the fabricated BCPCs was mid-way between pure polymer and dense ceramic, and closer to the range of hardness values seen with enamel. Fracture toughness measurements revealed different toughening mechanisms inside the composite materials and the fracture toughness values were similar to dentine. The hardest composite material (BCPC4) was machinable and had good edge definition. These initial results indicated that the BCPCs, with ceramic volume fractions from 70 vol.% to 76 vol.%, showed great promise as potential chairside CAD/CAM dental materials

In Summary, an anisotropic dental material with brick and mortar microstructure showed better fracture behaviour under loading compared to isotropic brittle dental materials. The unique structure of strong ceramic bricks infiltrated by ductile polymer mortar led to the desirable stable crack propagation. All ceramic and ceramic/polymer composite dental materials have isotropic microstructure that allows unstable crack propagation and hence catastrophic fracture under enough loading.

7.2 Future works

The novel biomimetic nacre-like ceramic/polymer composites fabricated in this research have the potential to be used as chairside CAD/CAM dental restorative materials. However,

further investigations are required to improve and optimise the physical and mechanical properties of the composite, as well as the aesthetics. Such work might include:

1. Testing the fracture toughness of the composite from the z direction, to observe the crack propagation parallel to the ceramic walls. This would give a better understanding of the material's behaviour loaded in different directions.
2. Studying the effect of different ratios of UDMA/TEGDMA on the mechanical properties, especially the fracture toughness.
3. Although the static mechanical properties (flexural strength, elastic modulus, fracture toughness and hardness) of the ceramic/polymer composites were tested in this research, it would also be worth investigating their fatigue property under cyclic loading in both wet and dry environments. This would allow observation of crack growth under simulated oral conditions and help predict the potential lifetime of the materials *in vivo*.
4. If the materials are to be used as aesthetic tooth restorations, then the long term colour stability requires investigation.
5. Linked to both the aesthetics and mechanical properties, the potential water absorption and hygroscopic expansion of the polymer component should be investigated. Water absorption might have a direct effect on aesthetics via colour change, but volumetric expansion may also cause deleterious stresses to develop within the composite and affect its longevity.
6. Evaluation of wear resistance of the composites would be beneficial to assess the material loss and roughness due to brushing and masticatory forces.
7. After CAD/CAM machining surface roughness is present and is worth further investigation, this might also have an effect on wear and aesthetics.

8. As the fabricated composites have an anisotropic structure, finite element analysis could be carried out to determine the best direction for cutting of the material during machining via the analysis of stress distribution.
9. Crack initiation fracture toughness (K_{IC}) measures the amount of energy absorbed by the material to initiate the crack propagation, while crack propagation fracture toughness (K_{JC}) measures the energy absorbed during crack propagation. It would be worthwhile measuring the K_{JC} to see if crack resistance increases with crack extension. This can be done under the SEM (in situ fracture toughness test), which provides a better indication of the toughness of CAD/CAM dental materials in the real application.

References

1. Spitznagel, F.A., J. Boldt, and P.C. Gierthmuehlen, *CAD/CAM ceramic restorative materials for natural teeth.* Journal of Dental Research, 2018. **97**(10): p. 1082-1091.
2. Miyazaki, T. and Y. Hotta, *CAD/CAM systems available for the fabrication of crown and bridge restorations.* Australian Dental Journal, 2011. **56**(1): p. 97-106.
3. Yin, L., et al., *An overview of in vitro abrasive finishing & CAD/CAM of bioceramics in restorative dentistry.* International Journal of Machine Tools & Manufacture, 2006. **46**(9): p. 1013-1026.
4. Rekow, D. and V.P. Thompson, *Near-surface damage - a persistent problem in crowns obtained by computer-aided design and manufacturing.* Proceedings of the Institution of Mechanical Engineers Part H-Journal of Engineering in Medicine, 2005. **219**(H4): p. 233-243.
5. Jingarwar, M., N. Bajwa, and A. Pathak, *Minimal intervention dentistry - a new frontier in clinical dentistry.* Journal of clinical and diagnostic research : JCDR, 2014. **8**(7): p. ZE04-ZE8.
6. *CAD/CAM Dentistry.* International Dental Journal, 2018. **68**(1): p. 18-19.
7. Lee, A., et al., *Wear behavior of human enamel against lithium disilicate glass ceramic and type III gold.* Journal of Prosthetic Dentistry, 2014. **112**(6): p. 1399-1405.
8. Awada, A. and D. Nathanson, *Mechanical properties of resin-ceramic CAD/CAM restorative materials.* Journal of Prosthetic Dentistry, 2015. **114**(4): p. 587-593.
9. Santos, F., et al., *Comparative study of the wear of the pair human teeth/Vita Enamic (R) vs commonly used dental ceramics through chewing simulation.* Journal of the Mechanical Behavior of Biomedical Materials, 2018. **88**: p. 251-260.
10. Coldea, A., M.V. Swain, and N. Thiel, *Mechanical properties of polymer-infiltrated-ceramic-network materials.* Dental Materials, 2013. **29**(4): p. 419-426.
11. Noort, R.v., *Introduction to dental materials* 3rd ed. 2007: Edinburgh : Mosby.
12. Hillson, S., *Teeth.* 2nd ed. 2005: Cambridge : Cambridge University Press
13. Launey, M.E. and R.O. Ritchie, *On the Fracture Toughness of Advanced Materials.* Advanced Materials, 2009. **21**(20): p. 2103-2110.
14. Barthelat, F. and H.D. Espinosa, *An experimental investigation of deformation and fracture of nacre-mother of pearl.* Experimental Mechanics, 2007. **47**(3): p. 311-324.
15. Hu, K., et al., *Written-in conductive patterns on robust graphene oxide biopaper by electrochemical microstamping.* Angewandte Chemi International Eidition, 2013. **52**(51): p. 13784-13788.
16. Wegst, U.G.K., et al., *Bioinspired structural materials.* Nature Materials, 2015. **14**(1): p. 23-36.
17. Launey, M.E., et al., *Designing highly toughened hybrid composites through nature-inspired hierarchical complexity.* Acta Materialia, 2009. **57**(10): p. 2919-2932.
18. Bai, H., et al., *Bioinspired hydroxyapatite/poly(methyl methacrylate) composite with a nacre-mimetic architecture by a bidirectional freezing method.* Advanced Materials, 2016. **28**(1): p. 50-56.
19. Bouville, F., et al., *Strong, tough and stiff bioinspired ceramics from brittle constituents (vol 13, pg 508, 2014).* Nature Materials, 2017. **16**(12): p. 1271-1271.

20. Petrini, M., M. Ferrante, and B. Su, *Fabrication and characterization of biomimetic ceramic/polymer composite materials for dental restoration.* Dental Materials, 2013. **29**(4): p. 375-381.
21. Al-Jawoosh, S., A. Ireland, and B. Su, *Fabrication and characterisation of a novel biomimetic anisotropic ceramic/polymer-infiltrated composite material.* Dental Materials, 2018. **34**(7): p. 994-1002.
22. Della Bona, A., *Bonding to ceramics: scientific evidence for clinical dentistry.* 2009: Editoria Artes Medica.
23. Li, R.W.K., T.W. Chow, and J.P. Matinlinna, *Ceramic dental biomaterials and CAD/CAM technology: State of the art.* Journal of Prosthodontic Research, 2014. **58**(4): p. 208-216.
24. Apholt, W., et al., *Flexural strength of Cerec 2 machined and jointed InCeram-Alumina and InCeram-Zirconia bars.* Dental Materials, 2001. **17**(3): p. 260-267.
25. Li, J., H. Liao, and L. Hermansson, *Sintering of partially-stabilized zirconia and partially-stabilized zirconia-hydroxyapatite composites by hot isostatic pressing and pressureless sintering.* Biomaterials, 1996. **17**(18): p. 1787-1790.
26. Deville, S., et al., *Freezing as a path to build complex composites.* Science, 2006. **311**(5760): p. 515-518.
27. Fukasawa, T., et al., *Synthesis of porous ceramics with complex pore structure by freeze-dry processing.* Journal of the American Ceramic Society, 2001. **84**(1): p. 230-232.
28. Fukasawa, T., et al., *Pore structure of porous ceramics synthesized from water-based slurry by freeze-dry process.* Journal of Materials Science, 2001. **36**(10): p. 2523-2527.
29. Ren, L., Y.P. Zeng, and D. Jiang, *Preparation of porous TiO2 by a novel freeze casting.* Ceramics International, 2009. **35**(3): p. 1267-1270.
30. Koh, Y.H., J.J. Sun, and H.E. Kim, *Freeze casting of porous Ni-YSZ cermets.* Materials Letters, 2007. **61**(6): p. 1283-1287.
31. Zuo, K.H., Y.P. Zeng, and D.L. Jiang, *Effect of polyvinyl alcohol additive on the pore structure and morphology of the freeze-cast hydroxyapatite ceramics.* Materials Science & Engineering C-Materials for Biological Applications, 2010. **30**(2): p. 283-287.
32. Fukushima, M., Y. Yoshizawa, and T. Ohji, *Macroporous Ceramics by Gelation-Freezing Route Using Gelatin.* Advanced Engineering Materials, 2014. **16**(6): p. 607-620.
33. Wegst, U.G.K., et al., *Biomaterials by freeze casting.* Philosophical Transactions of the Royal Society a-Mathematical Physical and Engineering Sciences, 2010. **368**(1917): p. 2099-2121.
34. Liu, R., T. Xu, and C. Wang, *A review of fabrication strategies and applications of porous ceramics prepared by freeze-casting method.* Ceramics International, 2016. **42**(2): p. 2907-2925.
35. Yoon, B.H., et al., *In-situ fabrication of porous hydroxyapatite (HA) scaffolds with dense shells by freezing HA/camphene slurry.* Materials Letters, 2008. **62**(10-11): p. 1700-1703.
36. Babaie, E. and S.B. Bhaduri, *Fabrication Aspects of Porous Biomaterials in Orthopedic Applications: A Review.* Acs Biomaterials Science & Engineering, 2018. **4**(1): p. 1-39.

37. Feiz, S., A.H. Navarchian, and O.M. Jazani, *Poly(vinyl alcohol) membranes in wound-dressing application: microstructure, physical properties, and drug release behavior.* Iranian Polymer Journal, 2018. **27**(3): p. 193-205.
38. Soltani, N., et al., *Fabrication of aligned porous LaNi0.6Fe0.4O3 perovskite by water based freeze casting.* Chemical Physics Letters, 2018. **700**: p. 138-144.
39. Zhu, S.Y., et al., *Enhanced piezoelectric properties of 3-1 type porous 0.94Bi(0.5)Na(0.5)TiO(3)-0.06BaTiO(3) ferroelectric ceramics.* Journal of the European Ceramic Society, 2018. **38**(4): p. 2251-2255.
40. Zeng, X.L., et al., *Facile Preparation of Superelastic and Ultra low Dielectric Boron Nitride Nanosheet Aerogels via Freeze-Casting Process.* Chemistry of Materials, 2015. **27**(17): p. 5849-5855.
41. Tang, Y.F., et al., *Fabrication of porous ceramics with double-pore structure by stepwise freeze casting using water/diphenyl methane emulsion.* Ceramics International, 2018. **44**(1): p. 1187-1192.
42. Rodrigues, J.R., N.M. Alves, and J.F. Mano, *Nacre-inspired nanocomposites produced using layer-by-layer assembly: Design strategies and biomedical applications.* Materials Science & Engineering C-Materials for Biological Applications, 2017. **76**: p. 1263-1273.
43. Zhao, H., Z. Yang, and L. Guo, *Nacre-inspired composites with different macroscopic dimensions: strategies for improved mechanical performance and applications.* NPG Asia Materials, 2018. **10**(4): p. 1-22.
44. Munch, E., et al., *Architectural Control of Freeze-Cast Ceramics Through Additives and Templating.* Journal of the American Ceramic Society, 2009. **92**(7): p. 1534-1539.
45. Bouville, F., et al., *Templated Grain Growth in Macroporous Materials.* Journal of the American Ceramic Society, 2014. **97**(6): p. 1736-1742.
46. Bai, H., et al., *Bioinspired large-scale aligned porous materials assembled with dual temperature gradients.* Science advances, 2015. **1**(11): p. e1500849.
47. Sakaguchi, R.L. and J.M. Powers, *Craig's restorative dental materials* 2012, Philadelphia, Pa. : Mosby Elsevier.
48. Bath-Balogh, M. and M.J. Fehrenbach, *Illustrated dental embryology, histology, and anatomy*. 2nd ed. 2006: St. Louis, Missouri : Elsevier Saunders.
49. Spears, I.R., et al., *The effects of enamel anisotropy on the distribution of stress in a tooth.* Journal of Dental Research, 1993. **72**(11): p. 1526-1531.
50. Cui, F.-Z. and J. Ge, *New observations of the hierarchical structure of human enamel, from nanoscale to microscale.* Journal of Tissue Engineering and Regenerative Medicine, 2007. **1**(3): p. 185-191.
51. Özcoban, H., E.D. Yilmaz, and G.A. Schneider, *Hierarchical microcrack model for materials exemplified at enamel.* Dental Materials, 2018. **34**(1): p. 69-77.
52. Habelitz, S., et al., *Mechanical properties of human dental enamel on the nanometre scale.* Archives of Oral Biology, 2001. **46**(2): p. 173-183.
53. Van Meerbeek, B., et al., *Buonocore Memorial Lecture - Adhesion to enamel and dentin: Current status and future challenges.* Operative Dentistry, 2003. **28**(3): p. 215-235.
54. Weiss, L., *Cell and tissue biology : a textbook of histology*. 6th ed. 1988, Baltimore: Urban & Schwarzenberg.

55. Zaslansky, P., S. Zabler, and P. Fratzl, *3D variations in human crown dentin tubule orientation: A phase-contrast microtomography study.* Dental Materials, 2010. **26**(1): p. E1-E10.
56. Huo, B., *An inhomogeneous and anisotropic constitutive model of human dentin.* Journal of Biomechanics, 2005. **38**(3): p. 587-594.
57. Chen, H. and Y. Liu, *Chapter 2 - Teeth*, in *Advanced Ceramics for Dentistry*, J.Z. Shen and T. Kosmač, Editors. 2014, Butterworth-Heinemann: Oxford. p. 5-21.
58. Sviridov, A., et al., *Intensity profiles of linearly polarized light backscattered from skin and tissue-like phantoms.* Journal of Biomedical Optics, 2005. **10**(1): p. 9.
59. Kinney, J.H., et al., *Collagen orientation and crystallite size in human dentin: A small angle X-ray scattering study.* Calcified Tissue International, 2001. **69**(1): p. 31-37.
60. Miura, J., et al., *Multiscale analysis of stress distribution in teeth under applied forces.* Dental Materials, 2009. **25**(1): p. 67-73.
61. Hayasaki, H., et al., *Occlusal contact area of mandibular teeth during lateral excursion.* International Journal of Prosthodontics, 2004. **17**(1): p. 72-76.
62. Pruitt, L.A. and A.M. Chakravartula, *Mechanics of biomaterials : fundamental principles for implant design* 2011: Cambridge : Cambridge University Press.
63. Ausiello, P., et al., *Stress distributions in adhesively cemented ceramic and resin-composite Class II inlay restorations: a 3D-FEA study.* Dental Materials, 2004. **20**(9): p. 862-872.
64. He, L.H. and M.V. Swain, *Understanding the mechanical behaviour of human enamel from its structural and compositional characteristics.* Journal of the Mechanical Behavior of Biomedical Materials, 2008. **1**(1): p. 18-29.
65. Park, S., et al., *On the brittleness of enamel and selected dental materials.* Dental Materials, 2008. **24**(11): p. 1477-1485.
66. Min, J., et al., *Comparison of human enamel and polymer-infiltrated-ceramic network material "ENAMIC" through micro- and nano-mechanical testing.* Ceramics International, 2016. **42**(9): p. 10631-10637.
67. He, L.H. and M.V. Swain, *Nanoindentation derived stress-strain properties of dental materials.* Dental Materials, 2007. **23**(7): p. 814-821.
68. Nizam, B.R.H., et al., *Nanoindentation study of human premolars subjected to bleaching agent.* Journal of Biomechanics, 2005. **38**(11): p. 2204-2211.
69. Yan, J., B. Taskonak, and J.J. Mecholsky, *Fractography and fracture toughness of human dentin.* Journal of the Mechanical Behavior of Biomedical Materials, 2009. **2**(5): p. 478-484.
70. Lawn, B.R. and J.J.W. Lee, *Analysis of fracture and deformation modes in teeth subjected to occlusal loading.* Acta Biomaterialia, 2009. **5**(6): p. 2213-2221.
71. Mahoney, E., et al., *The hardness and modulus of elasticity of primary molar teeth: an ultra-micro-indentation study.* Journal of Dentistry, 2000. **28**(8): p. 589-594.
72. Magne, P., *Composite resins and bonded porcelain: the postamalgam era?* Journal of the California Dental Association, 2006. **34**(2): p. 135-47.
73. Park, J., *Bioceramics Properties, Characterizations, and Applications*. 2008, New York City: Springer. 363.
74. Peutzfeldt, A., *Resin composites in dentistry: The monomer systems.* European Journal of Oral Sciences, 1997. **105**(2): p. 97-116.
75. Hervas-Garcia, A., et al., *Composite resins. A review of the materials and clinical indications.* Medicina oral, patologia oral y cirugia bucal, 2006. **11**(2): p. E215-20.

76. Kerby, R.E., et al., *Synthesis and evaluation of modified urethane dimethacrylate resins with reduced water sorption and solubility.* Dental Materials, 2009. **25**(3): p. 302-313.
77. Beatty, M.W., et al., *Effect of Crosslinking Agent Content, Monomer Functionality, and Repeat Unit Chemistry on Properties of Unfilled Resins.* Journal of Biomedical Materials Research, 1993. **27**(3): p. 403-413.
78. Ferracane, J.L., *Current trends in dental composites.* Critical Reviews in Oral Biology and Medicine, 1995. **6**(4): p. 302-318.
79. Chen, M.H., *Update on Dental Nanocomposites.* Journal of Dental Research, 2010. **89**(6): p. 549-560.
80. Lizenboim, K., et al., *Bisphenol-A free dental polymeric materials.* Journal of Adhesion Science and Technology, 2013. **27**(4): p. 354-370.
81. Chen, L. and B.I. Suh, *Bisphenol A in Dental Materials: A Review.* JSM Dentistry, 2013. **1: 1004.**: p. 1-5.
82. Moszner, N. and U. Salz, *Recent developments of new components for dental adhesives and composites.* Macromolecular Materials and Engineering, 2007. **292**(3): p. 245-271.
83. Palin, W.M., et al., *In vitro cuspal deflection and microleakage of maxillary premolars restored with novel low-shrink dental composites.* Dental Materials, 2005. **21**(4): p. 324-335.
84. Kumar, S.R., A. Patnaik, and I.K. Bhat, *Development and characterization of marble dust-filled dental composite.* Journal of Composite Materials, 2017. **51**(14): p. 1997-2008.
85. Ilie, N. and R. Hickel, *Investigations on mechanical behaviour of dental composites.* Clinical Oral Investigations, 2009. **13**(4): p. 427-438.
86. Klapdohr, S. and N. Moszner, *New inorganic components for dental filling composites.* Monatshefte Fur Chemie, 2005. **136**(1): p. 21-45.
87. Ferracane, J.L., *Resin composite-State of the art.* Dental Materials, 2011. **27**(1): p. 29-38.
88. Mitra, S.B., D. Wu, and B.N. Holmes, *An application of nanotechnology in advanced dental materials.* Journal of the American Dental Association, 2003. **134**(10): p. 1382-1390.
89. Garoushi, S., P.K. Vallittu, and L.V.J. Lassila, *Short glass fiber reinforced restorative composite resin with semi-inter penetrating polymer network matrix.* Dental Materials, 2007. **23**(11): p. 1356-1362.
90. Xu, H.H.K., et al., *Effects of different whiskers on the reinforcement of dental resin composites.* Dental Materials, 2003. **19**(5): p. 359-367.
91. Jandt, K.D., et al., *Mechanical properties and radiopacity of experimental glass-silica-metal hybrid composites.* Dental Materials, 2002. **18**(6): p. 429-435.
92. Karabela, M.M. and I.D. Sideridou, *Effect of the structure of silane coupling agent on sorption characteristics of solvents by dental resin-nanocomposites.* Dental Materials, 2008. **24**(12): p. 1631-1639.
93. O'Brien, W.J., *Dental materials and their selection* 3rd ed. 2002: Chicago : Quintessence.
94. Lee, T.Y., et al., *(Meth)acrylate vinyl ester hybrid polymerizations.* 2009. **47**(10): p. 2509-2517.

95. Stansbury, J.W., *Curing Dental Resins and Composites by Photopolymerization.* 2000. **12**(6): p. 300-308.
96. Kaisarly, D. and M.E. Gezawi, *Polymerization shrinkage assessment of dental resin composites: a literature review.* Odontology, 2016. **104**(3): p. 257-270.
97. Chung, K.H. and E.H. Greener, *Correlation between degree of conversion, filler concentration and mechanical properties of posterior composite resins.* Journal of Oral Rehabilitation, 1990. **17**(5): p. 487-494.
98. Ozturk, B., et al., *Conversion degrees of resin composites using different light sources.* Eur J Dent, 2013. **7**(1): p. 102-9.
99. Shahrbaf, S., et al., *Fracture strength of machined ceramic crowns as a function of tooth preparation design and the elastic modulus of the cement.* Dental Materials, 2014. **30**(2): p. 234-241.
100. Griggs, J.A., *Recent advances in materials for all-ceramic restorations.* Dental clinics of North America, 2007. **51**(3): p. 713-27, viii.
101. Rizkalla, A.S. and D.W. Jones, *Indentation fracture toughness and dynamic elastic moduli for commercial feldspathic dental porcelain materials.* Dental materials, 2004. **20**(2): p. 198-206.
102. Shenoy, A. and N. Shenoy, *Dental ceramics: An update.* Journal of conservative dentistry, 2010. **13**(4): p. 195-203.
103. Anusavice, K.J. and R.W. Phillips, *Phillips' Science of Dental Materials*. 11th ed. 2003: Philadelphia, Pa., London : Saunders.
104. Hämmerle, C., et al., *Dental ceramics : essential aspects for clinical practice*. 2008: Quintessence.
105. Ho, G.W. and J.P. Matinlinna, *Insights on Ceramics as Dental Materials. Part I: Ceramic Material Types in Dentistry.* Silicon, 2011. **3**(3): p. 109-115.
106. Pereira, C.L., et al., *Flexural strength of composites: influences of polyethylene fiber reinforcement and type of composite.* Clinical Oral Investigations, 2003. **7**(2): p. 116-119.
107. Coldea, A., M.V. Swain, and N. Thiel, *In-vitro strength degradation of dental ceramics and novel PICN material by sharp indentation.* Journal of the Mechanical Behavior of Biomedical Materials, 2013. **26**: p. 34-42.
108. Chen, C.F., et al., *The fracture resistance of a CAD/CAM Resin Nano Ceramic (RNC) and a CAD ceramic at different thicknesses.* Dental Materials, 2014. **30**(9): p. 954-962.
109. Homaei, E., et al., *Fatigue resistance of monolithic CAD/CAM ceramic crowns on human premolars.* Ceramics International, 2016. **42**(14): p. 15709-15717.
110. Daou, E.E., *The zirconia ceramic: strengths and weaknesses.* The open dentistry journal, 2014. **8**: p. 33-42.
111. Serbena, F.C., et al., *Crystallization toughening of a model glass-ceramic.* Acta Materialia, 2015. **86**: p. 216-228.
112. McLaren, E., *CAD/CAM Dental Technology: A Perspective on Its Evolution and Status.* Compendium of Continuing Education in Dentistry, 2011. **32**(4): p. 74-75.
113. Mormann, W.H. and A. Bindl, *All-ceramic, chair-side computer-aided design/computer-aided machining restorations.* Dental clinics of North America, 2002. **46**(2): p. 405-26, viii.

114. Liu, P.R. and M.E. Essig, *Panorama of dental CAD/CAM restorative systems.* Compendium of continuing education in dentistry, 2008. **29**(8): p. 482, 484, 486-8 passim.
115. Miyazaki, T., et al., *A review of dental CAD/CAM: current status and future perspectives from 20 years of experience.* Dental Materials Journal, 2009. **28**(1): p. 44-56.
116. Sannino, G., et al., *CEREC CAD/CAM Chairside System.* Oral Implantol (Rome), 2014. **7**(3): p. 57-70.
117. Otto, T. and S. De Nisco, *Computer-aided direct ceramic restorations: A 10-year prospective clinical study of Cerec CAD/CAM inlays and onlays.* International Journal of Prosthodontics, 2002. **15**(2): p. 122-128.
118. Giordano, R., *Materials for chairside CAD/CAM-produced restorations.* Journal of the American Dental Association, 2006. **137**: p. 14S-21S.
119. Mörmann, W.H., *State of the art of CAD/CAM restorations : 20 years of CEREC*. 2006: Quintessence.
120. Keshvad, A., et al., *Marginal Gap, Internal Fit, and Fracture Load of Leucite-Reinforced Ceramic Inlays Fabricated by CEREC inLab and Hot-Pressed Techniques.* Journal of Prosthodontics-Implant Esthetic and Reconstructive Dentistry, 2011. **20**(7): p. 535-540.
121. Giordano, R. and E.A. McLaren, *Ceramics overview: classification by microstructure and processing methods.* Compendium of continuing education in dentistry, 2010. **31**(9): p. 682-4, 686, 688 passim; quiz 698, 700.
122. Tysowsky, G.W., *The science behind lithium disilicate: a metal-free alternative.* Dentistry Today, 2009. **28**(3): p. 112-3.
123. Belli, R., et al., *Chairside CAD/CAM materials. Part 1: Measurement of elastic constants and microstructural characterization.* Dental Materials, 2017. **33**(1): p. 84-98.
124. D'Arcangelo, C., et al., *Wear properties of dental ceramics and porcelains compared with human enamel.* Journal of Prosthetic Dentistry, 2016. **115**(3): p. 350-355.
125. Lawson, N.C., R. Bansal, and J.O. Burgess, *Wear, strength, modulus and hardness of CAD/CAM restorative materials.* Dental Materials, 2016. **32**(11): p. e275-e283.
126. Kelly, J.R. and P. Benetti, *Ceramic materials in dentistry: historical evolution and current practice.* Australian Dental Journal, 2011. **56**: p. 84-96.
127. Kurtz, S.M., *PEEK biomaterials handbook*. 2012, Oxford UK: William Andrew Publishing.
128. Kurtz, S.M. and J.N. Devine, *PEEK biomaterials in trauma, orthopedic, and spinal implants.* Biomaterials, 2007. **28**(32): p. 4845-4869.
129. Schwitalla, A. and W.D. Muller, *PEEK Dental Implants: A Review of the Literature.* Journal of Oral Implantology, 2013. **39**(6): p. 743-749.
130. Harb, I.E., E.A. Abdel-Khalek, and S.A. Hegazy, *CAD/CAM Constructed Poly(etheretherketone) (PEEK) Framework of Kennedy Class I Removable Partial Denture: A Clinical Report.* Journal of Prosthodontics-Implant Esthetic and Reconstructive Dentistry, 2019. **28**(2): p. E595-E598.
131. Tartuk, B.K., E. Ayna, and E.G. Basaran, *Comparison of the Load-bearing Capacities of Monolithic PEEK, Zirconia and Hybrid Ceramic Molar Crowns.* Meandros Medical and Dental Journal, 2019. **20**(1): p. 45-50.

132. Elmougy, A., et al., *Characterisation of machinable structural polymers in restorative dentistry.* Dental Materials, 2018. **34**(10): p. 1509-1517.
133. Spitznagel, F.A., et al., *Resin Bond to Indirect Composite and New Ceramic/Polymer Materials: A Review of the Literature.* Journal of Esthetic and Restorative Dentistry, 2014. **26**(6): p. 382-393.
134. *Lava Ultimate CAD/CAM restorative. Technical product profile 1-24*. Available from: http://jensendental.com/wp-content/uploads/2015/04/Lava_Ultimate_Technical_Product_Profile.pdf (Accessed 04 JUL 2019).
135. He, L.H. and M. Swain, *A novel polymer infiltrated ceramic dental material.* Dental Materials, 2011. **27**(6): p. 527-534.
136. *No. 10025 VITA ENAMIC Technical and scientific documentation (Version 006)*. Available from: https://www.vitanorthamerica.com/en-US/VITA-ENAMIC-multiColor-276.html (Accssed 16 OCT 2019).
137. He, L.H., D. Purton, and M. Swain, *A novel polymer infiltrated ceramic for dental simulation.* Journal of Materials Science-Materials in Medicine, 2011. **22**(7): p. 1639-1643.
138. Bindl, A., H. Luthy, and W.H. Mormann, *Fracture load of CAD/CAM-generated slot-inlay FPDs.* International Journal of Prosthodontics, 2003. **16**(6): p. 653-660.
139. Conrad, H.J., W.J. Seong, and G.J. Pesun, *Current ceramic materials and systems with clinical recommendations: A systematic review.* Journal of Prosthetic Dentistry, 2007. **98**(5): p. 389-404.
140. Culp, L. and E.A. McLaren, *Lithium disilicate: the restorative material of multiple options.* Compendium of continuing education in dentistry, 2010. **31**(9): p. 716-20, 722, 724-5.
141. Guazzato, M., et al., *Mechanical properties of In-Ceram Alumina and In-Ceram Zirconia.* International Journal of Prosthodontics, 2002. **15**(4): p. 339-346.
142. Pinto, P.A., et al., *Surface and Mechanical Characterization of Dental Yttria-Stabilized Tetragonal Zirconia Polycrystals (3Y-TZP) After Different Aging Processes.* Microscopy and Microanalysis, 2016. **22**(6): p. 1179-1188.
143. Lauvahutanon, S., et al., *Mechanical properties of composite resin blocks for CAD/CAM.* Dental Materials Journal, 2014. **33**(5): p. 705-10.
144. Belli, R., et al., *Practical and theoretical considerations on the fracture toughness testing of dental restorative materials.* Dental Materials, 2018. **34**(1): p. 97-119.
145. Quinn, J.B., V. Sundar, and I.K. Lloyd, *Influence of microstructure and chemistry on the fracture toughness of dental ceramics.* Dental Materials, 2003. **19**(7): p. 603-611.
146. Holand, W., et al., *A comparison of the microstructure and properties of the IPS Empress (R) 2 and the IFS Empress (R) glass-ceramics.* Journal of Biomedical Materials Research, 2000. **53**(4): p. 297-303.
147. Apel, E., et al., *Phenomena and mechanisms of crack propagation in glass-ceramics.* Journal of the Mechanical Behavior of Biomedical Materials, 2008. **1**(4): p. 313-325.
148. Wendler, M., et al., *Chairside CAD/CAM materials. Part 3: Cyclic fatigue parameters and lifetime predictions.* Dental Materials, 2018. **34**(6): p. 910-921.
149. Borba, M., et al., *Effect of the microstructure on the lifetime of dental ceramics.* Dental Materials, 2011. **27**(7): p. 710-721.
150. Lepora, N.F., P. Verschure, and T.J. Prescott, *The state of the art in biomimetics.* Bioinspiration & Biomimetics, 2013. **8**(1): p. 11.

151. Fratzl, P., *Biomimetic materials research: what can we really learn from nature's structural materials?* Journal of the Royal Society Interface, 2007. **4**(15): p. 637-642.
152. Saratti, C.M., G.T. Rocca, and I. Krejci, *The potential of three-dimensional printing technologies to unlock the development of new 'bio-inspired' dental materials: an overview and research roadmap.* Journal of Prosthodontic Research, 2019. **63**(2): p. 131-139.
153. Munch, E., et al., *Tough, bio-inspired hybrid materials.* Science, 2008. **322**(5907): p. 1516-1520.
154. Chai, H., et al., *Remarkable resilience of teeth.* Proceedings of the National Academy of Sciences of the United States of America, 2009. **106**(18): p. 7289-7293.
155. Yeom, B., et al., *Abiotic tooth enamel.* Nature, 2017. **543**(7643): p. 95-98.
156. Du, J., et al., *Bio-inspired dental multilayers: Effects of layer architecture on the contact-induced deformation.* Acta Biomaterialia, 2013. **9**(2): p. 5273-5279.
157. Niu, X.R., et al., *Bio-inspired design of dental multilayers: Experiments and model.* Journal of the Mechanical Behavior of Biomedical Materials, 2009. **2**(6): p. 596-602.
158. Ritchie, R.O., *The conflicts between strength and toughness.* Nature Materials, 2011. **10**(11): p. 817-822.
159. Wang, R.Z., et al., *Deformation mechanisms in nacre.* Journal of Materials Research, 2001. **16**(9): p. 2485-2493.
160. Scotti, K.L. and D.C. Dunand, *Freeze casting - A review of processing, microstructure and properties via the open data repository, FreezeCasting.net.* Progress in Materials Science, 2018. **94**: p. 243-305.
161. Naglieri, V., et al., *Developing strength and toughness in bio-inspired silicon carbide hybrid materials containing a compliant phase.* Acta Materialia, 2015. **98**: p. 141-151.
162. Tan, G.Q., et al., *Nature-Inspired Nacre-Like Composites Combining Human Tooth-Matching Elasticity and Hardness with Exceptional Damage Tolerance.* Advanced Materials, 2019. **31**(52): p. 9.
163. Cui, B., et al., *Mechanical properties of polymer-infiltrated-ceramic (sodium aluminum silicate) composites for dental restoration.* Journal of Dentistry, 2017. **62**: p. 91-97.
164. Hammel, E.C., O.L.R. Ighodaro, and O.I. Okoli, *Processing and properties of advanced porous ceramics: An application based review.* Ceramics International, 2014. **40**(10): p. 15351-15370.
165. Ohji, T. and M. Fukushima, *Macro-porous ceramics: processing and properties.* International Materials Reviews, 2012. **57**(2): p. 115-131.
166. Colombo, P., *Conventional and novel processing methods for cellular ceramics.* Philosophical Transactions of the Royal Society a-Mathematical Physical and Engineering Sciences, 2006. **364**(1838): p. 109-124.
167. Innocentini, M.D.M., et al., *Permeability and structure of cellular ceramics: A comparison between two preparation techniques.* Journal of the American Ceramic Society, 1998. **81**(12): p. 3349-3352.
168. Colombo, P. and J.R. Hellmann, *Ceramic foams from preceramic polymers.* Materials Research Innovations, 2002. **6**(5-6): p. 260-272.
169. Barg, S., D. Koch, and G. Grathwohl, *Processing and Properties of Graded Ceramic Filters.* Journal of the American Ceramic Society, 2009. **92**(12): p. 2854-2860.
170. Studart, A.R., et al., *Processing routes to macroporous ceramics: A review.* Journal of the American Ceramic Society, 2006. **89**(6): p. 1771-1789.

171. Jayaseelan, D.D., et al., *High-strength porous alumina ceramics by the pulse electric current sintering technique.* Journal of the American Ceramic Society, 2002. **85**(1): p. 267-269.
172. Dawood, A., et al., *3D printing in dentistry.* British Dental Journal, 2015. **219**(11): p. 521-529.
173. Deville, S., *Freeze-casting of porous ceramics: A review of current achievements and issues.* Advanced Engineering Materials, 2008. **10**(3): p. 155-169.
174. Deville, S., *Freeze-Casting of Porous Biomaterials: Structure, Properties and Opportunities.* Materials, 2010. **3**(3): p. 1913-1927.
175. Deville, S., *Ice-templating, freeze casting: Beyond materials processing.* Journal of Materials Research, 2013. **28**(17): p. 2202-2219.
176. Sofie, S.W. and F. Dogan, *Freeze casting of aqueous alumina slurries with glycerol.* Journal of the American Ceramic Society, 2001. **84**(7): p. 1459-1464.
177. Wettlaufer, J.S., M.G. Worster, and H.E. Huppert, *Natural convection during solidification of an alloy from above with application to the evolution of sea ice.* Journal of Fluid Mechanics, 1997. **344**: p. 291-316.
178. Mahler, W. and M.F. Bechtold, *Freeze-formed silica fibres.* Nature, 1980. **285**(5759): p. 27-28.
179. Schramm, L., *Emulsions, Foams,and Suspensions*. 1st ed. 2005: Wiley-VCH.
180. Hunter, R.J., *Foundations of colloid science*. 2nd ed. 2001: Oxford : Oxford University Press.
181. Dhara, S. and P. Bhargava, *Influence of slurry characteristics on porosity and mechanical properties of alumina foams.* International Journal of Applied Ceramic Technology, 2006. **3**(5): p. 382-392.
182. Besra, L. and M. Liu, *A review on fundamentals and applications of electrophoretic deposition (EPD).* Progress in Materials Science, 2007. **52**(1): p. 1-61.
183. Zarbov, M., I. Schuster, and L. Gal-Or, *Methodology for selection of charging agents for electrophoretic deposition of ceramic particles.* Journal of Materials Science, 2004. **39**(3): p. 813-817.
184. Lewis, J.A., *Colloidal processing of ceramics.* Journal of the American Ceramic Society, 2000. **83**(10): p. 2341-2359.
185. Williams, P.M., *Zeta Potential*, in *Encyclopedia of Membranes*, E. Drioli and L. Giorno, Editors. 2016, Springer Berlin Heidelberg: Berlin, Heidelberg. p. 2063-2064.
186. Lee, S.K., S.S. Ryu, and D.H. Yoon, *Synthesis of fine Ca-doped BaTiO3 powders by solid-state reaction method - Part II: Rheological study on milling.* Journal of Electroceramics, 2007. **18**(1-2): p. 1-7.
187. Davies, J. and J.G.P. Binner, *The role of ammonium polyacrylate in dispersing concentrated alumina suspensions.* Journal of the European Ceramic Society, 2000. **20**(10): p. 1539-1553.
188. Waldbillig, D. and O. Kesler, *The effect of solids and dispersant loadings on the suspension viscosities and deposition rates of suspension plasma sprayed YSZ coatings.* Surface & Coatings Technology, 2009. **203**(15): p. 2098-2101.
189. Hargreaves, T., *Chemical formulation : an overview of surfactant-based preparations used in everyday life*. 2003: Cambridge : Royal Society of Chemistry.
190. Butt, H.-J., K. Graf, and M. Kappl, *Physics and chemistry of interfaces* 3rd ed. 2013: Weinheim : Wiley-VCH

191. S Mohanty, B Das, and S. Dhara, *Poly(maleic acid) – A novel dispersant for aqueous alumina slurry.* Journal of Asian Ceramic Societies, 2013. **1**(2): p. 184–190.
192. Schoof, H., et al., *Control of pore structure and size in freeze-dried collagen sponges.* Journal of Biomedical Materials Research, 2001. **58**(4): p. 352-357.
193. Moon, J.W., et al., *Preparation of NiO-YSZ tubular support with radially aligned pore channels.* Materials Letters, 2003. **57**(8): p. 1428-1434.
194. Deville, S., E. Saiz, and A.P. Tomsia, *Freeze casting of hydroxyapatite scaffolds for bone tissue engineering.* Biomaterials, 2006. **27**(32): p. 5480-5489.
195. Fukasawa, T., et al., *Synthesis of porous silicon nitride with unidirectionally aligned channels using freeze-drying process.* Journal of the American Ceramic Society, 2002. **85**(9): p. 2151-2155.
196. Koh, Y.-H., et al., *Effect of polystyrene addition on freeze casting of ceramic/camphene slurry for ultra-high porosity ceramics with aligned pore channels.* Journal of the American Ceramic Society, 2006. **89**(12): p. 3646-3653.
197. Shanti, N.O., K. Araki, and J.W. Halloran, *Particle redistribution during dendritic solidification of particle suspensions.* Journal of the American Ceramic Society, 2006. **89**(8): p. 2444-2447.
198. Araki, K. and J.W. Halloran, *New freeze-casting technique for ceramics with sublimable vehicles.* Journal of the American Ceramic Society, 2004. **87**(10): p. 1859-1863.
199. Araki, K. and J.W. Halloran, *Room-temperature freeze casting for ceramics with nonaqueous sublimable vehicles in the naphthalene-camphor eutectic system.* Journal of the American Ceramic Society, 2004. **87**(11): p. 2014-2019.
200. Sofie, S.W., *Fabrication of functionally graded and aligned porosity in thin ceramic substrates with the novel freeze-tape-casting process.* Journal of the American Ceramic Society, 2007. **90**(7): p. 2024-2031.
201. Chen, R., et al., *Ceramics with special porous structures fabricated by freeze-gelcasting: Using tert-butyl alcohol as a template.* Journal of the American Ceramic Society, 2007. **90**(11): p. 3478-3484.
202. Hu, L., et al., *Control of pore channel size during freeze casting of porous YSZ ceramics with unidirectionally aligned channels using different freezing temperatures.* Journal of the European Ceramic Society, 2010. **30**(16): p. 3389-3396.
203. Liu, R., J. Yuan, and C.-a. Wang, *A novel way to fabricate tubular porous mullite membrane supports by TBA-based freezing casting method.* Journal of the European Ceramic Society, 2013. **33**(15-16): p. 3249-3256.
204. Macchetta, A., I.G. Turner, and C.R. Bowen, *Fabrication of HA/TCP scaffolds with a graded and porous structure using a camphene-based freeze-casting method.* Acta Biomaterialia, 2009. **5**(4): p. 1319-1327.
205. Yook, S.-W., H.-E. Kim, and Y.-H. Koh, *Fabrication of porous titanium scaffolds with high compressive strength using camphene-based freeze casting.* Materials Letters, 2009. **63**(17): p. 1502-1504.
206. Jung, H.-D., et al., *Fabrication of titanium scaffolds with porosity and pore size gradients by sequential freeze casting.* Materials Letters, 2009. **63**(17): p. 1545-1547.
207. Deville, S., E. Saiz, and A.P. Tomsia, *Ice-templated porous alumina structures.* Acta Materialia, 2007. **55**(6): p. 1965-1974.

208. Koh, Y.-H., et al., *Freezing dilute ceramic/camphene slurry for ultra-high porosity ceramics with completely interconnected pore networks.* Journal of the American Ceramic Society, 2006. **89**(10): p. 3089-3093.
209. Preiss, A., et al., *Tailored graded pore structure in zirconia toughened alumina ceramics using double-side cooling freeze casting.* Journal of the European Ceramic Society, 2012. **32**(8): p. 1575-1583.
210. Johnson, D.L., *New Method of Obtaining Volume, Grain-Boundary, and Surface Diffusion Coefficients from Sintering Data.* Journal of Applied Physics, 1969. **40**(1): p. 192-200.
211. Mittemeijer, E.J., *Fundamentals of Materials Science: The Microstructure–Property Relationship Using Metals as Model Systems* 1ed. 2011, Berlin Heidelberg: Springer-Verlag.
212. Bae, I.-J. and S. Baik, *Abnormal Grain Growth of Alumina.* Journal of the American Ceramic Society, 1997. **80**(5): p. 1149-1156.
213. Bae, S.I. and S. Baik, *Critical concentration of MgO for the prevention of abnormal grain growth in alumina.* Journal of the American Ceramic Society, 1994. **77**(10): p. 2499-2504.
214. Chan, T.Y., S.J. Liu, and S.T. Lin, *Effects of high concentrations of liquid phase and magnesia on the grain growth of alumina.* Ceramics International, 1998. **24**(8): p. 617-625.
215. Lahiri, S., et al., *Rationalizing the role of magnesia and titania on sintering of α-alumina.* Ceramics International, 2016. **42**(14): p. 15405-15413.
216. Korber, C., et al., *Interaction of particles and a moving ice-liquid interface.* Journal of Crystal Growth, 1985. **72**(3): p. 649-662.
217. Mullins, W.W. and R.F. Sekerka, *Stability of a Planar Interface During Solidification of a Dilute Binary Alloy* Journal of Applied Physics 1964. **35**(2): p. 444-451.
218. Farhangdoust, S., et al., *Evaluating Initial Content of the Slurry and Cooling Rate on the Microstructural and Mechanical Characteristics of Freeze casted Hydroxyapatite Macroporous Scaffolds*, in *Bioceramics 24*, K. Ishikawa and Y. Iwamoto, Editors. 2013, Trans Tech Publications Ltd: Stafa-Zurich. p. 147-152.
219. Li, W.L., K. Lu, and J.Y. Walz, *Effects of Solids Loading on Sintering and Properties of Freeze-Cast Kaolinite-Silica Porous Composites.* Journal of the American Ceramic Society, 2013. **96**(6): p. 1763-1771.
220. Zeng, J., et al., *Effects of alcohol additives on pore structure and morphology of freeze-cast ceramics.* Transactions of Nonferrous Metals Society of China, 2014. **24**(3): p. 718-722.
221. Guo, R.F., et al., *Effects of composition and sintering temperature on the structure and compressive property of the lamellar Al2O3-ZrO2 scaffolds prepared by freeze casting.* Journal of Materials Science, 2015. **50**(14): p. 5039-5046.
222. Deville, S., S. Meille, and J. Seuba, *A meta-analysis of the mechanical properties of ice-templated ceramics and metals.* Science and Technology of Advanced Materials, 2015. **16**(4).
223. Lahiri, S., et al., *Rationalizing the role of magnesia and titania on sintering of alpha-alumina.* Ceramics International, 2016. **42**(14): p. 15405-15413.
224. Tari, G., J.M.F. Ferreira, and O. Lyckfeldt, *Influence of magnesia on colloidal processing of alumina.* Journal of the European Ceramic Society, 1997. **17**(11): p. 1341-1350.

225. Zuo, K.H., Y.P. Zeng, and D.L. Jiang, *Effect of cooling rate and polyvinyl alcohol on the morphology of porous hydroxyapatite ceramics.* Materials & Design, 2010. **31**(6): p. 3090-3094.
226. *Piranha solution*. Available from: https://en.wikipedia.org/wiki/Piranha_solution (Accessed 23 OCT 2019).
227. Schindelin, J., et al., *Fiji: an open-source platform for biological-image analysis.* Nature Methods, 2012. **9**(7): p. 676-682.
228. ASTM-C373-16, *Standard Test Methods for Determination of Water Absorption and Associated Properties by Vacuum Method for Pressed Ceramic Tiles and Glass Tiles and Boil Method for Extruded Ceramic Tiles and Non-tile Fired Ceramic Whiteware Products*. 2016, ASTM international: West Conshohocken, PA.
229. Ilie, N., et al., *Academy of Dental Materials guidance- Resin composites: Part I-Mechanical propertiesN.* Dental Materials, 2017. **33**(8): p. 880-894.
230. ASTM-D790-15, *Standard Test Methods for Flexural Properties of Unreinforced and Reinforced Plastics and Electrical Insulating Materials1*. 2016, ASTM International: West Conshohocken, PA.
231. ASTM-E1820-18, *Standard Test Method for Measurement of Fracture Toughness1*. 2018, ASTM International: West Conshohocken,PA.
232. BSEN-843-4:2005, *Advanced technical ceramics. Mechanical properties of monolithic ceramics at room temperature. Vickers, Knoop and Rockwell superficial hardness*. 2007, BSI.
233. Porter, M.M., et al., *Bioinspired Scaffolds with Varying Pore Architectures and Mechanical Properties.* Advanced Functional Materials, 2014. **24**(14): p. 1978-1987.
234. Park, H., et al., *Microstructure and compressive behavior of ice-templated copper foams with directional, lamellar pores.* Materials Science and Engineering a-Structural Materials Properties Microstructure and Processing, 2017. **679**: p. 435-445.
235. Sekhar, J.A. and R. Trivedi, *Solidification microstructure evolution in the presence of inert particles.* Materials Science and Engineering a-Structural Materials Properties Microstructure and Processing, 1991. **147**(1): p. 9-21.
236. Li, W.L., K. Lu, and J.Y. Walz, *Freeze casting of porous materials: review of critical factors in microstructure evolution.* International Materials Reviews, 2012. **57**(1): p. 37-60.
237. Gurbuz, S.N. and A.F. Dericioglu, *Effect of reinforcement surface functionalization on the mechanical properties of nacre-like bulk lamellar composites processed by a hybrid conventional method.* Materials Science & Engineering. C, Materials for Biological Applications, 2013. **33**(4): p. 2011-9.
238. Handwerker, C.A., P.A. Morris, and R.L. Coble, *Effects of Chemical Inhomogeneities on Grain Growth and Microstructure in Al2O3.* Journal of the American Ceramic Society, 1989. **72**(1): p. 130-136.
239. Rami, M.L., et al., *Colloidal Stability for Concentrated Zirconia Aqueous Suspensions.* Journal of the American Ceramic Society, 2009. **92**(1): p. S50-S56.
240. Lange, F.F., *Powder Processing Science and Technology for Increased Reliability.* Journal of the American Ceramic Society, 1989. **72**(1): p. 3-15.
241. Tari, G., F. Doreau, and J.M.F. Ferreira, *Influence of the suspension preparation procedure on the sintered magnesia-doped alumina microstructure.* Journal of Materials Science Letters, 2000. **19**(19): p. 1751-1753.

242. Kim, B.K., et al., *Alternative explanation for the role of magnesia in the sintering of alumina containing small amounts of a liquid phase.* Journal of the American Ceramic Society, 2003. **86**(4): p. 634-639.
243. Wang, D.-W., et al., *Effect of sintering temperature and time on densification, microstructure and properties of the PZT/ZnO nanowhisker piezoelectric composites.* Journal of Alloys and Compounds, 2011. **509**(24): p. 6980-6986.
244. Okada, K., et al., *A novel technique for preparing dental CAD/CAM composite resin blocks using the filler press and monomer infiltration method.* Dental Materials Journal, 2014. **33**(2): p. 203-209.
245. Gajewski, V.E., et al., *Monomers used in resin composites: degree of conversion, mechanical properties and water sorption/solubility.* Brazilian Dental Journal, 2012. **23**(5): p. 508-514.
246. Reed, B.B., et al., *Effect of resin composition on kinetics of dimethacrylate photopolymerization.* American Chemical Society, Polymer Preprints, Division of Polymer Chemistry, 1997. **38**: p. 108-109.
247. Yap, A.U.J., J.S. Low, and L. Ong, *Effect of food-simulating liquids on surface characteristics of composite and polyacid-modified composite restoratives.* Operative Dentistry, 2000. **25**(3): p. 170-176.
248. Chaiyabutr, Y., R. Giordano, and R. Pober, *The Effect of Different Powder Particle Size on Mechanical Properties of Sintered Alumina, Resin- and Glass-Infused Alumina.* Journal of Biomedical Materials Research Part B-Applied Biomaterials, 2009. **88B**(2): p. 502-508.
249. Della Bona, A., P.H. Corazza, and Y. Zhang, *Characterization of a polymer-infiltrated ceramic-network material.* Dental Materials, 2014. **30**(5): p. 564-569.
250. Blatz, M.B., A. Sadan, and M. Kern, *Resin-ceramic bonding: A review of the literature.* The Journal of Prosthetic Dentistry, 2003. **89**(3): p. 268-274.
251. Pape, P.G., *25 - Adhesion Promoters: Silane Coupling Agents*, in *Applied Plastics Engineering Handbook (Second Edition)*, M. Kutz, Editor. 2017, William Andrew Publishing. p. 555-572.
252. Naik, A., S.M. Best, and R.E. Cameron, *The influence of silanisation on the mechanical and degradation behaviour of PLGA/HA composites.* Materials Science & Engineering C-Materials for Biological Applications, 2015. **48**: p. 642-650.
253. Gré, C., et al., *Effect of Silanization on Microtensile Bond Strength of Different Resin Cements to a Lithium Disilicate Glass Ceramic.* The Journal of Contemporary Dental Practice, 2016. **17**: p. 149-153.
254. Brentel, A.S., et al., *Microtensile bond strength of a resin cement to feldpathic ceramic after different etching and silanization regimens in dry and aged conditions.* Dental Materials, 2007. **23**(11): p. 1323-1331.
255. Bona, A., K. Anusavice, and C. Shen, *Microtensile strength of composite bonded to hot-pressed ceramic.* The Journal of Adhesive Dentistry, 2000. **2**(4): p. 305-313.
256. Kupiec, K.A., et al., *Evaluation of porcelain surface treatments and agents for composite-to-porcelain repair.* The Journal of Prosthetic Dentistry, 1996. **76**(2): p. 119-124.
257. Guazzato, M., et al., *Strength, fracture toughness and microstructure of a selection of all-ceramic materials. Part I. Pressable and alumina glass-infiltrated ceramics.* Dental Materials, 2004. **20**(5): p. 441-448.

258. Jongsma, L.A., C.J. Kleverlaan, and A.J. Feilzer, *Clinical success and survival of indirect resin composite crowns: Results of a 3-year prospective study.* Dental Materials, 2012. **28**(9): p. 952-960.
259. Arsecularatne, J.A., J.P. Dingeldein, and M. Hoffman, *An in vitro study of the wear mechanism of a leucite glass dental ceramic.* Biosurface and Biotribology, 2015. **1**(1): p. 50-61.
260. Daou, E.E., *Esthetic Prosthetic Restorations: Reliability and Effects on Antagonist Dentition.* Open Dentistry Journal, 2015. **9**: p. 473-481.
261. Donovan, T.E., *Factors essential for successful all-ceramic restorations.* Journal of the American Dental Association, 2008. **139**: p. 14S-18S.
262. Archard, J.F., *Contact and Rubbing of Flat Surfaces.* Journal of Applied Physics, 1953. **24**(8): p. 981-988.
263. Wegner, L.D. and L.J. Gibson, *The fracture toughness behaviour of interpenetrating phase composites.* International Journal of Mechanical Sciences, 2001. **43**(8): p. 1771-1791.
264. Kim, K.H., J.L. Ong, and O. Okuno, *The effect of filler loading and morphology on the mechanical properties of contemporary composites.* Journal of Prosthetic Dentistry, 2002. **87**(6): p. 642-649.
265. da Silva, L.H., et al., *Dental ceramics: a review of new materials and processing methods.* Brazilian Oral Research, 2017. **31**: p. 133-146.
266. Andersson, M. and A. Odén, *A new all-ceramic crown: A dense-sintered, high-purity alumina coping with porcelain.* Acta Odontologica Scandinavica, 1993. **51**(1): p. 59-64.
267. Zeng, K.Y., A. Oden, and D. Rowcliffe, *Flexure tests on dental ceramics.* International Journal of Prosthodontics, 1996. **9**(5): p. 434-439.
268. Li, W. and J. Sun, *Effects of Ceramic Density and Sintering Temperature on the Mechanical Properties of a Novel Polymer-Infiltrated Ceramic-Network Zirconia Dental Restorative (Filling) Material.* Medical Science Monitor, 2018. **24**: p. 3068-3076.
269. Wong, C.P. and R.S. Bollampally, *Thermal conductivity, elastic modulus, and coefficient of thermal expansion of polymer composites filled with ceramic particles for electronic packaging.* Journal of Applied Polymer Science, 1999. **74**(14): p. 3396-3403.
270. Gracis, S., et al., *A new classification system for all-ceramic and ceramic-like restorative materials.* The International Journal of Prosthodontics, 2015. **28**(3): p. 227-35.
271. Cadenaro, M., et al., *Contraction stress, elastic modulus, and degree of conversion of three flowable composites.* European Journal of Oral Sciences, 2011. **119**(3): p. 241-245.
272. Ichim, I.P., et al., *Restoration of non-carious cervical lesions - Part II. Restorative material selection to minimise fracture.* Dental Materials, 2007. **23**(12): p. 1562-1569.
273. Hudson, J.D., G.R. Goldstein, and M. Georgescu, *Enamel wear caused by three different restorative materials.* The Journal of Prosthetic Dentistry, 1995. **74**(6): p. 647-654.

274. Koizumi, H., et al., *Surface roughness and gloss of current CAD/CAM resin composites before and after toothbrush abrasion.* Dental Materials Journal, 2015. **34**(6): p. 881-887.
275. Chavali, R., A.H. Nejat, and N.C. Lawson, *Machinability of CAD-CAM materials.* Journal of Prosthetic Dentistry, 2017. **118**(2): p. 194-199.
276. Badawy, R., O. El-Mowafy, and L.E. Tam, *Fracture toughness of chairside CAD/CAM materials – Alternative loading approach for compact tension test.* Dental Materials, 2016. **32**(7): p. 847-852.
277. Awaji, H., T. Matsunaga, and S.M. Choi, *Relation between strength, fracture toughness, and critical frontal process zone size in ceramics.* Materials Transactions, 2006. **47**(6): p. 1532-1539.
278. Zhao, H., et al., *Cloning Nacre's 3D Interlocking Skeleton in Engineering Composites to Achieve Exceptional Mechanical Properties.* Advanced Materials, 2016. **28**(25): p. 5099-5105.
279. Walmsley, A.D., *Restorative Dentistry E-Book*. 2007: Churchill Livingstone.
280. Naleway, S.E., et al., *Reproducibility of ZrO2-based freeze casting for biomaterials.* Materials Science and Engineering: C, 2016. **61**: p. 105-112.

Appendix: Publications, presentations and awards

1. A published paper from the results of Chapter 4.

Journal of the European Ceramic Society 39 (2019) 514–521

Contents lists available at ScienceDirect

Journal of the European Ceramic Society

journal homepage: www.elsevier.com/locate/jeurceramsoc

Original Article

Bi-directional freeze casting of porous alumina ceramics: A study of the effects of different processing parameters on microstructure

Sana Algharaibeh[a,b,*], Anthony J. Ireland[a], Bo Su[a,*]

[a] Biomaterials Engineering Group (bioMEG), Bristol Dental School, University of Bristol, UK
[b] Prosthodontics Department, Faculty of Dentistry, Jordan University of Science and Technology, Jordan

2. Received best poster presentation award by presenting a poster titled “Fabrication and characterisation of biomimetic ceramic/polymer composites for CAD/CAM dental blocks “at Postgraduate research day event held by the Faculty of health sciences on September 2018. Authors: Sana Algharaibeh, Hongbo Wan, Antony J. Ireland, Bo Su.
3. Presented a poster on the topic “Preparation and Characterization of Aligned Alumina Scaffolds using Bi-directional Freeze Casting” in the 15th Conference and Exhibition of the European Ceramic Society (ECerS2017) held at Budapest, Hungry (July 2017). Authors: Sana Algharaibeh, Bo Su.